

UNIVERSITY OF CALGARY

Some Analytical and Numerical Solutions for the Horizontal Displacement that Results
from the Loading of Simple Earth Models

by

Kimberley Ivy Marie O'Keefe

A THESIS

SUBMITTED TO THE FACULTY OF GRADUATE STUDIES
IN PARTIAL FULFILLMENT OF THE REQUIREMENTS FOR THE
DEGREE OF MASTER OF SCIENCE

DEPARTMENT OF GEOLOGY AND GEOPHYSICS

CALGARY, ALBERTA

APRIL, 2000

© Kim O'Keefe 2000



National Library
of Canada

Acquisitions and
Bibliographic Services

395 Wellington Street
Ottawa ON K1A 0N4
Canada

Bibliothèque nationale
du Canada

Acquisitions et
services bibliographiques

395, rue Wellington
Ottawa ON K1A 0N4
Canada

Your file Votre référence

Our file Notre référence

The author has granted a non-exclusive licence allowing the National Library of Canada to reproduce, loan, distribute or sell copies of this thesis in microform, paper or electronic formats.

The author retains ownership of the copyright in this thesis. Neither the thesis nor substantial extracts from it may be printed or otherwise reproduced without the author's permission.

L'auteur a accordé une licence non exclusive permettant à la Bibliothèque nationale du Canada de reproduire, prêter, distribuer ou vendre des copies de cette thèse sous la forme de microfiche/film, de reproduction sur papier ou sur format électronique.

L'auteur conserve la propriété du droit d'auteur qui protège cette thèse. Ni la thèse ni des extraits substantiels de celle-ci ne doivent être imprimés ou autrement reproduits sans son autorisation.

0-612-55231-4

Canada

Abstract

As a result of glacial isostatic adjustment the Earth's surface is experiencing a slow, three-dimensional deformation. This thesis presents a detailed study of the horizontal aspect of this deformation, parallel to the surface of the Earth. The analytical solutions for the horizontal displacement that results from the loading of simple earth models are derived from the set of equations that describe the system. Numerical results using the mathematical manipulation program, Matlab, and the finite element modeling program, ABAQUS, are found to be accurate through comparisons with the analytical solutions. ABAQUS is used to study the effect of loading on more complex earth models that include lateral variations, nonlinear rheology and time dependent creep. For most models a maximum horizontal displacement is obtained at the edge of the load. This motion is found to be most sensitive to the thickness of the elastic lithosphere, lateral variations and nonlinear rheology.

Acknowledgments

I would like to thank my supervisor, Patrick Wu, for his financial and moral support, and his invaluable advice and guidance. I would also like to thank NSERC and the University of Calgary for their financial support. Lastly, I would like to thank my husband for his helpful suggestions.

Table Of Contents

	Page
Approval Page	ii
Abstract	iii
Acknowledgments	iv
Table of Contents	v
List of Tables	vii
List of Figures	viii
List of Symbols	xvi
1. INTRODUCTION	1
2. BASIC THEORETICAL CONCEPTS	
2.1 Basic Equations	9
2.2 The Theorem of Correspondence	12
2.3 Equations of Motion in the Transformed (k,s) Domain	
2.3a Differential Equations for the Incompressible Earth	16
2.3b Solution to the Differential Equations	27
2.4 Solution in the Time Domain	
2.4a Spectral Method	34
2.4b Numerical Application of the Spectral Method	39
2.5 Numerical Solution in the Space Domain	
2.5a Solution Using the Inverse Hankel Transform	42
2.5b Solution from the Finite Element Method	46
3. INCOMPRESSIBLE, SELF-GRAVITATING UNIFORM EARTH: ANALYTICAL AND NUMERICAL SOLUTIONS	
3.1 The Analytical Solution in the (k,s) Domain	48
3.2 Relaxation Diagram	53
3.3 Excitation Strength Diagrams	60
3.4 Space Domain Solution	65

4.	ANALYSIS OF MORE COMPLICATED EARTH MODELS IN THE (k,s) DOMAIN	
4.1	The Channel Model	
4.1a	The Analytical Solution	70
4.1b	The Relaxation and Excitation Strength Diagrams	73
4.2	The Model of an Elastic Lithosphere Overlying a Halfspace	
4.2a	Analytical Solution for the Model of a Lithosphere Overlying a Fluid Halfspace	84
4.2b	Relaxation and Excitation Strength Diagrams for the Model of a Lithosphere Overlying a Viscoelastic Halfspace	88
4.3	Relaxation and Excitation Strength Diagrams for More Complicated Earth Models	
4.3a	Models with a Single Density Discontinuity	101
4.3b	Models with a Single Shear Modulus Discontinuity	110
4.3c	Models with a Low Viscosity Channel	118
5.	SPACE DOMAIN SOLUTIONS	
5.1	Halfspace and Channel Models	122
5.2	The Lithosphere over a Halfspace Model	
5.2a	Models with Lateral Homogeneity	131
5.2b	Models with Lateral Heterogeneity	136
5.3	The Low Viscosity Asthenosphere with a Lithosphere Model	144
5.4	Nonlinear Rheology	155
5.5	Time Dependent Creep	167
6.	CONCLUSIONS	171
	REFERENCES	175
APPENDIX A	THE EQUATION OF MOTION	179
APPENDIX B	THE CONSTITUTIVE RELATION	185
APPENDIX C	DERIVATION OF THE CORRESPONDENCE THEOREM	187
APPENDIX D	THE ANALYTICAL SOLUTION FOR THE HALFSPACE MODEL	191
APPENDIX E	THE ANALYTICAL SOLUTION FOR THE CHANNEL MODEL	201

List of Tables

	Page
Table 1: The Normalization Scheme	24
Table 2: The Material Properties of the Halfspace Model	51
Table 3: The Material Properties of the Channel Model	72
Table 4: The Material Properties of the Model of a Lithosphere over a Fluid	86
Table 5: The Material Properties of the Lithosphere Model	88
Table 6: The Material Properties of the Model with a Single Density Discontinuity	102
Table 7: The Material Properties of the Model with a Single Shear Modulus Discontinuity	110
Table 8: The Material Properties of the Model with a Low Viscosity Layer	118
Table 9: The Material Properties of the Lithosphere Model for Comparison with Nonlinear Rheology Models	156
Table 10: The Material Properties of the Models with Nonlinear Rheology	157

List of Figures

	Page
Figure 1.1: An example of VLBI baselines used to obtain baseline length rates (Mitrovica et al., 1993)	2
Figure 1.2: An example of the rates of change of the baseline lengths (Mitrovica et al., 1993)	3
Figure 1.3: Results from seismic tomography (Li and Romanowicz, 1996)	5
Figure 1.4: The halfspace and channel models	6
Figure 3.1.1: A graph of the vertical displacement at a depth of 100 km in the (k,s) domain that results from the loading of a halfspace	52
Figure 3.1.2: A graph of the horizontal displacement at a depth of 100 km in the (k,s) domain that results from the loading of a halfspace	52
Figure 3.2.1: The analytical determinant function of the halfspace model as a function of s compared with numerical results from Matlab	55
Figure 3.2.2: A comparison between the normalized and unnormalized determinant functions of the halfspace model with both the numerical and analytical results	55
Figure 3.2.3: The relaxation diagram for the halfspace model (reference model)	58
Figure 3.2.4: The relaxation diagram for a halfspace with a viscosity of 1×10^{23} Pa s (black) and the reference model (grey)	58
Figure 3.2.5: The relaxation diagram for a halfspace with a density of 3380 kg m^{-3} (black) and the reference model (grey)	59
Figure 3.2.6: The relaxation diagram for a halfspace with a density of 3380 kg m^{-3} and a shear modulus of $0.67 \times 10^{11} \text{ N m}^{-2}$ (black) and the reference model (grey)	59
Figure 3.3.1: The vertical displacement excitation strength for the halfspace model (reference model)	63
Figure 3.3.2: The vertical displacement excitation strength for a halfspace with a viscosity of 1×10^{23} Pa s (black) and the reference model (grey)	63
Figure 3.3.3: The vertical displacement excitation strength for a halfspace with a density of 3380 kg m^{-3} (black) and the reference model (grey)	64
Figure 3.3.4: The vertical displacement excitation strength for a halfspace	64

	with a density of 3380 kg m^{-3} and a shear modulus of $0.67 \times 10^{11} \text{ N m}^{-2}$ (black) and the reference model (grey)	
Figure 3.4.1:	Graph of the vertical displacement that results from the loading of a halfspace with a viscosity of $1 \times 10^{21} \text{ Pa s}$ and a load radius of 2000 km; results from the analytical solution, the Matlab numerical solution and the ABAQUS numerical solution	67
Figure 3.4.2:	The vertical displacement of a halfspace with a viscosity of $1 \times 10^{23} \text{ Pa s}$	68
Figure 3.4.3:	The vertical displacement for a halfspace with a 1000 km radius load	68
Figure 4.1.1:	The relaxation diagram of the channel model (reference model)	74
Figure 4.1.2:	The horizontal displacement excitation strength for the channel model (reference model)	75
Figure 4.1.3:	The vertical displacement excitation strength for the channel model (reference model)	75
Figure 4.1.4:	The relaxation diagram for a channel with a viscosity of $1 \times 10^{19} \text{ Pa s}$ (black) and the reference model (grey)	78
Figure 4.1.5:	The relaxation diagram for a channel with a density of 3380 kg m^{-3} (black) and the reference model (grey)	78
Figure 4.1.6:	The relaxation diagram for a channel with a shear modulus of $0.67 \times 10^{11} \text{ N m}^{-2}$ (black) and the reference model (grey)	79
Figure 4.1.7:	The relaxation diagram for a 200 km thick channel (black) and the reference model (grey)	79
Figure 4.1.8:	The horizontal displacement excitation strength for a channel with a viscosity of $1 \times 10^{19} \text{ Pa s}$ (black) and the reference model (grey)	80
Figure 4.1.9:	The horizontal displacement excitation strength for a channel with a density of 3380 kg m^{-3} (black) and the reference model (grey)	80
Figure 4.1.10:	The horizontal displacement excitation strength for a channel with a shear modulus of $0.67 \times 10^{11} \text{ N m}^{-2}$ (black) and the reference model (grey)	81
Figure 4.1.11:	The horizontal displacement excitation strength for a 200 km thick channel (black) and the reference model (grey)	81
Figure 4.1.12:	The vertical displacement excitation strength for a channel with a viscosity of $1 \times 10^{19} \text{ Pa s}$ (black) and the reference model (grey)	82

Figure 4.1.13: The vertical displacement excitation strength for a channel with a density of 3380 kg m^{-3} (black) and the reference model (grey)	82
Figure 4.1.14: The vertical displacement excitation strength for a channel with a shear modulus of $0.67 \times 10^{11} \text{ N m}^{-2}$ (black) and the reference model (grey)	83
Figure 4.1.15: The vertical displacement excitation strength for a 200 km thick channel (black) and the reference model (grey)	83
Figure 4.2.1: The reference model for a lithosphere overlying a fluid	84
Figure 4.2.2: A comparison between the analytical and numerical solutions for the horizontal displacement in the k domain of the model of a lithosphere overlying a fluid	87
Figure 4.2.3: A comparison between the analytical and numerical solutions for the vertical displacement in the k domain of the model of a lithosphere overlying a fluid	87
Figure 4.2.4: The lithosphere model	91
Figure 4.2.5: The relaxation diagram for the model of an elastic lithosphere overlying a viscoelastic halfspace (reference model)	91
Figure 4.2.6: The horizontal displacement excitation strength for the model of an elastic lithosphere overlying a viscoelastic halfspace (reference model)	92
Figure 4.2.7: The vertical displacement excitation strength for the model of an elastic lithosphere overlying a viscoelastic halfspace (reference model)	92
Figure 4.2.8: The relaxation diagram for the lithosphere model with a halfspace viscosity of $1 \times 10^{23} \text{ Pa s}$ and the reference model	95
Figure 4.2.9: The relaxation diagram for the lithosphere model with a model density of 3380 kg m^{-3} and the reference model	95
Figure 4.2.10: The relaxation diagram for the lithosphere model with a halfspace shear modulus of $0.67 \times 10^{11} \text{ N m}^{-2}$ and the reference model	96
Figure 4.2.11: The relaxation diagram for a lithosphere model with a 50 km thick lithosphere and the reference model	96
Figure 4.2.12: The horizontal displacement excitation strength for the lithosphere model with a halfspace viscosity of $1 \times 10^{23} \text{ Pa s}$ and the reference model	97
Figure 4.2.13: The horizontal displacement excitation strength for the lithosphere model with a model density of 3380 kg m^{-3}	97

	and the reference model	
Figure 4.2.14:	The horizontal displacement excitation strength for the lithosphere model with a halfspace shear modulus of $0.67 \times 10^{11} \text{ N m}^{-2}$ and the reference model	98
Figure 4.2.15:	The horizontal displacement excitation strength for a lithosphere model with a 50 km thick lithosphere and the reference model	98
Figure 4.2.16:	The vertical displacement excitation strength for the lithosphere model with a halfspace viscosity of $1 \times 10^{23} \text{ Pa s}$ and the reference model	99
Figure 4.2.17:	The vertical displacement excitation strength for the lithosphere model with a model density of 3380 kg m^{-3} and the reference model	99
Figure 4.2.18:	The vertical displacement excitation strength for the lithosphere model with a halfspace shear modulus of $0.67 \times 10^{11} \text{ N m}^{-2}$ and the reference model	100
Figure 4.2.19:	The vertical displacement excitation strength for a lithosphere model with a 50 km thick lithosphere and the reference model	100
Figure 4.3.1:	The reference model with a single density discontinuity	102
Figure 4.3.2:	The relaxation diagram for a model a model with a single density discontinuity (reference model)	105
Figure 4.3.3:	The relaxation diagram for a model with a single density discontinuity at a depth of 200 km and the reference model	105
Figure 4.3.4:	The relaxation diagram for a model with a single density discontinuity and an upper layer density of 3380 kg m^{-3} and the reference model	106
Figure 4.3.5:	The horizontal displacement excitation strength for a model with a single density discontinuity (reference model)	106
Figure 4.3.6:	The horizontal displacement excitation strength for a model with a single density discontinuity at a depth of 200 km and the reference model	107
Figure 4.3.7:	The horizontal displacement excitation strength for a model with a single density discontinuity and an upper layer density of 3380 kg m^{-3} and the reference model	107
Figure 4.3.8:	The vertical displacement excitation strength for a model with a single density discontinuity (reference model)	108
Figure 4.3.9:	The vertical displacement excitation strength for a model with a single density discontinuity at a depth of 200 km	108

	and the reference model	
Figure 4.3.10:	The vertical displacement excitation strength for a model with a single density discontinuity and an upper layer density of 3380 kg m^{-3} and the reference model	109
Figure 4.3.11:	The reference model with a single shear modulus discontinuity	110
Figure 4.3.12:	The relaxation diagram for a model with a single shear modulus discontinuity (reference model)	113
Figure 4.3.13:	The relaxation diagram for a model with a single shear modulus discontinuity with an upper layer shear modulus of $0.67 \times 10^{11} \text{ N m}^{-2}$ and the reference model	113
Figure 4.3.14:	The relaxation diagram for a model with a single shear modulus at a depth of 200 km and the reference model	114
Figure 4.3.15:	The horizontal displacement excitation strength for a model with a single shear modulus discontinuity (reference model)	114
Figure 4.3.16:	The horizontal displacement excitation strength for a model with a single shear modulus discontinuity with an upper layer shear modulus of $0.67 \times 10^{11} \text{ N m}^{-2}$ and the reference model	115
Figure 4.3.17:	The horizontal displacement excitation strength for a model with a single shear modulus discontinuity at a depth of 200 km and the reference model	115
Figure 4.3.18:	The vertical displacement excitation strength for a model with a single shear modulus discontinuity (reference model)	116
Figure 4.3.19:	The vertical displacement excitation strength for a model with a single shear modulus discontinuity with an upper layer shear modulus of $0.67 \times 10^{11} \text{ N m}^{-2}$ and the reference model	116
Figure 4.3.20:	The vertical displacement excitation strength for a model with a single shear modulus discontinuity at a depth of 200 km and the reference model	117
Figure 4.3.21:	The reference model for a model with a low viscosity asthenosphere	117
Figure 4.3.22:	The relaxation diagram for the low viscosity channel model	120
Figure 4.3.23:	The horizontal displacement excitation strength for the low viscosity channel model	120
Figure 4.3.24:	The vertical displacement excitation strength for the low viscosity channel model	121

Figure 5.1.1: The vertical displacement for the halfspace model	124
Figure 5.1.2: The vertical displacement for a halfspace with viscosity variations	125
Figure 5.1.3: The horizontal displacement for a halfspace with radial viscosity variations	125
Figure 5.1.4: Comparison between different methods for the horizontal displacement that results from the loading of a channel model	126
Figure 5.1.5: Comparison between different methods for the vertical displacement that results from the loading of a channel model	126
Figure 5.1.6: The horizontal displacement for a channel with a viscosity of 1×10^{19} Pa s	129
Figure 5.1.7: The horizontal displacement for a channel with a 1000 km radius load and a viscosity of 1×10^{21} Pa s	129
Figure 5.1.8: The vertical displacement for a channel with a viscosity of 1×10^{19} Pa s	130
Figure 5.1.9: The vertical displacement for a channel with a 1000 km radius load and a viscosity of 1×10^{21} Pa s	130
Figure 5.2.1: The comparison of four different methods in determining the displacement that results from the loading of a 150 km thick, elastic lithosphere overlying a fluid	132
Figure 5.2.2: A comparison between two different methods for the horizontal displacement that results from the loading of a lithosphere model with a 150 km thick lithosphere	134
Figure 5.2.3: A comparison between two different methods for the vertical displacement that results from the loading of a lithosphere model with a 150 km thick lithosphere	135
Figure 5.2.4: The earth model of a laterally heterogeneous halfspace viscosity	139
Figure 5.2.5: The earth model of a laterally heterogeneous lithospheric thickness	139
Figure 5.2.6: The horizontal displacement for the lithosphere with a halfspace viscosity of 1×10^{23} Pa s	140
Figure 5.2.7: The horizontal displacement for the model in Figure 5.2.4	140
Figure 5.2.8: The vertical displacement for the lithosphere with a halfspace viscosity of 1×10^{23} Pa s	141
Figure 5.2.9: The vertical displacement for the model in Figure 5.2.4	141
Figure 5.2.10: The horizontal displacement for the lithosphere model with a 50 km thick lithosphere	142

Figure 5.2.11: The horizontal displacement for the model in Figure 5.2.5	142
Figure 5.2.12: The vertical displacement for the lithosphere model with a 50 km thick lithosphere	143
Figure 5.2.13: The vertical displacement for the model in Figure 5.2.5	143
Figure 5.3.1: The horizontal displacement for the low viscosity asthenosphere model	146
Figure 5.3.2: The vertical displacement for the low viscosity asthenosphere model	146
Figure 5.3.3: The earth model of a laterally heterogeneous low viscosity asthenosphere viscosity	150
Figure 5.3.4: The earth model of a laterally heterogeneous low viscosity asthenosphere thickness	150
Figure 5.3.5: The horizontal displacement for the low viscosity asthenosphere model with an asthenosphere viscosity of 1×10^{20} Pa s	151
Figure 5.3.6: The horizontal displacement for the model in Figure 5.3.3	151
Figure 5.3.7: The vertical displacement for the low viscosity asthenosphere model with an asthenosphere viscosity of 1×10^{20} Pa s	152
Figure 5.3.8: The vertical displacement for the model in Figure 5.3.3	152
Figure 5.3.9: The horizontal displacement for the low viscosity asthenosphere model with a 200 km thick asthenosphere	153
Figure 5.3.10: The horizontal displacement for the model in Figure 5.3.4	153
Figure 5.3.11: The vertical displacement for the low viscosity asthenosphere model with a 200 km thick asthenosphere	154
Figure 5.3.12: The vertical displacement for the model in Figure 5.3.4	154
Figure 5.4.1: The earth models with nonlinear zones	160
Figure 5.4.2: The horizontal displacement for the lithosphere model with linear rheology	161
Figure 5.4.3: The vertical displacement for the lithosphere model with linear rheology	161
Figure 5.4.4: The horizontal displacement for the nonlinear halfspace model	162
Figure 5.4.5: The vertical displacement for the nonlinear halfspace model	162
Figure 5.4.6: The horizontal displacement for the model in Figure 5.4.1a	163
Figure 5.4.7: The vertical displacement for the model in Figure 5.4.1a	163
Figure 5.4.8: The horizontal displacement for the model in Figure 5.4.1b	164
Figure 5.4.9: The vertical displacement for the model in Figure 5.4.1b	164
Figure 5.4.10: The horizontal displacement for the model in Figure 5.4.1c	165
Figure 5.4.11: The vertical displacement for the model in Figure 5.4.1c	165

Figure 5.4.12: The horizontal displacement for the model in Figure 5.4.1d	166
Figure 5.4.13: The vertical displacement for the model in Figure 5.4.1d	166
Figure 5.5.1: The horizontal displacement for a time dependent creep model with $m = -0.05$ in the mantle	169
Figure 5.5.2: The vertical displacement for a time dependent creep model with $m = -0.05$ in the mantle	169
Figure 5.5.3: The horizontal displacement for a time dependent creep model with $m = -0.2$ in the mantle	170
Figure 5.5.4: The vertical displacement for a time dependent creep model with $m = -0.2$ in the mantle	170

List of Symbols

<u>symbol</u>	<u>definition</u>
U, u	horizontal displacement
W, w	vertical displacement
T_{rz}	shear stress
T_{zz}	normal stress
ρ	density
μ	shear modulus
k	radial wavenumber
g	gravitational acceleration
ν	viscosity
z	depth
s	Laplace transform variable
t	time
r	radial distance

Chapter 1: Introduction

Periodically, large ice masses have formed to cover most of North America and Northern Europe. Each glacial event is defined by a slow accumulation of snow and ice to form continental sized ice sheets followed by a rapid disappearance of the glaciers.

Accumulation occurs over a period of about 100 000 years and the disappearance occurs within 20 000 years. The most recent glacial maximum occurred about 18 000 years ago.

The weight of these ice masses caused the land to subside. The subsequent removal of the ice occurred relatively quickly in geological time. Since the rate of the rebound of the land depends on the viscosity of the mantle, which is relatively high, regions previously covered by glaciers are still adjusting to the new isostatic conditions. This glacial isostatic adjustment of the Earth's surface involves three dimensional motion of the surface and variations in the stresses experienced within the crust. The evolution of the stresses and displacements of the surface can be determined and compared with predicted values obtained from computer modeling to estimate the evolution of the glacial load, the structure of the subsurface and the time and location of glacial induced earthquakes.

The most commonly studied aspect of glacial isostatic adjustment is the vertical displacement associated with land uplift (Peltier, 1973; Cathles, 1975). This is due to the fact that it is the most easily measured aspect of the adjustment since the height and age of ancient beaches can be directly measured. However, another important aspect of the motion is the horizontal motion, which, until recently, has been very difficult to measure. With the advent of new technologies such as GPS (Global Positioning System) and VLBI (Very Long Baseline Interferometry), it is now possible to obtain accurate measurements of the three dimensional motion of the Earth's surface (Tushingham, 1991; James and

Lambert, 1993; Mitrovica et al., 1994). If measurements are taken in regions that were previously covered by glaciers and far from the significant effects of tectonics then any motion present is interpreted as glacial isostatic adjustment. This gives an additional constraint in determining both ice and earth models. An example of the data obtained from VLBI is given in Figures 1.1 and 1.2. Figure 1.1 shows the locations of the base stations and Figure 1.2 gives the rates of change of the baseline lengths.

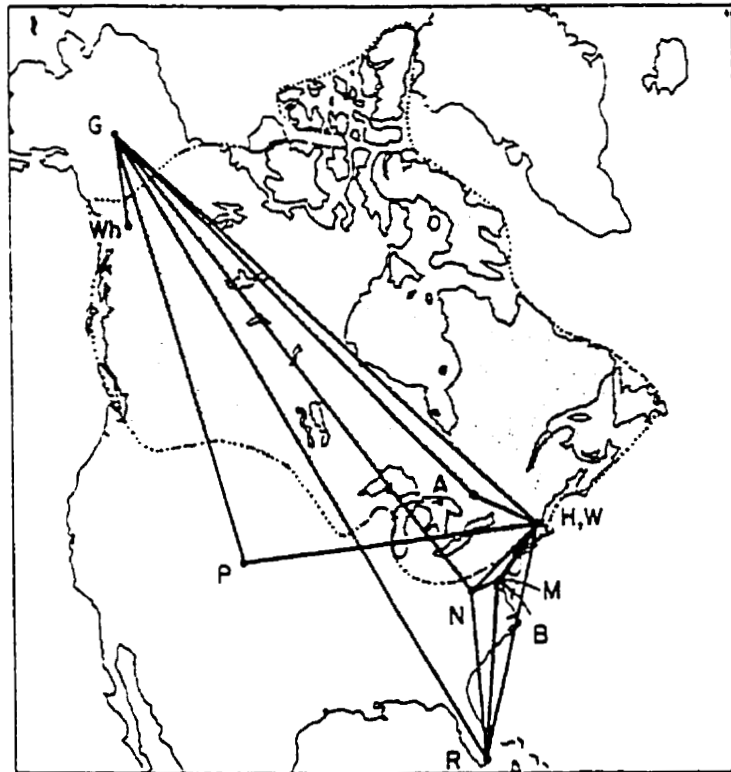


Figure 1.1: An example of VLBI baselines used to obtain baseline length rates (Mitrovica et al., 1993)

TABLE 1. GLBS6S Baseline Length Rates

Baseline	Rate (mm/yr)
Algonquin Park (A)-Gilmore Ck (G)	3.3 ± 0.5
Algonquin Park (A)-Westford (W)	-0.7 ± 0.5
Gilmore Ck (G)-Haystack (H)	-2.3 ± 2.2
Gilmore Ck (G)-NRAO 85 (N1)	-0.5 ± 1.1
Gilmore Ck (G)-Platteville (P)	5.5 ± 2.3
Gilmore Ck (G)-Richmond (R)	1.1 ± 1.2
Gilmore Ck (G)-Westford (W)	-0.4 ± 0.5
Gilmore Ck (G)-Whithorse (Wh)	-3.8 ± 3.5
Beltsville (B)-NRAO 85 (N1)	3.4 ± 1.3
Beltsville (B)-Richmond (R)	6.9 ± 2.5
Beltsville (B)-Westford (W)	0.0 ± 3.0
Haystack (H)-NRAO 140 (N2)	1.4 ± 2.0
Maryland Pt (M)-Richmond (R)	0.6 ± 4.4
Maryland Pt (M)-Westford (W)	1.4 ± 1.5
NRAO 85 (N1)-Richmond (R)	2.2 ± 0.9
NRAO 85 (N1)-Westford (W)	4.0 ± 2.0
NRAO 140 (N2)-Westford (W)	0.5 ± 0.3
Platteville (P)-Westford (W)	3.3 ± 2.2
Richmond (R)-Westford (W)	-0.2 ± 0.15

Figure 1.2: An example of the rates of change of the baseline lengths (Mitrovica et al., 1993)

The first study to investigate the horizontal motions that result from the removal of a load was done by James and Morgan (1990). Their preliminary results indicated that horizontal motions were more sensitive to changes in the thickness of the lithosphere than are vertical motions. Based on these findings it was recognized that a careful analysis of the horizontal motions that results from the removal of a load could constrain the possible characteristics of the subsurface. However, the ice and earth models that they used were rather simplistic and their results were not very accurate. As a result, James and Lambert (1993) undertook to characterize the horizontal motions using the more realistic ICE-3G deglaciation chronology (Tushingham and Peltier, 1991). They found that glacial rebound should be detectable by VLBI and that tangential velocities contributed more to baseline length change rates of shorter baselines. Mitrovica et al. (1993) determined that VLBI could be used to assess the acceptability of ice history and earth model pairings. Neither

of these studies, however, gave any indication of what types of tangential motions were experienced or what types of models might produce these motions.

Mitrovica et al. (1994) conducted a more detailed analysis of the displacement for various models by using realistic earth models and the ICE-3G loading history to obtain predicted patterns of the horizontal motions for North America and Europe based on specific earth and ice models. Results of Mitrovica et al. (1994) did not support the theory that the tangential motions are much more sensitive to details of the earth model (James and Lambert, 1993), but rather that the sensitivities are a strong function of geographic location and the specific parameter of the earth model and that lateral variations could have a significant impact on the results. The most recent consideration of horizontal motions have been done by D'Agostino et al. (1997) and Giunchi et al. (1997). Both of these papers studied the effect of lateral viscosity variations and deep mantle stratification on glacial rebound. They found that horizontal motions are more susceptible to changes in lateral variations than the corresponding vertical motions.

Recent seismological data suggest that lateral variations in the subsurface are widespread and significant. Figure 1.3 shows the results of seismic tomographic analysis. It is apparent that there does exist significant lateral variations. Therefore any accurate earth model must incorporate lateral variations in addition to radial variations. However, to date, there has been little attempt to systematically determine the effects of combined lateral and radial variations in viscosity together with changes in the thickness of the lithosphere. The only exceptions are Kaufmann et al. (1997) and Wu et al. (1998). In addition, it is difficult to determine whether the horizontal displacement predicted by the different models is accurate since there has been little analytical study of the horizontal displacement that results from the removal of a load.

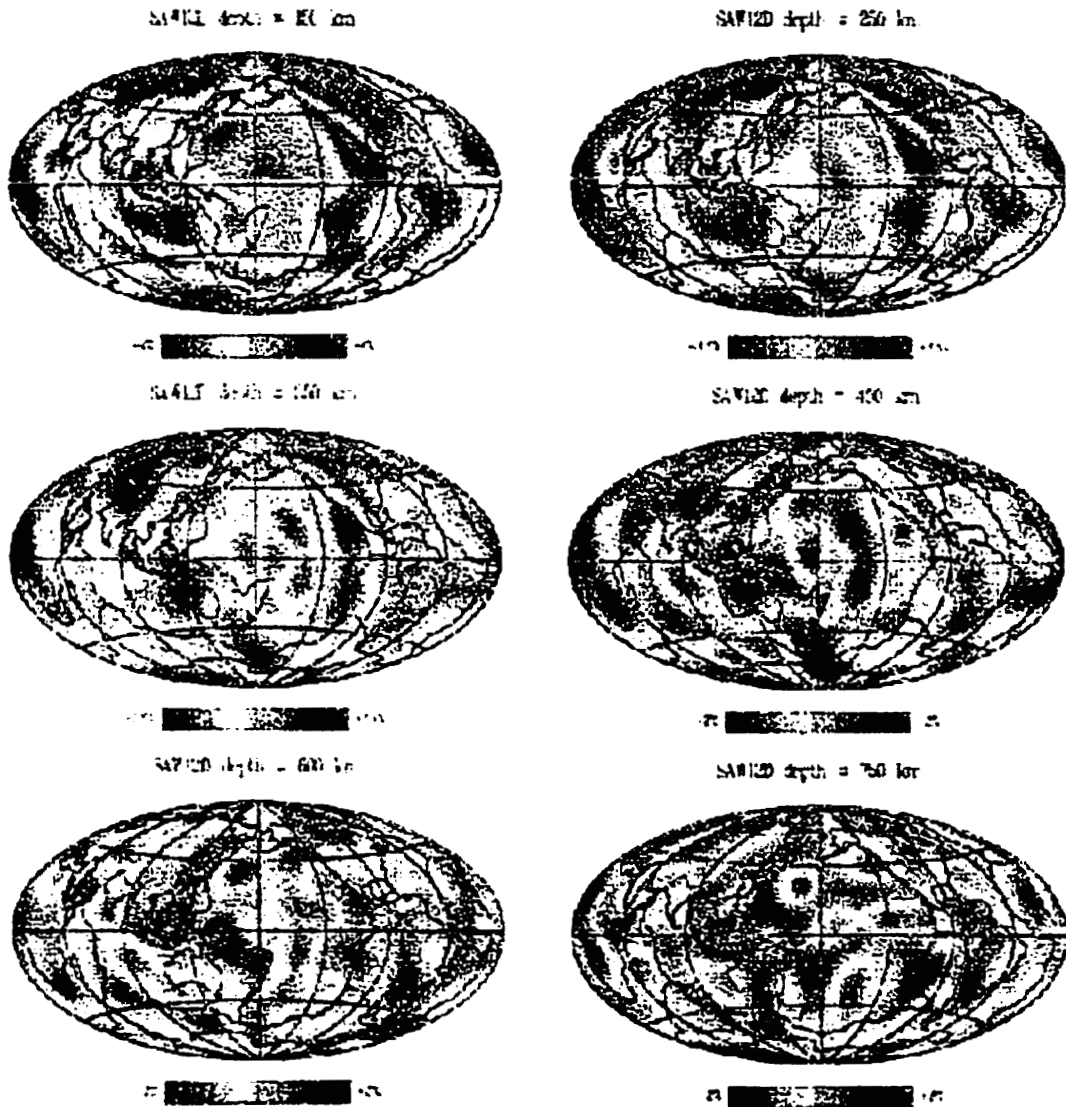


Figure 1.3: Results from seismic tomography (Li and Romanowicz, 1996)

The horizontal displacement has been shown to be sensitive to lateral variations in the subsurface (James and Morgan, 1990) while the vertical displacement tends to be more sensitive to radial variations. The combination of horizontal and vertical displacements provides additional information which can be used to more accurately characterize the structure and properties of the subsurface. While several papers have been written

analyzing horizontal motion data (James and Morgan, 1990; James and Lambert, 1993; Mitrovica et al., 1994; Wu and Ni, 1996), there has been no systematic study of the horizontal solutions which are required to constrain the numerical modeling.

The horizontal and vertical displacements that result from the loading of several different models have been examined in this thesis. Historically, there were two basic hypotheses proposed to explain the motion associated with glacial isostatic adjustment. These are the “down-punching hypothesis”, associated with the deep flow model, and the “bulge hypothesis” associated with the channel flow model (Cathles, 1975). These are illustrated in Figure 1.4.

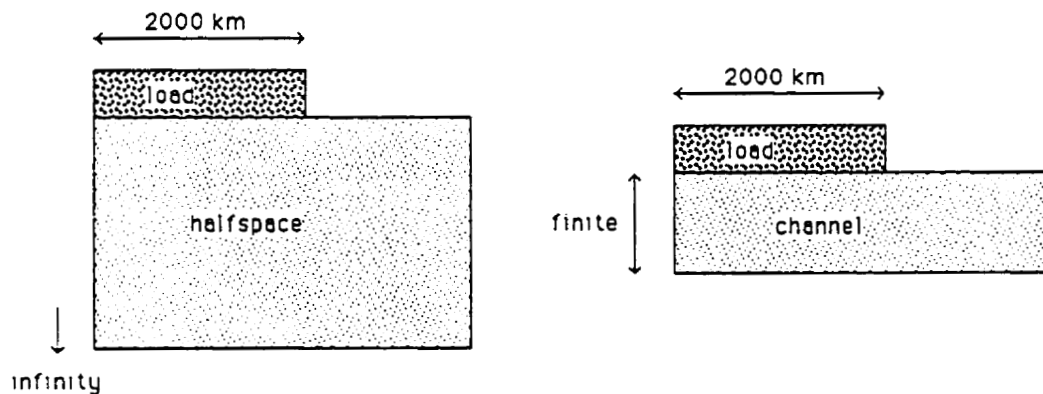


Figure 1.4: The halfspace (deep flow) and channel models

In the deep flow model there is an infinite amount of material to compensate for the weight of the load and the motion under the load is dominantly vertical; whereas the channel model has a finite amount of material and necessarily horizontal motions occur as well. These two simplistic models form the basis for the development of more detailed subsurface models.

The analytical solutions for the horizontal and vertical displacements associated with these two models are discussed in Chapters 3 and 4, as is the analytical solution for an elastic lithosphere overlying a fluid halfspace. These results are compared with some numerical calculations. In this way, not only are the motions well characterized, but the accuracy of the numerical methods is determined. The effects of variations in the density, the shear modulus and the thickness of various layers were determined. Using an advanced finite element modeling package called ABAQUS (Hibbitt, Karlsson and Sorensen, 1992) to determine the results numerically, it was possible to examine models with lateral variations, nonlinear rheology and time dependent creep. By analyzing the responses of these various models to loading it is possible to estimate the structure of the earth based on a comparison with known motions of the Earth's crust. Although the displacement is dependent on the ice loading history as well as the subsurface structure, it is possible to eliminate those models which are not appropriate.

The purpose of this thesis is to analyze the horizontal displacement that results from Heaviside loading of simple earth models. First a systematic study of the horizontal motions was completed so that the impact of various earth parameters on the horizontal displacement could be determined. This was done through the analysis of the analytical solutions for various models, and a comparison of the relaxation and excitation strength diagrams. The methods used for the analytical and numerical analyses are discussed in Chapters 2 and 3 and the analysis of the various models in the wavenumber domain is discussed in Chapter 4. All of the models are based on a flat, incompressible, viscoelastic earth. Next, the accuracy of the finite element modeling program ABAQUS (Hibbitt et al., 1992) was tested for the horizontal displacements. Once accuracy had been established, ABAQUS was used to determine the results of loading more complex models. The third goal of this thesis was to examine the horizontal motion that resulted from the

loading of earth models that included lateral heterogeneity, nonlinear rheology and time dependent creep. These results are discussed in Chapter 5. Based on these results the acceptability of various models was determined.

Modeling the subsurface is important not only to constrain tectonic and mantle convection models, but also to predict future motions of the crust. This will not only enable scientists to obtain more accurate GPS and VLBI readings for use with other applications, but also to estimate the occurrence of future earthquakes.

Chapter 2: Basic Theoretical Concepts

Many methods are used to study the effects of glacial isostatic adjustment. One method is to attempt to describe the motion in terms of a finite set of equations relating the properties of the system. In this thesis, the system is defined as a flat earth that may be stratified, though each layer has constant properties, with an impulse load in time. This load is defined as a circular disc load with constant mass, radius and height. This load is most easily described in cylindrical coordinates so this is the coordinate system used. In this chapter, the basic equations used to describe the loading of a viscoelastic layer will be discussed. These differential equations are solved for an appropriate load and appropriate boundary conditions. This is most easily accomplished through the use of the correspondence theorem which will be discussed in more detail in section 2.2. The correspondence theorem states that the viscoelastic solution in the Laplace transform domain can be obtained from the equivalent elastic solution where the elastic moduli are replaced by variables dependent on the Laplace transform variable, s . The solution is most easily obtained in the wavenumber domain since in this transform domain the function of the displacement is multiplied by the function of the load rather than requiring a convolution between the two. The equations that describe the system will be discussed in section 2.1 and the methods used to determine the solutions in the (k,s) domain, the time domain and the space domain will be given in sections 2.3, 2.4 and 2.5 respectively. These methods will be used to determine the analytical and numerical solutions associated with various earth models. The impact of variations in density, shear modulus, viscosity and layer thickness are discussed in Chapters 3, 4 and 5.

2.1: Basic Equations

This section will review the set of equations used to describe the loading of a viscoelastic layer. There are three basic equations to consider. These are:

- a. the equation of motion for a flat earth (Cathles, 1975, Appendix II)

$$\nabla \cdot \sigma - \rho g \nabla w + \rho g \hat{e}_z = 0 \quad (2.1.1)$$

where σ is the stress dyadic.

ρ is the density.

g is the gravitational acceleration.

w is the vertical displacement.

ε is the dilatation.

and \hat{e}_z is the unit vector in the vertical direction.

- b. the constitutive relation for a viscoelastic medium (the Navier-Stokes equation for a homogeneous, isotropic, elastic solid, i.e. Hookean elastic solid) (equation C.16)

$$\partial_i \sigma_{kl} + \frac{\mu}{\nu} (\sigma_{kl} - \frac{1}{3} \sigma_{kk} \delta_{kl}) = 2\mu \partial_i \varepsilon_{kl} + \lambda \partial_i \varepsilon_{kk} \delta_{kl} \quad (2.1.2)$$

where e_{kl} is the kl^{th} component of the strain tensor,

σ_{kl} is the kl^{th} component of the stress tensor.

λ and μ are the Lamé parameters,

δ_{kl} is the Dirac delta function,

and ν is the viscosity.

Note that for the incompressible case (Love, 1911):

$$\nabla \cdot \mathbf{u} = \varepsilon = 0 \quad (2.1.3)$$

where ε is the dilatation.

$$\varepsilon = \sum e_{ii} = e_{rr} + e_{\theta\theta} + e_{zz}$$

and \mathbf{u} is the displacement vector.

c. and the equation for the strain tensor (Malvern, 1969, equation (4.2.10))

$$e_{kl} = \frac{1}{2} \left(\frac{\partial u_k}{\partial x_l} + \frac{\partial u_l}{\partial x_k} \right) \quad (2.1.4)$$

where e_{kl} is the kl^{th} component of the strain tensor.

and $\frac{\partial u_k}{\partial x_l}$ is the displacement gradient.

Some of the assumptions associated with these equations are that the deformation processes are isothermal (constant temperature), that the displacements and displacement gradients are small, and that the Earth is flat, isotropic, and homogeneous with constant gravitational acceleration and density.

2.2: The Theorem of Correspondence

The correspondence theorem simply states that any viscoelastic system can be described by the set of equations for the corresponding elastic system expressed in the transformed Laplace domain, if λ is replaced by $\lambda(s)$ and μ is replaced by $\mu(s)$. This is useful in the interpretation of problems involving a viscous fluid because usually the equations for an elastic body are easier to solve.

Here is a brief example:

Consider the constitutive relations for two different cases: a Newtonian fluid and a Maxwell body. A Newtonian fluid is defined as a material in which there is a linear relationship between the stress and the rate of strain. The elastic solid (Hookean solid) and the viscous fluid (Newtonian fluid) represent the end members of viscoelastic bodies. When an elastic solid deforms, it experiences a strain proportional to the stress applied. Once the stress is removed, the body returns to its original state instantaneously. A simple example is a spring where the stress, σ , is proportional to the deformation or strain, e , and G is the constant of proportionality or spring strength; $\sigma = Ge$. A viscous fluid, however, experiences a stress proportional to the rate of deformation and has no tendency to return to its original state when the applied stress is removed. A simple example is a dashpot where the stress is related to the strain rate and η is called the viscosity; $\sigma = \eta \partial e$.

A simple viscoelastic model is the Maxwell model. It involves the combination of a spring and a dashpot in series. The constitutive relation for the one-dimensional case is (Mase, 1970, equation 9.3)

$$\frac{1}{G} \partial_i \sigma + \frac{1}{\eta} \sigma = \partial_i e \quad (2.2.1)$$

To determine the constitutive relation for the three dimensional case, the three dimensional expressions for the Hookean and Newtonian bodies are used. For the general three dimensional case the constitutive relation for the Hookean solid is

$$\sigma_{ij}^e = \lambda \delta_{ij} e_{kk}^e - 2\mu e_{ij}^e \quad (2.2.2)$$

where $\sigma_{rr}^e = (3\lambda + 2\mu) e_{rr}^e = 3\kappa^e \varepsilon = \kappa^e e_{rr}^e \delta_{ki}$

κ^e is the bulk modulus.

and ε is the dilatation.

and the constitutive relation for a Newtonian fluid is

$$\sigma_{ij}^v = (-P - \eta \partial_t e_{rr}^v) \delta_{ij} - 2\nu \partial_t e_{ij}^v \quad (2.2.3)$$

where η is the viscous dissipative coefficient,

ν is the Newtonian viscosity,

P is the thermodynamic pressure,

and $\sigma_{rr}^v = -3P + 3(\eta + \frac{2}{3}\nu) \partial_t e_{rr}^v$.

Following the derivation of the constitutive relation for a Maxwell body in three dimensions as given in Appendix C, we obtain equation (C.16):

$$\partial_i \sigma_{kl} + \frac{\mu}{\nu} (\sigma_{kl} - \frac{1}{3} \sigma_{kk} \delta_{kl}) = 2\mu \partial_i \epsilon_{kl} + \lambda \partial_i \epsilon_{kk} \delta_{kl}$$

This can be reduced to the following by performing the Laplace transform.

$$\sigma_{kl} \left(s + \frac{\mu}{\nu} \right) = 2\mu s \epsilon_{kl} + \left[\lambda s + \left(\lambda + \frac{2}{3} \mu \right) \frac{\mu}{\nu} \right] \epsilon_{rr} \delta_{kl} \quad (2.2.4)$$

or
$$\sigma_{kl} = 2\mu(s) \epsilon_{kl} - \lambda(s) \epsilon_{rr} \quad (2.2.5)$$

$$\text{where } \mu(s) = \frac{\mu s}{s + \frac{\mu}{\nu}} \quad (2.2.6)$$

$$\text{and } \lambda(s) = \frac{\left[\lambda s + \left(\lambda + \frac{2}{3} \mu \right) \frac{\mu}{\nu} \right]}{s + \frac{\mu}{\nu}} = \frac{\lambda s + \frac{\kappa \mu}{\nu}}{s + \frac{\mu}{\nu}} \quad (2.2.7)$$

where κ is the bulk modulus.

μ is the shear modulus.

λ is a Lamé constant,

and ν is the Newtonian viscosity.

Note that the bold variables represent variables in the transformed s domain. When equation (2.2.5) is compared with the constitutive relation for the elastic solid, they are identical in form with the exception that the stresses and strains have been transformed from the time domain to the s domain and the Lamé constants are dependent on s . This

demonstrates how the theorem of correspondence can be applied to the analysis of a viscoelastic problem. The viscoelastic problem and solution in the transformed domain have the same form as the elastic problem in the time domain so if the solution for the elastic case is known then the solution for the viscoelastic solution can easily be obtained by replacing μ and λ with $\mu(s)$ and $\lambda(s)$ respectively and performing the inverse Laplace transform. Also note that the impulse loading boundary condition for the viscoelastic earth is the same as constant loading on an elastic earth since the transform of $P_0\delta(t)$ is P_0 where P_0 is the constant pressure of the load.

2.3: Equations of Motion in the Transformed (k,s) Domain

This section will give the details of how the equations from section 2.1 are solved in the transformed domain. Transforming to the k domain removes a spatial differentiation so that a partial differential equation becomes an ordinary differential equation which is much easier to solve. The following section will give the solution in the time domain. Cylindrical coordinates are used with the variables r , θ , and z , to represent the three degrees of freedom. The (r, θ, z) components of the displacement correspond to (u, v, w) . Cylindrical symmetry is assumed so that all derivatives in terms of θ are zero and the displacement in the θ direction, v , is equal to zero.

2.3a: Differential Equations for the Incompressible Earth

The constraints for the incompressible case are that $\nabla \cdot \bar{u} = \varepsilon = 0$ and $\lim_{\substack{\varepsilon \rightarrow 0 \\ \lambda \rightarrow \infty}} \varepsilon \lambda = \Pi$.

The equation of motion for the incompressible flat earth, from section 2.1, is

$$\nabla \cdot \sigma - \rho g \nabla w = 0 \quad (2.3.1)$$

$$r\text{-component: } \partial_r \sigma_{rr} + \frac{1}{r} \partial_\theta \sigma_{r\theta} + \partial_z \sigma_{rz} + \frac{1}{r} (\sigma_{rr} - \sigma_{\theta\theta}) - \rho g \partial_r w = 0 \quad (2.3.2)$$

$$\theta\text{-component: } \partial_r \sigma_{r\theta} + 2 \frac{1}{r} \sigma_{r\theta} + \frac{1}{r} \partial_\theta \sigma_{\theta\theta} + \partial_z \sigma_{\theta z} - \frac{1}{r} \rho g \partial_\theta w = 0 \quad (2.3.3)$$

$$z\text{-component: } \partial_r \sigma_{rz} + \frac{1}{r} \sigma_{rz} + \frac{1}{r} \partial_\theta \sigma_{\theta z} + \partial_z \sigma_{zz} - \rho g \partial_z w = 0 \quad (2.3.4)$$

(from Malvern, 1969, Appendix II.4.C11)

The strain equations can be written as (from Malvern, 1969, Appendix II.4.C9)

$$\begin{aligned}
 e_{rr} &= \partial_r u \\
 e_{\theta\theta} &= \frac{u}{r} \\
 e_{zz} &= \partial_z w \\
 e_{\theta z} &= 0 \\
 e_{r\theta} &= 0 \\
 e_{rz} &= \frac{1}{2}(\partial_r w + \partial_z u) \\
 e &= e_{rr} + e_{\theta\theta} + e_{zz} = \frac{1}{r}\partial_r(ru) + \partial_z w
 \end{aligned} \tag{2.3.5}$$

and the stress-strain relationships are

$$\begin{aligned}
 \sigma_{rz} &= \mu(\partial_r w + \partial_z u) \\
 \sigma_{zz} &= -P + 2\mu(\partial_z w) \\
 \\
 \sigma_{r\theta} &= 0 \\
 \sigma_{\theta z} &= 0 \\
 \\
 \sigma_{rr} &= -P + 2\mu(\partial_r u) \\
 \sigma_{\theta\theta} &= -P + 2\mu\left(\frac{u}{r}\right)
 \end{aligned} \tag{2.3.6}$$

By inserting the appropriate stresses and strains into the equation of motion we obtain the following for the r and z components to the equation of motion, while the θ component reduces to zero.

$$r\text{-component: } -\partial_r P + 2\mu\partial_r^2 u + \partial_z \sigma_{rz} + \frac{2\mu}{r}\partial_r u - \frac{2\mu}{r}\frac{u}{r} - \rho g\partial_r w = 0 \tag{2.3.7}$$

$$z\text{-component: } \partial_r \sigma_{rz} + \frac{\mu}{r} \partial_r w + \frac{\mu}{r} \partial_z u + \partial_z \sigma_{zz} - \rho g \partial_z w = 0 \quad (2.3.8)$$

The stress divergence can also be written in terms of the displacement field. Therefore the equation of motion can be expressed exclusively by displacements. Therefore only the displacement field needs to be determined. According to the Helmholtz Decomposition Theorem, any vector can be expressed in terms of the gradient of a scalar potential and the curl of a vector potential. Therefore the displacement vector can be in the following way.

$$\bar{u} = u\hat{r} + v\hat{\theta} + w\hat{z} = \nabla\varphi + \nabla \times \bar{\Psi} \quad (2.3.9)$$

where φ is the scalar potential
and $\bar{\Psi}$ is the vector potential.

For cases where the material properties vary only as functions of z , the motion can be separated into poloidal and toroidal components. The poloidal component of motion involves motion in the z direction whereas the toroidal motion occurs in the r and θ directions. The poloidal component is a function of φ and the toroidal component is a function of $\bar{\Psi}$. For surface loading in an isotropic medium, toroidal deformation is not excited so this term is neglected. Therefore it is only necessary to solve $\bar{u} = \nabla\varphi$. For the incompressible case $\nabla \cdot \bar{u} = \nabla^2\varphi = 0$. Therefore the displacements are related to the scalar potential in the following way.

$$\begin{aligned}
 u &= \partial_r \varphi \\
 v &= \frac{1}{r} \partial_\theta \varphi \\
 w &= \partial_z \varphi
 \end{aligned} \tag{2.3.10}$$

If the solution is assumed to be linear in r , θ , and z and have the form $\varphi = R(r)Q(\theta)Z(z)$, then the following differential equations are obtained from $\nabla^2 \varphi = 0$.

$$\begin{aligned}
 \partial_z^2 Z - k^2 Z &= 0 \\
 \partial_\theta^2 Q + \nu^2 Q &= 0 \\
 \partial_r^2 R + \frac{1}{r} \partial_r R + \left(k^2 - \frac{\nu^2}{r^2} \right) R &= 0
 \end{aligned} \tag{2.3.11}$$

Solving the above equations, sufficiently satisfies the equation of motion. These equations have the following solutions, respectively.

$$\begin{aligned}
 Z &= e^{-kz} \\
 Q &= e^{i\nu\theta} \\
 R &= J_\nu(kr)
 \end{aligned} \tag{2.3.12}$$

where k and ν are constants and

$J_\nu(kr)$ is a Bessel function of the first kind and order ν .

Therefore, any variables dependent upon r can be expanded in terms of the Bessel function and any that are dependent on z can be expanded using an exponential function. Since there is no dependence on θ , the constant ν must be equal to zero. Therefore the solution is:

$$\varphi = J_0(kr)e^{-kz} \quad (2.3.13)$$

Now we can express the system of differential equations in terms of φ . This reduces the partial differential equation to an ordinary differential equation. It is possible to express not only the displacements, but also the stresses in terms of φ .

$$\begin{aligned} \sigma_{rr} &= 2\mu\partial_r\partial_r\varphi \\ \sigma_{rz} &= 2\mu\partial_r\partial_z\varphi \\ \sigma_{zz} &= 2\mu\partial_z\partial_z\varphi \end{aligned} \quad (2.3.14)$$

Knowing that $J_0(kr)$ satisfies the following differential equations (Tranter, 1968),

$$\begin{aligned} \partial_r^2 J_0(kr) + \frac{1}{r}\partial_r J_0(kr) + k^2 J_0(kr) &= 0 \\ \partial_r J_0(kr) &= -kJ_1(kr) \end{aligned} \quad (2.3.15)$$

$$J_0(0) = 1 \quad (2.3.16)$$

$$J_1(0) = 0 \quad (2.3.17)$$

the following Bessel function substitutions are obtained, which will be used to calculate the Hankel transform of these variables.

$$\begin{aligned}
u &= \partial_r \varphi = -ke^{-kz} J_1(kr) \\
w &= \partial_z \varphi = -ke^{-kz} J_0(kr) \\
\sigma_{rr} &= 2\mu \partial_r \partial_r \varphi = 2\mu e^{-kz} \left[\frac{1}{r} J_1(kr) - k^2 J_0(kr) \right] \\
\sigma_{rz} &= 2\mu \partial_r \partial_z \varphi = 2\mu e^{-kz} k^2 J_1(kr) \\
\sigma_{zz} &= 2\mu \partial_z \partial_z \varphi = 2\mu e^{-kz} k^2 J_0(kr)
\end{aligned} \tag{2.3.18}$$

For a vertically stratified halfspace, the vertical component is more complicated than a simple exponential. Instead, let $A = A(k, z)$ be the vertical component of the k^{th} wavenumber. Therefore we will have

$$\varphi = \int_0^{\infty} A J_0(kr) dk \tag{2.3.19}$$

Using this form of φ we obtain the following solutions for the displacements and stresses. These are the Hankel transforms associated with each of the different variables.

$$\begin{aligned}
u &= -\int_0^{\infty} k U J_1(kr) dk \\
w &= \int_0^{\infty} k W J_0(kr) dk \\
\sigma_{rr} &= \int_0^{\infty} k T_r \left[\frac{1}{r} J_1(kr) - k J_0(kr) \right] dk \\
\sigma_{rz} &= -\int_0^{\infty} k T_r J_1(kr) dk \\
\sigma_{zz} &= \int_0^{\infty} k T_z J_0(kr) dk \\
P &= \int_0^{\infty} k \Pi J_0(kr) dk
\end{aligned} \tag{2.3.20}$$

$$\begin{aligned}
\partial_r u &= -\int_0^{\infty} kU [kJ_0(kr) - \frac{1}{r}J_1(kr)] dk \\
\partial_r w &= -\int_0^{\infty} k^2 WJ_1(kr) dk \\
\partial_r \sigma_r &= -\int_0^{\infty} kT_r [kJ_0(kr) - \frac{1}{r}J_1(kr)] dk \quad (2.3.21) \\
\partial_r P &= -\int_0^{\infty} k^2 \Pi J_1(kr) dk \\
\partial_r^2 u &= -\int_0^{\infty} kU \left[-\frac{1}{r}J_0(kr) - \frac{(k^2 r^2 - 2)}{r}J_1(kr) \right] dk
\end{aligned}$$

$$\partial_r^2 u + \frac{1}{r}\partial_r u - \frac{1}{r^2}u = \int_0^{\infty} k^3 UJ_1(kr) dk \quad (2.3.22)$$

Recall that the r and z components of the equation of motion, the stress-strain relations for σ_r and σ_{zz} , and the divergence equation (dilatation) for the incompressible case are

$$\begin{aligned}
-\partial_r P + 2\mu\partial_r^2 u + 2\mu\frac{1}{r}\partial_r u - 2\mu\frac{1}{r^2}u + \partial_z \sigma_r - \rho g\partial_r w &= 0 \\
\partial_r \sigma_r + \mu\frac{1}{r}\partial_r w + \mu\frac{1}{r}\partial_z u + \partial_z \sigma_{zz} - \rho g\partial_z w &= 0 \\
\sigma_r &= \mu\partial_r w + \mu\partial_z u \\
\sigma_{zz} &= -P + 2\mu\partial_z w \\
\nabla \cdot \vec{u} = 0 &= \frac{1}{r}\partial_r(ru) + \partial_z w
\end{aligned} \quad (2.3.23)$$

The formulae for the displacements and stresses as given by equations (2.3.20), (2.3.21), and (2.3.22) can be substituted into equation (2.3.23) and they are transformed into the k domain using the Hankel transform to get

$$\begin{aligned}
-\partial_z T_r &= -2\mu k^2 U - \rho g k W - \Pi k \\
\frac{1}{r} J_1 T_r - k J_0 T_r - \frac{\mu}{r} k J_1 W - \frac{\mu}{r} J_1 \partial_z U - \rho g J_0 \partial_z W + J_0 \partial_z T_z &= 0 \\
-T_r &= -\mu k W - \mu \partial_z U \\
-k J_0 U + J_0 \partial_z W &= 0 \\
T_z &= -\Pi + 2\mu \partial_z W
\end{aligned} \tag{2.3.24}$$

These five equations are reorganized and the Π term is eliminated to get the following four differential equations:

$$\begin{aligned}
\partial_z T_r &= 4\mu k^2 U + \rho g k W - k T_z \\
\partial_z T_z &= \rho g k U + k T_r \\
\partial_z U &= \frac{1}{\mu} T_r - k W \\
\partial_z W &= k U
\end{aligned} \tag{2.3.25}$$

These can be expressed in matrix form.

$$\frac{\partial}{\partial z} \begin{pmatrix} U \\ W \\ T_r \\ T_z \end{pmatrix} = \begin{pmatrix} 0 & -k & \frac{1}{\mu} & 0 \\ k & 0 & 0 & 0 \\ 4\mu k^2 & \rho g k & 0 & -k \\ \rho g k & 0 & k & 0 \end{pmatrix} \begin{pmatrix} U \\ W \\ T_r \\ T_z \end{pmatrix} \tag{2.3.26}$$

This matrix can be shown to agree with the matrix given in Cathles (1975) for an incompressible, elastic, flat earth, where U equals iU and T_r equals iT_r . This method of using the Hankel transform in cylindrical coordinates is equivalent to using the Fourier transform in Cartesian coordinates as used by Cathles (1975).

These equations can be normalized so that the variables are dimensionless. This is done to ensure accurate numerical calculations. Since the viscosity used in this thesis is

relatively large as compared with the other material properties, the numerical calculations can introduce errors due to rounding errors. To minimize this problem, the values for the material properties are normalized. The normalization scheme is given in the table below. The form of the equations remains the same despite the normalization so the above differential equations can also be used to represent the dimensionless problem.

Table 1: The Normalization Scheme

<u>variable</u>	<u>unit</u>	<u>normalization</u> <u>factor</u>	<u>value</u>
length	$[L]$	a	radius of the Earth (6371000 m)
mass	$[M]$	$\bar{\rho} a^3$	mean mass of the Earth
density	$\left[\frac{M}{L^3}\right]$	$\bar{\rho}$	mean density (5517 kg m ⁻³)
time	$[T]$	$a \sqrt{\frac{\bar{\rho}}{\mu^*}}$	derived from the acceleration
stress	$\left[\frac{M}{LT^2}\right]$	μ^*	mean stress at surface of the Earth ($\pi a^2 \bar{\rho}^2 G = 2.589 \times 10^{11} \text{ N m}^{-2}$)
gravitational acceleration	$\left[\frac{L}{T^2}\right]$	$\frac{\mu^*}{a \bar{\rho}}$	mean gravitational acceleration of the Earth (7.365 m s ⁻²)
elastic modulus	$\left[\frac{M}{LT^2}\right]$	μ^*	mean stress at surface of the Earth ($\pi a^2 \bar{\rho}^2 G = 2.589 \times 10^{11} \text{ N m}^{-2}$)
viscosity	$\left[\frac{M}{LT}\right]$	$\mu^* \times 1\text{kyr}$	stress over one thousand years ($8.17 \times 10^{21} \text{ Pa s}$)

The normalized values of s are in terms of thousands of years.

Therefore if $\tilde{\cdot}$ represents the normalized form, then the following expressions apply.

$$\begin{aligned}\bar{U} &= \frac{U}{a} \\ \bar{W} &= \frac{W}{a} \\ \bar{T}_r &= \frac{T_r}{\mu} \\ \bar{T}_{zz} &= \frac{T_{zz}}{\mu} \\ \bar{\mu} &= \frac{\mu}{\mu} \\ \bar{\lambda} &= \frac{\lambda}{\mu} \\ \bar{z} &= \frac{z}{a} \\ \bar{k} &= ka \\ \bar{\rho} &= \frac{\rho}{\rho} \\ \bar{g} &= \frac{g\bar{\rho}a}{\mu} \\ \bar{v} &= \frac{v}{\mu \times 1\text{kyr}}\end{aligned}$$

The linearized boundary conditions are determined by balancing the stress at the surface with the weight of the displaced material and relating the perturbed potential to the surface mass density. The boundary conditions can be derived from the equations of motion using the pillbox technique (Cathles, 1975). The stress is continuous in the viscous case, but for the elastic case there is also the advection of prestress term. Therefore, the linearized boundary conditions are

$$\text{elastic:} \quad [\sigma \cdot \hat{n}]_-^+ = 0 \quad (2.3.27)$$

$$\text{viscous:} \quad [\sigma \cdot \hat{n} + \rho_0 g_0 u \hat{n}]_-^+ = 0 \quad (2.3.28)$$

When considering a viscoelastic problem, one uses the correspondence principle to relate the linearized equations of motion for the elastic and viscous cases.

$$\text{elastic:} \quad \nabla \cdot \sigma - \rho_1 g_0 \hat{n} - \rho_0 \nabla \phi_1 - \nabla(\rho_0 g_0 \bar{u} \cdot \hat{n}) = 0 \quad (2.3.29)$$

$$\text{viscous:} \quad \nabla \cdot \sigma - \rho_1 g_0 \hat{n} - \rho_0 \nabla \phi_1 = 0 \quad (2.3.30)$$

In the viscous limit, the advection of prestress term becomes part of the overall stress. Therefore, the following can be defined.

$$\sigma' = \sigma - \rho_0 g_0 u \hat{n} \quad (2.3.31)$$

$$\text{Therefore} \quad \nabla \cdot \sigma' = \nabla \cdot \sigma - \nabla(\rho_0 g_0 u)$$

So the linearized equation of motion for the elastic case can be written

$$\nabla \cdot \sigma' - \rho_1 g_0 \hat{n} - \rho_0 \nabla \phi_1 = 0 \quad (2.3.32)$$

This is equivalent to the equation for a viscous fluid (equation (2.3.30)). This can also be applied to the boundary conditions so that for the elastic case

$$[\sigma' \cdot \hat{n} + \rho_0 g_0 u \hat{n}]_- = 0 \quad (2.3.33)$$

This is also equivalent to that of the viscous fluid. Note that with this definition, the stress needs to be reinterpreted as time progresses.

2.3b: Solution to the Differential Equations

In general the system of equations given by equation (2.3.26) can be written as $\partial_z \bar{Y} = \mathbf{A} \bar{Y}$, where \mathbf{A} is the square matrix. This is useful for numerical integration. This system of equations can be solved by finding the eigenvalues and eigenvectors of the matrix \mathbf{A} . For a fourth order differential equation the solution is expressed in the following way assuming there is no redundancy in the eigenvalues.

$$\bar{Y} = c_1 \bar{v}_1 e^{-\lambda_1 z} + c_2 \bar{v}_2 e^{-\lambda_2 z} + c_3 \bar{v}_3 e^{-\lambda_3 z} + c_4 \bar{v}_4 e^{-\lambda_4 z} \quad (2.3.34)$$

where \bar{v}_n represents the n^{th} eigenvector,

λ_n represents the n^{th} eigenvalue,

c_n represents the n^{th} constant as determined by the boundary conditions.

and z represents the depth.

In terms of the differential equations derived in the previous section this method will give the solution in the (k,s) domain. Based on the correspondence theorem the viscoelastic solution can be obtained from this solution by substituting $\mu(s)$ for μ and performing the inverse Laplace transform to return to the time domain. Finally to return to the space domain from the wavenumber domain, the inverse Hankel transform will be performed. The solution for a uniform layer in a flat earth is obtained below. These equations apply only if the material properties are constant throughout the layer.

The eigenvalues are determined by solving

$$|\mathbf{A} - \lambda\mathbf{I}| = 0 \quad (2.3.35)$$

where \mathbf{A} represents a square matrix,

λ are the eigenvalues,

and \mathbf{I} is the identity matrix.

For the case of the incompressible, flat Earth, the values of the eigenvalues are $\pm k$, as demonstrated below.

$$\frac{\partial}{\partial z} \begin{pmatrix} U \\ W \\ T_r \\ T_z \end{pmatrix} = \begin{pmatrix} 0 & -k & \frac{1}{\mu} & 0 \\ k & 0 & 0 & 0 \\ 4\mu k^2 & \rho g k & 0 & -k \\ \rho g k & 0 & k & 0 \end{pmatrix} \begin{pmatrix} U \\ W \\ T_r \\ T_z \end{pmatrix} \quad (2.3.36)$$

$$\begin{vmatrix} -\lambda & -k & \frac{1}{\mu} & 0 \\ k & -\lambda & 0 & 0 \\ 4\mu k^2 & \rho g k & -\lambda & -k \\ \rho g k & 0 & k & -\lambda \end{vmatrix} = 0 \quad (2.3.37)$$

$$\lambda^4 + k^4 - 2\lambda^2 k^2 = 0$$

The above equation shows that the eigenvalues are degenerate, i.e., from this fourth order equation only two unique eigenvalues are obtained. Note that there are only two independent eigenvalues with only two associated eigenvectors while four are needed to uniquely describe the system. There is a standard technique used in linear algebra to obtain two additional eigenvectors from the two existing eigenvectors (Boyce and DiPrima, 1986, p. 368).

The first two eigenvectors are determined by solving

$$(\mathbf{A} - \lambda_n \mathbf{I})\bar{v}_n = 0 \quad (2.3.38)$$

where \bar{v}_n are the eigenvectors associated with λ_n .

The second two eigenvectors are determined by solving

$$(\mathbf{A} - \lambda_n \mathbf{I})\bar{u}_n = \bar{v}_n \quad (2.3.39)$$

where \bar{u}_n are the second set of eigenvectors associated with λ_n and \bar{v}_n .

The four eigenvectors obtained through this method are

$$\begin{aligned} \bar{v}_k &= \begin{pmatrix} 1 \\ 1 \\ 2\mu k \\ 2\mu k + \rho g \end{pmatrix} & \bar{u}_k &= \begin{pmatrix} \frac{1}{k} \\ 0 \\ 2\mu \\ 0 \end{pmatrix} \\ \bar{v}_{-k} &= \begin{pmatrix} 1 \\ -1 \\ -2\mu k \\ 2\mu k - \rho g \end{pmatrix} & \bar{u}_{-k} &= \begin{pmatrix} -\frac{1}{k} \\ 0 \\ 2\mu \\ 0 \end{pmatrix} \end{aligned} \quad (2.3.40)$$

The final solution, in the most general form for a problem where only two unique eigenvalues are obtained, is given below.

$$\bar{Y} = c_1 \bar{v}_k e^{kz} + c_2 \bar{v}_{-k} e^{-kz} + c_3 (\bar{v}_k z + \bar{u}_k) e^{kz} + c_4 (\bar{v}_{-k} z + \bar{u}_{-k}) e^{-kz}$$

In matrix form this is expressed as

$$\bar{Y} = \begin{pmatrix} e^{kz} & e^{-kz} & (z + \frac{1}{k})e^{kz} & (z - \frac{1}{k})e^{-kz} \\ e^{kz} & -e^{-kz} & ze^{kz} & -ze^{-kz} \\ 2\mu k e^{kz} & -2\mu k e^{-kz} & 2\mu(kz + 1)e^{kz} & 2\mu(1 - kz)e^{-kz} \\ (2\mu k + \rho g)e^{kz} & (2\mu k - \rho g)e^{-kz} & z(2\mu k + \rho g)e^{kz} & z(2\mu k - \rho g)e^{-kz} \end{pmatrix} \bar{C} \quad (2.3.41)$$

$$\text{where } \bar{Y} = \begin{pmatrix} U \\ W \\ T_{rz} \\ T_{zz} \end{pmatrix} \text{ and } \bar{C} = \begin{pmatrix} c_1 \\ c_2 \\ c_3 \\ c_4 \end{pmatrix}.$$

Therefore the solution can be written as $\bar{Y}(z) = \mathbf{P}(z)\bar{C}$ where \bar{C} is a vector of the constant coefficients, c_i , and $\mathbf{P}(z)$ is a matrix whose columns are equal to the eigenvectors. This satisfies the differential equation (2.3.26). This represents the solution of an incompressible layer within a flat Earth with constant density, gravitational acceleration, viscosity and shear modulus. To obtain the solution for a stratified earth model, the appropriate boundary conditions are applied to determine the values of the constants. The surface boundary conditions are that the shear stress is zero and the normal stress is constant due to the mass of the applied load. The surface boundary conditions can be expressed as $\bar{Y}'(0) = \begin{pmatrix} T_{rz} \\ T_{zz} \end{pmatrix} = \mathbf{M}(0)\bar{C}' = \begin{pmatrix} 0 \\ -\sigma \end{pmatrix}$, where \bar{Y}' is a vector of only the stresses.

\mathbf{M} is a 2×2 matrix taken from the appropriate elements of matrix \mathbf{P} to obtain equations

for the stresses, \bar{C}' is made up of the two constants, c_1 and c_3 , used to satisfy these boundary conditions and $-\sigma$ is the magnitude of the impulse loading of the earth. These surface boundary conditions are used for all of the analytic models, since they are designed to investigate the response of an earth model to a constant load on the surface. The lower boundary conditions however vary from model to model. For the halfspace model the boundary condition as the depth goes to negative infinity (z is defined as positive upwards) is that the solution must be finite. Therefore the value for the constants c_2 and c_4 is zero. The solution for the halfspace model without the application of the surface boundary conditions is

$$\bar{Y}_H = \begin{pmatrix} e^{kz} & (z + \frac{1}{k})e^{kz} \\ e^{kz} & ze^{kz} \\ 2\mu ke^{kz} & 2\mu(kz + 1)e^{kz} \\ (2\mu k + \rho g)e^{kz} & z(2\mu k + \rho g)e^{kz} \end{pmatrix} \bar{C}' = \mathbf{P}_H \bar{C}' \quad (2.4.42)$$

where \bar{C}' is a 2×1 matrix made up of constants c_1 and c_3 .

For the channel model the lower boundary is fixed and does not move, therefore the vertical and horizontal displacements are zero. The lower boundary conditions can be expressed as

$$\bar{Y}_C(z_l) = \begin{pmatrix} U(z_l) \\ W(z_l) \\ T_x(z_l) \\ T_z(z_l) \end{pmatrix} = \mathbf{P}_C(z_l) \bar{C}'' = \begin{pmatrix} 0 & 0 \\ 0 & 0 \\ 1 & 0 \\ 0 & \rho g \end{pmatrix} \bar{C}'' \quad (2.3.43)$$

where z_l is the depth of the lower boundary,

\bar{C} is the 4×1 matrix made up of constants c_1 , c_2 , c_3 , and c_4 ,
and \bar{C}'' is a 2×1 matrix made up of constants c_2 and c_4 .

For the model of an elastic lithosphere over a fluid halfspace the conditions at the lower boundary are that the shear stress is zero and that the normal stress is caused by the buoyancy force due to the vertical displacement, i.e. $\rho g W$. These can be expressed as

$$\bar{Y}_L(z_l) = \begin{pmatrix} U(z_l) \\ W(z_l) \\ T_{rz}(z_l) \\ T_{zz}(z_l) \end{pmatrix} = \mathbf{P}_L(z_l) \bar{C} = \begin{pmatrix} 1 & 0 \\ 0 & 1 \\ 0 & 0 \\ 0 & \rho g \end{pmatrix} \bar{C}'' \quad (2.3.44)$$

where z_l is the depth of the lower boundary,

\bar{C} is the 4×1 matrix made up of constants c_1 , c_2 , c_3 , and c_4 ,
and \bar{C}'' is a 2×1 matrix made up of constants c_2 and c_4 .

For multi-layer models additional boundary conditions are needed. The boundary condition at any common boundary is that the solutions within the upper and lower layers must be continuous. It is assumed that the properties within each layer are constant. In this way a complex model made up of many layers, each with constant properties, can be used to approximate the smooth variation in the properties as seen in the Earth where the bottom layer is a halfspace. A starting solution $\mathbf{P}_1(z_1)$ is chosen, based on the model, to be \mathbf{P}_H , \mathbf{P}_C or \mathbf{P}_L and the solution is propagated through the layers by matrix propagation. Therefore, for n distinct layers, the solution can be written as

$$\tilde{Y}_n(z) = \left[\prod_{m=2}^n \mathbf{P}_m(z_m) \mathbf{P}_m^{-1}(z_{m-1}) \right] \mathbf{P}_1(z_1) \bar{\mathbf{C}}_1 \quad (2.3.45)$$

The two remaining constants are determined by applying the surface boundary conditions.

2.4: Solution in the Time Domain

In the last section the solution to the loading of a viscoelastic medium was obtained in the (k,s) domain so now it is necessary to invert the solution back to the (x,t) domain. The final two sections of this chapter will demonstrate the methods used to obtain the solutions in the inverse transformed domains; first in the (k,t) domain and then in the (x,t) domain. Both of these methods assume that the solution in the (k,s) domain has been determined and that all boundary conditions have been satisfied. Let the solution in the (k,s) domain be a linear function of n independent solutions, each satisfying the differential equations.

2.4a: Spectral Method

To determine the solution in the time domain the new normal mode method was used. The steps of this method are detailed below (Wu, 1978; Wu, 1990).

1. Find the matrix \mathbf{M} based on the boundary conditions applied at $z = 0$. For all of the models discussed in this thesis the boundary conditions at the surface are that the shear stress is zero and the normal stress is a constant equal to the weight of the ice load. The matrix \mathbf{M} is a portion of the matrix \mathbf{P} .

If the solution from equation (2.3.41) is written as

$$\bar{Y}(z,s) = \mathbf{P}(z,s)\bar{C}(s) \quad (2.4.1)$$

then the matrix \mathbf{M} is defined as

$$\bar{Y}(z=0, s) = \mathbf{M}(s)\bar{C}'(s) = \bar{b}(s) \quad (2.4.2)$$

where \bar{b} is a 2×1 matrix defining the boundary conditions at the surface,

\bar{C}' is a 2×1 matrix of the constants determined by the surface boundary conditions.

\mathbf{M} is the 2×2 matrix used to apply these boundary conditions.

and $\bar{Y}(z=0)$ involves only the stresses.

Therefore
$$\bar{b} = \begin{pmatrix} 0 \\ -\sigma \end{pmatrix}$$

Therefore
$$\bar{C} = \mathbf{M}^{-1}\bar{b} \quad (2.4.3)$$

$$\bar{C} = \frac{\mathbf{M}^*}{\det \mathbf{M}} \bar{b} \quad (2.4.4)$$

or
$$C_i = \sum_j \frac{M_{ij}^*(s)b_j}{\det M(s)} \quad (2.4.5)$$

where \mathbf{M}^* is the transpose matrix of the cofactors M_{ij}^* .

Therefore the solution can be written as

$$\bar{Y}(z, s) = \sum_j \frac{M_{ij}^*(s)b_j}{\det M(s)} \bar{T}_i(z, s) \quad (2.4.6)$$

where \bar{T}_i are the column vectors of \mathbf{P} .

2. To determine the singularities of the solution, the values of s for which $\det \mathbf{M} = 0$ are determined. These s values are equal to the inverse of the relaxation times.
3. Define a vector \bar{Q} which is dependent on the original matrix \mathbf{P} , the inverse of \mathbf{M} and the boundary conditions.

$$\bar{Q}(z, s) = \sum_{ii} M_{ii}^{-1}(s) b_j \bar{T}_i(z, s). \quad (2.4.7)$$

so that

$$\bar{Y}(z, s) = \frac{\bar{Q}(z, s)}{\det \mathbf{M}(s)} \quad (2.4.8)$$

4. The solution can be expressed as the sum of an elastic component (independent of s) and a viscous component (s dependent). The elastic component is the solution at the initial time, i.e. as s goes to infinity. This elastic component can be subtracted from the total s dependent solution to obtain the viscous component. The viscous component of \bar{Q} can be obtained from the viscous component of the solution.

$$\bar{Y}(z, s) = \bar{Y}^v(z, s) + \bar{Y}^E(z) \quad (2.4.9)$$

$$\bar{Y}^E(z) = \lim_{s \rightarrow \infty} \bar{Y}(z, s) \quad (2.4.10)$$

$$\bar{Y}^v(z, s) = \bar{Y}(z, s) - \bar{Y}^E(z) = \frac{\bar{Q}^v(z, s)}{\det \mathbf{M}} \quad (2.4.11)$$

where by definition $\bar{Q}^V(z, s) = \bar{Q}(z, s) - \bar{Q}^E(z) \frac{\det \mathbf{M}}{\det \mathbf{M}^E}$.

5. The solution in the time domain can be obtained by performing the inverse Laplace transform.

$$\bar{Y}(z, t) = \frac{1}{2\pi i} \int_L \frac{\bar{Q}^V(z, s)}{\det \mathbf{M}} e^{st} ds + \bar{Y}^E \delta(t) \quad (2.4.12)$$

6. This integral can be simplified using the Residue Theorem. The Residue Theorem states that the integral of a function around a curve can be expressed as a sum of the residues. The residue can be evaluated by first identifying singularities in the function, then taking the numerator of the integral evaluated at these singularities, divided by the slope of the denominator evaluated at these singularities (Marsden, 1973). The residue then becomes independent of s . For example, if the value of $\det \mathbf{M}$ is zero at s_i , and there are m_i such singularities, then

$$\frac{1}{2\pi i} \int_L \frac{\bar{Q}^V(z, s) e^{st}}{\det \mathbf{M}(s)} ds = \sum_{i=1}^m \operatorname{Re} s_i \left\{ \frac{\bar{Q}^V(z, s) e^{st}}{\det \mathbf{M}(s)} \right\}_{s_i} = \sum_{i=1}^m \frac{\bar{Q}^V(z, s_i) e^{s_i t}}{\frac{d}{ds} [\det \mathbf{M}(s)]_{s_i}} \quad (2.4.13)$$

Therefore equation (2.4.12) becomes

$$\bar{Y}(z, t) = \sum_{i=1}^m \bar{R}_i(z) e^{s_i t} + \bar{Y}^E(z) \delta(t) \quad (2.4.14)$$

where $\bar{R}_i(z) = \frac{\bar{Q}^V(z, s_i)}{\frac{d}{ds} [\det \mathbf{M}(s)]_{s_i}}$ are the residues. (2.4.15)

7. Finally the elastic portion of the solution is obtained by calculating the value of the solution as s goes to infinity, according to equation 2.4.9.

$$\bar{Y}^E(z) = \lim_{s \rightarrow \infty} \bar{Y}(z, s)$$

8. Therefore the time dependent solution is a combination of the elastic solution and the sum of the residues. If a Heaviside load is assumed, then the solution has the following form.

$$\bar{Y}(z, t) = \sum_{i=1}^m \frac{\bar{R}_i(z)}{s_i} (1 - e^{s_i t}) + \bar{Y}^E(z) \quad (2.4.16)$$

where $\frac{\bar{R}_i(z)}{s_i}$ is the excitation strength.

2.4b: Numerical Application of the Spectral Method

The analytical derivations of the time dependent solutions for three different basic models can be found in Appendices D, E, and F. These basic models are the halfspace model, the channel model and the model of a lithosphere over a fluid.

The results of the spectral method are used to check the results of the finite element method, especially the horizontal displacement. Analytical results exist only for relatively simple models, but the results for models with lithospheres and stratified viscoelastic halfspaces also need to be analyzed. For this reason Matlab programs were written to compute the deformation in a laterally homogeneous earth model using the spectral method.

A series of Matlab programs was written to calculate the solution in the (k,s) domain and then to employ the method outlined in section 2.4a to calculate the solution in the (k,t) domain. These programs calculate the relaxation times, residues, excitation strengths and time dependent solutions for any laterally homogeneous model. The solutions for the three basic models were calculated numerically using the Matlab programs and the results were compared with the analytical solutions. They were found to agree so further results from the Matlab programs could be used with confidence. These comparisons will be discussed in more detail in the upcoming chapters.

The Matlab programs were structured in a manner to facilitate the use of the normal mode method in determining the solution in the time domain. First a starting solution is chosen to reflect the desired structure of the model, either halfspace, channel, or lithosphere over a fluid. This allowed all three model types to be incorporated into one set of programs.

This is done through the use of a flag. If the flag has a value of 1, then the starting solution is the halfspace solution, if 2 then the channel solution and if 3 then the lithosphere over a fluid solution. The starting solution for the halfspace model is based on the eigenvalues and eigenvectors obtained for the incompressible flat earth. The starting solutions for the channel and lithosphere over a fluid are the boundary conditions at the lower boundary as discussed in the previous section (equations (2.3.43) and (2.3.44)). The material parameters of the model are then entered into the program in the form of a vector, each element of the vector corresponding to a particular layer. The material parameters required are the density of the layers, the shear modulus, the viscosity, the gravitational acceleration and the depth of the top of the layers. The solution in the (k,s) domain was obtained by propagating the starting solution through the various layers to the surface where the surface boundary conditions are applied. The solution in any given layer is based on the eigenvectors as discussed in section 2.3 and given in equation (2.3.41). Upon testing of the programs, it was noticed that for large values of k the eigenvectors were similar, hence the matrix \mathbf{P} was singular for large values of k . Therefore the inversion of the matrix \mathbf{P} , required in the matrix propagation, became numerically unstable. Conceptually, for large values of k the model is sampled to only small depths and the eigenvectors approach those of the halfspace model, instead of the solution for an arbitrary layer. To accommodate this effect an effective depth was calculated below which the model is not sampled. This effective depth was chosen to be $1/(5k)$. The matrix propagation then started from this effective depth using the halfspace solution no matter what the initial model. Since the material below this depth is not being sampled then it can be modeled as a halfspace without the loss of information.

Once the solution in the (k,s) domain had been obtained the next step was to calculate the items necessary to determine the solution in the (k,t) domain. These items are (a) the

elastic part of this solution, which can be easily obtained by determining the value of the solution as s gets very large, (b) the matrix \mathbf{M} based on the matrix used to determine the constants from the surface boundary conditions, (c) the relaxation times by solving the determinant function, $\det\mathbf{M} = 0$, (d) the viscous part of the solution by subtracting the elastic part from the total, (e) the viscous \bar{Q} vector as given by the viscous solution multiplied by $\det\mathbf{M}$, and (f) the residues obtained by dividing the viscous \bar{Q} vector by the slope of $\det\mathbf{M}$ evaluated at the inverses of the relaxation times. A further series of programs was written to calculate these items and to combine them to determine the solution in the time domain.

2.5: Numerical Solution in the Space domain

From the solution in the time domain, the final step needed to obtain the solution in the space domain is to perform the inverse Hankel transform. The solution can then be investigated to determine how it varies both in time and in space.

2.5a: Solution Using the Inverse Hankel Transform

For the cases where an analytical solution was available in the (k, t) domain, the formula was directly incorporated into the FORTRAN program designed to perform the inverse Hankel transform using the Continued Fraction Expansion by Chave (1983). The solution in the space domain was obtained for different values of r at a particular time t . The formulae used to compute the inverse Hankel transform are determined from the equations used in the initial derivation of the differential equations in equation (2.3.20). The Hankel transform of a disc load with small radius (Farrell, 1972, equation 8) is $J_1(kR)$ $R k$. The solutions $W(k, t)$ and $U(k, t)$ are for a harmonic load with wavenumber k and amplitude σ , thus to obtain the space-time solution for a disc load they have to be multiplied by the function of the load in the k domain and then the inverse Hankel transform is performed on this product. The formulae used to calculate the displacement at $r = 0$ are

$$w(r, t) = \int_0^{\infty} W(k, t) R J_1(kR) dk \quad (2.5.1)$$

$$u(r, t) = -\int_0^{\infty} U(k, t) R J_1(kr) dk \quad (2.5.2)$$

and at all other values of r are

$$w(r, t) = \int_0^{\infty} W(k, t) R J_1(kR) J_0(kr) dk \quad (2.5.3)$$

$$u(r, t) = -\int_0^{\infty} U(k, t) R J_1(kR) J_1(kr) dk \quad (2.5.4)$$

where $W(k, t)$ and $w(r, t)$ are the vertical displacements,

$U(k, t)$ and $u(r, t)$ are the horizontal displacements,

$J_1(kr)$ is the Bessel function of first order,

$J_0(kr)$ is the Bessel function of zero order,

and R is the radius of the cylindrical load.

By investigating the analytical solutions for the vertical and horizontal displacements, it was possible to determine that the horizontal displacement was antisymmetrical around the $k = 0$ axis while the vertical displacement was symmetrical. This is due to the order of the Bessel functions used in the above equations since $J_1(x)$ is an anti-symmetrical function and $J_0(x)$ is symmetrical. The formula for $w(r)$ at $r = 0$ can be obtained from equation 2.5.3 by taking $r = 0$ since $J_0(0) = 1$ (see equation (2.3.16)). Also notice that the load function is not present in the formula for $u(r)$ at $r = 0$. This is due to that fact that $J_1(kr)$ is zero at $r = 0$ (see equation (2.3.17)), so the horizontal displacement at the center of the load is zero regardless of the magnitude of the load.

It can be shown that the k domain solution for the horizontal displacement is singular where $k = 0$, however its product with $J_1(kr)$ becomes finite since $J_1(0)$ is zero. Since the

Fourier transform is similar to the Hankel transform and the differential equations are the same. originally the problem of this thesis was analysed using Cartesian coordinates (with a boxcar load that extends to plus and minus infinity in the y-direction). However, it was noted that the Fourier transform of a boxcar load is the sinc function which has a finite value at $k = 0$. This posed a problem when trying to calculate $u(x)$ due to the singular nature of $u(k)$ at $k = 0$. For this reason the calculations were performed in cylindrical coordinates instead.

The Matlab programs output the numerical calculations as lists of numbers corresponding to the displacements for specific values of k . These lists are then imported into the FORTRAN program and values are interpolated and extrapolated as required so that continuous functions of k are obtained for both the vertical and horizontal displacements. The interpolation was done by assuming a linear relationship between consecutive values with respect to k . The extrapolation required the limits of the displacement functions for large and small k values to be evaluated.

A comparison of the analytical results for the three basic models of the halfspace, channel and lithosphere over a fluid was done to determine the trends of these models as k goes from zero to positive infinity for both the horizontal and vertical displacements. From this investigation it was determined that the halfspace and lithosphere models had similar limits. The channel model was found to give a slightly different form to the limits since it did not have an underlying halfspace. Therefore the limits used for the extrapolation of the horizontal displacement are

$$\text{for } k \rightarrow 0, \quad u(k) = -\frac{\sigma}{2\mu k} \left(1 + \frac{2\mu k}{\rho g} \left(1 - e^{-\frac{\mu}{\nu} r} \right) \right) \quad (2.5.5)$$

$$\text{for } k \rightarrow \infty, \quad u(k) = \frac{\sigma H^2 k}{2\mu e^{2Hk}} \left(1 + \frac{2\mu k}{\rho g} \left(1 - e^{-\frac{\sigma}{2\mu k} t} \right) \right) \quad (2.5.6)$$

and the limits used for the vertical displacement are

$$\text{for } k \rightarrow 0, \quad w(k) = -\frac{\sigma}{\rho g} \left(1 + \frac{2\mu k}{\rho g} \left(1 - e^{-\frac{\sigma}{2\mu k} t} \right) \right) \quad (2.5.7)$$

$$\text{for } k \rightarrow \infty, \quad w(k) = -\frac{\sigma}{2\mu k} \left(1 + \frac{2\mu k}{\rho g} \left(1 - e^{-\frac{\sigma}{2\mu k} t} \right) \right) \quad (2.5.8)$$

where the properties used for the $k \rightarrow 0$ limit are those of the deepest layer or halfspace and the properties used in the $k \rightarrow \infty$ limit are those of the surface layer.

Since the limits given in equations (2.5.5) through (2.5.8) represent extreme values it was necessary to ensure that an appropriate range of k was used to generate the list of values that represent the displacements as a function of k . It was found that a suitable range was from 10^{-9} m^{-1} to 10^{-4} m^{-1} . It was also important to ensure that this range was finely sampled since a linear interpolation method was used. For the range given above it was determined that a suitable number of divisions would be 10^4 with a logarithmic sampling interval, however, testing showed that 250 divisions were sufficient. It was also found that the accuracy of the results was more dependent on the range of k values rather than the size of the sampling interval. The numerical results from the Matlab programs could then be transformed into the space domain so that comparisons could be made with the analytical results.

2.5b: Solution from the Finite Element Method

Another method used to generate the displacements that result from the loading of the Earth was to use the finite element modeling package called ABAQUS. This modeling program is fairly simple to use and it is easy to create complicated Earth models. The advantage of using this package is its ease in studying the influence of lateral variations, non-linear Earth rheology and time dependent creep, none of which can be easily incorporated into any of the other modeling methods discussed so far. ABAQUS requires only the description of the dimensions of the subsurface as well as the material properties and it produces the displacements that result from any type of loading. One important detail in modeling with ABAQUS is to ensure that any particular layer is defined by an appropriate number of elements so that accurate displacements are generated.

Since numerous methods were used to generate the solutions, a series of checks was carried out. The first step was to calculate the analytical solutions in the (k,s) domain, the (k,t) domain and the (x,t) domain for the most simple models, the channel and halfspace models. The theoretical solution in the (k,s) domain was also determined for the model of an elastic lithosphere over a fluid. These theoretical solutions were compared with the solutions generated by the Matlab and FORTRAN programs. These solutions were also compared with the results of the finite element modeling program ABAQUS. Once it was determined that the Matlab and FORTRAN programs were reliable some more complicated models were considered. The displacements produced by these complicated models were compared with ABAQUS output to ensure the validity of the finite element modeling program. All of the above comparisons will be discussed in more detail in Chapters 3, 4 and 5.

In this chapter all of the basic tools used in the analyses discussed in all subsequent chapters has been reviewed. The next chapter will apply these methods to the halfspace model. Chapters 4 and 5 will use these methods in the analysis of more complicated models.

Chapter 3: Incompressible, Self-gravitating, Uniform Earth: Analytical and Numerical Solutions

This chapter will present the analytical solution for the loading of the halfspace model. This chapter will also serve to illustrate the steps taken in the analysis of the different models to be discussed in subsequent chapters. In the first section the solution in the (k,s) domain will be given. It will be compared with the numerical solution generated by the Matlab programs. In section 3.2 the analytical solution for the relaxation times will be derived and this will also be compared with the Matlab output. Similarly in section 3.3 the excitation strengths will be discussed. Finally in section 3.4 the solution in space and time will be reviewed and the results will be compared with the results from the Matlab and FORTRAN programs and the finite element modeling package ABAQUS. The full derivation of all of the analytical solutions for the halfspace model can be found in Appendix D.

3.1: The Analytical Solution in the (k,s) Domain

This section will begin with a brief review of the method used to determine the solution in the (k,s) domain as discussed in section 2.3a. This solution is compared with the output of the Matlab programs to test the validity of the numerical calculations. The differential equations that describe the loading of a halfspace can be written as

$$\partial_z \bar{Y} = \mathbf{A} \bar{Y} \quad (3.1.1)$$

$$\text{where } \bar{Y} = \begin{pmatrix} U \\ W \\ T_{rz} \\ T_{zz} \end{pmatrix} \text{ and } A = \begin{pmatrix} 0 & -k & \frac{1}{\mu} & 0 \\ k & 0 & 0 & 0 \\ 4\mu k^2 & \rho g k & 0 & -k \\ \rho g k & 0 & k & 0 \end{pmatrix}.$$

These differential equations can be solved using the eigenvalues and eigenvectors of the matrix A. In this way the general solution is found to be

$$\bar{Y} = Ae^{kz} \begin{pmatrix} 1 \\ 1 \\ 2\mu k \\ 2\mu k + \rho g \end{pmatrix} + Be^{-kz} \begin{pmatrix} 1 \\ -1 \\ -2\mu k \\ 2\mu k - \rho g \end{pmatrix} + Ce^{kz} \begin{pmatrix} \frac{kz+1}{z} \\ k \\ 2\mu(kz+1) \\ (2\mu k + \rho g)z \end{pmatrix} + De^{-kz} \begin{pmatrix} \frac{kz-1}{z} \\ k \\ -z \\ 2\mu(1-kz) \\ (2\mu k - \rho g)z \end{pmatrix} \quad (3.1.2)$$

where μ is $\mu(s)$ and U, W, T_{rz} , and T_{zz} are in the Laplace transform and wavenumber domains.

This is the general solution given by equation (2.3.41). There are four constants in this solution, A, B, C, and D which are determined by applying the appropriate boundary conditions. The boundary conditions for the upper boundary, $z = 0$, are that the shear stress, T_{rz} , is zero and the vertical normal stress, T_{zz} , is a constant equal to the weight of the load. The lower boundary is defined as negative infinity and the condition that must be satisfied at this boundary is that the solution must remain finite. Applying all the boundary conditions, the four constants are determined to have values of

$$\begin{aligned}
A &= -\frac{\sigma}{2\mu(s)k + \rho g} \\
B &= 0 \\
C &= \frac{\sigma}{2\mu(s)k + \rho g} \\
D &= \bar{u}
\end{aligned} \tag{3.1.3}$$

where - $\sigma = \rho_L g h$ is the constant weight of the load with density ρ_L and height h .

Therefore the solution for the halfspace model under a constant load is

$$\bar{Y}(k, \mu(s)) = \frac{\sigma e^{-kz}}{2\mu(s)k + \rho g} \begin{pmatrix} kz \\ kz - 1 \\ 2\mu(s)k^2 z \\ (kz - 1)(2\mu(s)k + \rho g) \end{pmatrix} \tag{3.1.4}$$

Therefore the analytical solution for the horizontal displacement resulting from the loading of a halfspace is

$$\bar{Y}_1(k, \mu(s)) = U(k, \mu(s)) = \frac{\sigma e^{-kz} kz}{2\mu(s)k + \rho g} \tag{3.1.5}$$

and the vertical displacement is

$$\bar{Y}_2(k, \mu(s)) = W(k, \mu(s)) = \frac{\sigma e^{-kz} (kz - 1)}{2\mu(s)k + \rho g} \tag{3.1.6}$$

As is evident by this solution the horizontal displacement has a value of zero at the surface.

The two graphs that follow show the correlation between the Matlab output for the horizontal and vertical displacement and the analytical solution given above. Since the horizontal displacement has a value of zero at the surface, the solutions are investigated at a depth of 100 km. Figures 3.1.1 and 3.1.2 show that the two different methods yield the same results indicating that the numerical calculations are accurate.

The values used for the material properties of the halfspace are given in Table 2. They were chosen to represent the average values for the Earth.

Table 2: The Material Properties of the Halfspace Model

density	$\rho = 5517 \text{ kg m}^{-3}$
gravitational acceleration	$g = 7.365 \text{ m s}^{-2}$
viscosity	$\nu = 1 \times 10^{21} \text{ Pa s}$
shear modulus	$\mu = 1.452 \times 10^{11} \text{ N m}^{-2}$
wavenumber	$k = 1 \times 10^{-6} \text{ m}^{-1}$
depth	$z = -1 \times 10^6 \text{ m}$
load	$\sigma = 1 \times 10^7 \text{ Pa}$

Recall that the solutions have been normalized so that the displacements are dimensionless and the s values are in terms of per thousand years.

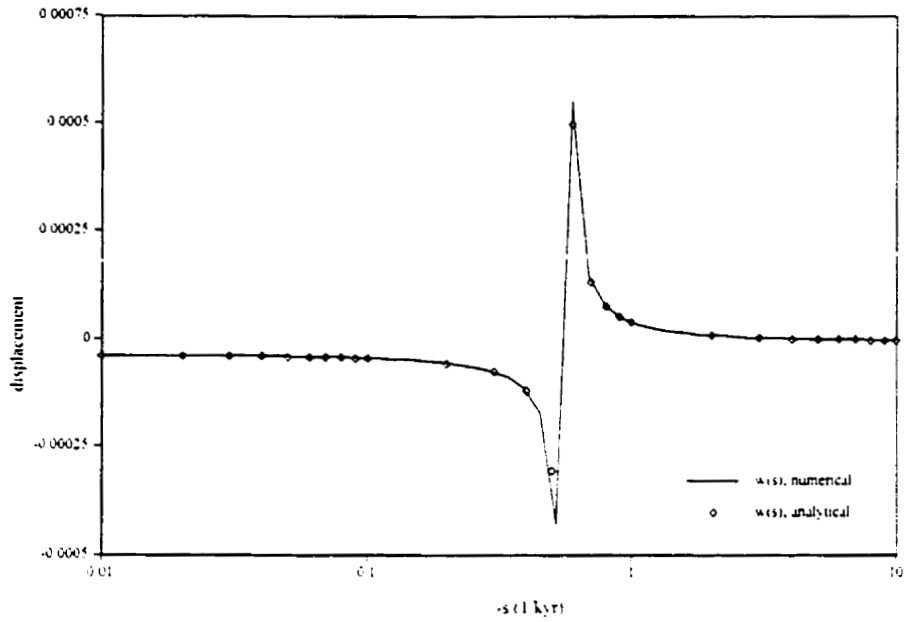


Figure 3.1.1: A graph of the vertical displacement at a depth of 100 km in the (k,s) domain that results from the loading of a halfspace

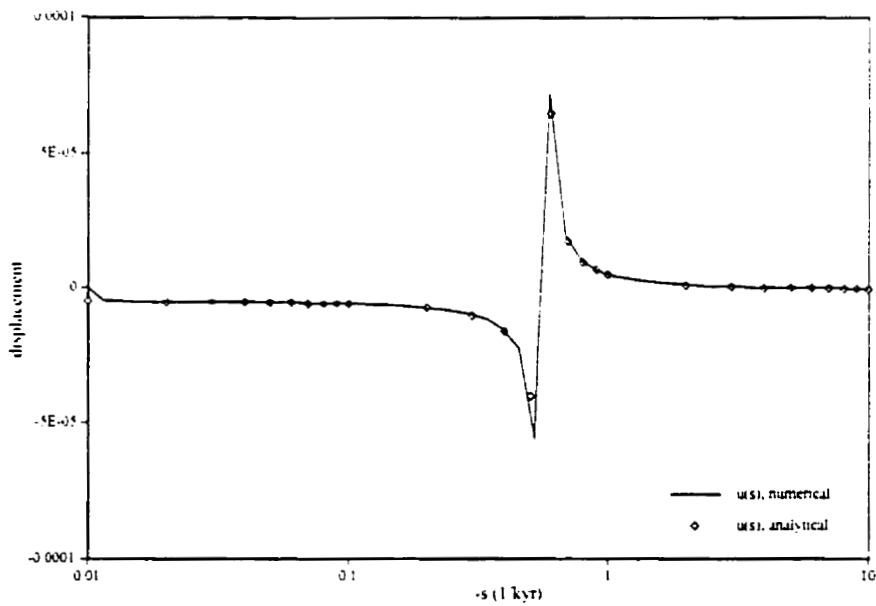


Figure 3.1.2: A graph of the horizontal displacement at a depth of 100 km in the (k,s) domain that results from the loading of a halfspace

3.2: Relaxation Diagram

To plot the relaxation diagram, it is necessary to determine the determinant function as a function of s . This determinant function is obtained from the matrix, \mathbf{M} , used to determine the constants from the boundary conditions at the surface, as shown in equation (2.4.2). For the halfspace model this matrix is

$$\mathbf{M} = \begin{pmatrix} 2\mu(s)k & 2\mu(s) \\ 2\mu(s)k + \rho g & 0 \end{pmatrix} \quad (3.2.1)$$

Therefore by solving for $\det \mathbf{M} = 0$ and substituting the formula for $\mu(s)$ as given in equation (2.2.6) the following equation is obtained.

$$-\frac{2\mu s [2\mu s k + \rho g (s + \frac{\mu}{\nu})]}{(s + \frac{\mu}{\nu})^2} = 0 \quad (3.2.2)$$

This is the determinant function for the halfspace model. There are three possible solutions. They are (a) $s = 0$

$$(b) s + \mu/\nu \rightarrow \infty$$

$$(c) 2\mu s k + \rho g (s + \frac{\mu}{\nu}) = 0$$

The first two solutions are not particularly informative and it is the third solution that will be analyzed. This gives the values of s for which the determinant function is zero. Note that these values are always negative.

$$s(k) = -\frac{\rho g \frac{\mu}{\nu}}{2\mu k + \rho g} \quad (3.2.3)$$

The relaxation times are the inverses of these values, $\tau = \frac{1}{-s(k)}$.

Also note that there is a singularity in the determinant function at $s = -\mu/\nu$. This can make it difficult to isolate the zeros of the function when it is being analyzed graphically, especially as the number of layers increases. As a remedy, the entire function is multiplied by a factor of $\sum_{i=1}^n (s + \mu_i/\nu_i)^2$, where there are n distinct layers within the model. This is referred to as the normalized determinant function (Wu and Ni, 1996).

The material parameters are the same as those used in the previous section, given in Table 2, except that these figures correspond to the solution at the surface. Figure 3.2.1 shows a graph of the determinant function for a halfspace as a function of s . It can be seen that the values for which this function is zero correspond to the solutions given by equation (3.2.3). It should also be noted that both the analytical and the numerical Matlab solutions are given. It is difficult to analyze this graph due to the singularity which can be clearly identified at the right hand side of the graph. Figure 3.2.2 shows the determinant function that has been multiplied by the factor $(s + \mu/\nu)^2$ to remove the singularity. Notice how it is much easier it is to identify the zeros. This graph also shows that the analytical and numerical results agree well.

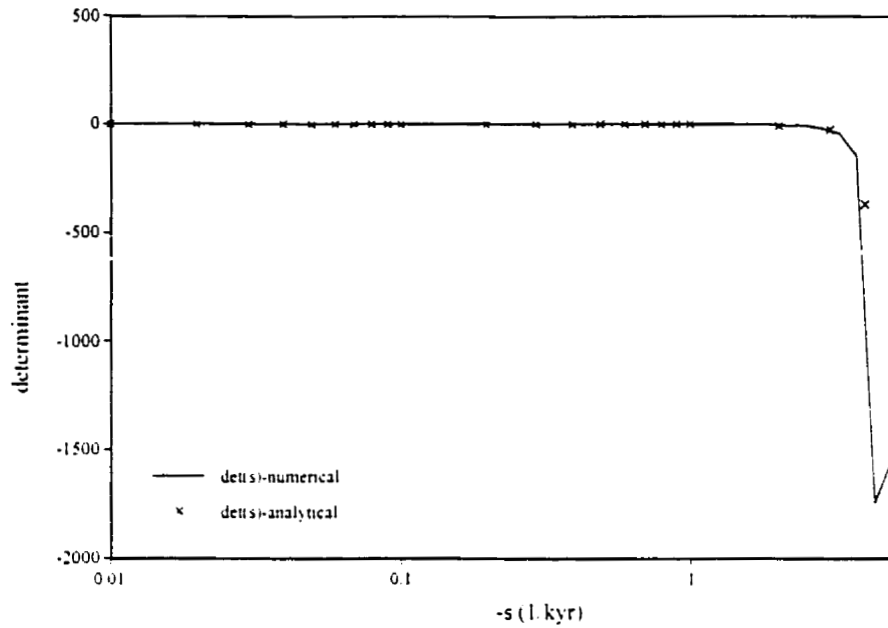


Figure 3.2.1: The analytical determinant function of the halfspace model as a function of s compared with the numerical results from Matlab

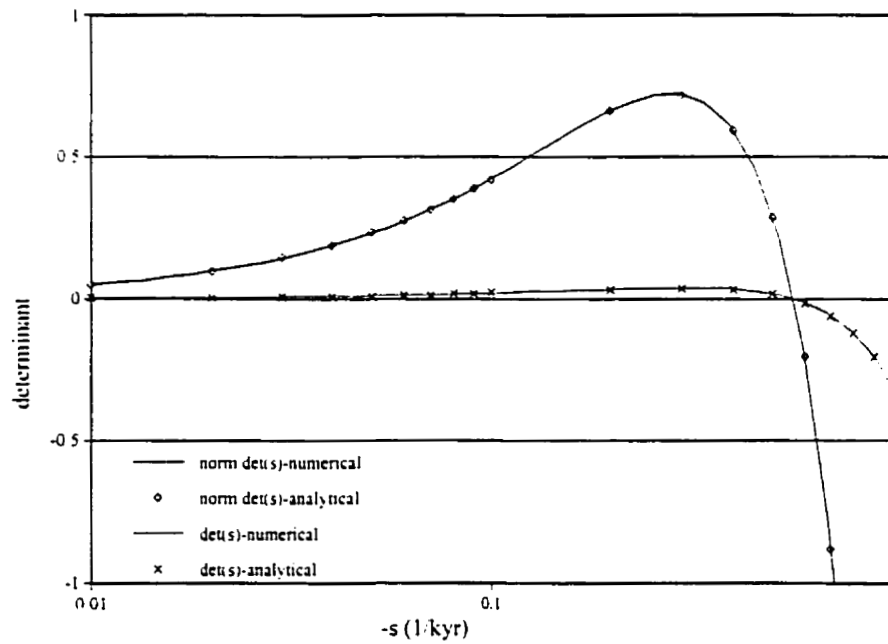


Figure 3.2.2: A comparison between the normalized and nonnormalized determinant functions of the halfspace model with numerical and analytical results

The values of s for which the determinant function are zero vary with wavenumber, k . A plot of these s values as a function of k is called the relaxation diagram. The relaxation diagram shows how the relaxation times (inverse of s) vary with wavenumber, k . In general the relaxation diagram for any particular model will have different modes of relaxation. The number of modes usually corresponds to the number of discontinuities in density and Maxwell times (Wu and Ni, 1996). The M modes refer to the buoyancy modes which arise from density contrasts. Relaxation diagrams can be used for diagnostic purposes through the analysis of the shape for large and small wavenumbers and the number of modes to determine the impact of variations in the material parameters on the response of a particular earth model to loading. The relaxation diagram for the halfspace model is shown in Figure 3.2.3. In this case there is only a single mode of relaxation due to the density contrast at the surface. This is called the M0 mode. This curve approaches a constant value for small values of k and becomes varies linearly for large values of k . The shape of this curve and the relaxation times associated with specific wavenumbers agrees well with the relaxation diagram given by Wu and Ni (1996, Figure 2) even though they use a spherical earth model. It should be noted that the angular order n for a spherical earth is related to the normalized wavenumber, k , by the following relationship $k = n - 1/2$.

The next series of figures demonstrates the effect of changing various earth properties on the relaxation diagram. In all of the following graphs the reference model is represented by grey points and all other models are represented by black points. Figure 3.2.4 shows the relaxation diagram for the original model (grey) and the model with an increase in the viscosity of the halfspace (black) from 1×10^{21} Pa s to 1×10^{23} Pa s. There is still only one mode of relaxation and the shape of the curve remains the same though it is displaced towards longer relaxation times; recall that the relaxation times are equal to the inverse of

the s values. This implies that an earth model with a higher viscosity will relax more slowly when subjected to a load. A decrease in density from 5517 kg m^{-3} to 3380 kg m^{-3} had little effect other than to increase the relaxation times slightly as demonstrated in Figure 3.2.5. This is due to that fact the density contrast at the surface is still relatively large. A model with a lower density will also relax more slowly. A change in the shear modulus within the halfspace, as shown in Figure 3.2.6, results in a slight increase in the relaxation times at small wavenumbers only. As the value of the shear modulus within the halfspace decreases from $1.45 \times 10^{11} \text{ N m}^{-2}$ to $0.67 \times 10^{11} \text{ N m}^{-2}$ only the small wavenumbers or large wavelengths are affected. The relaxation times for the small wavelength or shallow areas of the model are unaffected by the change in shear modulus.

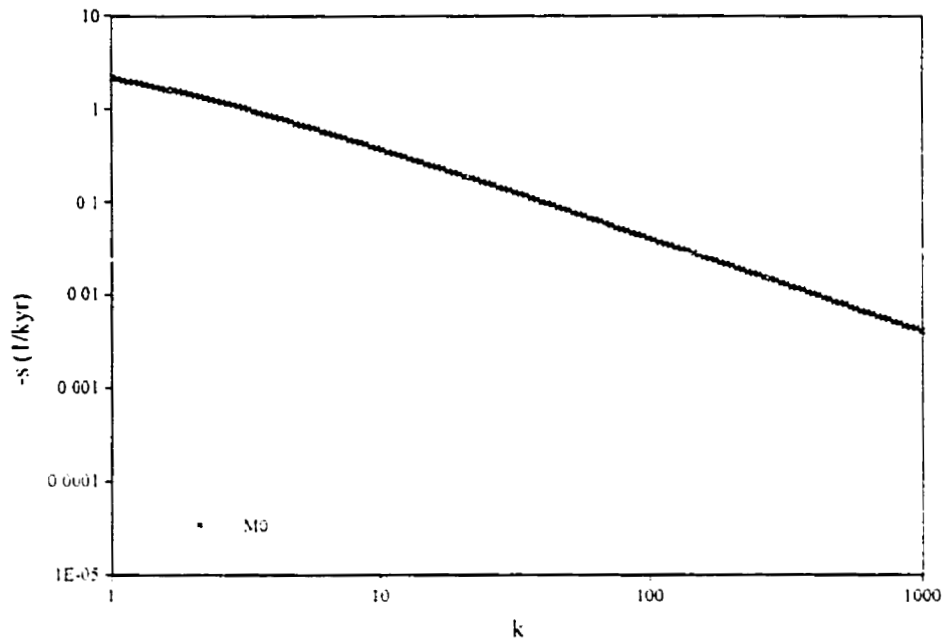


Figure 3.2.3: The relaxation diagram for the halfspace model (reference model)

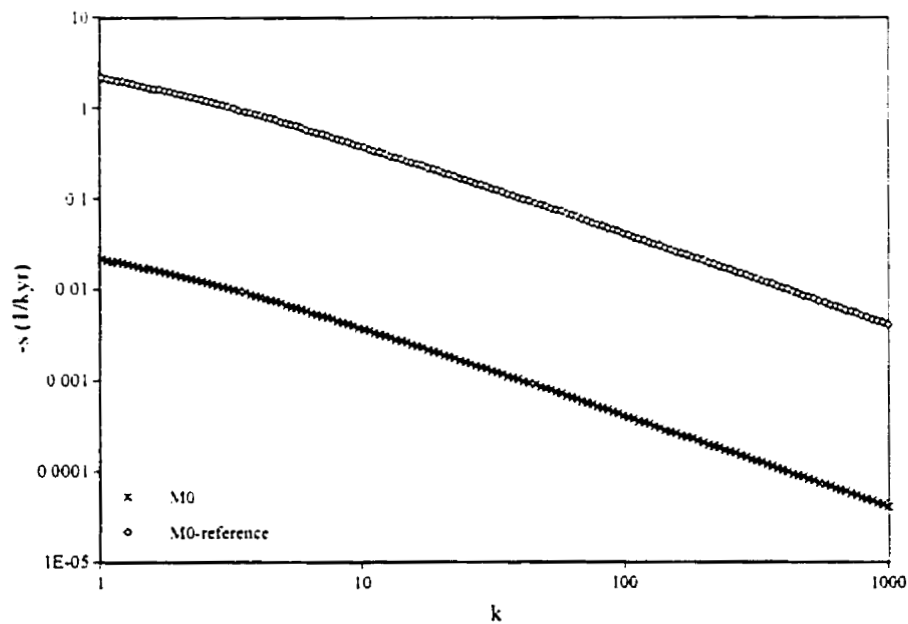


Figure 3.2.4: The relaxation diagram for a halfspace with a viscosity of 1×10^{23} Pa s (black) and the reference model (grey)

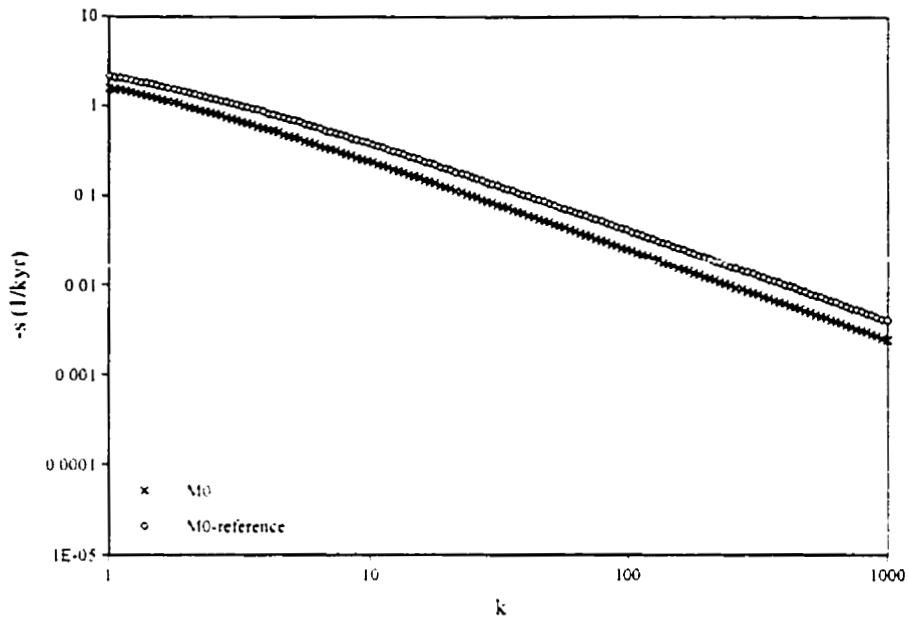


Figure 3.2.5: The relaxation diagram for a halfspace with a density of 3380 kg m^{-3} (black) and the reference model (grey)

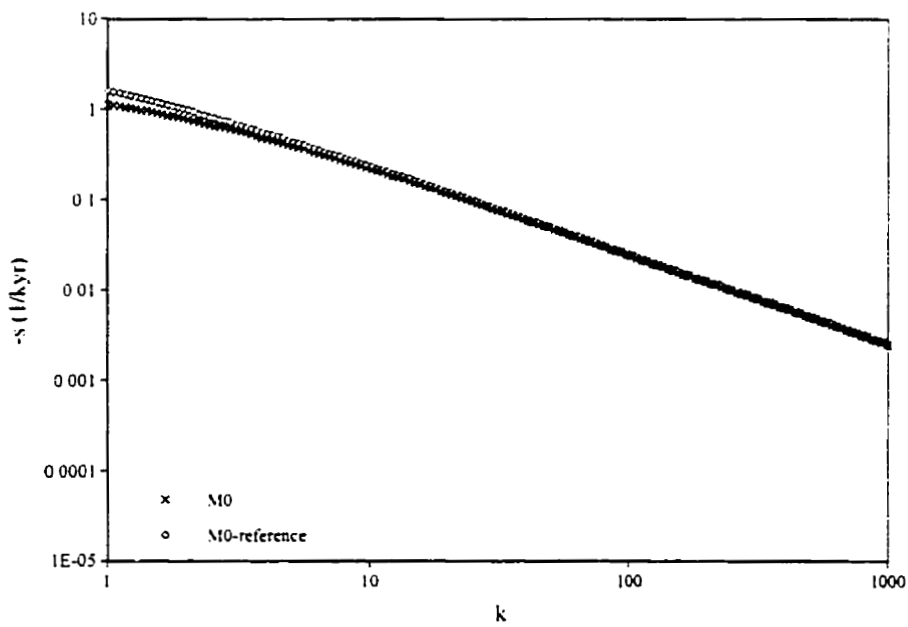


Figure 3.2.6: The relaxation diagram for a halfspace with a density of 3380 kg m^{-3} and a shear modulus of $0.67 \times 10^{11} \text{ N m}^{-2}$ (black) and the reference model (grey)

3.3: Excitation Strength Diagrams

Another method of comparing different models is to analyze differences in their excitation strengths. The excitation strength as defined after equation (2.4.16) and represents the viscous time independent component of the displacement. It is helpful in investigating the importance of properties at various depths throughout the model. This is done by making a plot of the excitation strength as a function of k . This is called an excitation strength diagram. As discussed in section 2.3, the excitation strength is defined as the residue multiplied by the relaxation time, $\frac{\bar{R}_i(z)}{s_i}$. In general residues are determined by equation (2.4.15).

$$R_i(z) = \frac{\bar{Q}^v(z, s_i)}{\frac{d}{ds} [\det \mathbf{M}(s)]},$$

where s_i are the solutions to $\det \mathbf{M} = 0$.

In the case of the halfspace model the vector \bar{Q}^v is found to be

$$\bar{Q}^v = \frac{\sigma \rho g e^{kz}}{k} \begin{pmatrix} kz \\ kz - 1 \\ -\rho g kz \\ 0 \end{pmatrix} \quad (3.3.1)$$

and the slope of the determinant function is

$$\frac{\partial}{\partial s} \det M = \frac{-2\mu^2 v [\rho g (vs + \mu) + 4\mu v ks]}{(vs + \mu)^3} \quad (3.3.2)$$

which is evaluated at, from equation (3.2.3).

$$s(k) = -\frac{\rho g \frac{\mu}{v}}{2\mu k + \rho g}.$$

For the halfspace there is a single residue and it is given by the following analytical equation.

$$\bar{R} = \frac{2\sigma\mu^2 ke^{kz}}{(2\mu k + \rho g)^2 v} \begin{pmatrix} kz \\ kz - 1 \\ -\rho g kz \\ 0 \end{pmatrix} \quad (3.3.3)$$

Therefore the excitation strengths are

$$\frac{\bar{R}}{s} = -\frac{2\sigma\mu ke^{kz}}{(2\mu k + \rho g)\rho g} \begin{pmatrix} kz \\ kz - 1 \\ -\rho g kz \\ 0 \end{pmatrix} \quad (3.3.4)$$

The excitation strength for the horizontal displacement is zero at the surface. The following figures show the excitation strength diagrams for the vertical displacement at the surface, i.e. $z = 0$. These diagrams plot the excitation strength as a function of the wavenumber, k . Figure 3.3.1 is the excitation strength of the halfspace model with material parameters as defined in Table 2 given in section 3.1. As with the relaxation

diagram there is a single mode. A constant value is approached for large values of k and for small values of k the excitation strength varies linearly. The proceeding figures demonstrate the effect of changing the properties within the halfspace on the excitation strength. These models are the same as those discussed with respect to the relaxation diagrams in section 3.2. Figures 3.3.2 through 3.3.4 contain both a reference curve, as given in Figure 3.3.1, identified by grey points and a curve identified by black points for a model with a variation from the reference. The excitation strength remains constant despite a change in the viscosity, (Figure 3.3.2), so although viscosity has a significant effect on the relaxation time (Figure 3.2.4) it has no effect on the excitation strength, as expected from an examination of equation (3.3.4). However the excitation strength increases significantly with decreasing density, as shown in Figure 3.3.3, while density has little effect on the relaxation time (Figure 3.2.5). A decrease in the shear modulus results in a decrease in the excitation strength for small values of k only, as shown in Figure 3.3.4. For both the relaxation time (Figure 3.2.6) and the excitation strength, a change in the shear modulus affects only the long wavelength (small wavenumber) response.

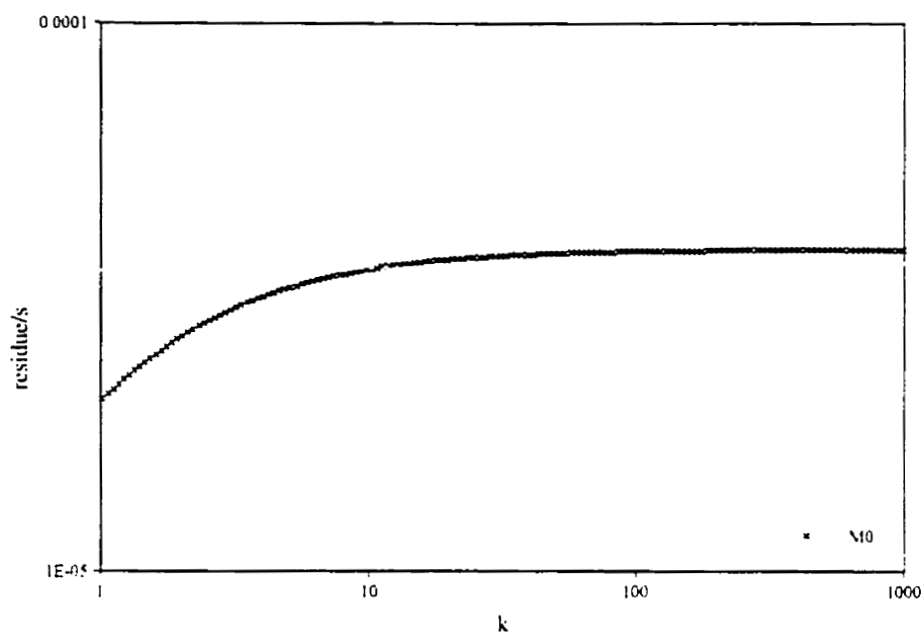


Figure 3.3.1: The vertical displacement excitation strength for the halfspace model (reference model)

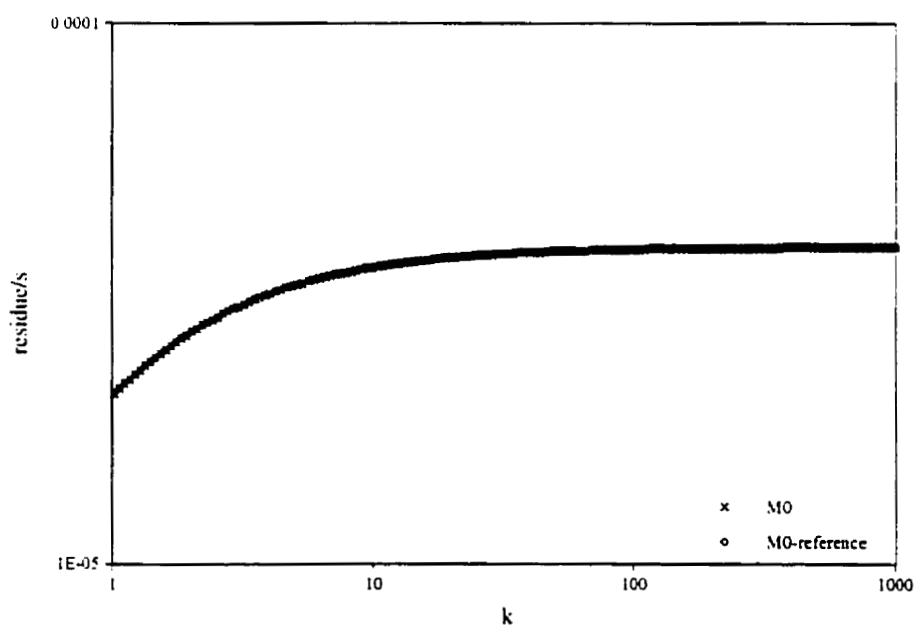


Figure 3.3.2: The vertical displacement excitation strength for a halfspace with a viscosity of 1×10^{23} Pa s (black) and the reference model (grey)

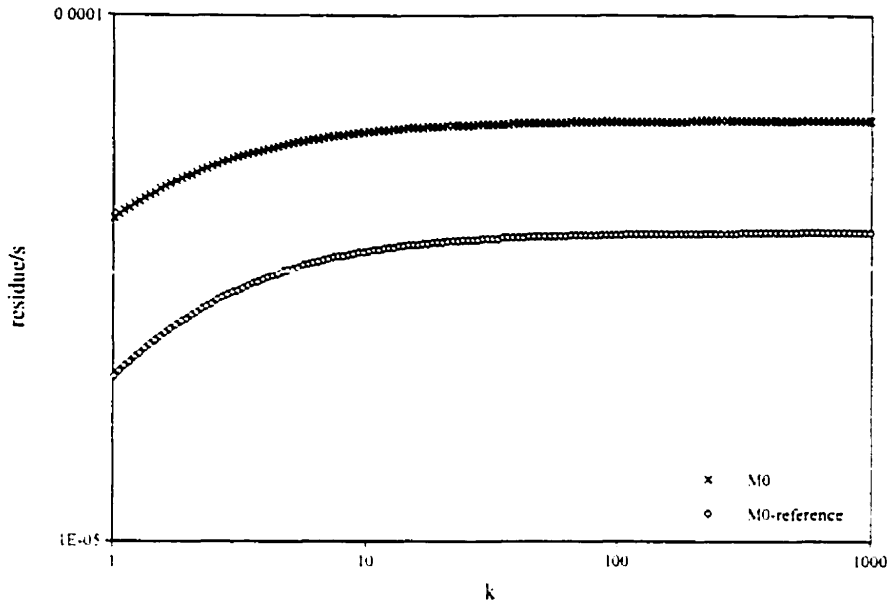


Figure 3.3.3: The vertical displacement excitation strength for a halfspace with a density of 3380 kg m^{-3} (black) and the reference model (grey)

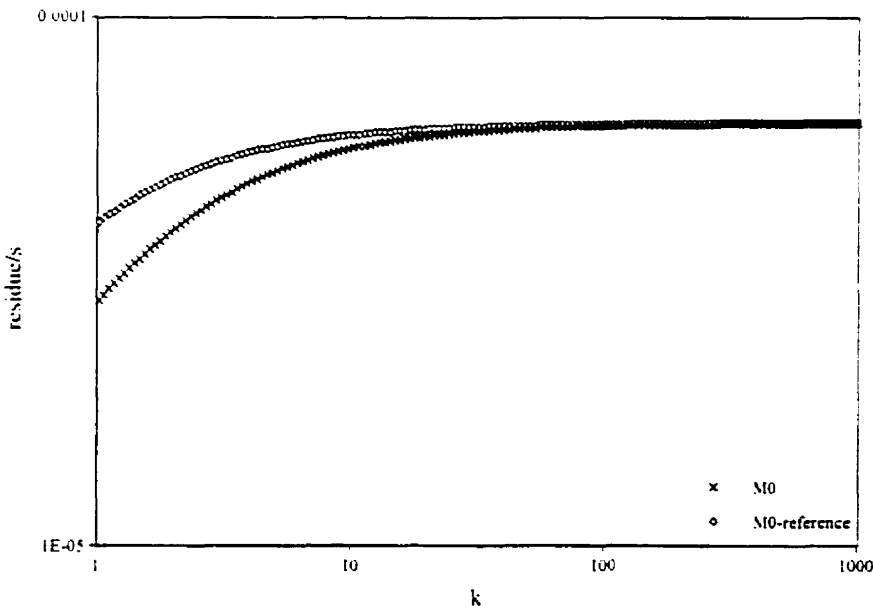


Figure 3.3.4: The vertical displacement excitation strength for a halfspace with a density of 3380 kg m^{-3} and a shear modulus of $0.67 \times 10^{11} \text{ N m}^{-2}$ (black) and the reference model (grey)

3.4: Space Domain Solution

This section will begin with a description of the analytical time domain solution obtained using the normal mode method. The space domain solution is difficult to determine analytically, so the analytical time domain solutions are entered into the FORTRAN program designed to perform the inverse Hankel transform to obtain the space domain solution. This solution will be compared with the solution obtained by importing the numerical Matlab data into the FORTRAN program. Finally both of these solutions will be compared with the solution obtained from the finite element modeling package, ABAQUS.

Using the normal mode method as described in section 2.4, the analytical time domain solution for the halfspace model with a disc load of magnitude $-\sigma$ is

$$\bar{Y}(k, t) = \frac{\sigma e^{kz}}{2\mu k + \rho g} \begin{pmatrix} kz \\ kz - 1 \\ 2\mu k^2 z \\ (kz - 1)(2\mu k + \rho g) \end{pmatrix} + \frac{2\sigma\mu k e^{kz}}{(2\mu k + \rho g)\rho g} \begin{pmatrix} kz \\ kz - 1 \\ -\rho g k z \\ 0 \end{pmatrix} \left(1 - e^{-\frac{\rho v \mu}{i(2\mu k + \rho g)v} t} \right). \quad (3.4.1)$$

The full derivation of this solution can be found in Appendix D.

Before the above equations for the time domain solution of the vertical and horizontal displacements were incorporated into the FORTRAN program to obtain the space domain solution the FORTRAN program was tested. The inverse Hankel transform was performed on some simple functions and the output was compared with the results given in a paper by Chave (1983).

The vertical displacement that results from the loading of a halfspace was examined using three different methods. The first was to substitute the analytical equation for the displacement in the (k,t) domain into the FORTRAN program. The second was to import the numerical results from the Matlab program into the FORTRAN program. The third was to use the finite element modeling package ABAQUS. A graph of the three results overlain can be seen in Figure 3.4.1. The data obtained from ABAQUS is much more dense which is why it is plotted as a curve rather than independent points. The results compare favorably. This gives confidence in ABAQUS as well as the FORTRAN program. Unfortunately the value of the horizontal displacement is zero at the surface so it was not possible to test the validity of the numerical methods in its calculation.

The vertical displacement that results from the loading of halfspace, Figure 3.4.1, has several distinct properties. The model parameters are given in Table 2, given in section 3.1, and the ice load has a radius of 2000 km, indicated by the arrow, and a height of 1 km. There is an initial elastic displacement followed by viscous relaxation at one, five and ten thousand years after the emplacement of the load. After a period of five thousand years, the maximum displacement has been obtained. There is also a peripheral bulge that develops by ten thousand years after the emplacement of the load. A peripheral bulge is defined as an area in the displacement curve that experiences uplift rather than submergence after the emplacement of the load. The largest gradient in the displacement curve is located at the edge of the load. The displacement quickly approaches a value of zero away from the load. Figure 3.4.2 shows the effect on the vertical displacement as the viscosity of the halfspace increases from 1×10^{21} Pa s to 1×10^{23} Pa s. The initial elastic displacement remains unchanged. This agrees with the analytical solution which shows that the elastic solution is independent of viscosity. However, the magnitude of

the viscous motion has decreased significantly so that the full extent of the deformation will take longer than ten thousand years to be realized. The final model to be considered in this section has a smaller load. In Figure 3.4.3 the load has a radius of 1000 km instead of 2000 km. In general the shape of the curves remains the same. The maximum displacement is unchanged and the steepest slope is still at the edge of the load. A peripheral bulge is still present in the curve for ten thousand years after the load is emplaced.

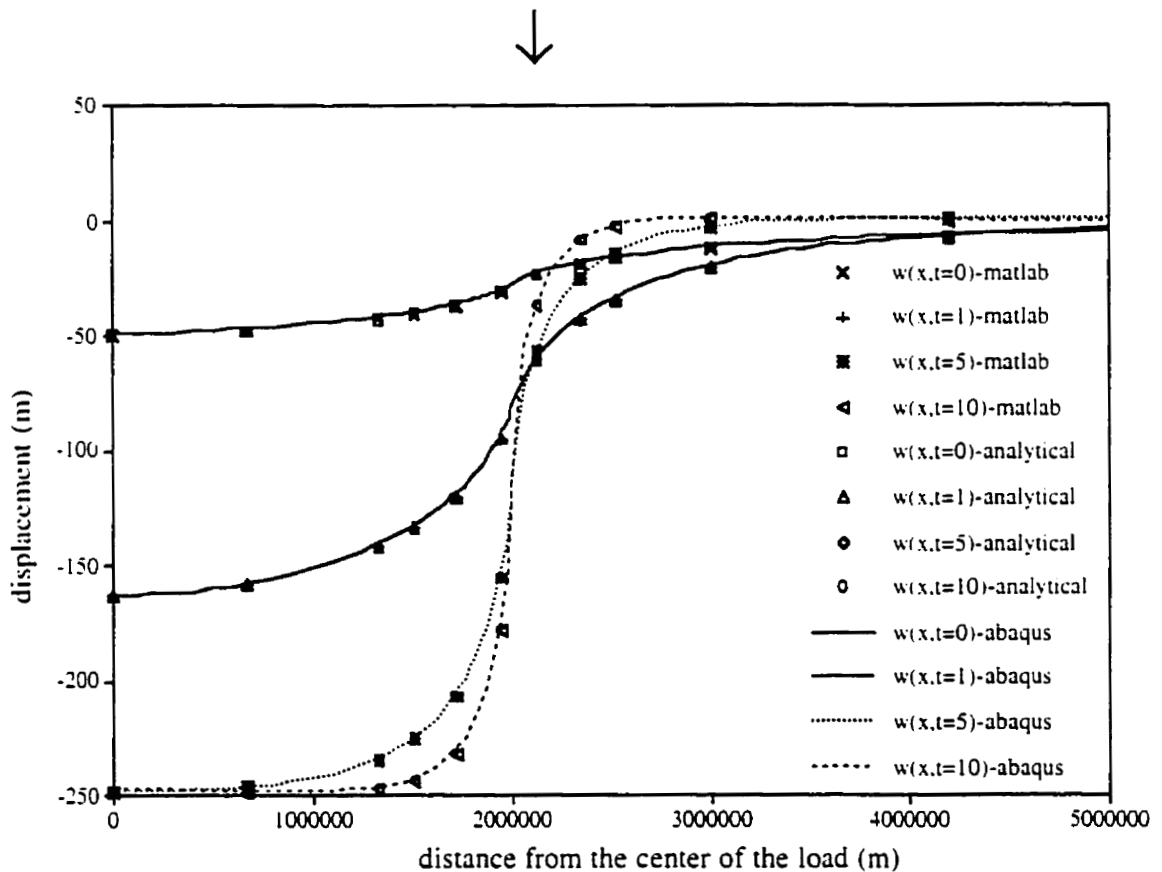


Figure 3.4.1: Graph of the vertical displacement that results from the loading of a halfspace with a viscosity of 1×10^{21} Pa s and a load radius of 2000 km; results from the analytical solution, the Matlab numerical solution and the ABAQUS numerical solution

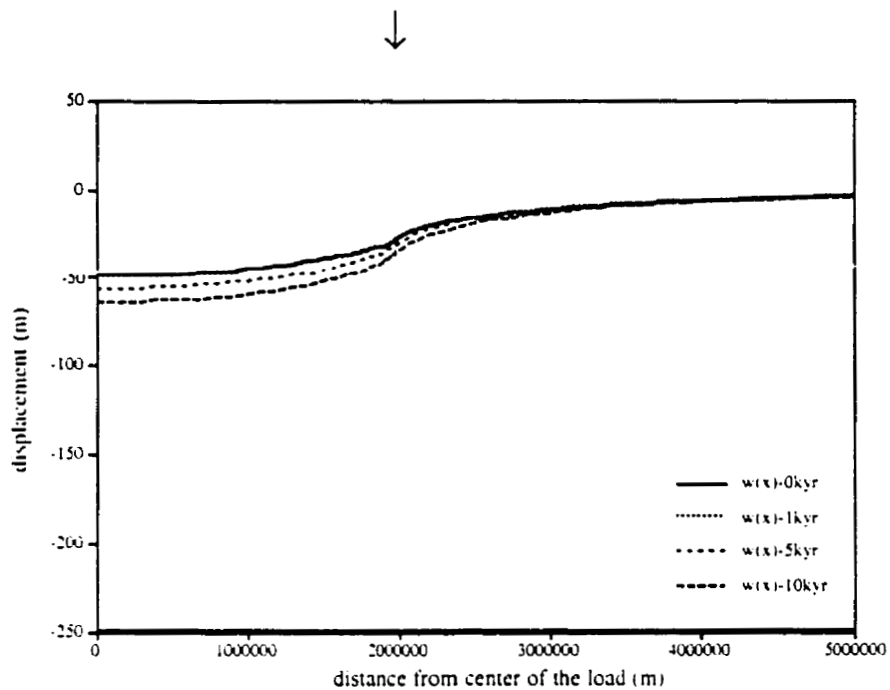


Figure 3.4.2: The vertical displacement of a halfspace with a viscosity of 1×10^{23} Pa s

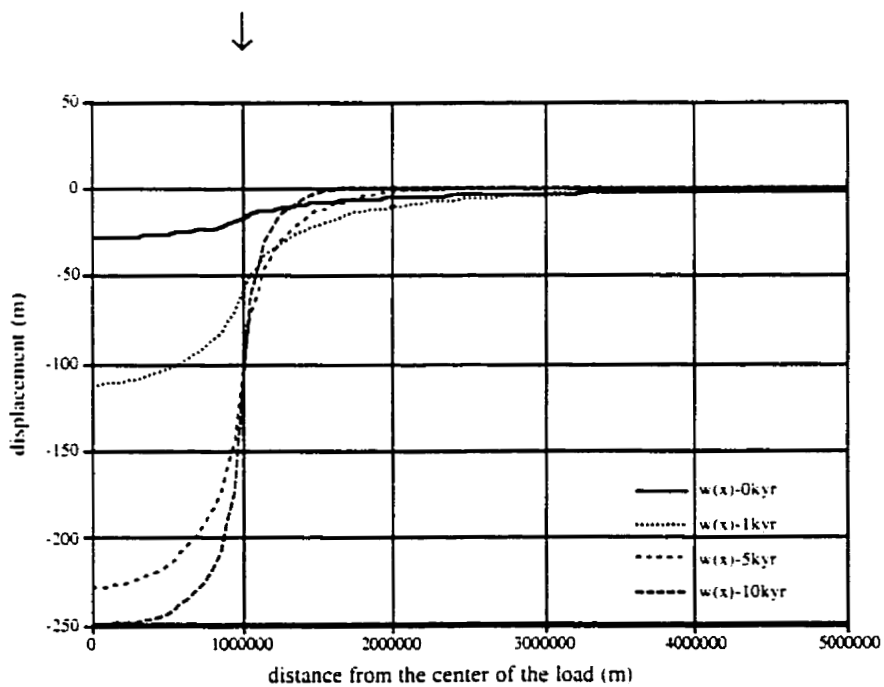


Figure 3.4.3: The vertical displacement for a halfspace with a 1000 km radius load

Chapter 4: Analysis of More Complicated Earth Models in the (k,s) Domain

This chapter will discuss the relaxation and excitation strength diagrams of some more complicated earth models. The first to be considered is the channel model where there is a finite amount of material to compensate for the load. The next to be considered is the model with an elastic lithosphere. The analytical solution for the loading of an elastic lithosphere over a fluid is presented and then the relaxation and excitation strength diagrams for a lithosphere over a viscoelastic halfspace are analyzed. In the final section the response of models with two or three distinct layers will be discussed. By studying these wide ranging models the impact of different parameters on the relaxation times and excitation strengths can be determined. This will facilitate the interpretation of the space and time domain solutions.

4.1: The Channel Model

A channel is defined as a layer with a fixed lower boundary such that all of the motion required to compensate for a load must occur within the channel. The viscoelastic channel extends from the surface to a depth, $-H$, where the boundary is absolutely rigid. Since the channel model is a fairly simple model the analytical solution was derived and a further check of the accuracy of the numerical methods was carried out. A channel is a very unique model because there is no underlying viscoelastic halfspace hence there is a finite amount of viscoelastic material available for compensation. If numerical results be could accurately obtained for this model then further results could be examined with greater confidence.

4.1a The Analytical Solution

The standard set of differential equations is solved with boundary conditions appropriate to a channel (equation (2.3.35)). By definition a channel has a rigid lower boundary. The conditions at the surface boundary remain the same, that is, the shear stress is zero and the normal stress is constant. However, in this case there is a lower boundary at some finite depth which is immobile. The weight of the load must be completely compensated by the limited material within the channel so strong horizontal flow is experienced. This is in contrast to the halfspace model where there is an infinite amount of material for compensation and dominantly vertical flow. For the channel model the condition at the lower surface is that it is rigid and no motion occurs below this depth; horizontal and vertical displacements are zero.

Following the method outlined in sections 2.3 and 2.4 the (k, t) domain analytical solutions for the displacements at the surface of the channel model with a Heaviside load were determined using a mathematical manipulation program called Mathview (Hoffner, 1997). The details of this derivation are given in Appendix E. The results are

$$U(k, t) = \frac{\sigma H^2 k^2}{(2\mu k \gamma + \rho g)(\cosh Hk \sinh Hk - Hk)} \left[1 + \frac{2\mu k \gamma}{\rho g} (1 - e^{-\alpha}) \right] \quad (4.1.1)$$

$$W(k, t) = -\frac{\sigma}{(2\mu k \gamma + \rho g)} \left[1 + \frac{2\mu k \gamma}{\rho g} (1 - e^{-\alpha}) \right] \quad (4.1.2)$$

$$\text{where } \alpha = \frac{\rho g \mu}{v(2\mu k \gamma + \rho g)}, \text{ and } \gamma = \frac{\cosh^2 Hk + H^2 k^2}{\cosh Hk \sinh Hk - Hk},$$

and H is the thickness of the channel.

It can be seen that this solution is very similar to the solution for the halfspace model given by equation (3.4.1), especially the vertical displacement. Therefore it can be seen that the relaxation times are given by the inverse of α .

$$\tau^{-1} = \alpha = \frac{\rho g \mu}{v(2\mu k \gamma + \rho g)} \quad (4.1.3)$$

the horizontal displacement excitation strengths are given by

$$U_{ES}(k) = \frac{\sigma H^2 k^2}{(2\mu k \gamma + \rho g)(\cosh Hk \sinh Hk - Hk)} \left[\frac{2\mu k \gamma}{\rho g} \right] \quad (4.1.4)$$

and the vertical displacement excitation strengths are given by

$$W_{ES}(k) = -\frac{\sigma}{(2\mu k \gamma + \rho g)} \left[\frac{2\mu k \gamma}{\rho g} \right] \quad (4.1.5)$$

These are also similar to the results obtained for the halfspace model as given by equations (3.2.3) and (3.3.4). For all of the figures in this section the reference channel model is given by the material properties given in the table below (Table 3).

Table 3: The Material Properties of the Channel Model

	<u>halfspace, below 670 km</u>	<u>channel, above 670 km</u>
density	$\rho = 5517 \text{ kg m}^{-3}$	$\rho = 5517 \text{ kg m}^{-3}$
gravitational acceleration	$g = 7.365 \text{ m s}^{-2}$	$g = 7.365 \text{ m s}^{-2}$
viscosity	$\nu = 1 \times 10^{21} \text{ Pa s}$	$\nu = 1 \times 10^{21} \text{ Pa s}$
shear modulus	$\mu = 1.452 \times 10^{11} \text{ N m}^{-2}$	$\mu = 1.452 \times 10^{11} \text{ N m}^{-2}$
radius of load		$R = 2 \times 10^6 \text{ m}$
load		$\sigma = 1 \times 10^7 \text{ Pa}$

4.1b The Relaxation and Excitation Strength Diagrams

The relaxation diagram, the horizontal displacement excitation strength diagram and the vertical displacement excitation strength diagram for the channel model can be found in Figures 4.1.1, 4.1.2, and 4.1.3 respectively. The relaxation diagram for the channel model, as shown in Figure 4.1.1, is very similar to that of the halfspace model (Figure 3.2.3), except that while the relaxation times approach a constant value at small k for the halfspace model, for the channel model the relaxation times increase linearly with k in the log-log plot. Therefore a minimum relaxation time is obtained at a specific value of k . This value of k corresponds to the depth of the base of the channel. For large wavenumber (small wavelength) the shallow part of the model is sampled and the response is that of the halfspace model. For smaller wavenumbers (larger wavelengths) deeper parts of the model are sampled and the rigid boundary below which no motion occur is encountered. Once this occurs the relaxation times increase. The excitation strength for the horizontal displacement goes to zero for large values of k and increases linearly for small values in the log-log plot, as demonstrated by Figure 4.1.2. Since there is zero horizontal excitation strength for the halfspace model it is expected that at large wavenumbers (small wavelengths) for the channel model the excitation strength would also be zero, which is observed. The vertical displacement excitation strength diagram is shown in Figure 4.1.3. It is also similar to that of the halfspace model (Figure 3.3.1) in that it has a constant value for large values of k , however, the vertical excitation strength for the channel model is also constant for small values of k . In fact it is almost independent of k . The only deviation from this constant value is experienced at k values which correspond to the depth of the channel. Note that both the horizontal and vertical displacement excitation strengths are positive. Since the excitation strength represents the

viscous portion of the time domain solution, this implies that the subsequent viscous motion will be in the same direction as the initial elastic displacement.

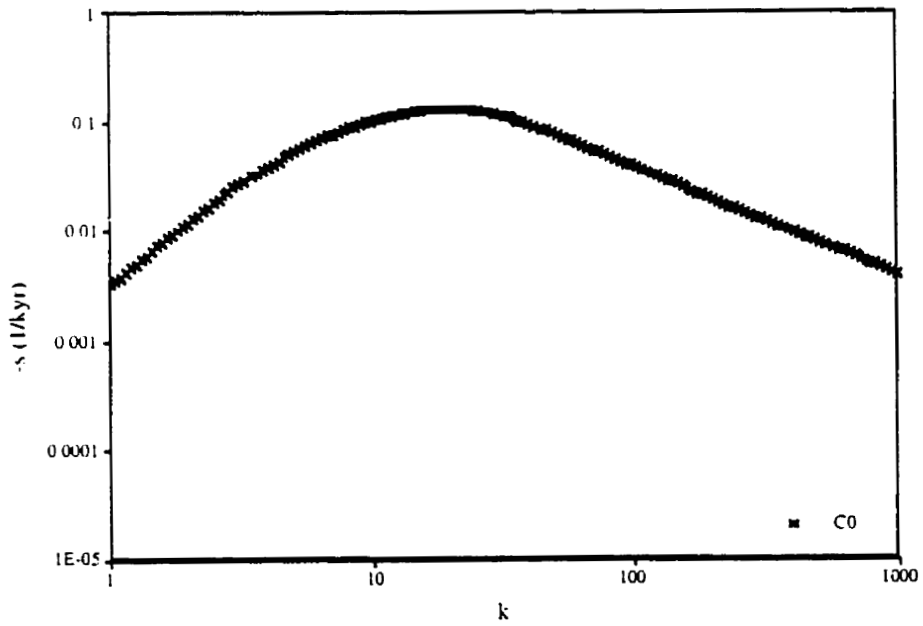


Figure 4.1.1: The relaxation diagram of the channel model (reference model)

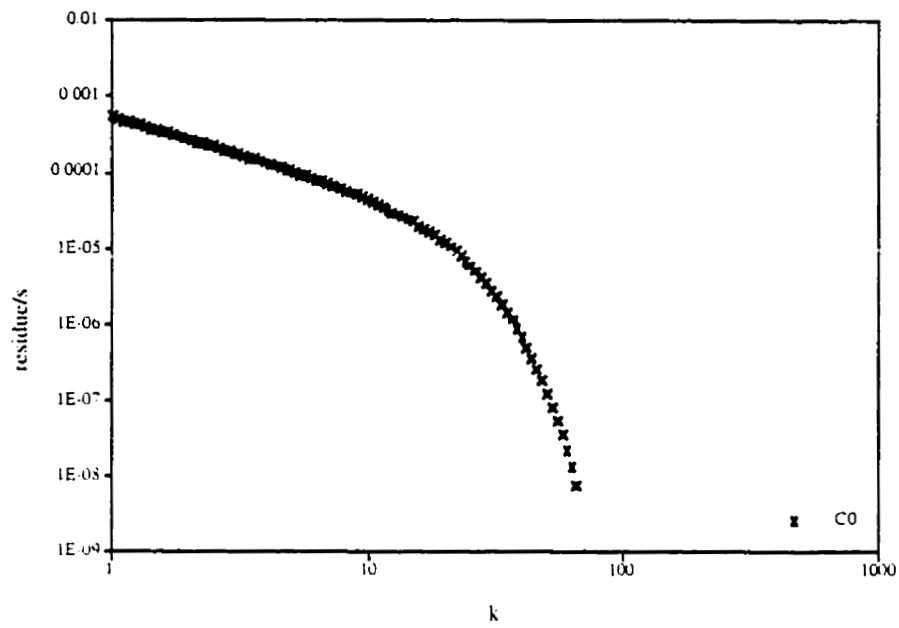


Figure 4.1.2: The horizontal displacement excitation strength for the channel model (reference model)

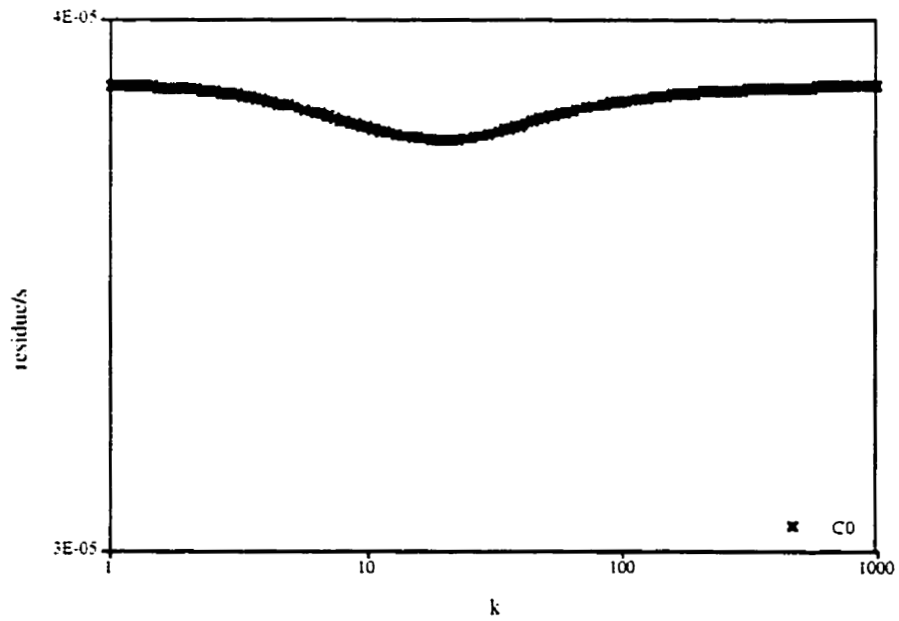


Figure 4.1.3: The vertical displacement excitation strength for the channel model (reference model)

Now the effect of the material properties of the channel are studied. In all of the remaining figures in this section include two curves. The curve represented by grey points corresponds to the reference channel curve while the black points correspond to the curve of the new model being considered. Figure 4.1.4 shows the effect of decreasing the viscosity within the channel. As seen with the halfspace model the shape of the curve of the relaxation times with respect to k remains constant, however, the relaxation times uniformly decrease as the viscosity decreases from 1×10^{21} Pa s to 1×10^{19} Pa s. As the density of the channel decreases from 5517 kg m^{-3} to 3380 kg m^{-3} , as shown in Figure 4.1.5, a response similar to that of an increase in the viscosity is observed. The values for relaxation times increase for all wavenumbers, k . No change is noted for a decrease in the shear modulus of the channel (Figure 4.1.6). The final diagram in this section, Figure 4.1.7, shows the effect of decreasing the thickness of the channel from 670 km to 200 km. For small wavenumbers the relaxation times increase and the location of the minimum relaxation time shifts towards larger values of k . This value of k is related to the depth of the channel which experiences the slowest relaxation.

The next set of figures shows how these same changes in the material parameters affect the excitation strengths of the horizontal displacement. Figure 4.1.8 shows that as the viscosity decreases the horizontal displacement excitation strength remains virtually unchanged. As the density decreases, as in Figure 4.1.9, the excitation strength increases slightly, while again no change is observed for a decrease in the shear modulus of the channel (Figure 4.1.10). As the thickness of the channel decreases not only does the excitation strength increase, but it remains finite for larger values of k , as shown in Figure 4.1.11.

The final set of figures in this section considers the excitation strengths of the vertical displacement. As seen with the horizontal displacement excitation strength (Figure 4.1.8) a change in viscosity has no effect on the vertical displacement excitation strength (Figure 4.1.12). A decrease in the density significantly increases the excitation strength of the vertical displacement, as seen in Figure 4.1.13. As opposed to the horizontal displacement excitation strength the excitation strength of the vertical displacement changes with decreasing shear modulus as illustrated in Figure 4.1.14. The minimum excitation strength decreases with decreasing shear modulus though the limits at large and small k remain constant. Figure 4.1.15 shows that a decrease in the thickness of the channel results in a wavenumber independent excitation strength curve. The minimum excitation strength is obtained at a larger wavenumber which corresponds to the decrease in the channel thickness.

Changes in viscosity have a significant effect on the relaxation times but no effect on the horizontal and vertical displacement excitation strengths. This agrees with the expected results based on the analytical solutions for the relaxation times and excitation strengths. This is also the same response as seen with the halfspace model. A change in density affects all of the diagrams, while a change in the shear modulus affects only the vertical displacement excitation strength. A change in the thickness of the channel affects the response at small wavenumbers (large wavelengths) only. Overall, the channel thickness is the most important quality in determining the relaxation times and horizontal displacement excitation strength. The vertical displacement excitation strength is affected most strongly by changes in the density of the channel.

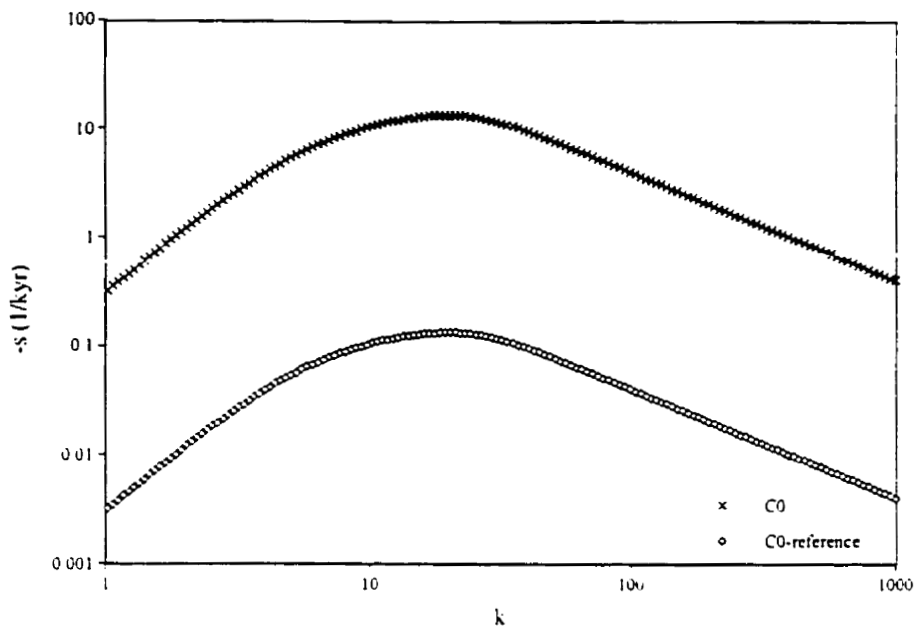


Figure 4.1.4: The relaxation diagram for a channel with a viscosity of 1×10^{19} Pa s (black) and the reference model (grey)

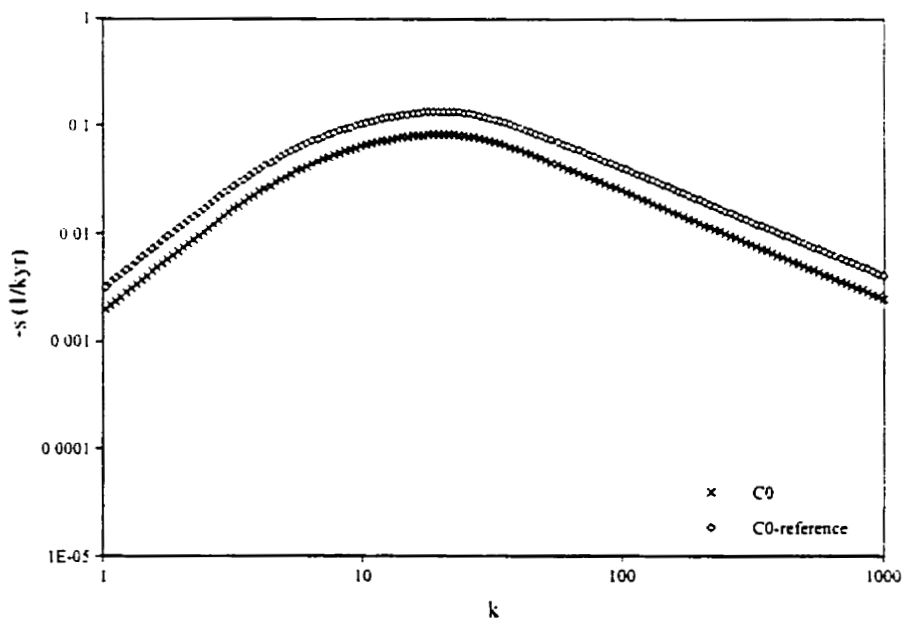


Figure 4.1.5: The relaxation diagram for a channel with a density of 3380 kg m^{-3} (black) and the reference model (grey)

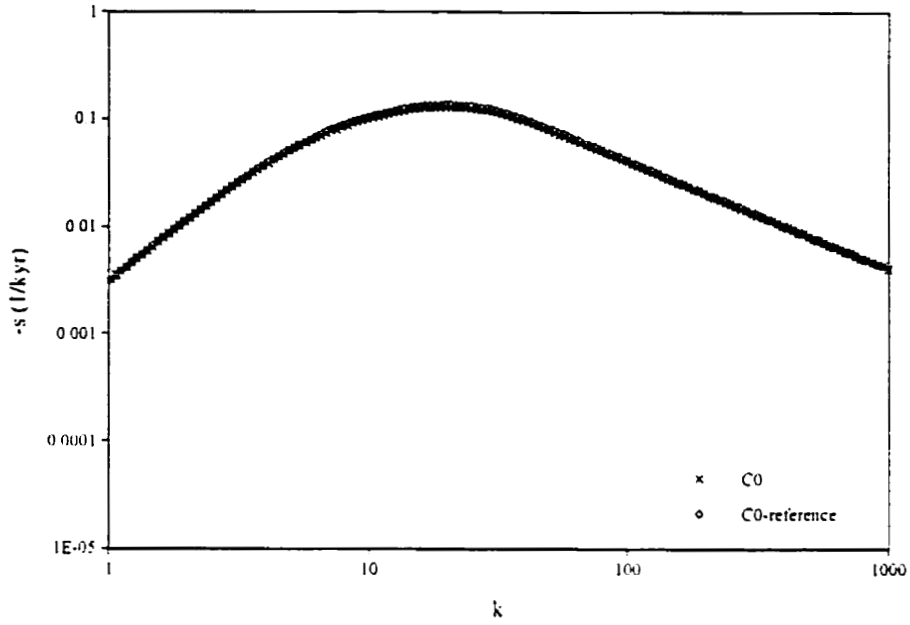


Figure 4.1.6: The relaxation diagram for a channel with a shear modulus of $0.67 \times 10^{11} \text{ N m}^{-2}$ (black) and the reference model (grey)

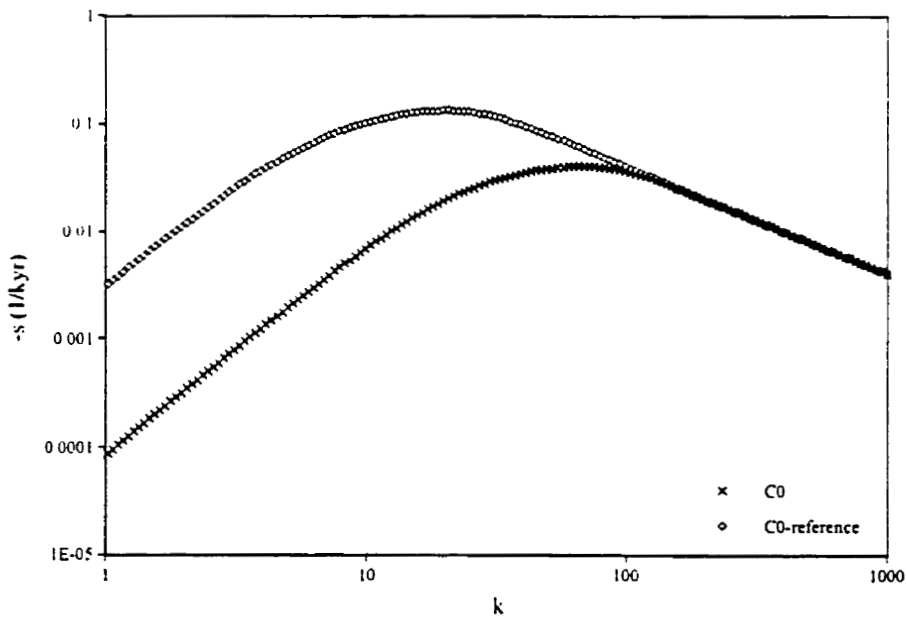


Figure 4.1.7: The relaxation diagram for a 200 km thick channel (black) and the reference model (grey)

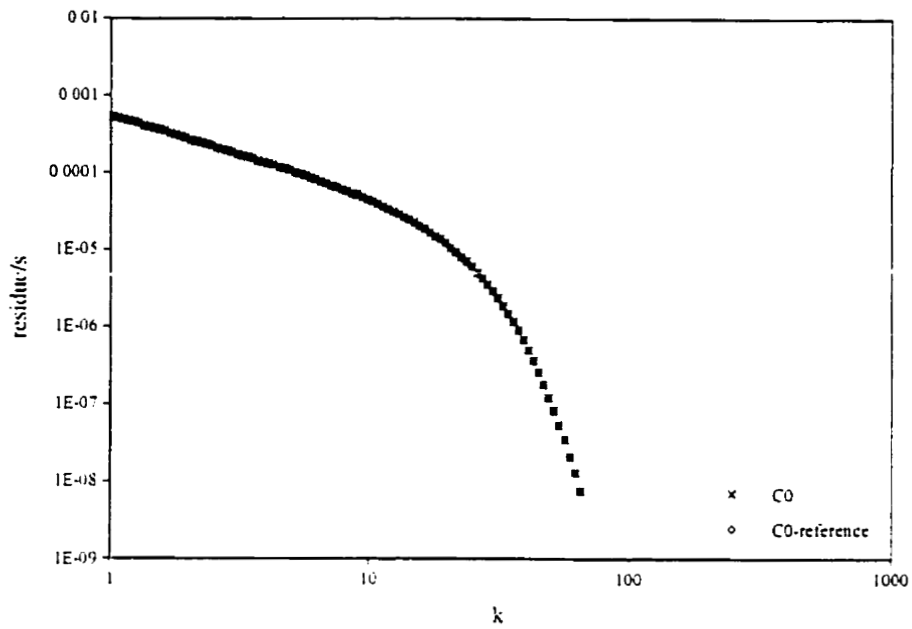


Figure 4.1.8: The horizontal displacement excitation strength for a channel with a viscosity of 1×10^{19} Pa s (black) and the reference model (grey)

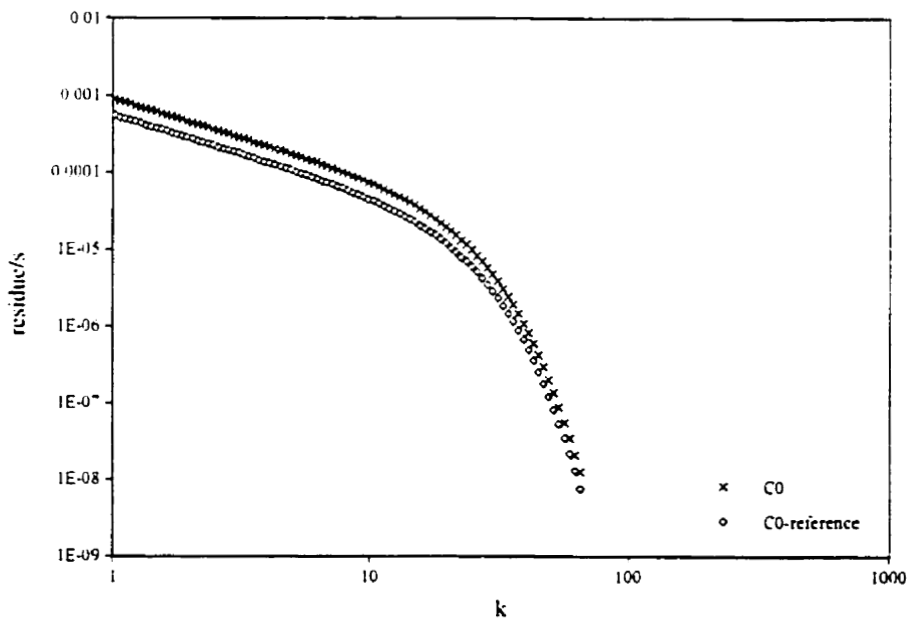


Figure 4.1.9: The horizontal displacement excitation strength for a channel with a density 3380 kg m^{-3} (black) and the reference model (grey)

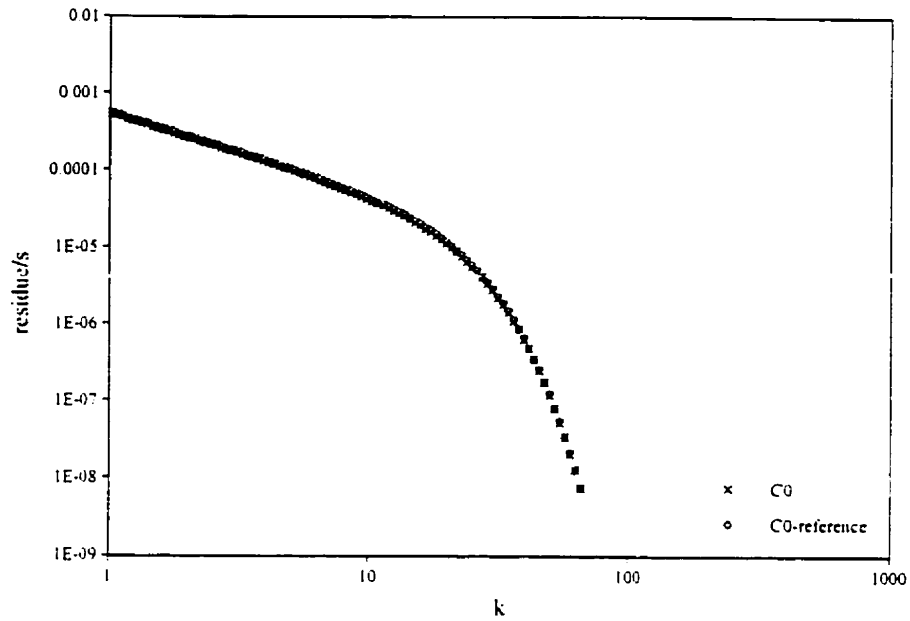


Figure 4.1.10: The horizontal displacement excitation strength for a channel with a shear modulus of $0.67 \times 10^{11} \text{ N m}^{-2}$ (black) and the reference model (grey)

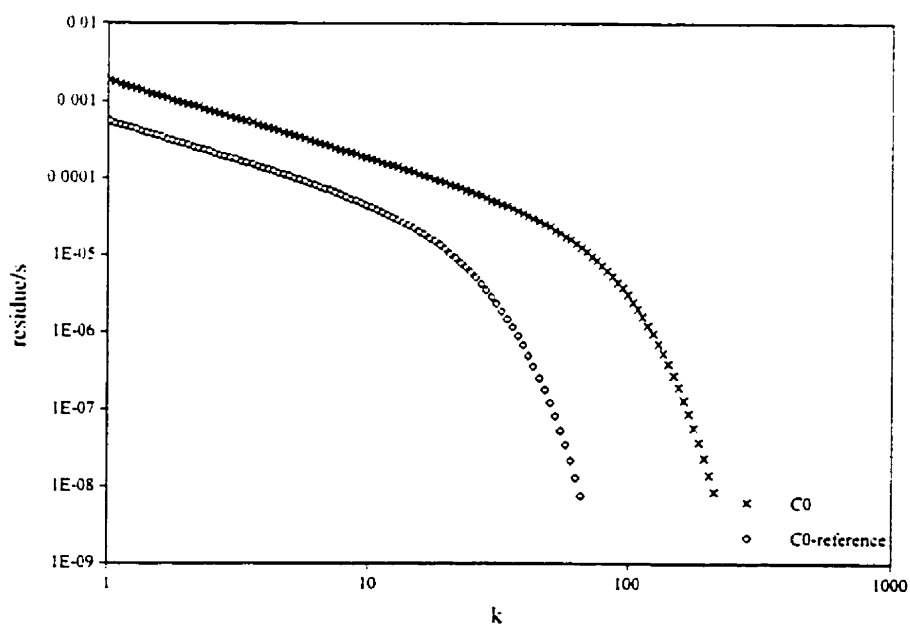


Figure 4.1.11: The horizontal displacement excitation strength for a 200 km thick channel (black) and the reference mode (grey)

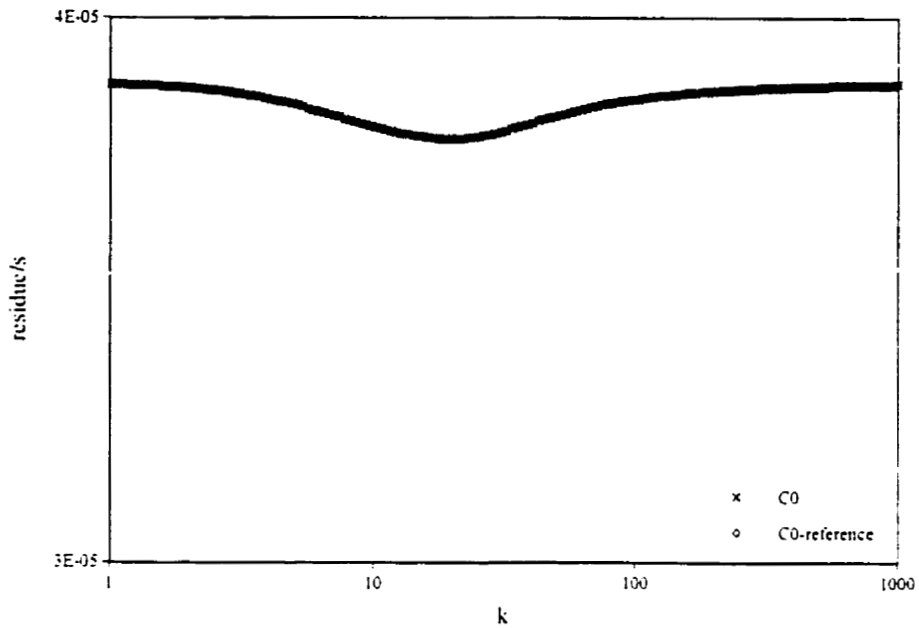


Figure 4.1.12: The vertical displacement excitation strength for a channel with a viscosity of 1×10^{19} Pa s (black) and the reference model (grey)

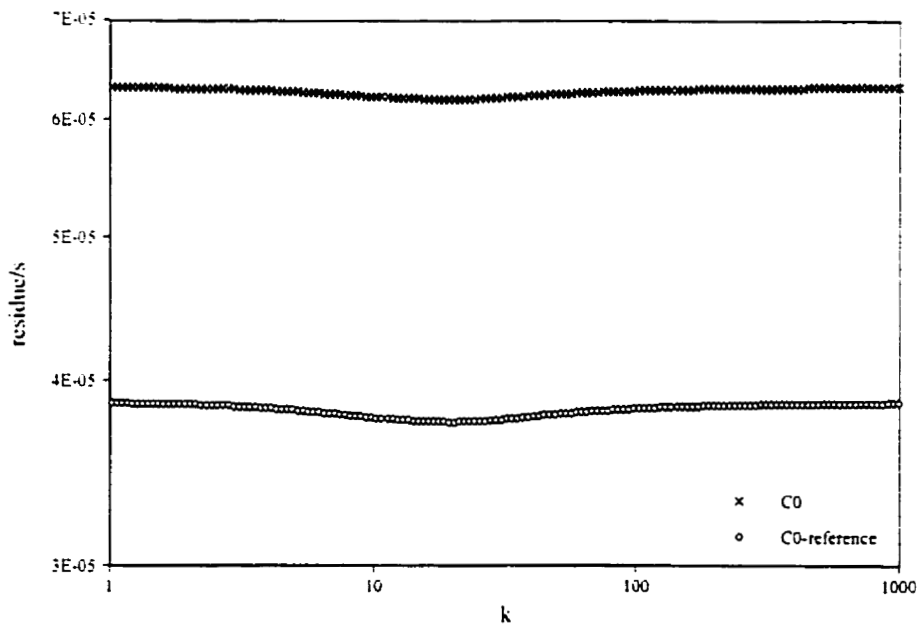


Figure 4.1.13: The vertical displacement excitation strength for a channel with a density of 3380 kg m^{-3} (black) and the reference model (grey)

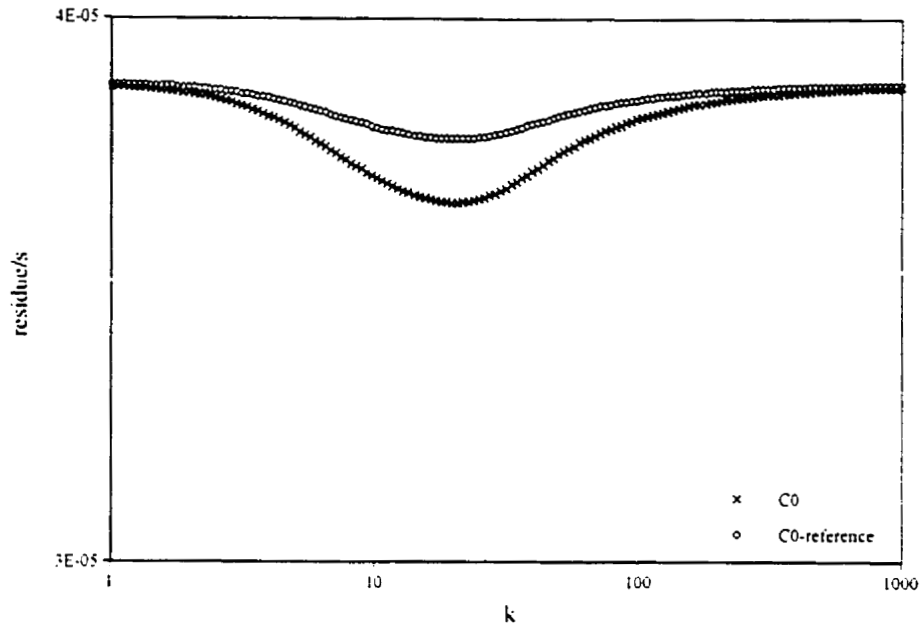


Figure 4.1.14: The vertical displacement excitation strength for a channel with a shear modulus of $0.67 \times 10^{11} \text{ N m}^{-2}$ (black) and the reference model (grey)

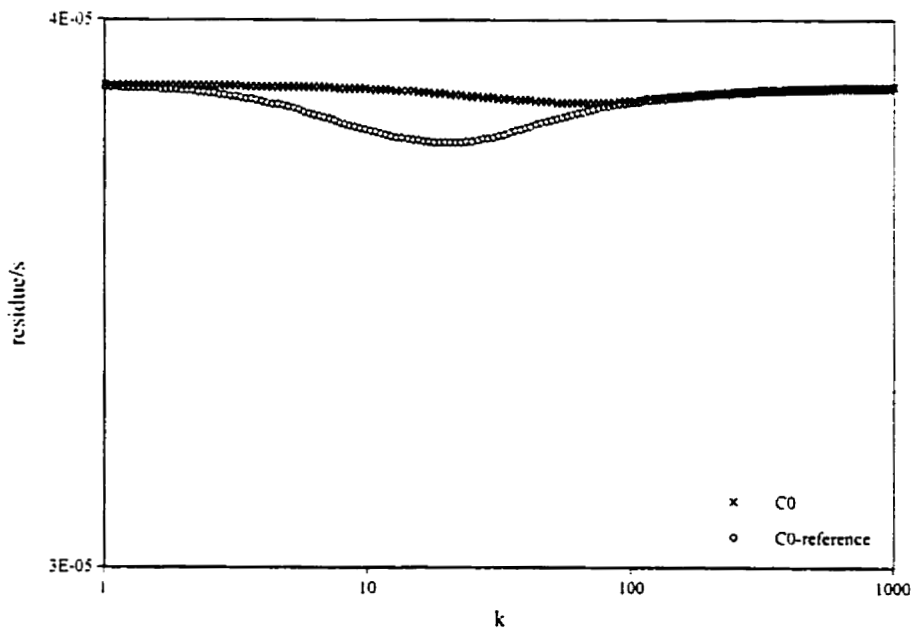


Figure 4.1.15: The vertical displacement excitation strength for a 200 km thick channel (black) and the reference model (grey)

4.2: The Model of an Elastic Lithosphere Overlying a Halfspace

This section will give the analytical solution for a model of a lithosphere over a fluid and discuss the relaxation diagrams and excitation strength diagrams for the model of a lithosphere over a viscoelastic halfspace. For this section the term lithosphere model refers to the model of an elastic lithosphere overlying a viscoelastic halfspace. There have been numerous papers written concerning multi-layered models and the results of this thesis will be compared with some of these.

4.2a: Analytical Solution for the Model of a Lithosphere Overlying a Fluid Halfspace

The model of an elastic lithosphere overlying a fluid halfspace, shown in Figure 4.2.1, is a fairly simple model and the analytical solution in the (k,s) domain was obtained using the symbolic manipulation program, Mathview. The derivation of this solution can be found in Appendix F.

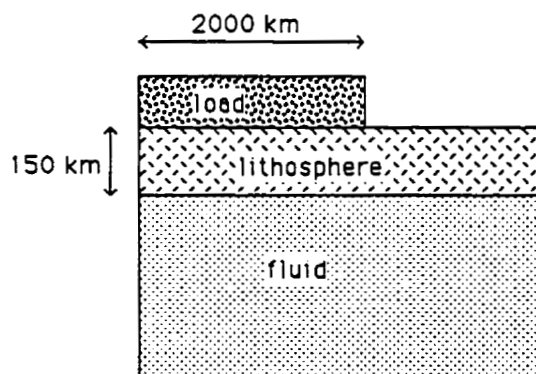


Figure 4.2.1: A reference model for a lithosphere overlying a fluid

The analytical solution is derived in a manner similar to that of the channel model except in this case the conditions at the lower boundary are that the shear stress is zero and the vertical normal stress is equal to the buoyancy, $-\rho g W$ where ρ is the density of the halfspace. The density of the halfspace is used rather than the density difference because the elastic boundary condition, not the fluid one, is being applied. When the boundary conditions for the lithosphere overlying a fluid are applied to the solution of the differential equations the analytical solution is found to be

$$U(k, \mu) = -\frac{4\sigma Hk(\delta\rho g - 2\mu Hk^2)}{-8\mu k(\rho + \delta\rho)gA + 16\mu^2 H^2 k^4 + (4\mu^2 k^2 + \rho\delta\rho g^2)B} \quad (4.2.1)$$

$$W(k, \mu) = -\frac{\sigma(2\mu kA + \delta\rho gB)}{-8\mu k(\rho + \delta\rho)gA + 16\mu^2 H^2 k^4 + (4\mu^2 k^2 + \rho\delta\rho g^2)B} \quad (4.2.2)$$

where $A = \cosh Hk \sinh Hk + Hk$,

$$B = 1 - \cosh^2 Hk.$$

and H is the thickness of the lithosphere.

Note that all of the above material parameters apply to the properties within the lithosphere and that $\delta\rho$ represents the density difference between the fluid halfspace and the lithosphere if one exists. Since the lithosphere is elastic, the shear modulus in the above equations is independent of s .

The above analytical result is compared with the numerical Matlab output. The comparison between these two methods for both the vertical and horizontal

displacements can be found in Figures 4.2.2 and 4.2.3. The values used as the material parameters for these figures are given in Table 4. The two different methods give results which agree very well. Note how both the horizontal and vertical displacements tend to zero for large k values which means that the small wavelength response is damped by the lithosphere. Also note that the vertical displacement reaches a constant value for small k whereas the horizontal displacement tends to negative infinity. This demonstrates the singular nature of the horizontal displacement as k goes to zero. Note that in these cases the thickness of the lithosphere is 100 km and that there is a density contrast between the halfspace and the lithosphere.

Table 4: The Material Properties of the Model of a Lithosphere Over a Fluid

	<u>halfspace, below 100 km</u>	<u>lithosphere, above 100 km</u>
density	$\rho = 5511 \text{ kg m}^{-3}$	$\rho = 4314 \text{ kg m}^{-3}$
gravitational acceleration	$g = 9.7109 \text{ m s}^{-2}$	$g = 9.7109 \text{ m s}^{-2}$
viscosity	$\nu = 0$	$\nu \rightarrow \infty$
shear modulus	$\mu = 0$	$\mu = 3.15 \times 10^{10} \text{ N m}^{-2}$
radius of load		$R = 2 \times 10^6 \text{ m}$
load		$\sigma = 1 \times 10^7 \text{ Pa}$

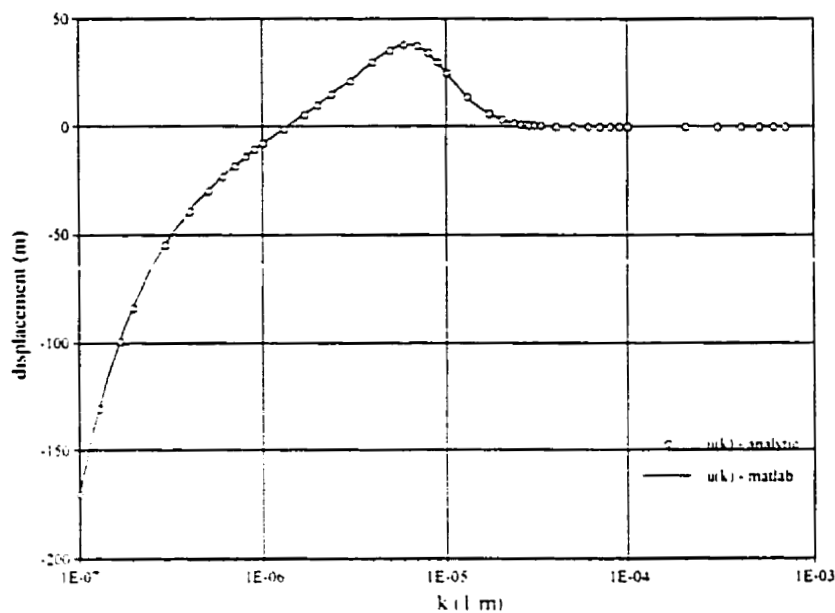


Figure 4.2.2: A comparison between the analytical and numerical solutions for the horizontal displacement in the k domain of the model of a lithosphere overlying a fluid

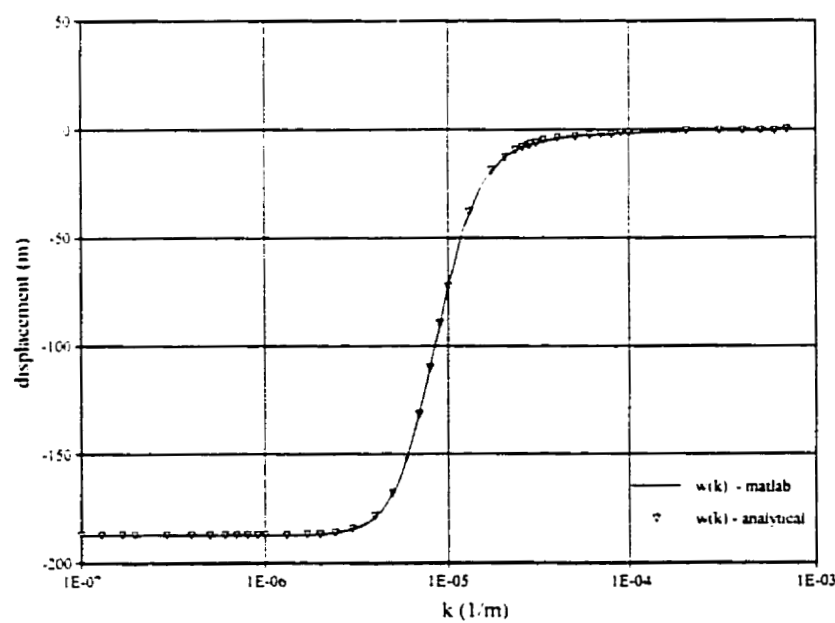


Figure 4.2.3: A comparison between the analytical and numerical solutions for the vertical displacement in the k domain of the model of a lithosphere overlying a fluid

4.2b: Relaxation and Excitation Strength Diagrams for the Model of a Lithosphere Overlying a Viscoelastic Halfspace

Since the previous model includes an elastic layer over a fluid halfspace there is no viscous relaxation, only an initial elastic response. Note that there is no s dependence in equations (4.2.1) and (4.2.2). In order to study the viscous relaxation of a model with an elastic lithosphere the model of an elastic lithosphere over a viscoelastic halfspace was studied. This is the model referred to as the lithosphere model and it is shown in Figure 4.2.4. The properties of the halfspace and lithosphere are given in Table 5.

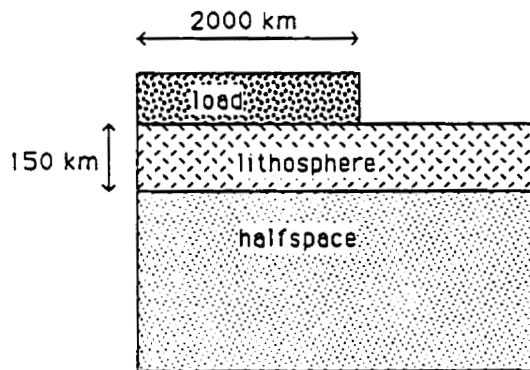


Figure 4.2.4: The lithosphere model

Table 5: The Material Properties of the Lithosphere Model

	<u>halfspace, below 150 km</u>	<u>lithosphere, above 150 km</u>
density	$\rho = 5517 \text{ kg m}^{-3}$	$\rho = 5517 \text{ kg m}^{-3}$
gravitational acceleration	$g = 7.365 \text{ m s}^{-2}$	$g = 7.365 \text{ m s}^{-2}$
viscosity	$\nu = 1 \times 10^{21} \text{ Pa s}$	$\nu \rightarrow \infty$
shear modulus	$\mu = 1.452 \times 10^{11} \text{ N m}^{-2}$	$\mu = 1.452 \times 10^{11} \text{ N m}^{-2}$
radius of load		$R = 2 \times 10^6 \text{ m}$
load		$\sigma = 1 \times 10^7 \text{ Pa}$

No effects other than the presence of the lithosphere are desired so the model has a constant density and shear modulus. The solutions for this model are obtained by applying the lower boundary condition to the halfspace and then using matrix propagation to arrive at the solution at the surface. All of the following figures were obtained using the Matlab programs.

The relaxation diagram, Figure 4.2.5, for the lithosphere model is quite distinct. There are two modes, a buoyancy mode associated with the halfspace, M0, and a lithospheric mode, L0 (Peltier, 1976). The M0 mode is due to the density contrast at the surface and the L0 mode is due to the contrast in elastic properties of the lithosphere. At large values of k , these modes approach one another and eventually coincide. At this point the numerical methods used to find the zeros can no longer identify either as a true zero and this is why there are no values for $k > 150$. If this relaxation diagram is compared with that of the halfspace model (Figure 3.2.3) then it is noted that for small wavenumbers the M0 mode has similar values however for larger wavenumbers this mode in the lithosphere

model experiences a reduction in relaxation times. Also note that the M0 and L0 modes cross at a wavenumber of $k \sim 7$, which is the thickness of the lithosphere. This is characteristic of models which incorporate an elastic lithosphere. Wu and Ni (1996) had an almost identical form, even though their work was for a spherical earth and the calculations in this thesis are for a flat earth model. Wolf (1989) also analyzed the response of an elastic lithosphere over a halfspace for a flat earth and again the shape of the curve and the values match extremely well.

The excitation strength of the horizontal displacement of the lithosphere model is shown in Figure 4.2.6. There appears to be a singularity where the two modes change sign. The magnitude of the negative excitation strength is larger than the positive. In general the L0 mode approaches zero from the positive vertical axis for large wavenumber and becomes constant for wavenumbers less than one. The M0 mode approaches zero from the positive axis for small wavenumber and approaches zero from the negative axis for large wavenumber. Though the trends of the excitation strength are similar to those shown by Wu and Ni (1996) for the spherical case the results are very different. This might mean that the spherical nature of the earth has a significant effect on the excitation strength of the horizontal displacement.

The excitation strength diagrams for the vertical displacement of the lithosphere model are also quite distinct since the two modes have the same strength at the wavenumber that corresponds to the thickness of the lithosphere. For the excitation strength of the vertical displacement, as shown in Figure 4.2.7, the M0 mode resembles the excitation strength of the vertical displacement as seen in the halfspace model (Figure 3.3.1) except that the excitation strength decreases at high values of k . Figure 4.2.7 is similar to the diagrams given by Wu and Ni (1996) and Wolf (1985). The M0 mode always has the most

strength but at a particular wavenumber, where the modes cross in the relaxation diagram. the two modes meet in the excitation strength diagram and the L0 mode has a strength equal to that of the halfspace mode. Both of the modes tend to zero for larger wavenumbers.

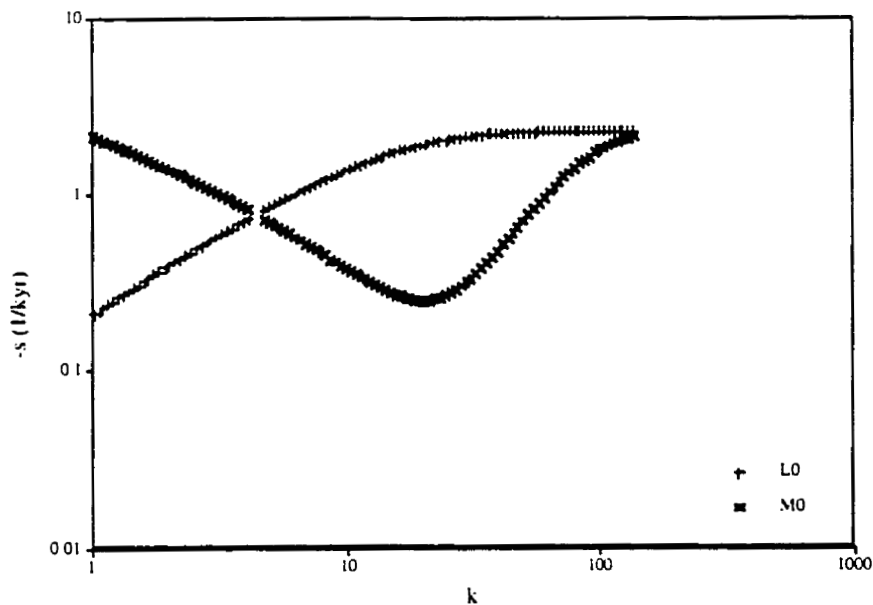


Figure 4.2.5: The relaxation diagram for the model of an elastic lithosphere overlying a viscoelastic halfspace (reference model)

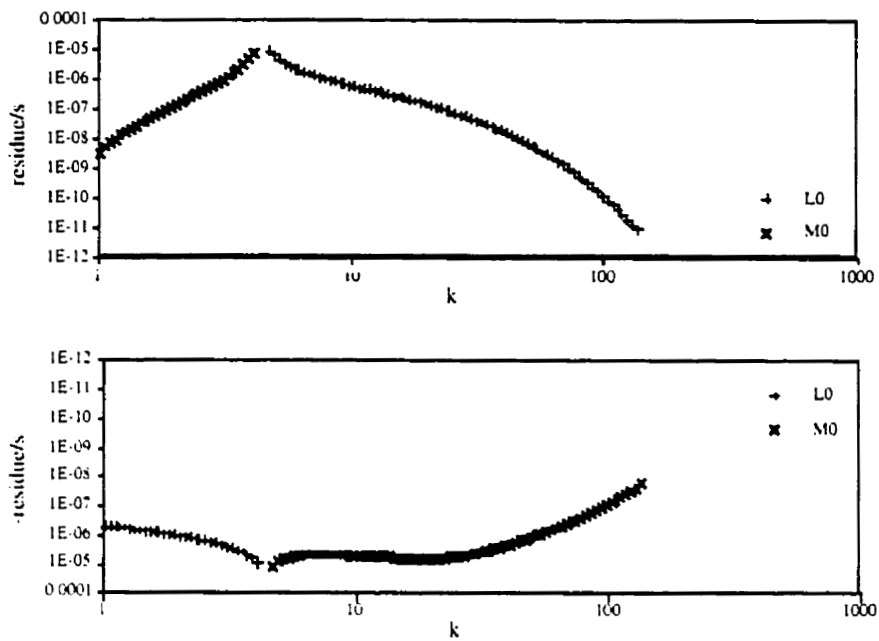


Figure 4.2.6: The horizontal displacement excitation strength for the model of an elastic lithosphere overlying a viscoelastic halfspace (reference model)

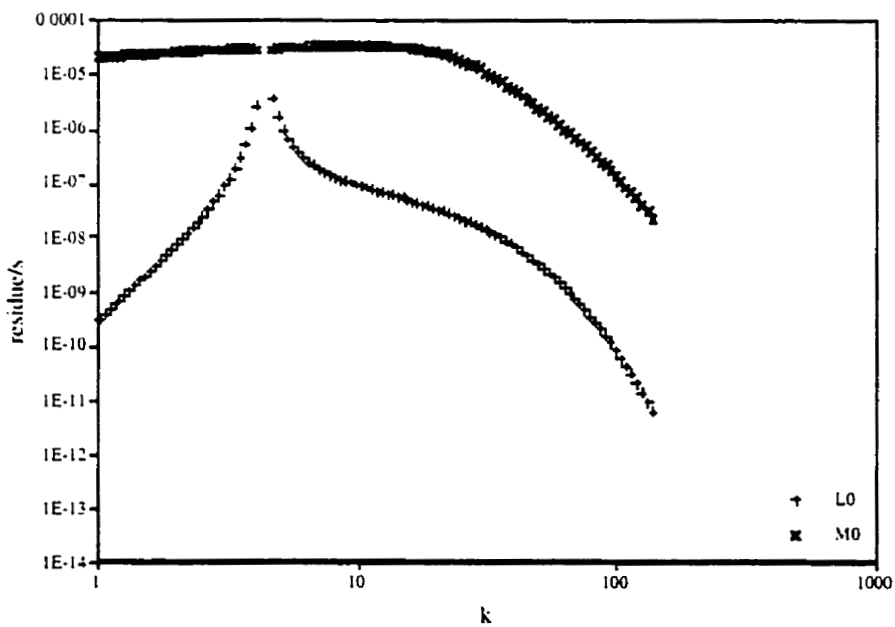


Figure 4.2.7: The vertical displacement excitation strength for the model of an elastic lithosphere overlying a viscoelastic halfspace (reference model)

As with previous models, the material parameters of the lithosphere model are varied so that the effect on the relaxation and excitation strength diagrams can be determined. All of these figures include the results for a specific model and the results for the reference model so that comparisons can be made more easily. Figure 4.2.8 demonstrates the effect of increasing the halfspace viscosity. As previously, the most significant effect is an increase in the relaxation times. A change in the density of the whole earth has little effect on the relaxation times as demonstrated in Figure 4.2.9. The relaxation times increase for small wavenumbers only and the values at large k remain constant. A decrease in the halfspace shear modulus, Figure 4.2.10, results in an increase in the relaxation times similar to the effect of increasing the viscosity, however, the wavenumber at which the two modes cross increases with decreasing shear modulus. A change in the lithospheric thickness also affects predominantly the L0 mode, as shown in Figure 4.2.11. The M0 mode for small wavenumbers remains unchanged as expected since these correspond to the response at depth.

The next set of figures deals with the horizontal displacement excitation strength. The excitation strength of the horizontal displacement decreases for the L0 mode and increases for the M0 mode with increasing halfspace viscosity, as demonstrated in Figure 4.2.12. Changing the density has little effect other than a slight increase in the excitation strengths at large wavenumbers (Figure 4.2.13). The results of a decrease in the halfspace shear modulus is given in Figure 4.2.14 and it is evident that there is a significant shift towards higher wavenumber. Also note the additional sign change in the M0 mode at low wavenumbers. Figure 4.2.15 shows how the curves are shifted towards higher wavenumbers as the thickness of the lithosphere decreases. This is similar to the change seen with a decrease in the halfspace shear modulus.

The final set of figures to be discussed in this section includes the excitation strength diagrams for the vertical displacement of the lithosphere model. The results are similar to those of the horizontal displacement. Figure 4.2.16 shows that a change in halfspace viscosity has little effect on the excitation strength of the M0 mode and slightly decreases the excitation of the L0 mode at small k , but increases it at large k . A decrease in the density, as shown in Figure 4.2.17, increases the excitation strength of the M0 mode towards large wavenumbers. This results in increased strength at larger wavenumbers. A decrease in the shear modulus (Figure 4.2.18) shifts the excitation strengths of both modes. Figure 4.2.19 shows that an increase in the thickness of the lithosphere shifts the curves towards larger wavenumbers similar to the effect seen with a increase in shear modulus.

Unlike the halfspace and channel models a change in viscosity affects not only the relaxation times, but also the horizontal and vertical displacement excitation strengths. A change in density has a small impact on the diagrams while a change in the shear modulus shifts the curves in all of the diagrams. A change in the thickness also shifts the curves in all three diagrams. For the lithosphere models, the material parameters which have the greatest impact on the relaxation times and excitation strengths are the thickness of the lithosphere and the shear modulus of the halfspace.

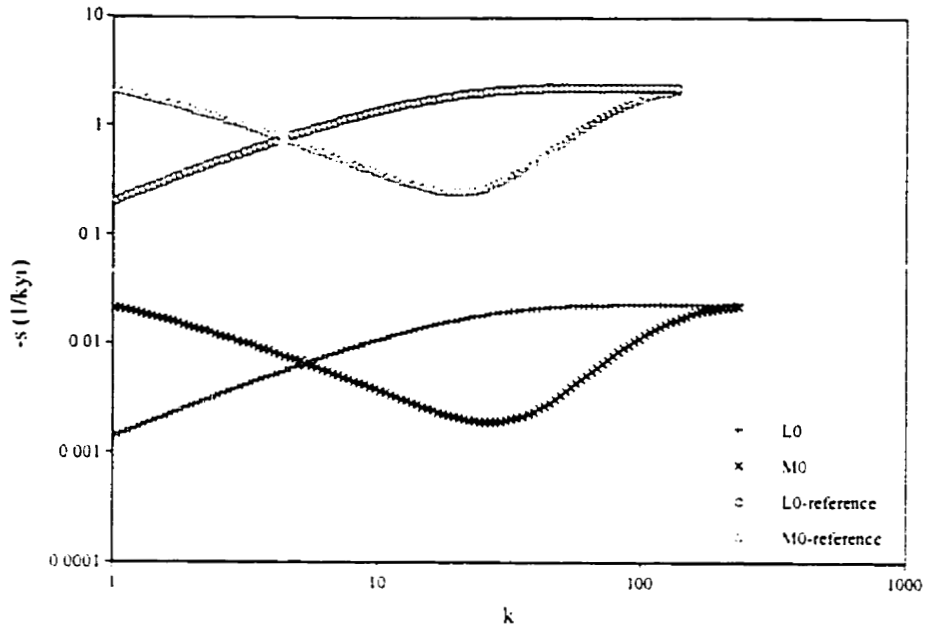


Figure 4.2.8: The relaxation diagram for the lithosphere model with a halfspace viscosity of 1×10^{23} Pa s and the reference model

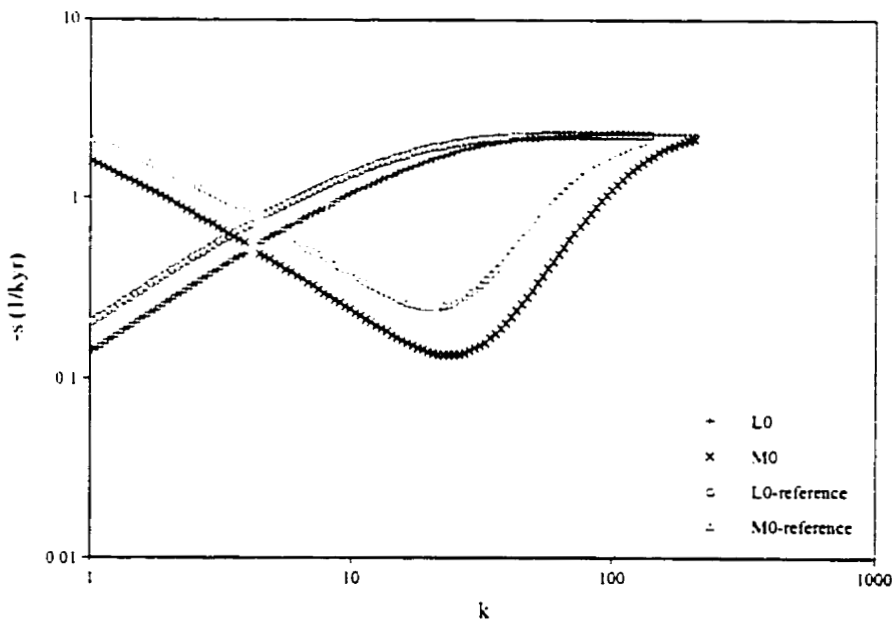


Figure 4.2.9: The relaxation diagram for a lithosphere model with a model density of 3380 kg m^{-3} and the reference model

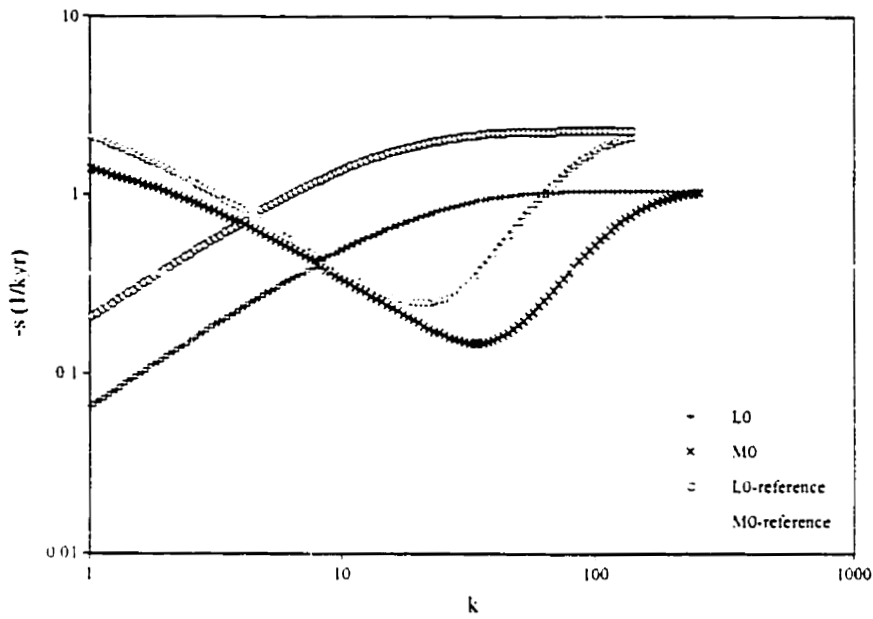


Figure 4.2.10: The relaxation diagram for a lithosphere model with a halfspace shear modulus of $0.67 \times 10^{11} \text{ N m}^{-2}$ and the reference model

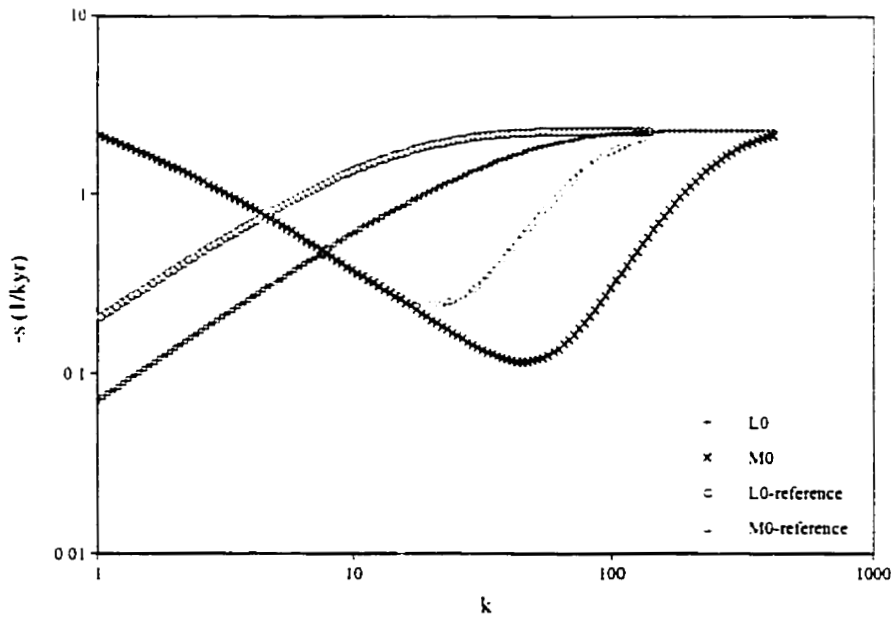


Figure 4.2.11: The relaxation diagram for a lithosphere model with a 50 km thick lithosphere and the reference model

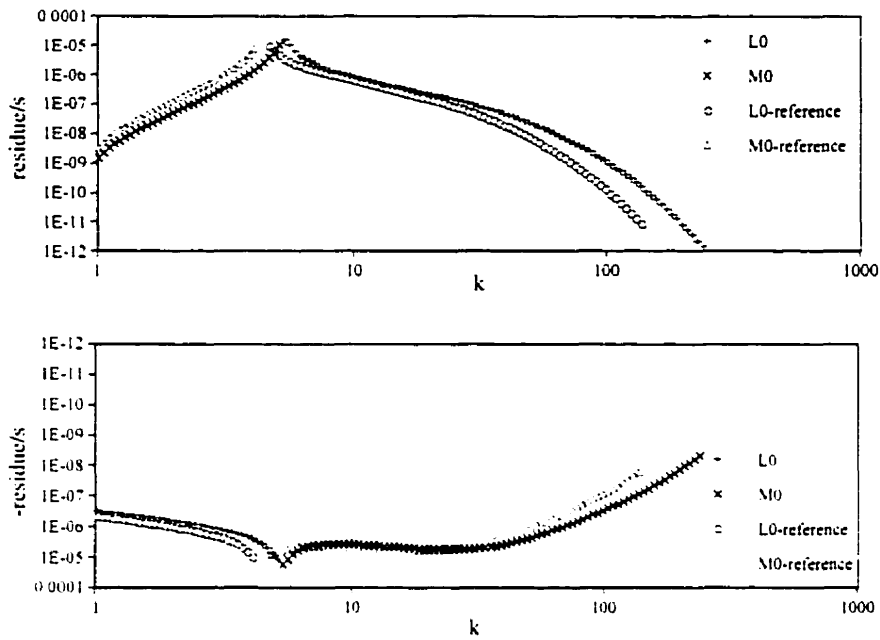


Figure 4.2.12: The horizontal displacement excitation strength for a lithosphere model with a halfspace viscosity of 1×10^{23} Pa s and the reference model

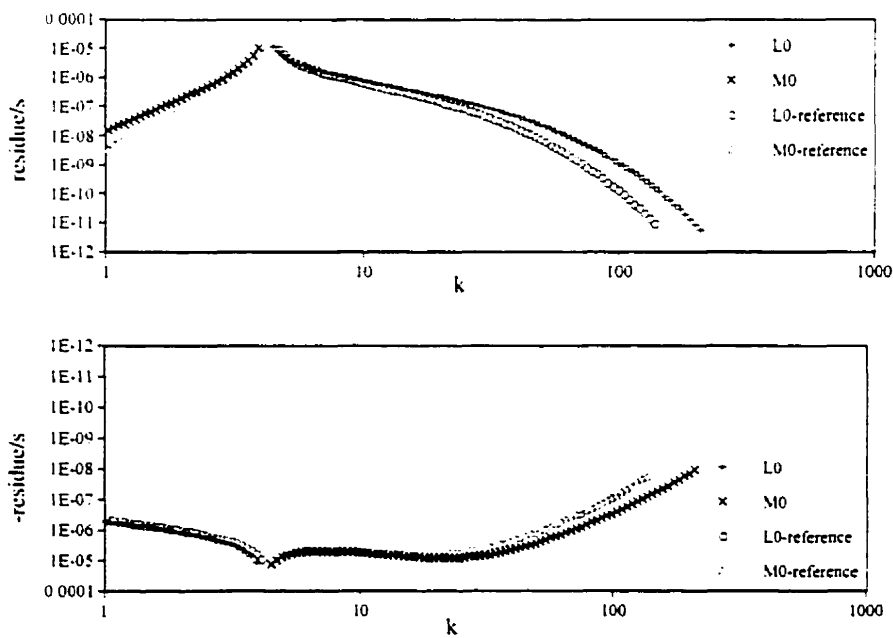


Figure 4.2.13: The horizontal displacement excitation strength for a lithosphere model with a model density of 3380 kg m^{-3} and the reference model

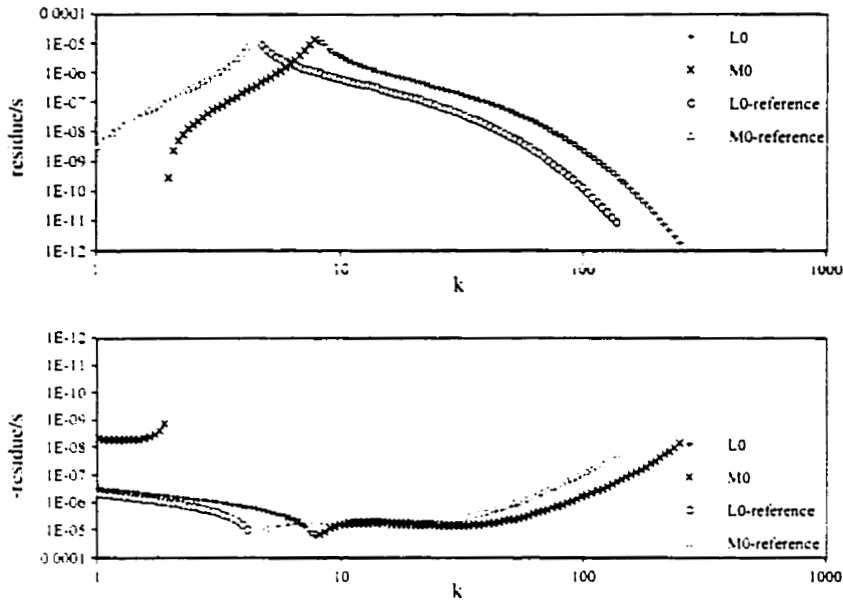


Figure 4.2.14: The horizontal displacement excitation strength for a lithosphere model with a halfspace shear modulus of $0.67 \times 10^{11} \text{ N m}^{-2}$ and the reference model

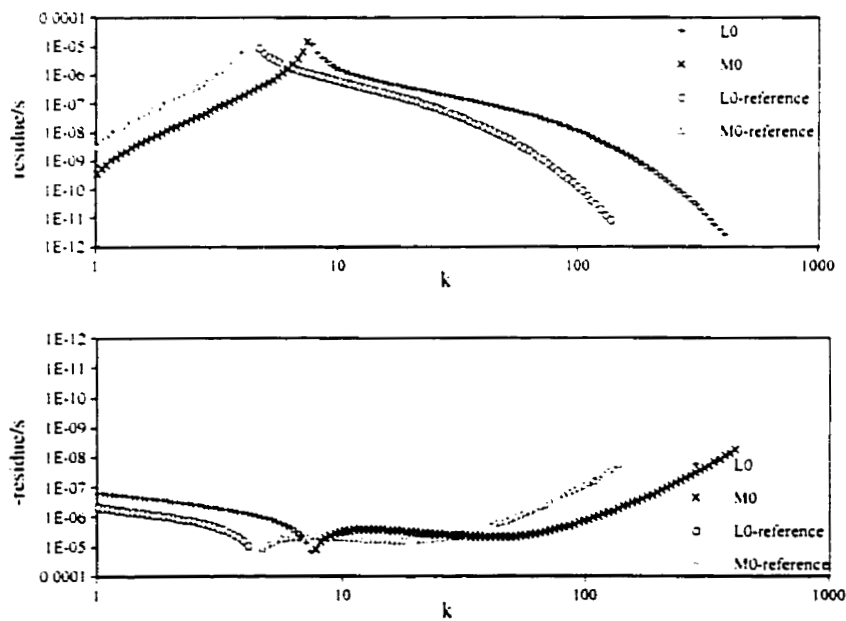


Figure 4.2.15: The horizontal displacement excitation strength for a lithosphere model with a 50 km thick lithosphere and the reference model

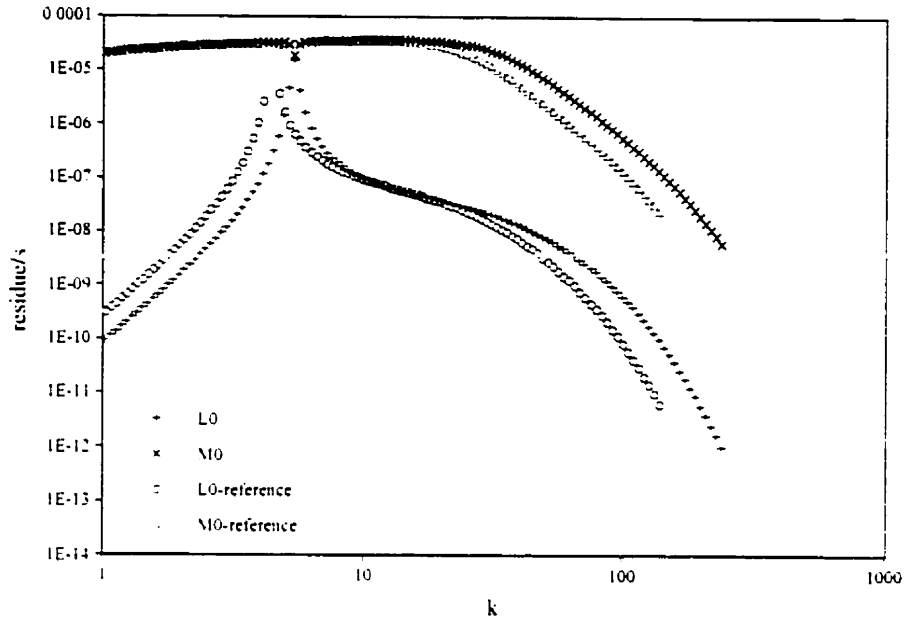


Figure 4.2.16: The vertical displacement excitation strength for a lithosphere model with a halfspace viscosity of 1×10^{23} Pa s and the reference model

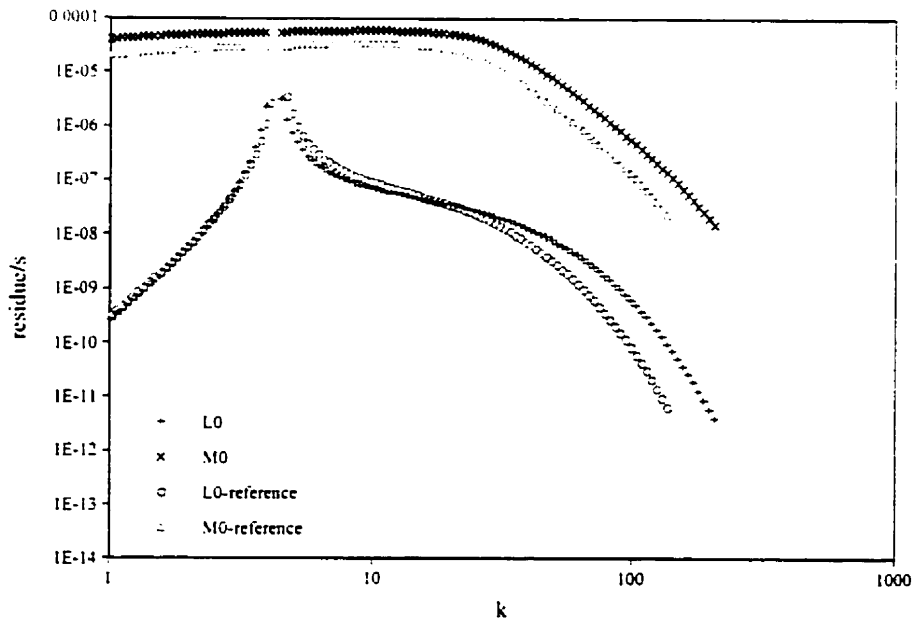


Figure 4.2.17: The vertical displacement excitation strength for a lithosphere model with a model density of 3380 kg m^{-3} and the reference model

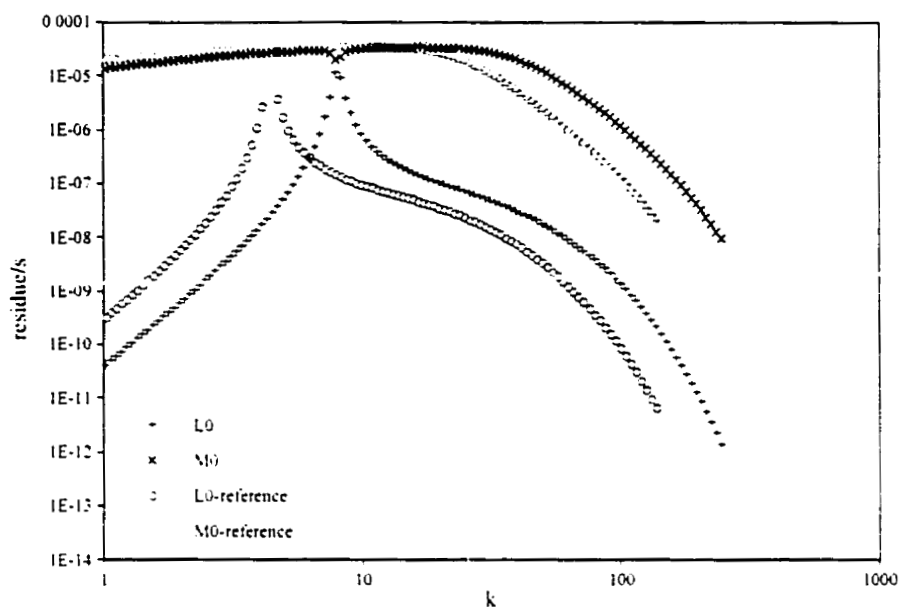


Figure 4.2.18: The vertical displacement excitation strength for a lithosphere model with a halfspace shear modulus of $0.67 \times 10^{11} \text{ N m}^{-2}$ and the reference model

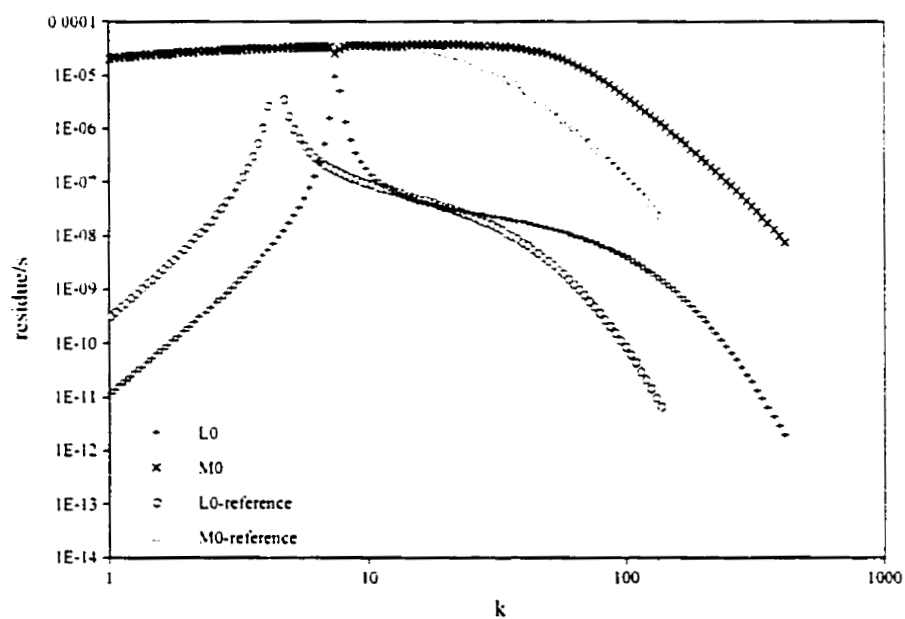


Figure 4.2.19: The vertical displacement excitation strength for a lithosphere model with a 50 km thick lithosphere and the reference model

4.3: Relaxation Diagrams and Excitation Strength Diagrams for More Complicated Earth Models

This section will discuss more two and three layer models. The first model to be considered is a two layer model defined by a single density variation, the second model is a two layer model defined by a change in the elastic properties, and the final one will be a three layer model with a low viscosity channel below an elastic lithosphere and over a viscoelastic halfspace. The primary motivation in analyzing these more complex models is to determine the various modes that arise in the relaxation and excitation strength diagrams and how they are affected by variations in the material parameters. These models are similar to ones studied by Wu and Ni (1996). In general the relaxation diagrams and excitation strengths of the vertical displacement agree with the ones studied by Wu and Ni (1996) and the excitation strengths of the horizontal displacements tend not to agree as well.

4.3a Models with a Single Density Discontinuity

The models that will be discussed in this section involve a single radial density discontinuity, as shown in Figure 4.3.1. The reference values for the material properties are given in Table 6. These values are based on those used in the paper by Wu and Ni (1996) so that comparisons between studies could be made. First the relaxation diagrams will be discussed, including how the relaxation times are affected by the density contrast and the depth of contrast, then the excitation strength diagrams will be discussed.

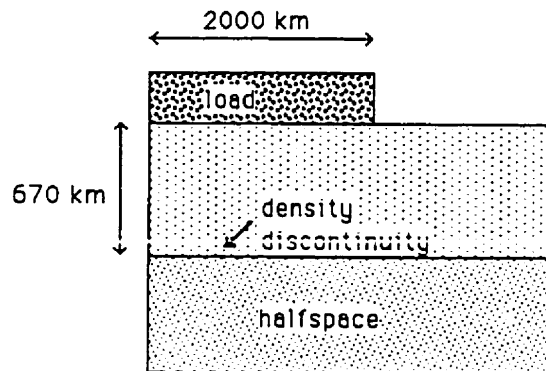


Figure 4.3.1: The reference model with a single density discontinuity

Table 6: The Material Properties of the Model with a Single Density Discontinuity

	<u>halfspace, below 670 km</u>	<u>upper layer, above 670 km</u>
density	$\rho = 6288 \text{ kg m}^{-3}$	$\rho = 3572 \text{ kg m}^{-3}$
gravitational acceleration	$g = 7.365 \text{ m s}^{-2}$	$g = 7.365 \text{ m s}^{-2}$
viscosity	$\nu = 1 \times 10^{21} \text{ Pa s}$	$\nu = 1 \times 10^{21} \text{ Pa s}$
shear modulus	$\mu = 1.452 \times 10^{11} \text{ N m}^{-2}$	$\mu = 1.452 \times 10^{11} \text{ N m}^{-2}$
radius of the load		$R = 2 \times 10^6 \text{ m}$
load		$\sigma = 1 \times 10^7 \text{ Pa}$

The relaxation diagram for a two layer model defined by a single density discontinuity is given in Figure 4.3.2. It is very similar to that of the halfspace model, except that there is an additional buoyancy mode due to the additional density contrast referred to as M1 (Peltier, 1976; Wu and Ni, 1996). This mode has a longer relaxation time as compared to the M0 mode since the density contrast is smaller than the one at the surface and it occurs

at depth (Wu and Ni, 1996, equation 22). The M0 mode is identical to the one of the halfspace model and the M1 mode resembles the relaxation curve obtained for the channel model. The shortest relaxation time occurs at a wavenumber which corresponds to the depth of the contrast, in this case $k \sim 20$. This figure matches well with the one given by Wu and Ni (1996, Figure 5a) for a similar model using a spherical earth. As the depth at which the density contrast occurs decreases, i.e. as it moves closer to the surface, the M1 mode is shifted towards longer relaxation times while the M0 mode remains relatively consistent, as shown in Figure 4.3.3. A decrease in the density value in the upper layer results in an increase in the density contrast between the two layers. This results in a very slight increase in the relaxation times for both the M0 and M1 modes (Figure 4.3.4).

The excitation strength of the horizontal displacement shows that the M0 mode has a negative excitation strength while the M1 mode has a positive excitation strength, as demonstrated by Figure 4.3.5. For small wavenumbers the M1 mode is stronger and at larger wavenumbers both modes tend towards zero. This figure is quite different from Figure 5c presented by Wu and Ni (1996). This could be due to the spherical nature of the model that they used. As the level of the discontinuity moves closer to the surface (Figure 4.3.6) the excitation strengths of both modes persist to larger wavenumbers before decaying rapidly to zero, as expected since the model can be sampled at a shorter wavelength (larger wavenumber) to distinguish the two independent layers. The strength of the M1 mode increases while the M0 mode decreases. The excitation strength of the M1 mode increases while that of the M0 mode decreases. Increasing the density contrast slightly decreases the excitation strength of both modes for larger wavenumbers only, as shown in Figure 4.3.7.

In Figures 4.3.8 to 4.3.10, the effect of this density discontinuity on the excitation strength of the vertical displacement can be seen. Figure 4.3.8 agrees well with a similar figure given in the paper by Wu and Ni (1996). For very small wavenumbers the M1 mode dominates, but for most of the relevant wavenumbers the M0 mode dominates, in fact the M1 mode quickly decays to zero for large wavenumbers. As the thickness of the upper layer decreases (Figure 4.3.9) the M1 mode extends to larger wavenumbers before decaying. This is also similar to the effect noted by Wu and Ni (1996). Figure 4.3.10 shows that for an increase in the density contrast at the discontinuity the excitation strength of the M1 mode increases slightly for all wavenumbers.

Since M0 is due to a density contrast at the surface and the M1 mode is due to a density contrast at depth, the M0 mode dominates the short wavelength (large k) and the M1 mode dominates at greater depth (small k). The location of the shortest relaxation time in the M1 mode corresponds to the depth of the density discontinuity. The depth of the contrast is more important than the magnitude of the contrast in terms of the effect on the relaxation times and the excitation strengths.

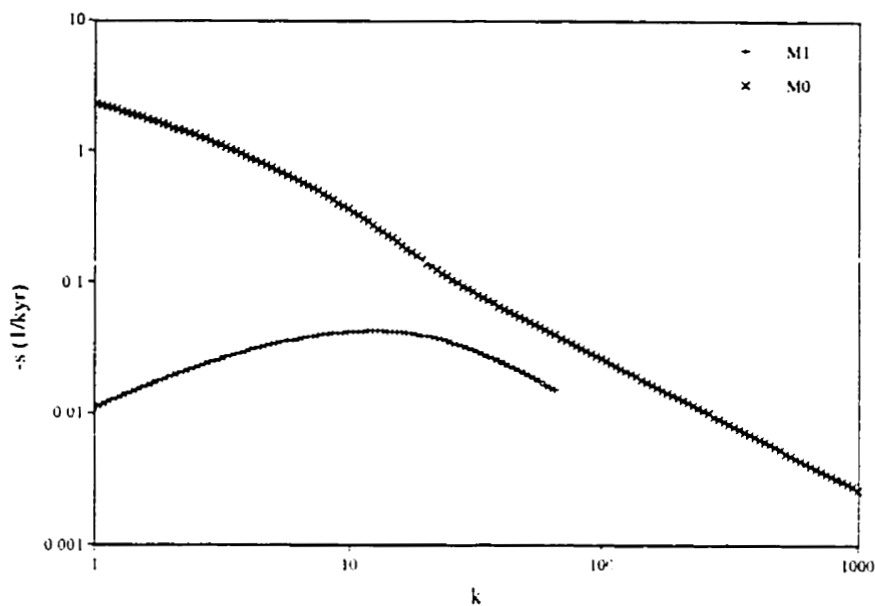


Figure 4.3.2: The relaxation diagram for a model with a single density discontinuity (reference model)

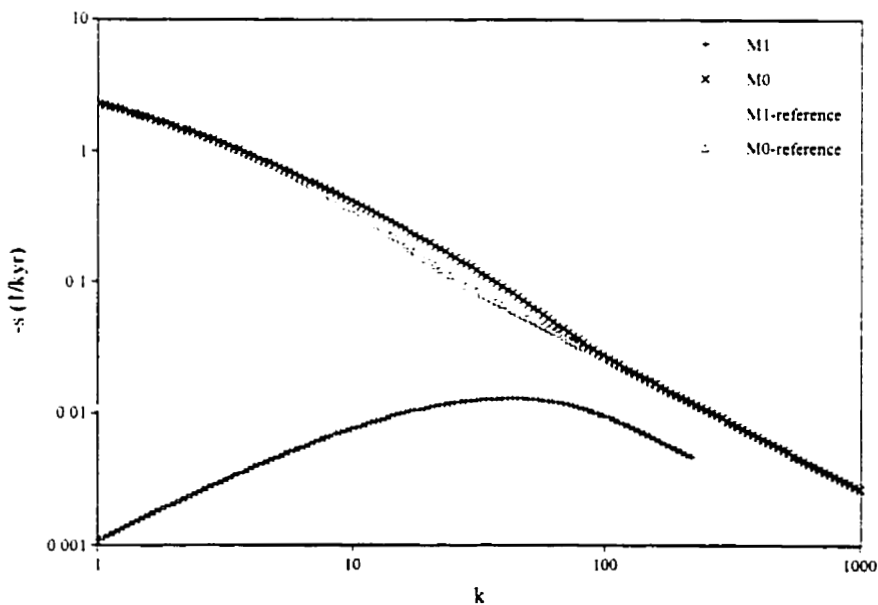


Figure 4.3.3: The relaxation diagram for a model with a single density discontinuity at a depth of 200 km and the reference model

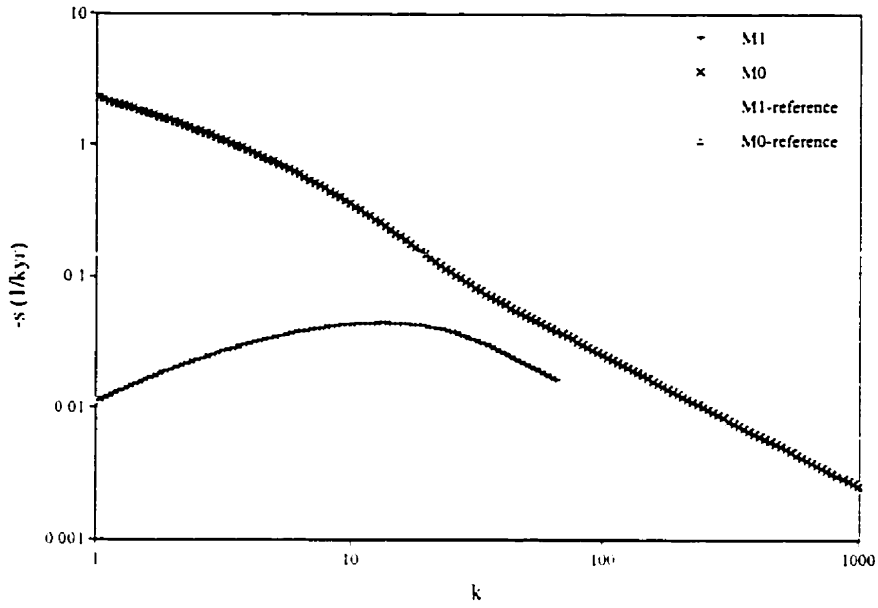


Figure 4.3.4: The relaxation diagram for a model with a single density discontinuity and an upper layer density of 3380 kg m^{-3} and the reference model

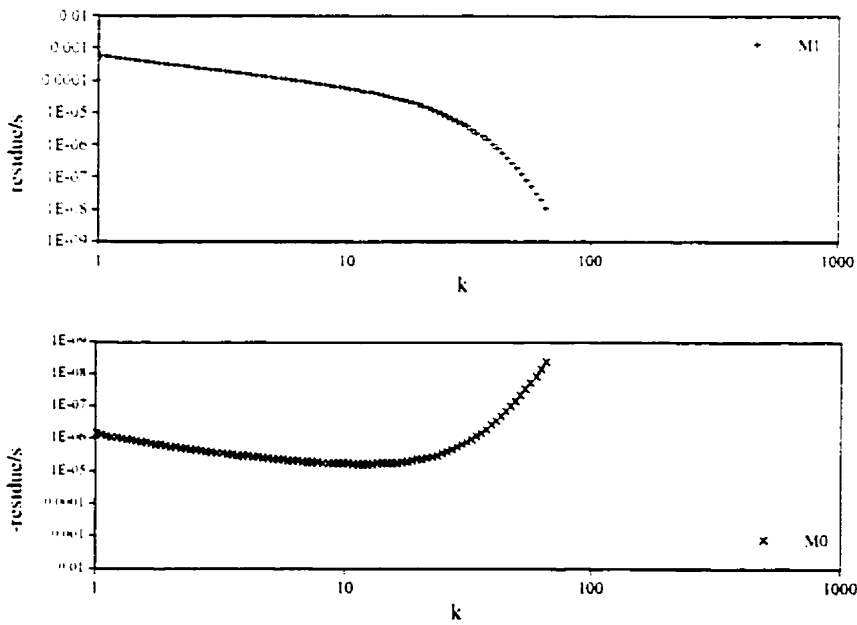


Figure 4.3.5: The horizontal displacement excitation strength for a model with a single density discontinuity (reference model)

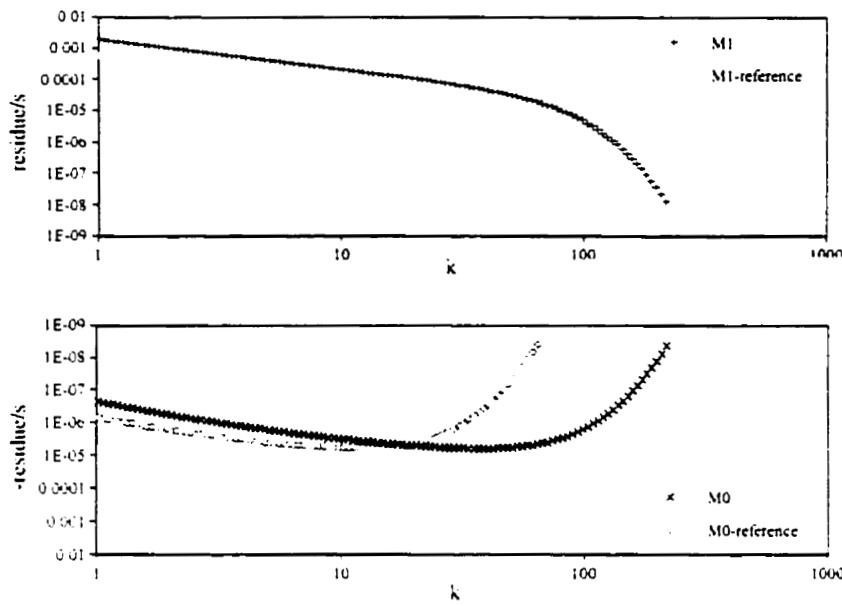


Figure 4.3.6: The horizontal displacement excitation strength for a model with a single density discontinuity at a depth of 200 km and the reference model

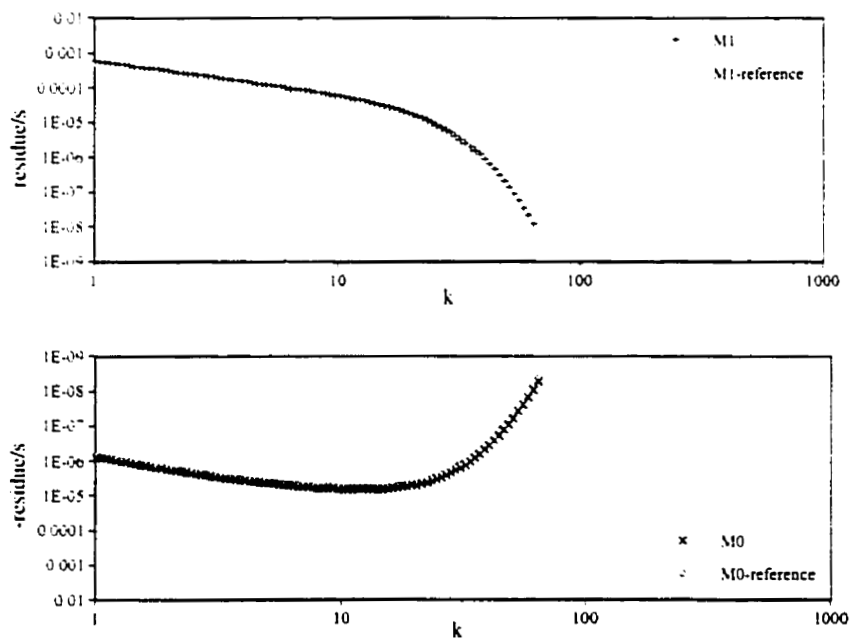


Figure 4.3.7: The horizontal displacement excitation strength for a model with a single density discontinuity and an upper layer density of 3380 kg m^{-3} and the reference model

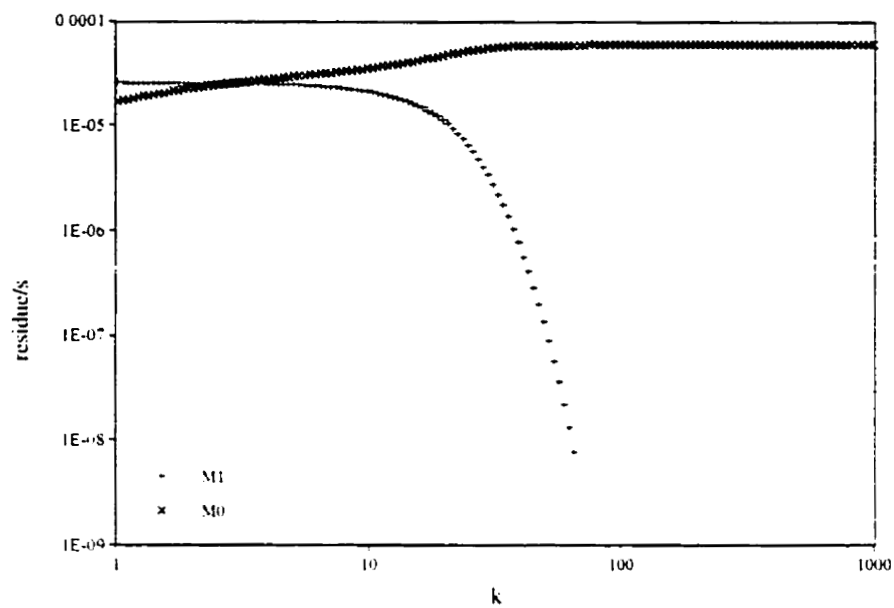


Figure 4.3.8: The vertical displacement excitation strength for a model with a single density discontinuity (reference model)

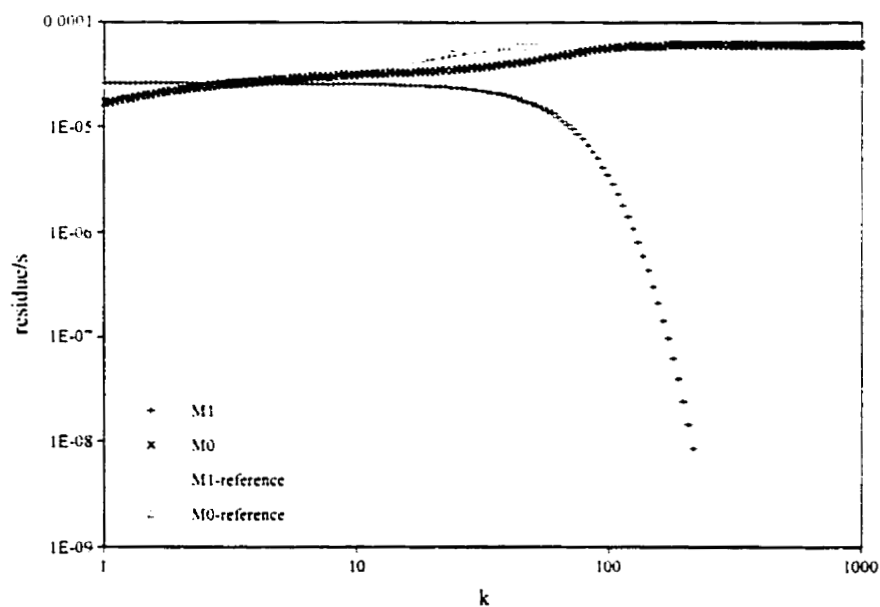


Figure 4.3.9: The vertical displacement excitation strength for a model with a single density discontinuity at a depth of 200 km and the reference model

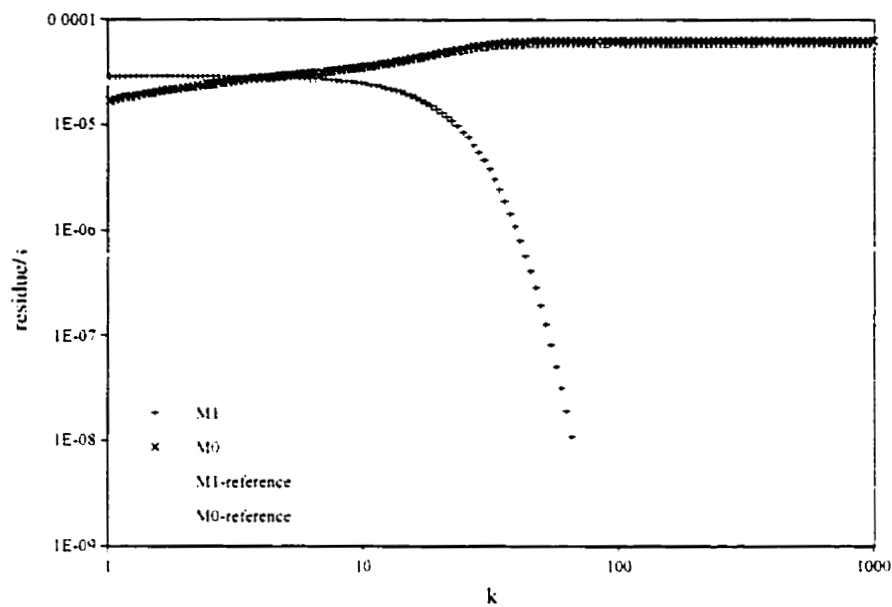


Figure 4.3.10: The vertical displacement excitation strength for a model with a single density discontinuity and an upper layer density of 3380 kg m^{-3} and the reference model

4.3b: Models with a Single Shear Modulus Discontinuity

The section will discuss the relaxation and the excitation strength diagrams for a model where there is a single radial discontinuity in the shear modulus. The reference model is shown in Figure 4.3.11. The default values for the material parameters are given in the Table 7 and they are based on the values used by Wu and Ni (1996).

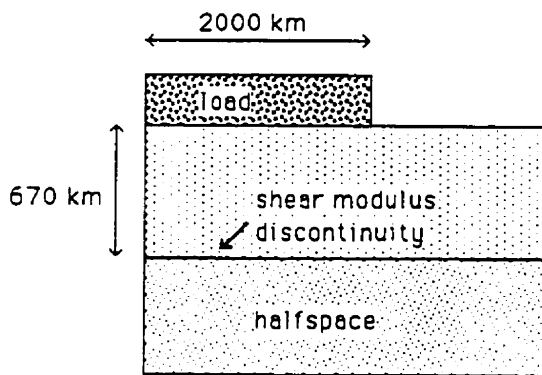


Figure 4.3.11: The reference model with a single shear modulus discontinuity

Table 7: The Material Properties of the Model with a Single Shear Modulus Discontinuity

	<u>halfspace, below 670 km</u>	<u>upper layer, above 670 km</u>
density	$\rho = 5517 \text{ kg m}^{-3}$	$\rho = 5517 \text{ kg m}^{-3}$
gravitational acceleration	$g = 7.365 \text{ m s}^{-2}$	$g = 7.365 \text{ m s}^{-2}$
viscosity	$\nu = 1 \times 10^{21} \text{ Pa s}$	$\nu = 1 \times 10^{21} \text{ Pa s}$
shear modulus	$\mu = 1.7147 \times 10^{11} \text{ N m}^{-2}$	$\mu = 0.8281 \times 10^{11} \text{ N m}^{-2}$
radius of load		$R = 2 \times 10^6 \text{ m}$
load		$\sigma = 1 \times 10^7 \text{ Pa}$

The relaxation diagram has three modes of relaxation. The M0 mode is due to the density contrast at the surface and the other two are due to the single discontinuity of the Maxwell time, μ/η , labeled the T1 and T2 modes (Peltier, 1976; Wu and Peltier, 1982; Wu and Ni, 1996), see Figure 4.3.12. The T modes are the viscoelastic or transition modes and they arise from contrasts in the elastic properties (Peltier, 1976). The relaxation times of these transition modes are found to coalesce for large and small wavenumbers such that they are indistinguishable. Again this agrees very well with Figure 8a given by Wu and Ni (1996). The result of a decrease in the shear modulus of the upper layer, as shown in Figure 4.3.13, is to increase the relaxation times of the transition modes, T1 and T2. As the depth of the discontinuity moves closer to the surface, as in Figure 4.3.14, and the transition modes are shifted towards larger wavenumbers.

The excitation strength of the horizontal displacement of the model with a discontinuity in the shear modulus is similar to that of the model with a single density discontinuity, which can be seen in a comparison of Figures 4.3.5 and 4.3.15. The M0 mode is always negative as is the T1 mode and the T2 mode is always positive. All of these modes have excitation strengths which tend towards zero for large wavenumbers. For all wavenumbers the M0 mode dominates. A decrease in the shear modulus of the upper layer increases the excitation strength of all of the modes, as shown in Figure 4.3.16, since the contrast in μ is increased. Figure 4.3.17 shows that as the level of the discontinuity moves closer to the surface the excitation strengths decrease and extend to larger wavenumbers before decaying to zero.

Figures 4.3.18, 4.3.19, and 4.3.20 show the excitation strength of the vertical displacement for the model with a single discontinuity in the shear modulus. The M0

mode is relatively independent of the wavenumber and the transition modes decay rapidly to zero for large wavenumbers. A decrease in the shear modulus of the upper layer increases the excitation strength of the transition modes (Figure 4.3.19) whereas a decrease in the depth of the discontinuity shifts the transition modes to larger wavenumbers, as shown in Figure 4.3.20. These results are similar to the effects noted for the excitation strength of the horizontal displacement. These figures agree very well with the results of the Wu and Ni (1996).

Therefore a discontinuity caused by a change in the shear modulus adds two additional modes of relaxation. The relaxation times of these modes are dependent not only on the magnitude of the contrast between the shear moduli of the two layers, but also on the depth at which this discontinuity occurs. As the contrast increases, the relaxation times decrease and as the depth of the discontinuity approaches the surface, the relaxation times are shifted towards shorter wavelengths (larger k). The excitation strengths are more sensitive to the depth of the discontinuity.

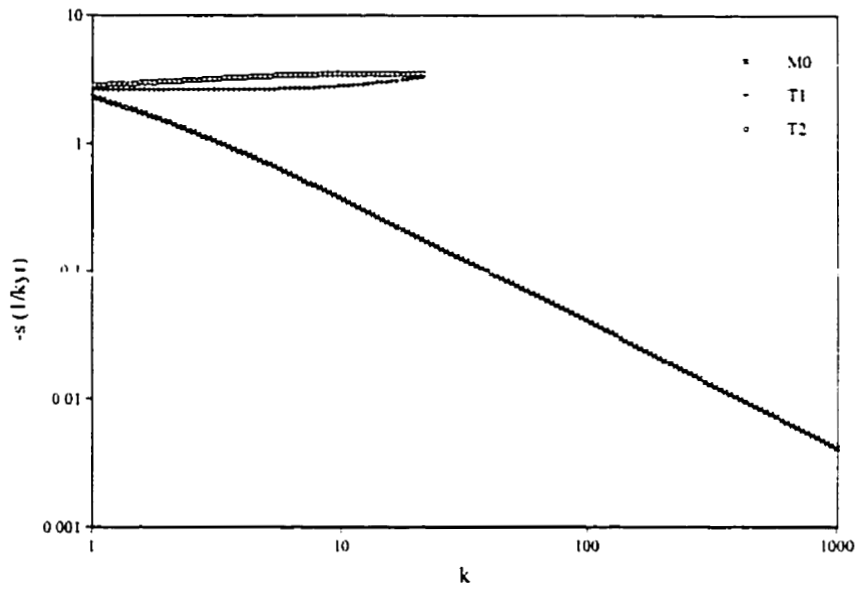


Figure 4.3.12: The relaxation diagram for a model with a single shear modulus discontinuity (reference model)

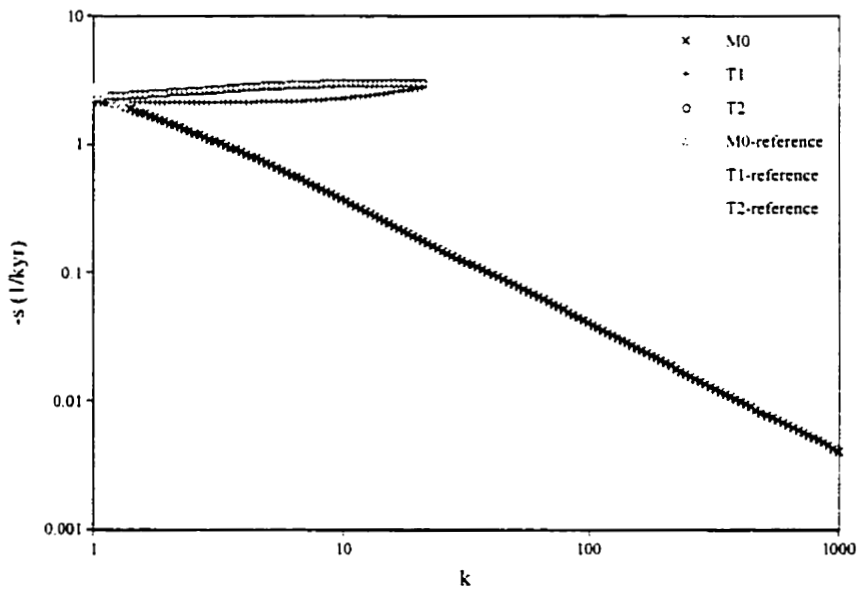


Figure 4.3.13: The relaxation diagram for a model with a single shear modulus discontinuity with an upper layer shear modulus of $0.67 \times 10^{11} \text{ N m}^{-2}$ and the reference model

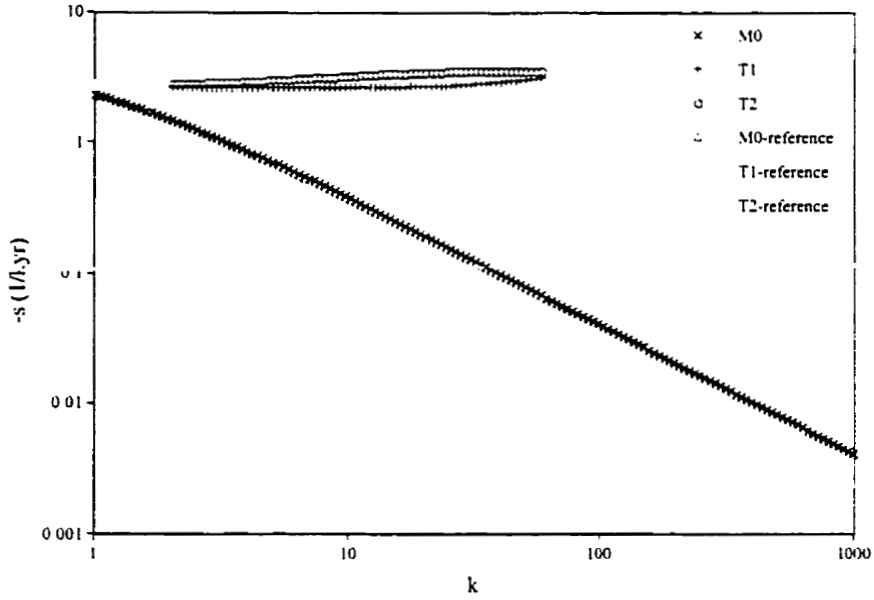


Figure 4.3.14: The relaxation diagram for a model with a single shear modulus discontinuity at a depth of 200 km and the reference model

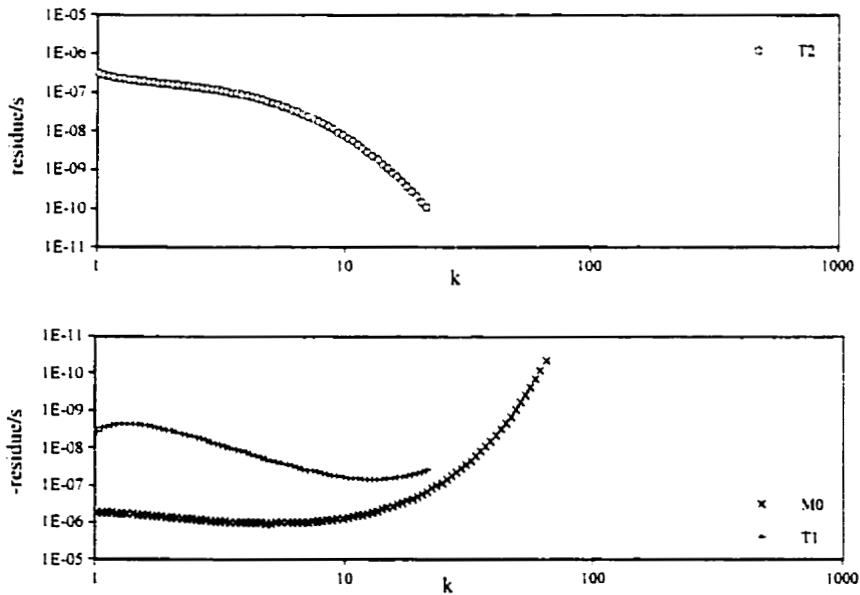


Figure 4.3.15: The horizontal displacement excitation strength for a model with a single shear modulus discontinuity (reference model)

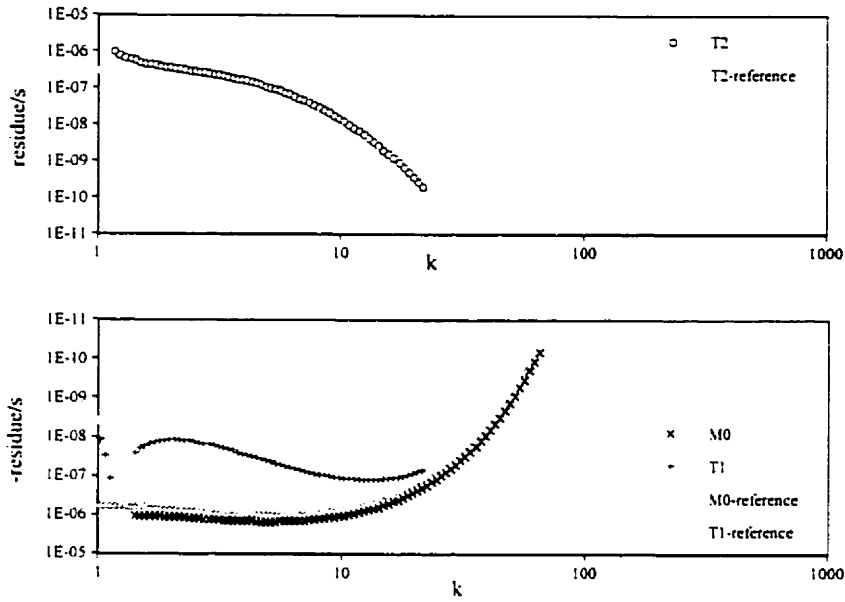


Figure 4.3.16: The horizontal displacement excitation strength for a model with a single shear modulus discontinuity with an upper layer shear modulus of $0.67 \times 10^{11} \text{ N m}^{-2}$ and the reference model

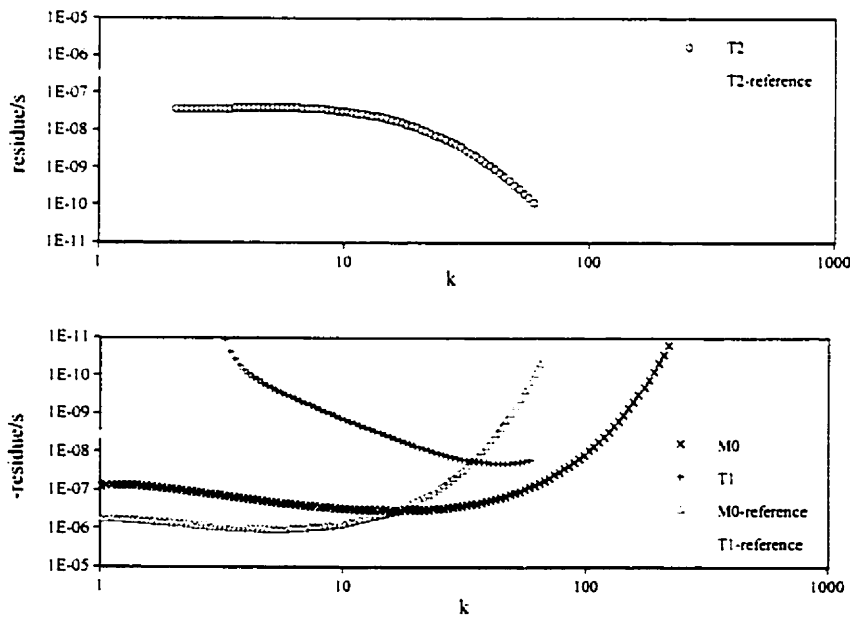


Figure 4.3.17: The horizontal displacement excitation strength for a model with a single shear modulus discontinuity at a depth of 200 km and the reference model

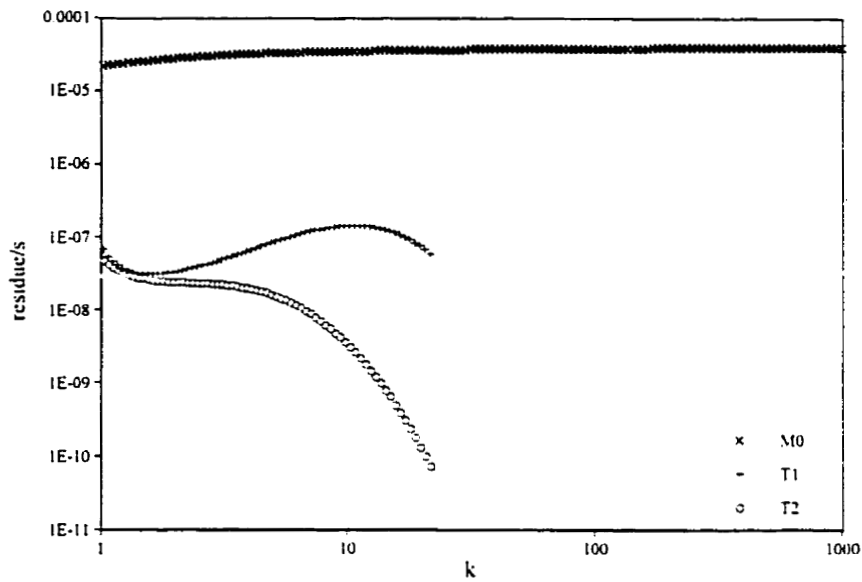


Figure 4.3.18: The vertical displacement excitation strength for a model with a single shear modulus discontinuity (reference model)

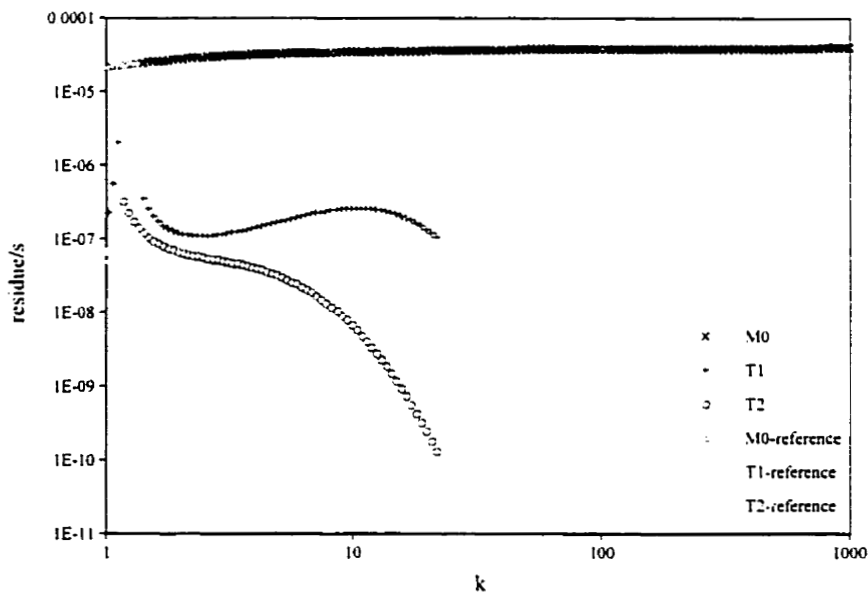


Figure 4.3.19: The vertical displacement excitation strength for a model with a single shear modulus discontinuity with an upper layer shear modulus of $0.67 \times 10^{11} \text{ N m}^{-2}$ and the reference model

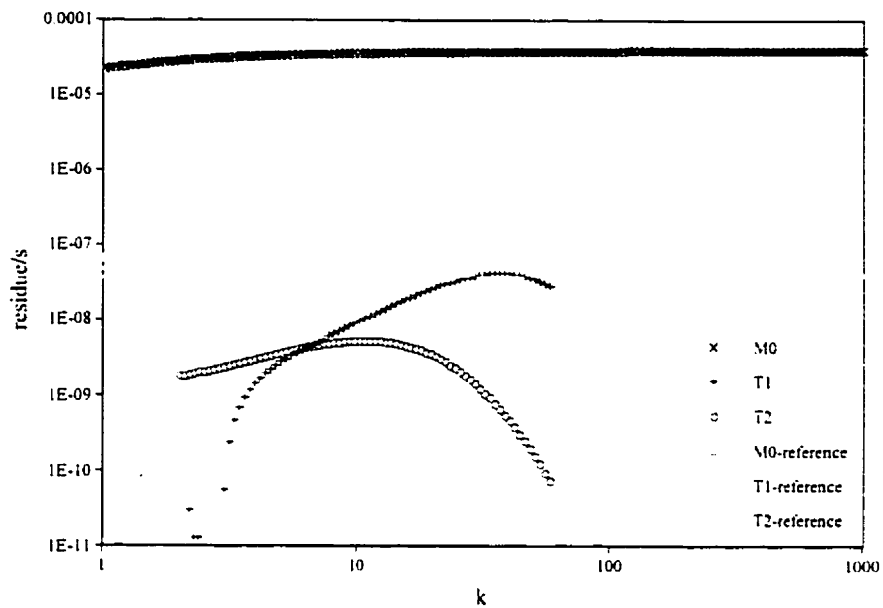


Figure 4.3.20: The vertical displacement excitation strength for a model with a single shear modulus discontinuity at a depth of 200 km and the reference model

4.3c Models with a Low Viscosity Asthenosphere

This is the only three layer model considered. The first layer is an elastic lithosphere and this is followed by a low viscosity channel and the bottom layer is a viscoelastic halfspace. The reference model is shown in Figure 4.3.21. The parameters used in this model are given in Table 8.

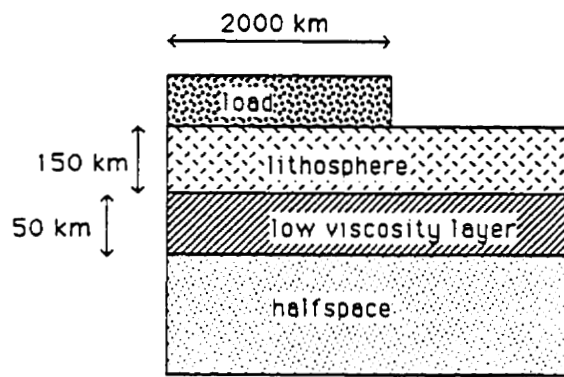


Figure 4.3.21: The reference model for a model with a low viscosity asthenosphere

Table 8: The Material Properties of the Model with a Low Viscosity Layer

	<u>halfspace, below 200 km</u>	<u>low viscosity layer, from 200 to 150 km</u>	<u>lithosphere, above 150 km</u>
density	$\rho = 5517 \text{ kg m}^{-3}$	$\rho = 5517 \text{ kg m}^{-3}$	$\rho = 5517 \text{ kg m}^{-3}$
gravitational acceleration	$g = 7.365 \text{ m s}^{-2}$	$g = 7.365 \text{ m s}^{-2}$	$g = 7.365 \text{ m s}^{-2}$
viscosity	$\eta = 1 \times 10^{21} \text{ Pa s}$	$\eta = 1 \times 10^{19} \text{ Pa s}$	$\eta \rightarrow \infty$
shear modulus	$\mu = 1.45 \times 10^{11} \text{ N m}^{-2}$	$\mu = 1.45 \times 10^{11} \text{ N m}^{-2}$	$\mu = 1.45 \times 10^{11} \text{ N m}^{-2}$
radius of load			$R = 2 \times 10^6 \text{ m}$
load			$\sigma = 1 \times 10^7 \text{ Pa}$

Based on the knowledge that every density discontinuity leads to one additional mode of relaxation and every discontinuity in the elastic properties leads to two additional modes, except for the lithosphere which leads to only one, four modes of relaxation are expected for this model; the halfspace mode, M0, a lithospheric mode, L0, and two transition modes corresponding to the change in the elastic properties of a layer, T1 and T2. These are demonstrated in the relaxation diagram given in Figure 4.3.22. The presence of the additional low viscosity layer reduces the relaxation times of the lithospheric and halfspace modes, as expected, due to the low viscosity of this layer. In terms of the excitation strength of the horizontal displacement for this model, as shown in Figure 4.3.23, all four modes appear to have negative excitation strengths while the L0 and T1 modes also have positive strengths. The halfspace and lithospheric modes are dominant. The excitation strength of the vertical displacement is also dominated by the M0 mode, Figure 4.3.24. The strength of all of the modes decay to zero for large wavenumbers. This is also seen in the excitation strength diagram for the horizontal displacement.

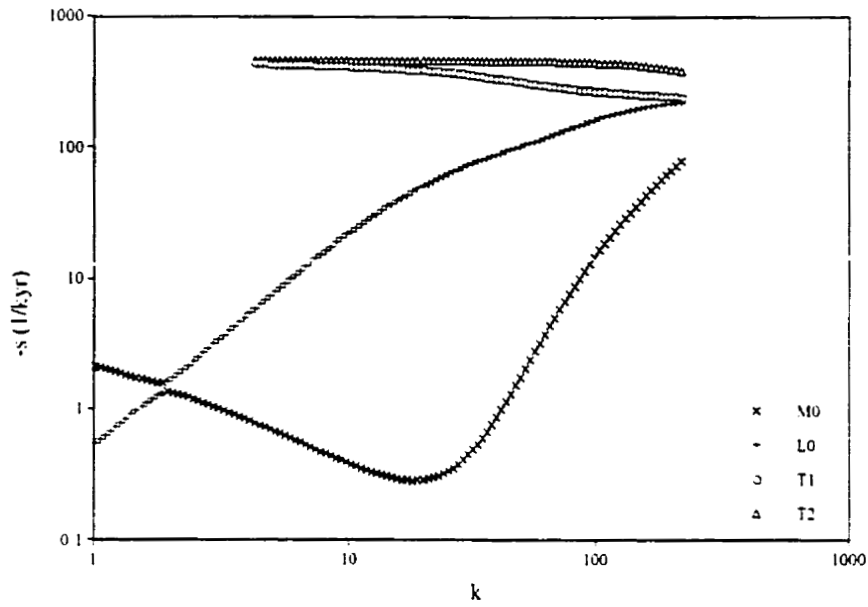


Figure 4.3.22: The relaxation diagram for the low viscosity channel model

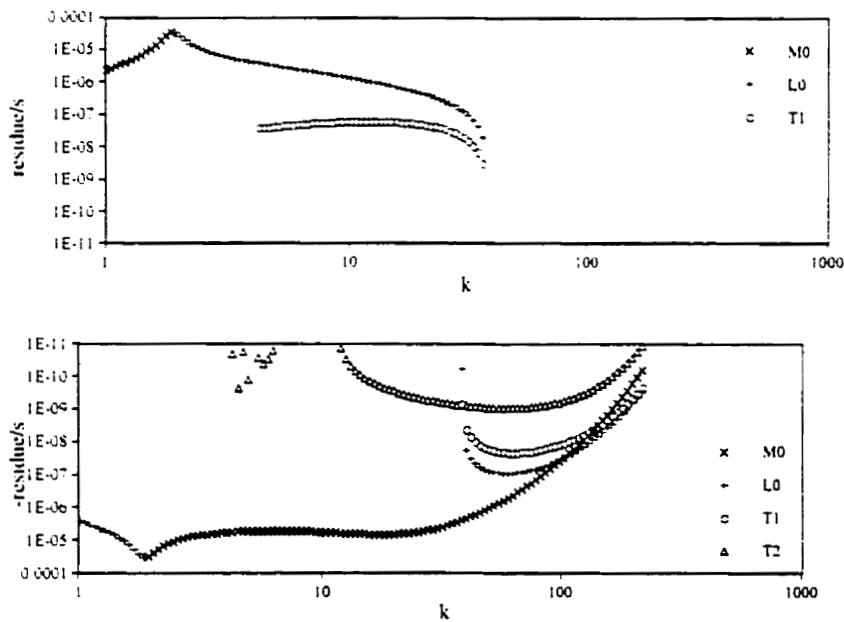


Figure 4.3.23: The horizontal displacement excitation strength for the low viscosity channel model

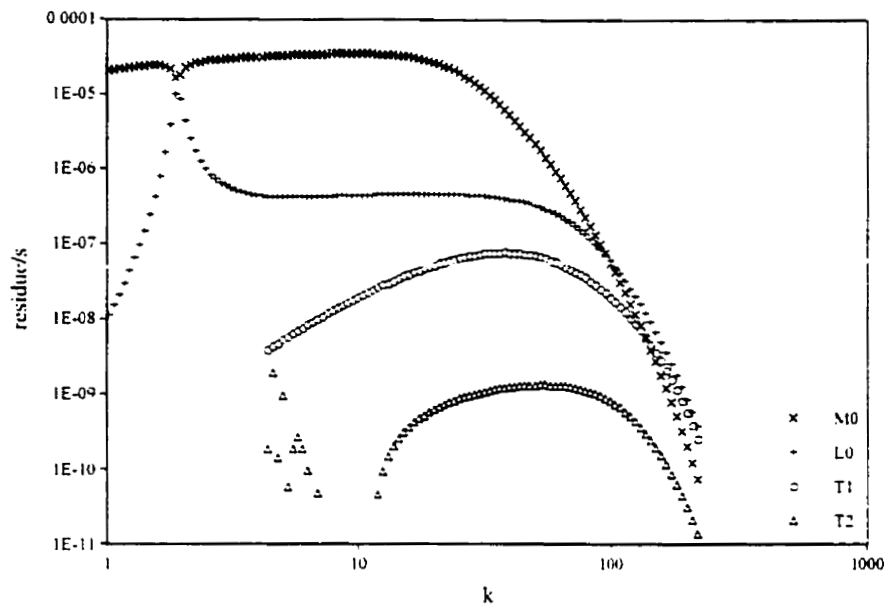


Figure 4.3.24: The vertical displacement excitation strength for the low viscosity channel model

Chapter 5: Space Domain Solutions

This chapter will investigate the space domain solutions for the models discussed in Chapter 4 in addition to models with lateral heterogeneity, nonlinear rheology and time dependent creep. The shape and magnitudes of both the vertical and horizontal displacements will be discussed as well as the effect of changing viscosity, density and thickness where appropriate. In general the material parameters used for the various models are given in the appropriate sections in Chapter 4. All of the disc loads have a radius of 2000 km and a height of 1 km with Heaviside loading. Most of the results were obtained using the finite element method, though in a few cases the solutions using the spectral method are shown to support the finite element method results from ABAQUS.

5.1: Halfspace and Channel Models

In this section the space domain solutions of the halfspace and channel models will be discussed. A comparison between the finite element method using the program ABAQUS and the spectral method will be presented as a check of the numerical results obtained from ABAQUS. This has been done for the vertical displacement, but not for the horizontal displacement. Several curves are included on each graph to show the variation in time of the horizontal and vertical displacements after the load has been emplaced: these times correspond to 0, 1, 5, and 10 thousand years after loading. In all of these figures, there is arrow at the top of the figure which indicates the edge of the ice load.

The vertical displacement that results from the loading of the halfspace model can be seen in Figure 5.1.1. This is identical to the figure given in section 3.4 (Figure 3.4.1). The

material parameters used in this model are given in Table 2 in section 3.4. Recall that for the halfspace model there is no horizontal displacement experienced upon loading. Most of the vertical displacement occurs within the region of the load with a small peripheral bulge outside of the load. In Figure 5.1.2 the effect of a viscosity stratification can be seen. This is done through ABAQUS by changing the properties of the appropriate elements. In this model the viscosity increases with depth; from the surface to a depth of 100 km the viscosity is 1×10^{21} Pa s and from 100 km to 200 km there is a viscosity of 1×10^{23} Pa s and below 200 km the viscosity is 1×10^{25} Pa s. The shape of these displacement curves resemble those of the channel model (Figure 5.1.4) which indicates that most of the viscous relaxation is occurring within the upper lower viscosity layers. Note that the magnitude of the elastic displacement is the same as that of the model with constant viscosity (Figure 5.1.1) and the increase in the magnitude of the displacement experienced in the peripheral bulge. Also note that the viscosity stratification produces horizontal displacement (Figure 5.1.3) unlike the constant halfspace. The horizontal displacement in this case is positive for all time periods after loading.

The Heaviside loading response of the basic channel model involves a positive horizontal displacement and a negative vertical displacement. For the channel model the results of the analytical solution, the numerical solution using Matlab and the numerical solution using ABAQUS can be seen in Figures 5.1.4 and 5.1.5. These figures show that the results compare favorably. The material parameters are the same as those used for the halfspace model and the thickness of the channel is 670 km. Table 3, in section 4.1, lists the material parameters used for the channel model discussed in all of the following cases except where indicated otherwise. The 0 thousand year curve shows the initial elastic displacement and the subsequent curves illustrate the viscous relaxation over time. The horizontal displacement that results from the loading of a channel model is positive. The

maximum displacement is obtained at the edge of the load. By contrast the vertical displacement is negative within the region of the load and positive outside of this region and the maximum is attained just within the load from the edge. There is a prominent peripheral bulge. The horizontal and vertical displacements experience approximately the same range of displacement.

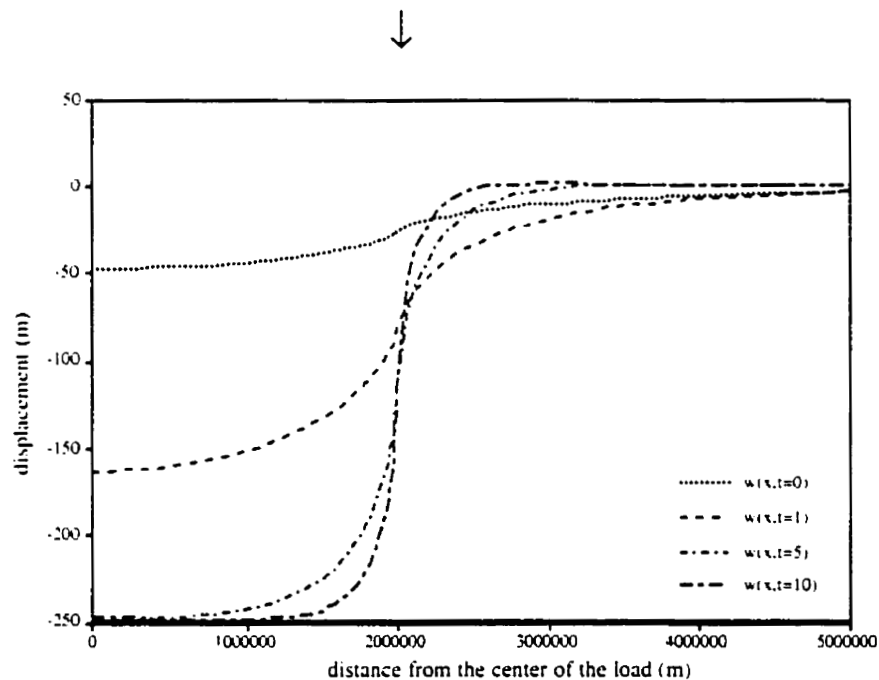


Figure 5.1.1: The vertical displacement for the halfspace model

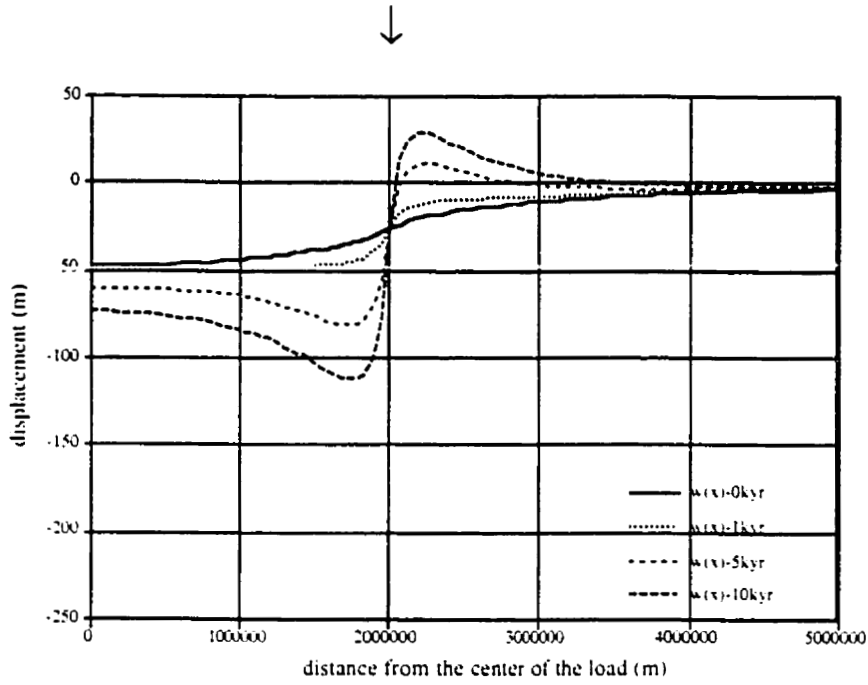


Figure 5.1.2: The vertical displacement for a halfspace with radial viscosity variations

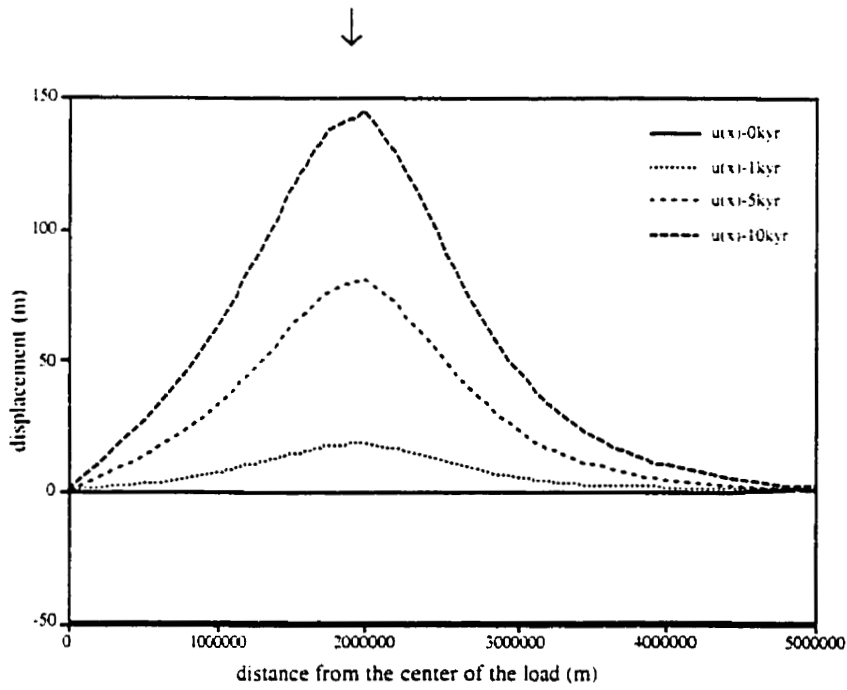


Figure 5.1.3: The horizontal displacement for a halfspace with radial viscosity variations

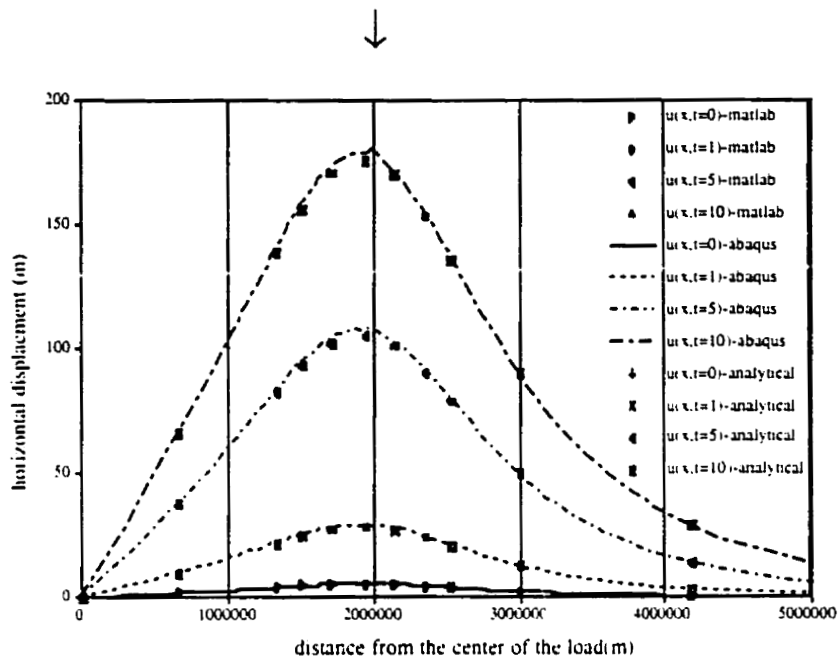


Figure 5.1.4: Comparison between different methods for the horizontal displacement that results from the loading of a channel model

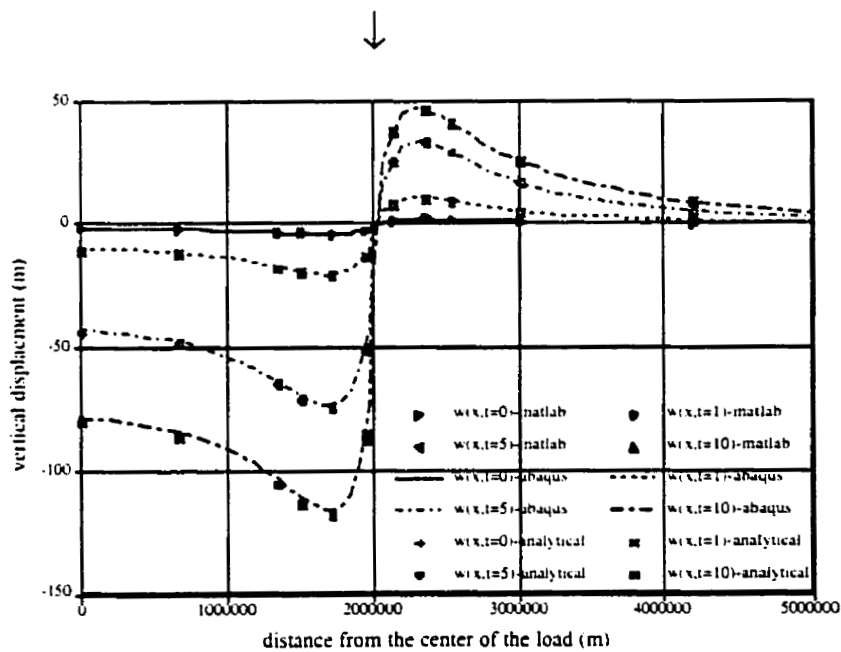


Figure 5.1.5: Comparison between different methods for the vertical displacement that results from the loading of a channel model

The next two figures show the effect of changing various material parameters on the horizontal displacement. The solid lines represent the results of ABAQUS, while the distinct points represent the results from the spectral method using MATLAB. Figure 5.1.6 shows the effect of a change in the channel viscosity. The displacement is drastically increased for an decrease in the viscosity, though the general shape of the curve remains the same with a maximum displacement occurring at the edge of the load, compare with Figure 5.1.4. A decrease in the viscosity increases the displacement experienced at the initial times. The displacement at infinite time remains the same regardless of the viscosity, but with a lower viscosity the material can reach this maximum displacement more quickly. Note the error in the displacement predicted by ABAQUS at the edge of the load. The result of having a load with a 1000 km radius is shown in Figure 5.1.7. Again the maximum displacement occurs at the edge of the load, though this maximum value is less for the smaller load.

Figures 5.1.8 and 5.1.9 show similar results for the vertical displacement. Figure 5.1.8 shows the results of a low viscosity channel. This is the same viscosity used in the low viscosity layer models discussed in section 4.3c. At this viscosity the vertical displacement is almost entirely confined within the region of the load and little displacement occurs outside of this region at times greater than 5 thousand years after the emplacement of the load. As with the horizontal displacement, the vertical displacement predicted by ABAQUS at the edge of the load exceeds the actual displacement as shown by the spectral method. This is due to the fact that there is a large displacement gradient at this point which implies that there is a large stress gradient. This leads to a breakdown of the finite element method which assumes that the displacements and stresses vary linearly from one grid to another. In Figure 5.1.9, the radius of the load is decreased from 2000 km to 1000 km. The vertical displacement within the region of the load increases

while the displacement outside of the region decreases, even for the initial elastic displacement.

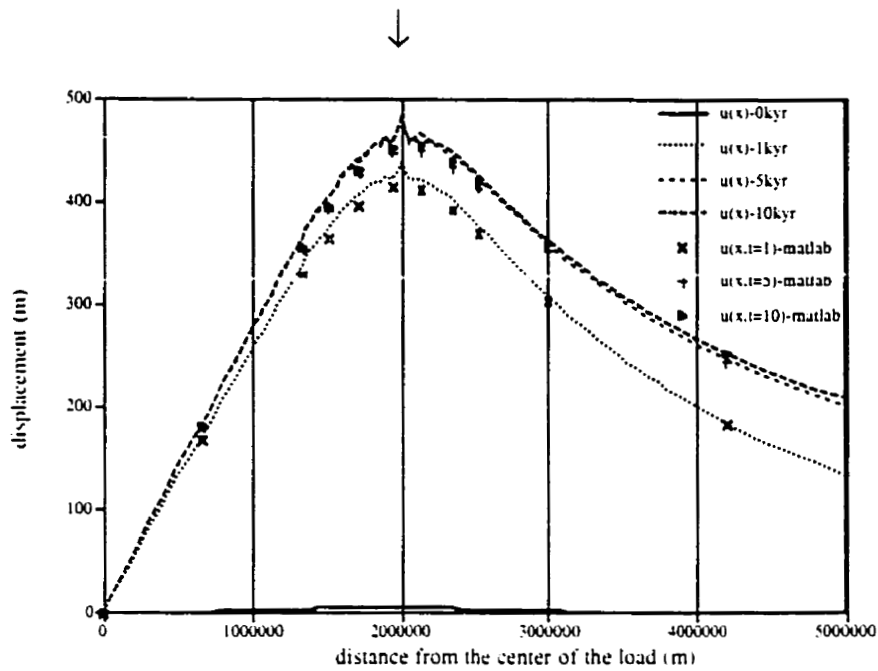


Figure 5.1.6: The horizontal displacement for a channel with a viscosity of 1×10^{19} Pa s

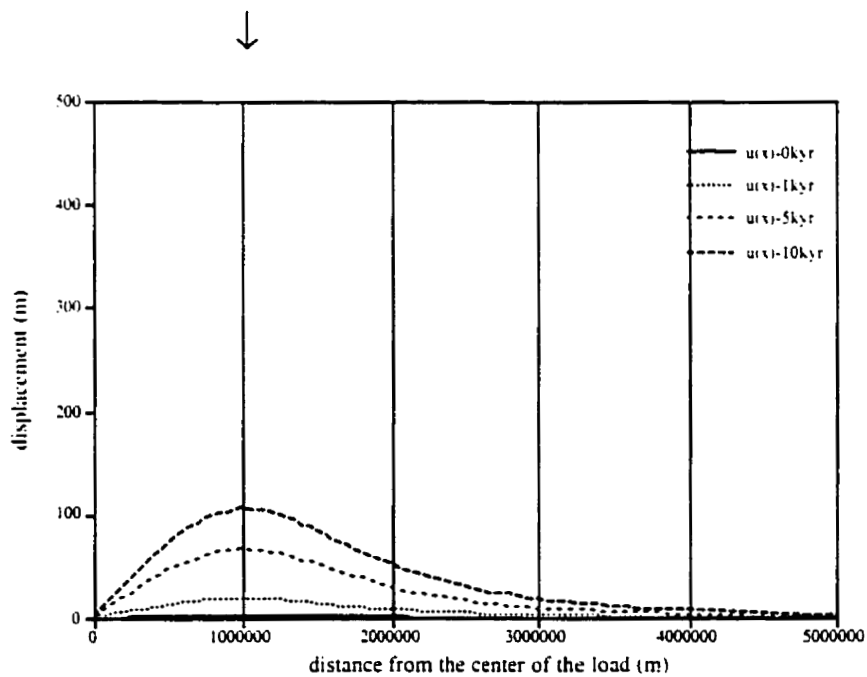


Figure 5.1.7: The horizontal displacement for a channel with a 1000 km radius load and a viscosity of 1×10^{21} Pa s

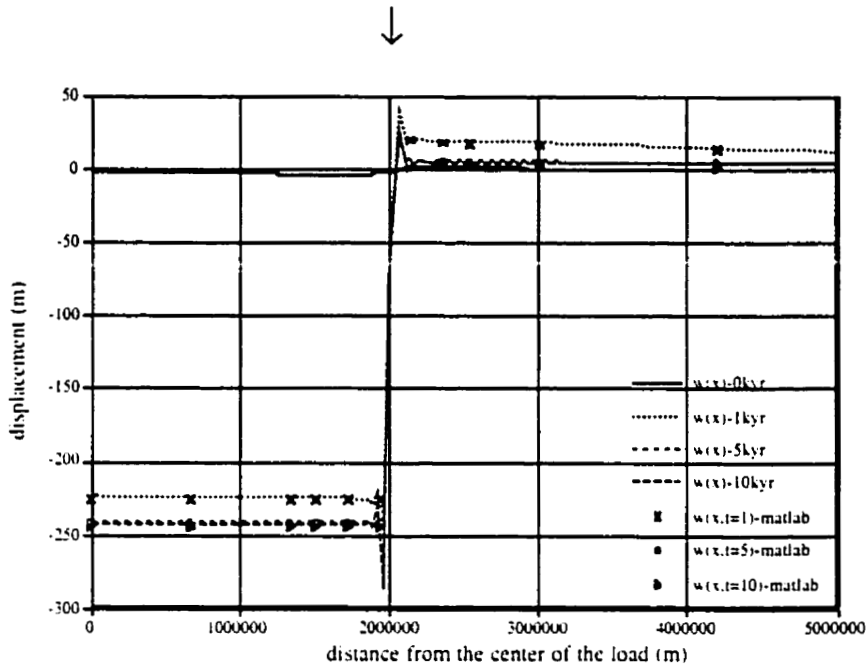


Figure 5.1.8: The vertical displacement for a channel with a viscosity of 1×10^{19} Pa s

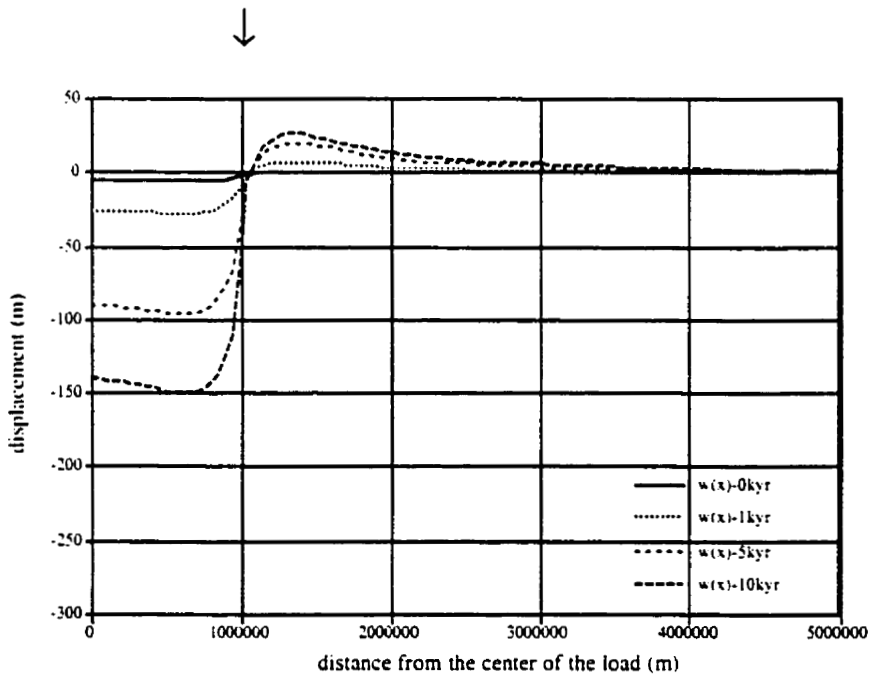


Figure 5.1.9: The vertical displacement for a channel with a 1000 km radius load and a viscosity of 1×10^{21} Pa s

5.2: The Lithosphere over a Halfspace Model

This section will discuss the space domain solutions of models with an elastic lithosphere. In general, there are four curves on each figure which correspond to the displacements experienced at four specific time intervals after the emplacement of the load. There is the initial elastic displacement followed by the displacement 1, 5, and 10 thousand years after loading. In all of the figures, there is an arrow located at the top of the figure to indicate the edge of the load.

5.2a: Models with Lateral Homogeneity

First, the numerical results obtained for the lithosphere over a fluid are tested. The material parameters of the model tested are given in Table 4, in section 4.2a. The lithosphere in this model has a thickness of 150 km. In Figure 5.2.1 four different methods are compared: the analytical solution as given by equations (4.2.1) and (4.2.2) transformed to the space domain, the numerical solution obtained from Matlab, the numerical solution obtained from the ABAQUS modeling package and the theoretical solution for the vertical displacement. The theoretical solution for the vertical displacement of an elastic lithosphere over a fluid halfspace was obtained from the Thin Plate Theory. The solution is given by

$$w(x) = \begin{cases} -\frac{\rho_L h}{(\rho_m - \rho_f)} \left[C_1 \cos \frac{x}{\alpha} \cosh \frac{x}{\alpha} + C_2 \sin \frac{x}{\alpha} \sinh \frac{x}{\alpha} - 1 \right], & x \leq L \\ \frac{\rho_L h}{(\rho_m - \rho_f)} e^{-\frac{x}{\alpha}} \left[F_1 \cos \frac{x}{\alpha} + F_2 \sin \frac{x}{\alpha} \right], & x \geq L \end{cases} \quad (5.2.1)$$

where ρ_L is the density of the load,

ρ_m is the density of the halfspace,

ρ_f is the density of the fluid,

α is the flexural parameter,

h is the height of the load,

L is the half-width of the load,

and C_1, C_2, F_1, F_2 are constants.

The derivation of this solution is based on the bending of a thin beam and can be found in Turcotte and Schubert (1982). The results of the four methods are compared in Figure 5.2.1 as a check of the validity of the numerical programs. The results agree well.

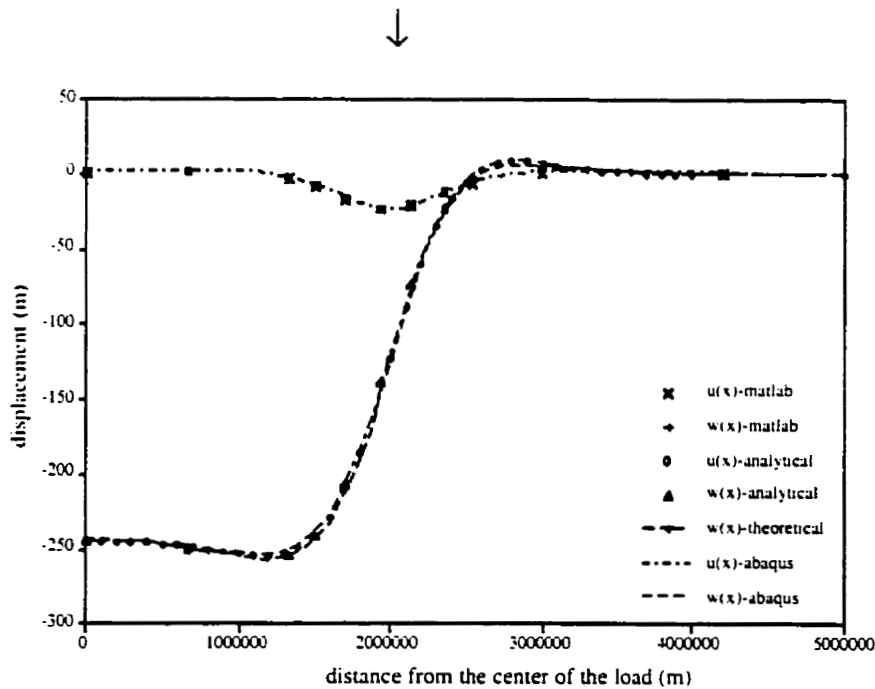


Figure 5.2.1: The comparison of four different methods in determining the vertical displacement that results from the loading of a 150 km thick, elastic lithosphere overlying a fluid

The next two figures, Figures 5.2.2 and 5.2.3, show the horizontal and vertical displacements that result from the loading of a lithosphere overlying a viscoelastic halfspace instead of a fluid. The load has a radius of 2000 km and a height of 1 km. The properties of the halfspace and lithosphere are given in Table 5 in section 4.2b. One important distinction to be noted immediately is the fact that in contrast to the channel model, the horizontal displacement experienced by this model is negative (Figure 5.2.2). This is not unexpected since from the analysis of the horizontal displacement excitation strengths of the two models, the channel model gives a positive excitation strength (Figure 4.1.2) while the lithosphere model gives a negative excitation strength for the M0 mode (Figure 4.2.5). In both cases the initial elastic displacement is positive, i.e. motion away from the center of the load, but with the channel model subsequent motion is also positive while for the lithosphere model subsequent motion is negative. Also, note that although the horizontal displacement that results from loading a halfspace model is zero, the presence of the lithosphere yields a non-zero horizontal displacement. The vertical displacement, shown in Figure 5.2.3, is similar to the displacement experienced by the channel model though for the lithosphere model the displacement within the region of the load is much greater than outside of this region. Note also the presence of the peripheral bulge in Figure 5.2.3 and how the maximum migrates over time. For the channel model the horizontal and vertical displacements are of the same order, however, for the lithosphere model the magnitude of the horizontal displacement is about one tenth of the vertical since the halfspace allows a significant component of the compensation of the load to be made through vertical rather than horizontal motion.

Figures 5.2.2 and 5.2.3 also show a comparison between the two different numerical methods. The first method uses the Matlab programs as discussed in Chapter 2 and the second uses the finite element modeling package ABAQUS. The results agree fairly well.

Note that the viscous relaxation of the horizontal displacement experienced at early times is not well represented by ABAQUS, though for longer times, the results are very accurate. Also note that the horizontal displacements predicted by ABAQUS for distances far from the load are not accurate. The displacement predicted by the Matlab programs approaches zero very quickly outside of the region of the load and the ABAQUS results do not reflect this. This tendency for the horizontal displacement to persist far from the load, as obtained by ABAQUS, is seen in many of the figures and it is important to recognize that this is most likely not representative of the true displacement. This is not thought to be due to aliasing of the transform method because Matlab gives accurate results for the channel model.

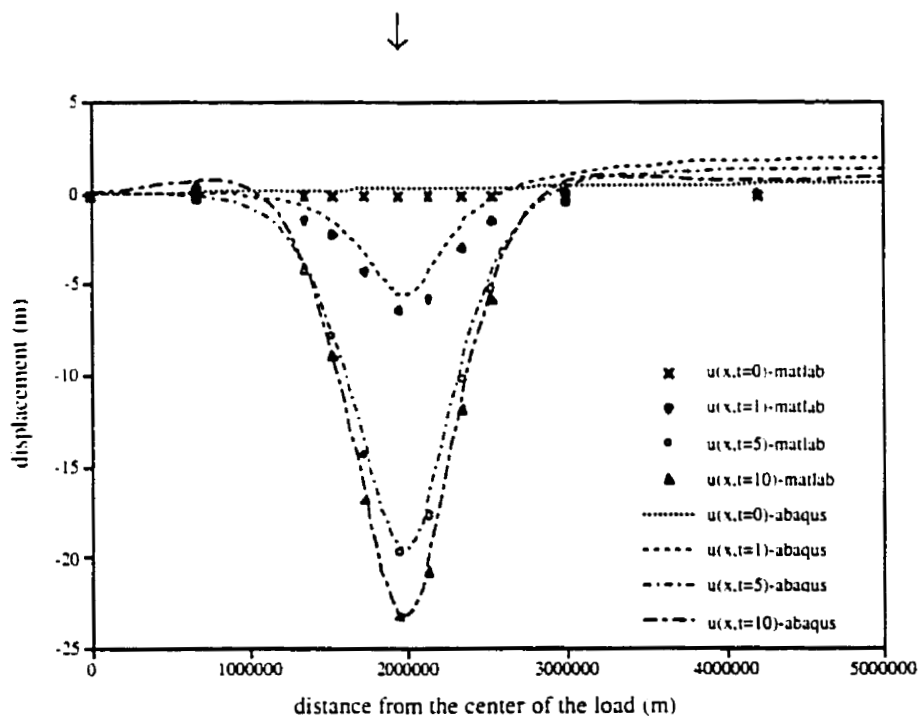


Figure 5.2.2: A comparison between two different methods for the horizontal displacement that results from the loading of a lithosphere model with a 150 km thick lithosphere

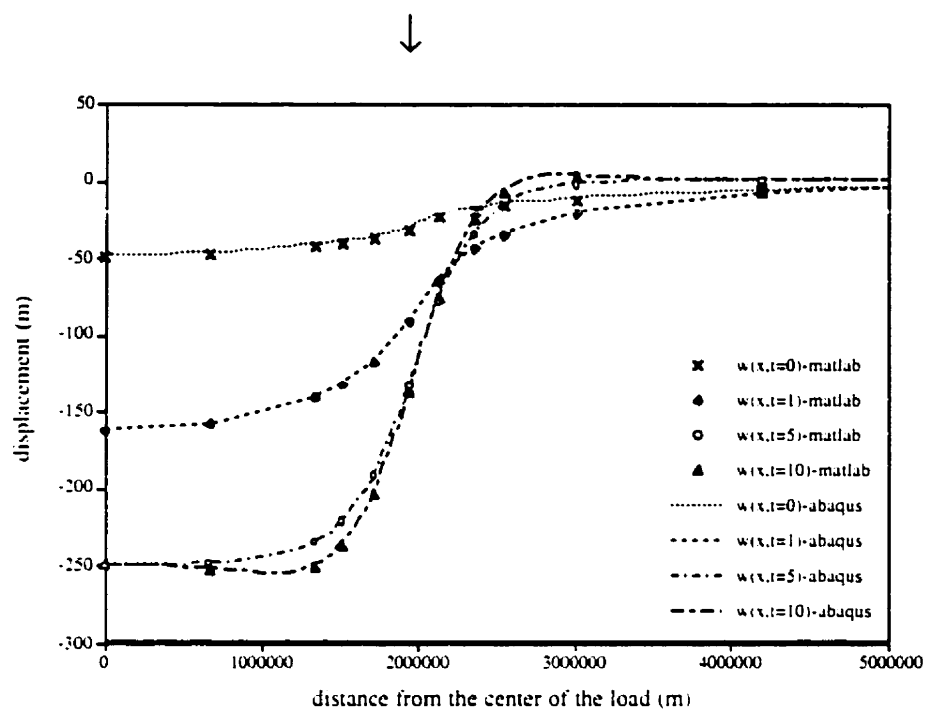


Figure 5.2.3: A comparison between two different methods for the vertical displacement that results from the loading of a lithosphere model with a 150 km thick lithosphere

5.2b: Models with Lateral Heterogeneity

The next set of figures is designed to investigate the effect of lateral variations within the subsurface in terms of the viscosity of the halfspace and the thickness of the lithosphere. Since seismic tomography has shown that lateral heterogeneity does exist in the subsurface, it is important to investigate its effect on the displacements that result from the loading of earth models.

The first set of figures is designed to investigate the impact of a lateral variation in viscosity. First the effect of a constant increase in the viscosity of the halfspace is determined. Figure 5.2.6 shows the effect of an increase in the halfspace viscosity on the horizontal displacement. The viscosity of the halfspace is increased from 1×10^{21} Pa s to 1×10^{23} Pa s. The increase in viscosity reduces the viscous relaxation such that very little displacement is experienced after the initial elastic displacement. Next a model with a lateral variation is considered. This model has a viscosity of 1×10^{23} Pa s under the region of the load to a depth of 670 km and a viscosity of 1×10^{21} Pa s everywhere else: see Figure 5.2.4 for an illustration of the earth model. Figure 5.2.7 shows the effect of a lateral variation in viscosity: the resultant horizontal displacement curve has a very distinct shape. The maximum displacement is no longer obtained at the edge of the load, but rather it is displaced away from the load.

The next two figures show the vertical displacement that results from these same two models, one with a constant, high viscosity halfspace and the second with a lateral variation in viscosity. Figure 5.2.8 shows that an increase in the viscosity of the halfspace decreases the viscous vertical displacement, though the elastic displacement remains constant. In Figure 5.2.9 the vertical displacement that results from the loading

of a model with lateral variation in viscosity are shown. The maximum displacement experienced at the center of the load has the same magnitude as obtained that for the model with a constant viscosity of 1×10^{21} Pa s (Figure 5.2.3), however, the shape of the displacement curve at the edge of the load has been modified by the presence of the lateral heterogeneity. In fact, the peripheral bulge has vanished and there is a more gradual variation in the displacement rather than the sharp gradient at the edge of the load observed previously.

The final set of figures in this section demonstrates the effect of a lateral variation in the thickness of the lithosphere. The first model to be studied has the same material parameters as given in Table 5 in section 4.2b, except that in this case the lithosphere has a thickness of only 50 km instead of 150 km. A change in the thickness of the lithosphere has a significant impact on the horizontal displacement. This can be seen by comparing Figures 5.2.2 and 5.2.10. As the thickness of the lithosphere decreases the horizontal displacement also decreases. Figure 5.2.11 shows that a lateral variation in the thickness of the lithosphere also has a significant impact. The earth model used in this case is given in Figure 5.2.5. The thickness of the lithosphere is 100 km within the region of the load and 50 km outside of this region. The halfspace viscosity is 1×10^{21} Pa s. This lateral variation results in a larger horizontal displacement outside the region of the load even for times long after the emplacement of the load. The maximum displacement still occurs at the edge of the load and the magnitude of this displacement is close to the maximum displacement observed for the 100 km thick lithosphere model.

In contrast to the horizontal displacement, there is little change in the vertical displacement with a change in the lithospheric thickness, as seen by comparing Figures 5.2.3 and 5.2.12. The only difference is a slight variation at the edge of the load, the

peripheral bulge is closer to the load and the slope of the curve at the edge of the load is steeper. Also, in contrast to the effect noted in the horizontal displacement, a lateral variation in the thickness of the lithosphere has only a small effect on the vertical displacement. The most notable area of change is in the magnitude of the peripheral bulge, as shown in Figure 5.2.13, which increases slightly.

In this section it has shown not only that ABAQUS is able to give accurate results for the displacements that result from the loading of a model with an elastic lithosphere, but also that lateral variations in the properties of the subsurface have a significant impact on displacement. In general, lateral variations are more easily distinguished from the curves of the horizontal displacement despite the fact that the magnitude of these displacements is less than the vertical displacement. Lateral variations result in a significant change in the magnitude of the horizontal displacements, not just the particular shape of the displacement curve as with the vertical displacement. Lateral viscosity variations produce a more significant effect on both the vertical and horizontal displacements as compared with lateral variations in lithospheric thickness.

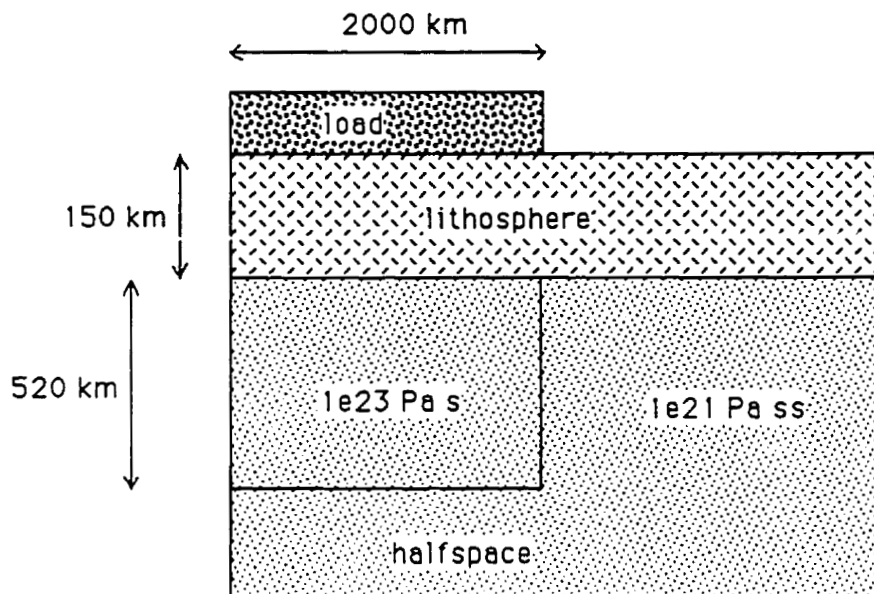


Figure 5.2.4: The earth model of a laterally heterogeneous halfspace viscosity

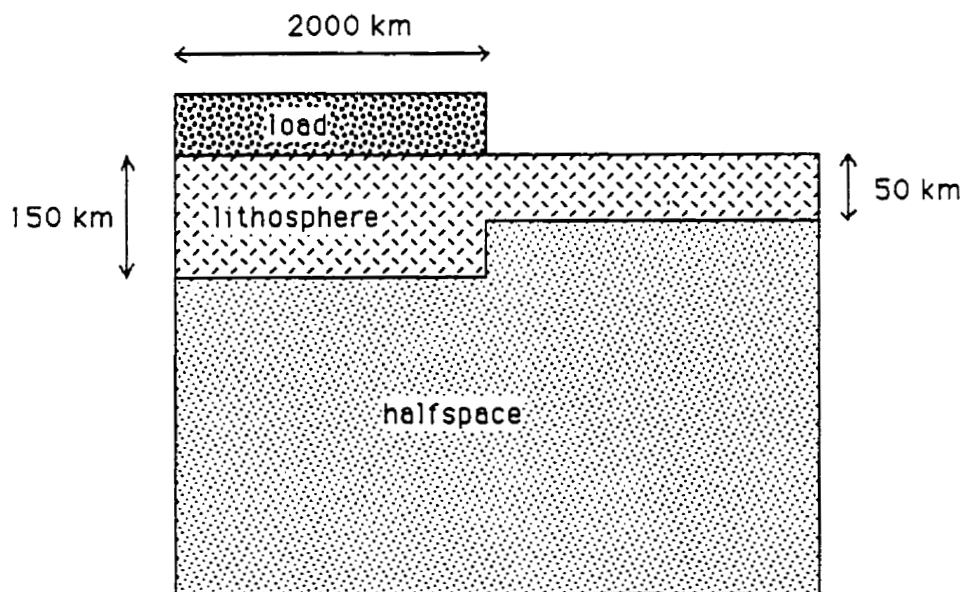


Figure 5.2.5: The earth model of a laterally heterogeneous lithospheric thickness

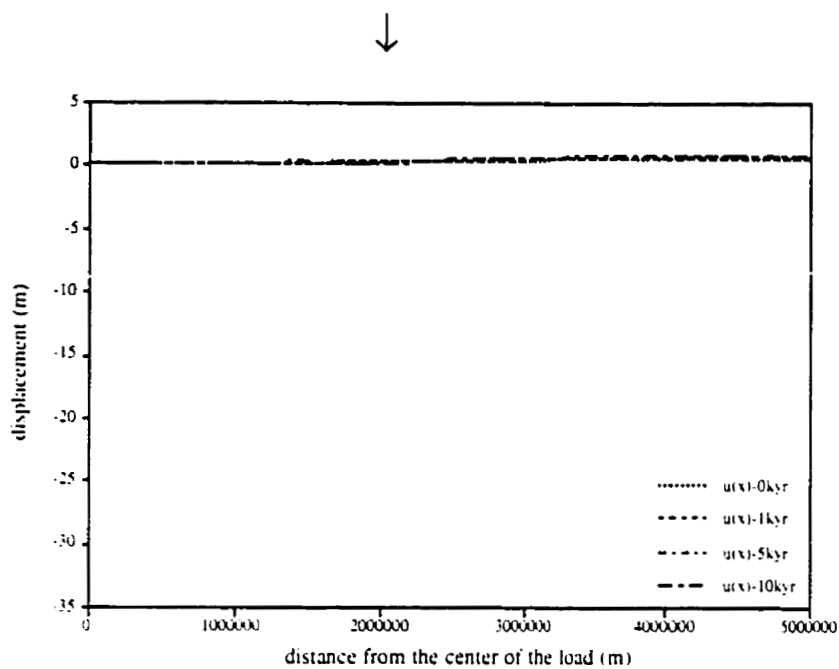


Figure 5.2.6: The horizontal displacement for the lithosphere model with a halfspace viscosity of 1×10^{23} Pa s

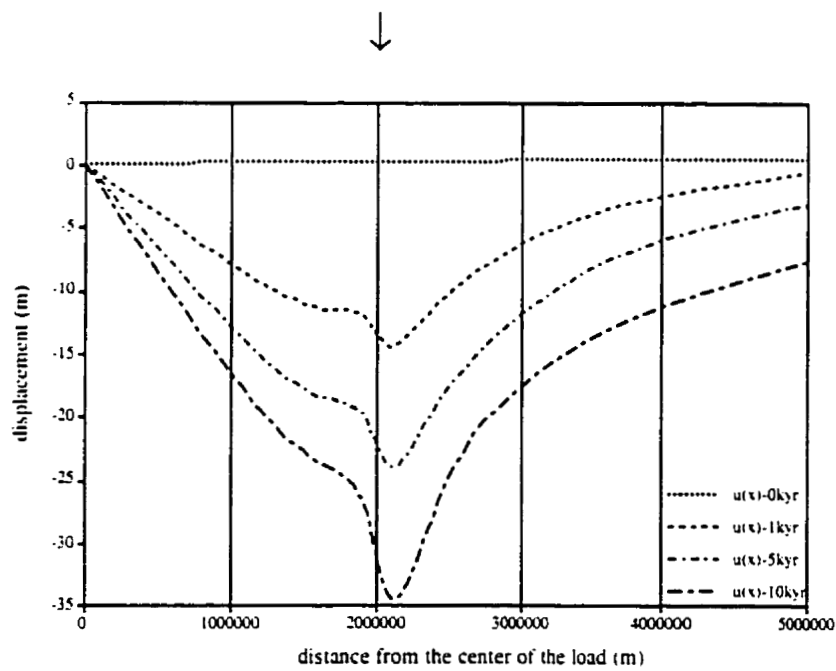


Figure 5.2.7: The horizontal displacement for the model in Figure 5.2.4

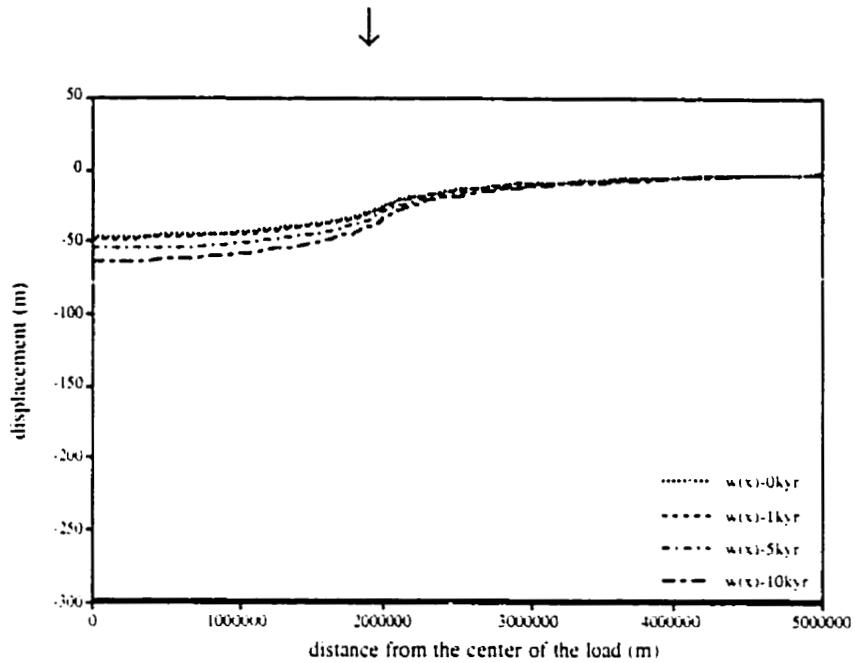


Figure 5.2.8: The vertical displacement for the lithosphere model with a halfspace viscosity of 1×10^{23} Pa s

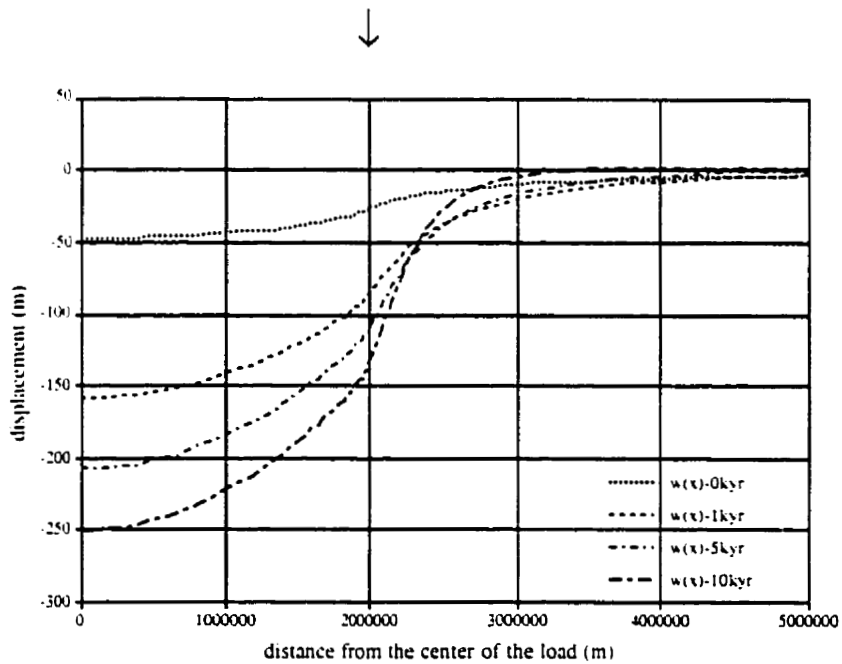


Figure 5.2.9: The vertical displacement for the model in Figure 5.2.4

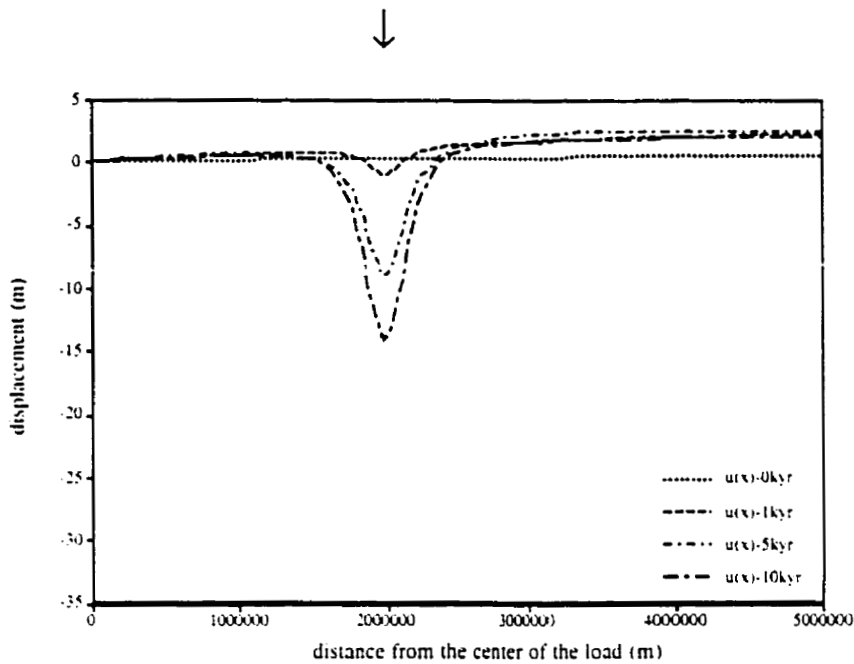


Figure 5.2.10: The horizontal displacement for the lithosphere model with a 50 km thick lithosphere

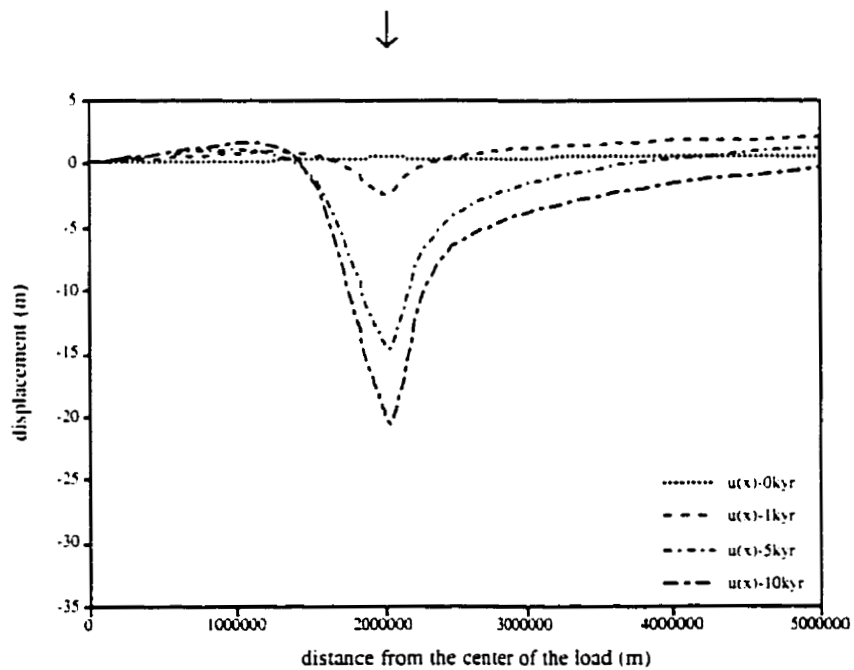


Figure 5.2.11: The horizontal displacement for the model in Figure 5.2.5

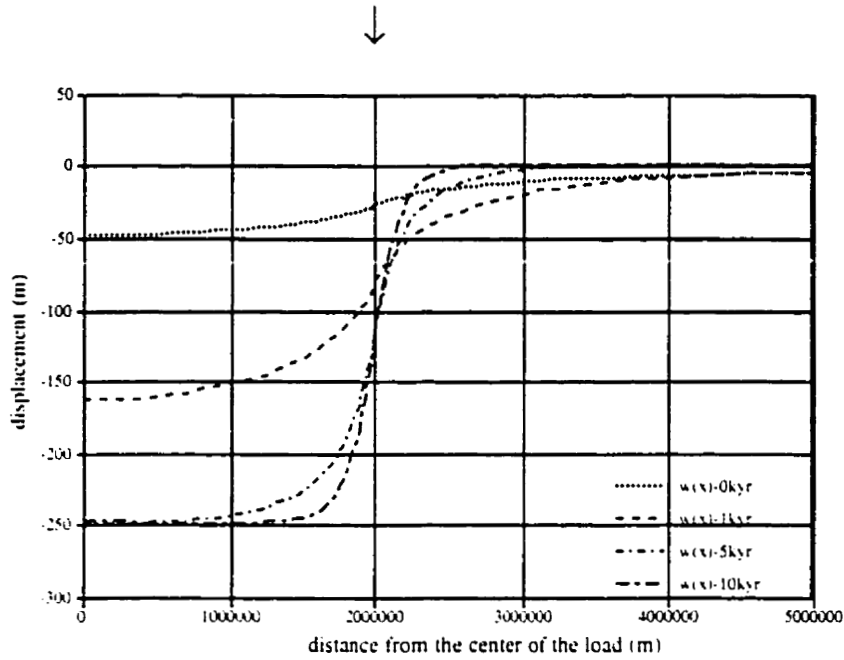


Figure 5.2.12: The vertical displacement for the lithosphere model with a 50 km thick lithosphere

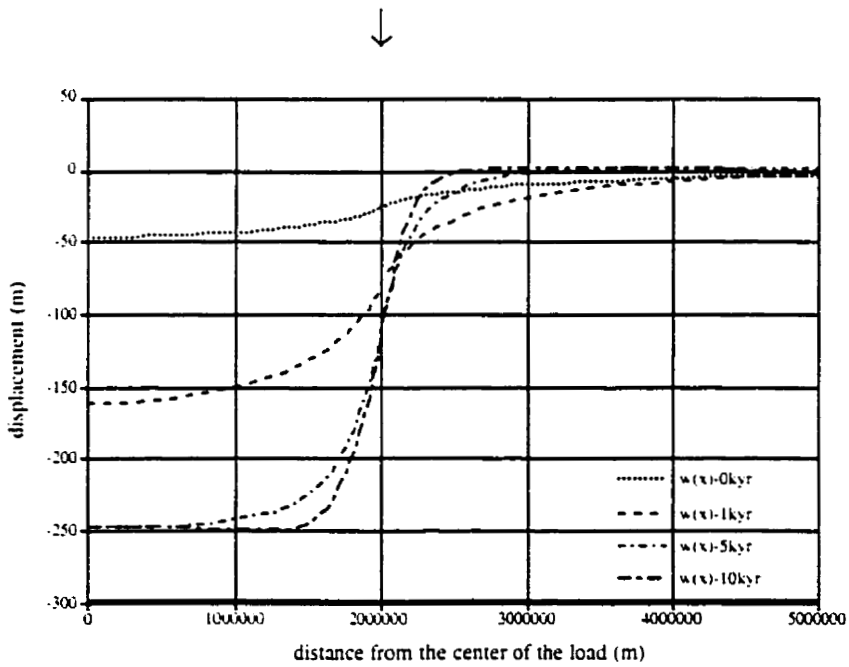


Figure 5.2.13: The vertical displacement for the model in Figure 5.2.5

5.3: The Low Viscosity Asthenosphere with a Lithosphere Model

This section will discuss the space domain solutions of models with a low viscosity asthenosphere beneath an elastic lithosphere. The low viscosity zone is defined by a decrease in the radial viscosity structure of the model. This zone can also have lateral heterogeneities. The low viscosity asthenosphere model has the same material parameters as used in section 4.3c, given in Table 8, except that the lithosphere and low viscosity asthenosphere both have a thickness of 100 km overlying a viscoelastic halfspace. The earth model is given in Figure 4.3.21. The default viscosity of the asthenosphere is 1×10^{19} Pa s which is two orders of magnitude less than that of the underlying halfspace. All of the figures give displacement curves as a function of the distance from the center of the load. Each graph contains four curves, each one representing the displacement for a different time after the load is emplaced. There is an arrow above each figure which represents the edge of the load. In all cases the cylindrical load has a constant radius of 2000 km and a constant height of 1 km.

The horizontal and vertical displacements that result from the loading of a model with a low viscosity asthenosphere are given in Figures 5.3.1 and 5.3.2 respectively. When these are compared with the results for the displacements experienced by a model with only a lithosphere (Figures 5.2.2 and 5.2.3), some significant differences are noted. First, the viscous relaxation experienced by the horizontal displacement soon after the emplacement of the load produces a strong positive displacement which then turns negative for longer time periods. The results for the lithosphere model do not show this positive displacement. For short times, the results are intermediate between the lithosphere model (Figure 5.2.2) and the channel model (Figure 5.1.4). This is due to the faster initial relaxation caused by the low viscosity layer. At long time periods the two

models match more closely, since the viscosity does not significantly affect the response at long times. In addition, the maximum magnitude of the displacement is slightly greater than expected since the lithosphere is thinner than the one used in the reference lithosphere models. The vertical displacement (Figure 5.3.2) demonstrates that the magnitude of the peripheral bulge is increased by the presence of the low viscosity layer. The curves of the vertical displacement also resemble a combination of the lithosphere model (Figure 5.2.3) and the channel model (Figure 5.1.5). The greatest impact of this low viscosity asthenosphere is to modify the vertical displacement in the region of the edge of the load.

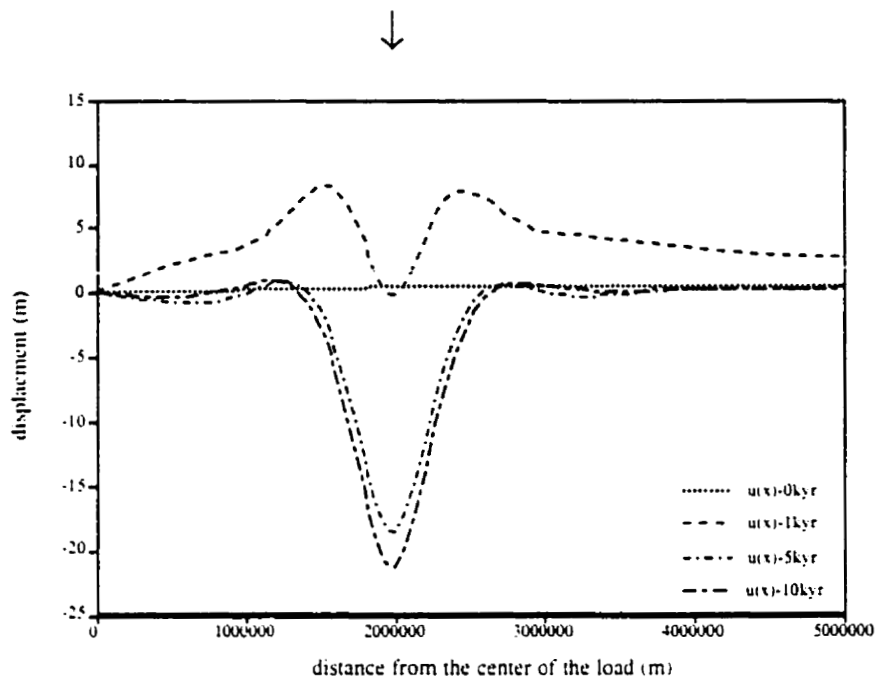


Figure 5.3.1: The horizontal displacement for the low viscosity asthenosphere model

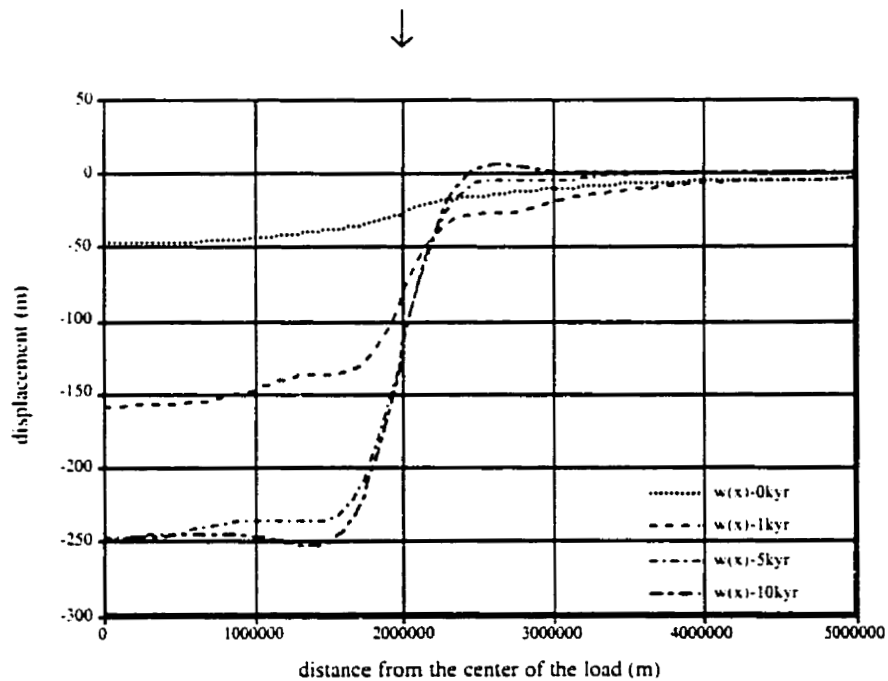


Figure 5.3.2: The vertical displacement for the low viscosity asthenosphere model

Two different parameters were investigated with the low viscosity asthenosphere model. The first was to determine the effect of the viscosity of the asthenosphere and how lateral variations in this viscosity might impact the displacement. The second was to determine how the thickness of the low viscosity layer and lateral variations in the thickness affect the displacement. Figure 5.3.5 demonstrates the impact of the viscosity within the low viscosity asthenosphere on the horizontal displacement. In this model the viscosity within the asthenosphere is increased from 1×10^{19} Pa s to 1×10^{20} Pa s. An increase in the viscosity decreases the initial viscous motions and the maximum displacement is attained more slowly. A model with a lateral variation of the viscosity within the asthenosphere is shown in Figure 5.3.3. In this model the viscosity directly below the load is increased to 1×10^{20} Pa s while the viscosity in the rest of the asthenosphere remains 1×10^{19} Pa s. The horizontal displacement that results from the loading of this model can be seen in Figure 5.3.6. A slight difference between the displacement within the region of the load and outside can be identified for longer time scales, especially in the peripheral regions. The displacement in the region outside of the load resembles the displacement observed for the reference model with a constant low viscosity asthenosphere viscosity of 1×10^{19} Pa s (Figure 5.3.1).

Figures 5.3.7 and 5.3.8 show the vertical displacement for the same two models discussed above. As the viscosity within the asthenosphere increases, the amplitude of the peripheral bulge decreases. A lateral variation in the viscosity, as shown in Figure 5.3.3, produces displacement curves similar to those obtained for the model with a constant 1×10^{20} Pa s viscosity within the region of the load and outside of this region the displacement curves resemble those of the model with a constant viscosity in the low viscosity layer of 1×10^{19} Pa s. Overall the lateral variation in the viscosity of the low

viscosity asthenosphere produces only small changes to the displacement curves. This type of model would be difficult to distinguish from models with lateral homogeneity.

A lateral variation in the thickness of the low viscosity asthenosphere was also investigated. An illustration of this earth model is given in Figure 5.3.4. Under the load, the thickness of the asthenosphere is 200 km and outside of this region the thickness is 100 km. First, the horizontal displacement that results from a low viscosity asthenosphere model with a constant in layer thickness was determined. This can be seen in Figure 5.3.9. In this case the thickness of the layer is increased to 200 km. An increase in the thickness of the low viscosity asthenosphere produces an effect similar to the one obtained with a decrease in the viscosity of the asthenosphere. Both an increase in the viscosity of the asthenosphere and a decrease in the thickness of the asthenosphere produce a result more closely resembling that of a model with a uniform halfspace. Figure 5.3.10 shows the effect of a lateral variation in the thickness of the low viscosity layer on the horizontal displacement. Similarly to the models with a lateral variation in viscosity, the displacement within the load margin is similar to the displacement observed for the model of constant thickness of 200 km and outside the displacement is similar to that experienced by the model with constant asthenosphere thickness of 100 km.

The response of the vertical displacement is also investigated for these two models. Figure 5.3.11 shows the displacement for a model with a constant low viscosity layer with a thickness of 200 km. This increase in thickness increases the amplitude of the peripheral bulge. Figure 5.3.12 shows the vertical displacement for the model with a lateral variation in the thickness of the asthenosphere, as given in Figure 5.3.4. In this case the displacement within the region of the load appears to be an average of the displacement that results from the models with constant asthenosphere thickness of 200

km and 100 km. However, outside of this region, the displacement is similar to the displacement observed for the model with a constant asthenosphere thickness of 100 km.

Overall, lateral changes in the low viscosity asthenosphere have very little impact on the displacement that results from the loading of these models. In general, the variations in the displacement curves are most significant for shorter time periods. Since it is only the viscosity within the halfspace that is changed, it would be expected that at infinite times the displacement would be the same regardless of the specific viscosity structure within the halfspace.

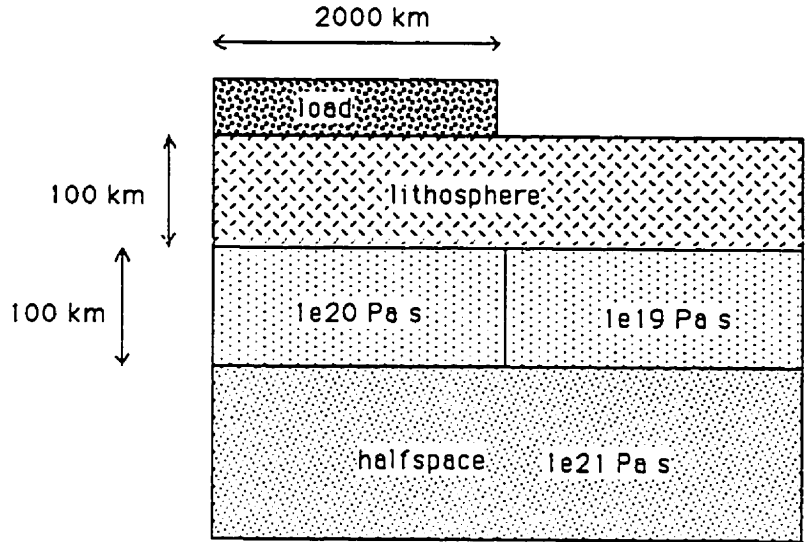


Figure 5.3.3: The earth model of a laterally heterogeneous low viscosity asthenosphere viscosity

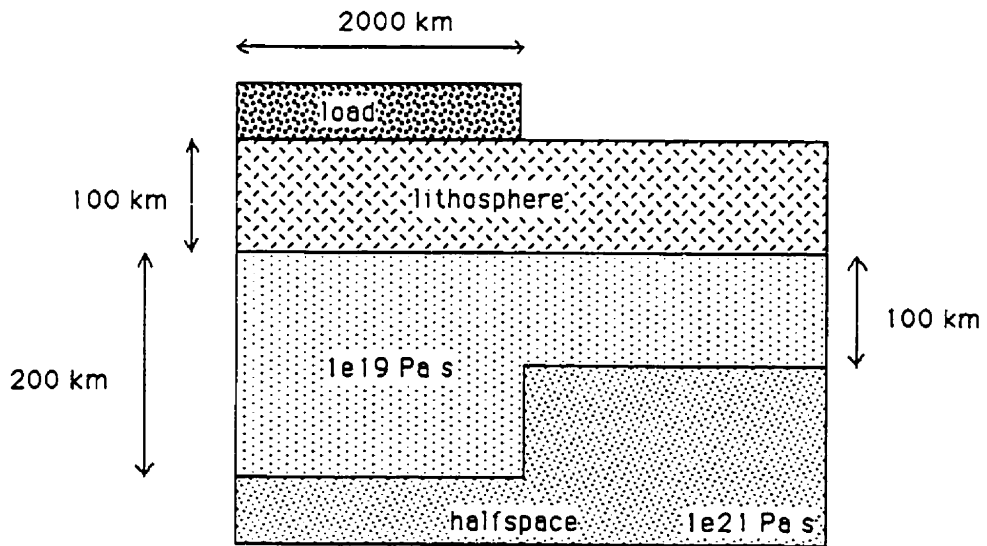


Figure 5.3.4: The earth model of a laterally heterogeneous low viscosity asthenosphere thickness

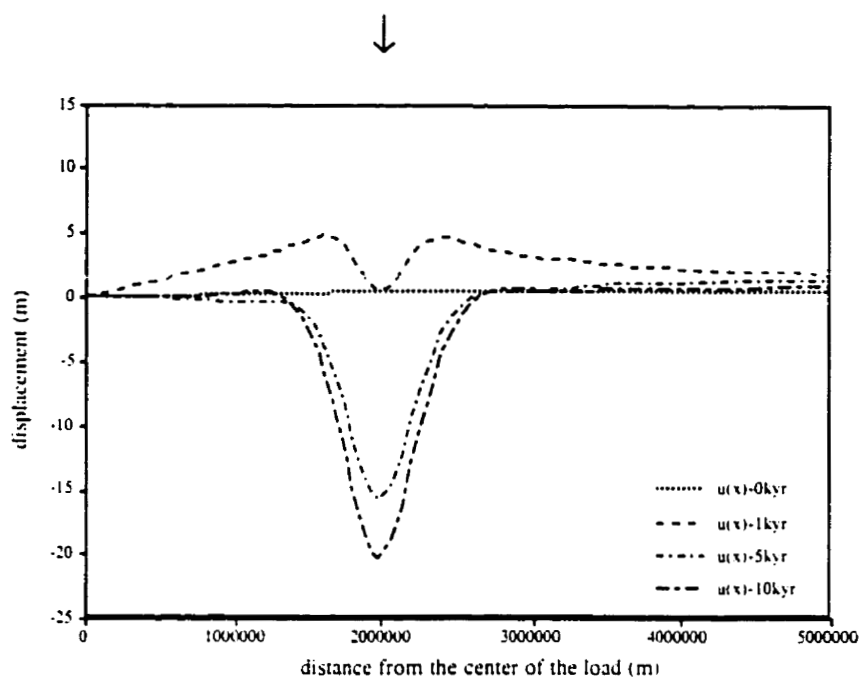


Figure 5.3.5: The horizontal displacement for the low viscosity asthenosphere model with an asthenosphere viscosity of 1×10^{20} Pa s

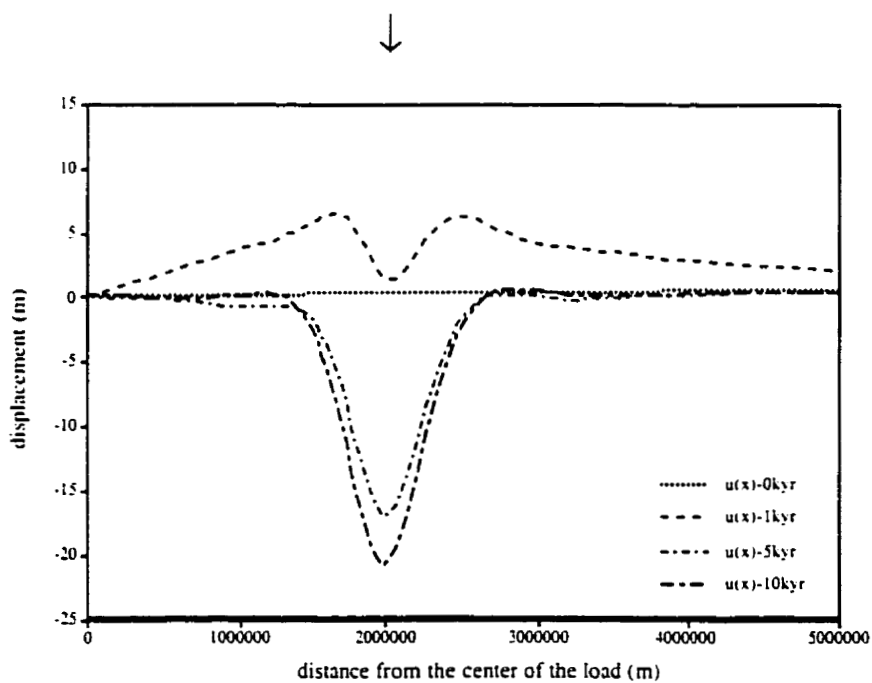


Figure 5.3.6: The horizontal displacement for the model in Figure 5.3.3

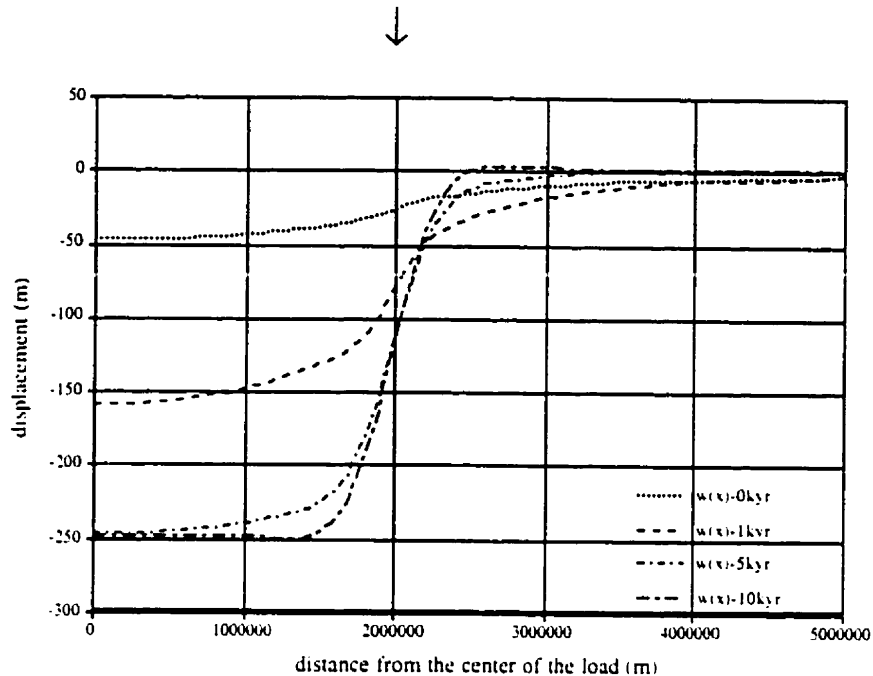


Figure 5.3.7: The vertical displacement for the low viscosity asthenosphere model with an asthenosphere viscosity of 1×10^{20} Pa s

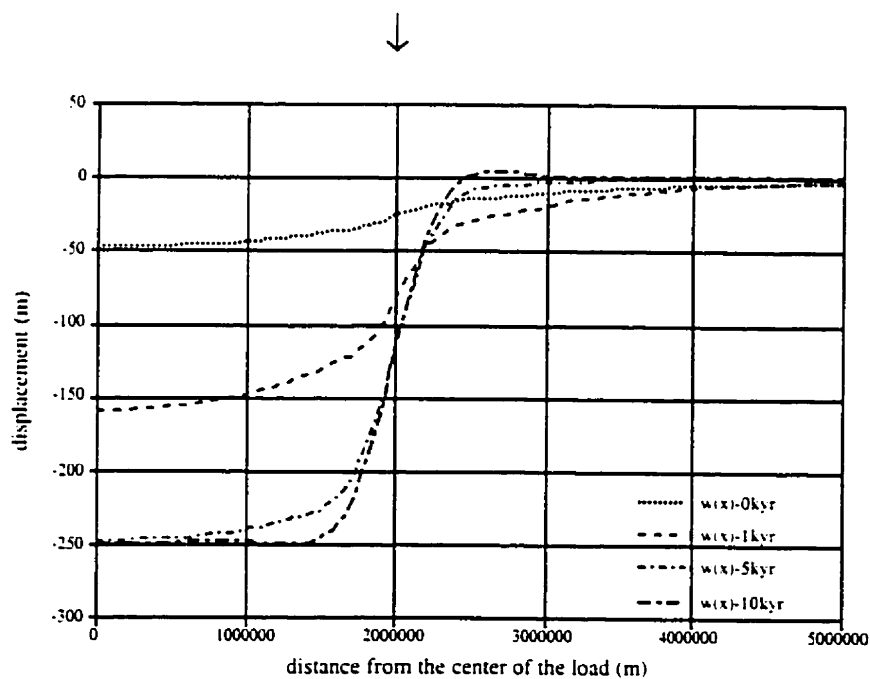


Figure 5.3.8: The vertical displacement for the model in Figure 5.3.3

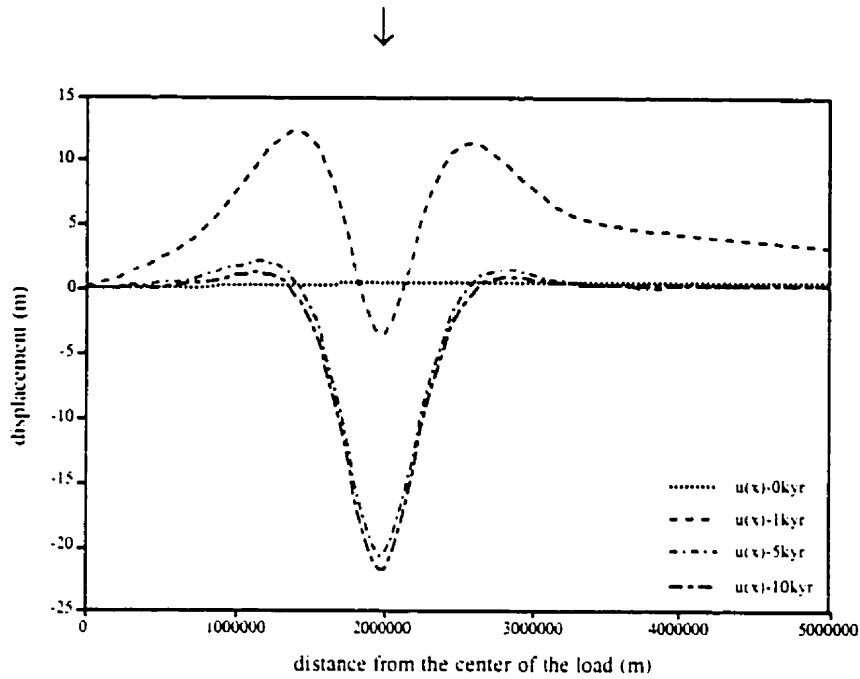


Figure 5.3.9: The horizontal displacement for the low viscosity asthenosphere model with a 200 km thick asthenosphere

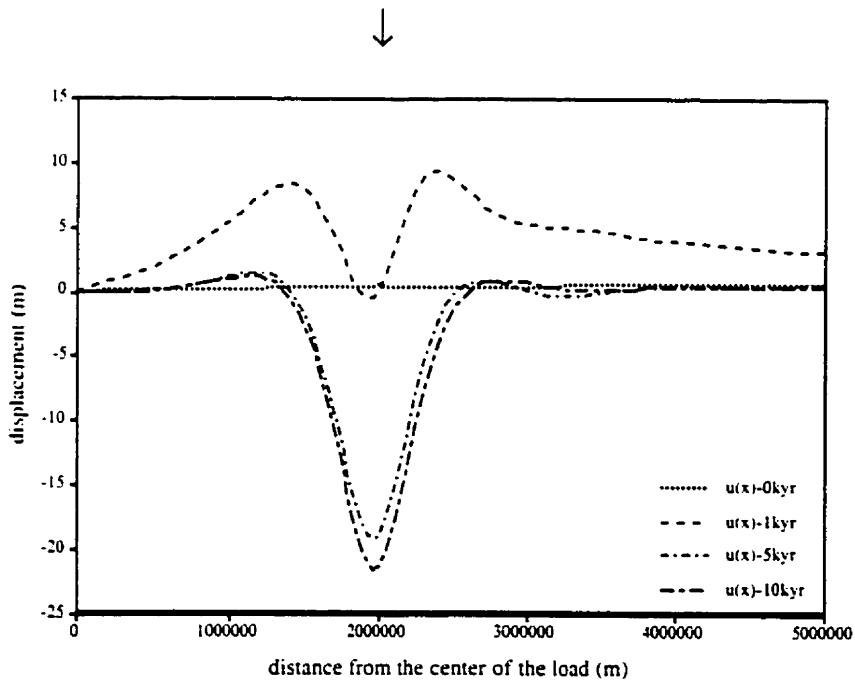


Figure 5.3.10: The horizontal displacement for the model in Figure 5.3.4

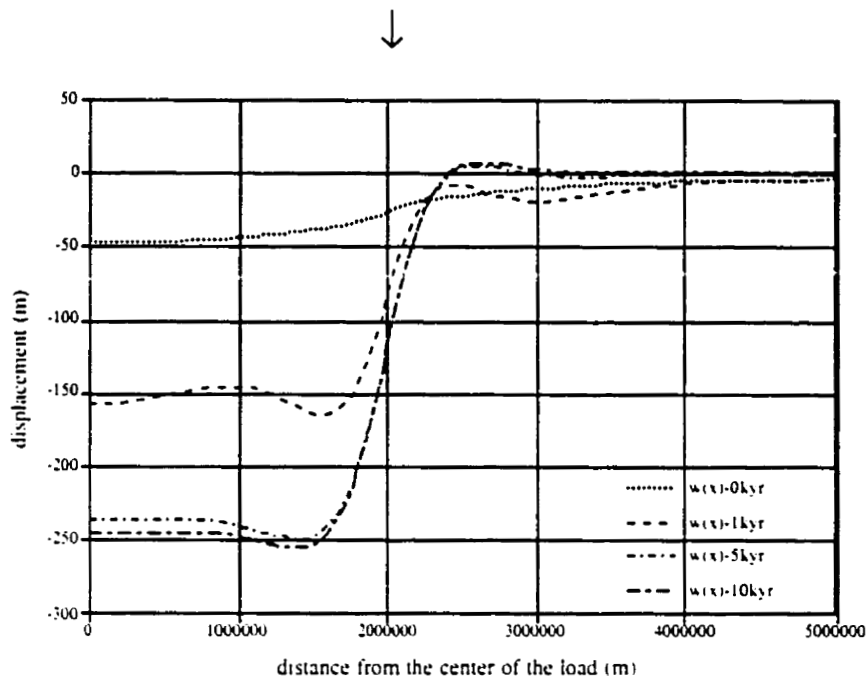


Figure 5.3.11: The vertical displacement for the low viscosity asthenosphere model with a 200 km thick asthenosphere

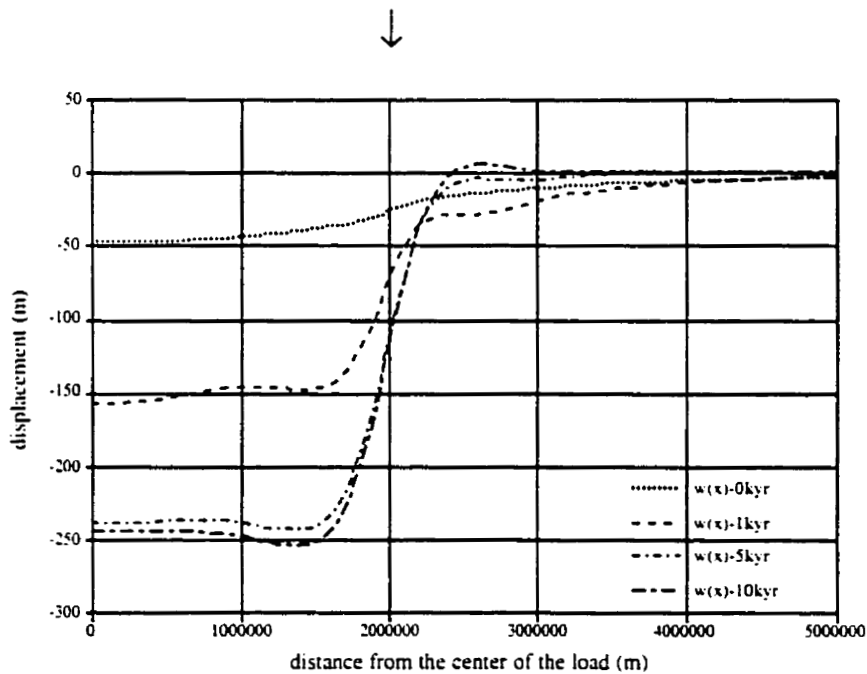


Figure 5.3.12: The vertical displacement for the model in Figure 5.3.4

5.4: Non-Linear Rheology

In all of the models discussed so far it has always been assumed that the rheology of the earth could be explained by a linear relationship between the stress and the rate of strain; see Appendix B for the constitutive relations used. However, it has been proposed that the rheology of the Earth may in fact follow a non-linear relationship between the stress and the strain rate. One of the most commonly used forms of this non-linearity is the power law relationship. This can be written as (Ranalli, 1987)

$$\frac{de}{dt} = A\sigma^n. \quad (5.4.1)$$

where e is the strain.

σ is the stress.

A is a constant determined by temperature, activation energy and volume.

and n is a constant greater than 1.

In the case where a linear rheology is assumed the value of the constant A is well known and it is related to the viscosity. However, in non-linear cases the viscosity is actually a function of the stress and so the constant A must be determined experimentally. In a recent paper by Wu (1999) various cases were studied. The results were compared with vertical motion data from the East Coast of North America. It was determined that the best fit to the data was obtained for a model comprised of an elastic lithosphere and a non-linear lower mantle with $n = 3$ and $A = 3 \times 10^{-35} \text{ Pa}^{-3} \text{ s}^{-1}$. Since only the vertical

displacement was investigated, this section will discuss the horizontal displacement that results from some of these non-linear models.

Several different models will be investigated so that the horizontal displacement can be characterized for models with a non-linear rheology. All of the results will be compared with the results obtained for a similar linear model defined by the parameters given in Table 9. This will help to illustrate the effect of the non-linearity. These values are chosen to agree with the values used by Wu (1999).

Table 9: The Material Properties of the Lithosphere Model for Comparison with Nonlinear Rheology Models

	<u>halfspace, below 150 km</u>	<u>lithosphere, above 150 km</u>
density	$\rho = 3888 \text{ kg m}^{-3}$	$\rho = 3475 \text{ kg m}^{-3}$
gravitational acceleration	$g = 7.365 \text{ m s}^{-2}$	$g = 7.365 \text{ m s}^{-2}$
viscosity	$\nu = 1 \times 10^{21} \text{ Pa s}$	$\nu \rightarrow \infty$
shear modulus	$\mu = 2.203 \times 10^{11} \text{ N m}^{-2}$	$\mu = 0.64 \times 10^{11} \text{ N m}^{-2}$
radius of load		$R = 2 \times 10^6 \text{ m}$
load		$\sigma = 1 \times 10^7 \text{ Pa}$

Several different types of models are investigated to determine the effect of nonlinearity. The first model has a nonlinear halfspace. This is followed by two different models with nonlinear zones in the upper mantle, and these are followed by two models with a nonlinear lower mantle. Refer to Figure 5.4.1 for an illustration of the four multi-layered models; the model with a nonlinear halfspace is not shown. For the all of the nonlinear

layers the following values were used: $n = 3$ and $A = 3.33 \times 10^{-35} \text{ Pa}^{-3} \text{ s}^{-1}$. The material parameters of each of these different models is given in Table 10. Only those properties that are different from the basic halfspace model are shown. Note that the shear moduli and densities are chosen to reflect the actual values at a specific depth.

Table 10: The Material Properties of the Models with Nonlinear Rheology

	<u>nonlinear</u> <u>zone-300 km</u>	<u>nonlinear</u> <u>zone-420 km</u>	<u>nonlinear</u> <u>lower mantle:</u> <u>upper mantle</u>	<u>with low</u> <u>viscosity</u> <u>layer</u>
density (kg m^{-3})	3475	3475	3546	3546
viscosity (Pa s)	nonlinear	nonlinear	1×10^{21}	1×10^{20}
shear modulus (N m^{-2})	7.20×10^{10}	7.20×10^{10}	9.03×10^{10}	9.03×10^{10}

The results for the model with a linear halfspace and an elastic lithosphere, as described by Table 9, are given in Figures 5.4.2 and 5.4.3. These will be used as the reference figures. Figures 5.4.4 and 5.4.5 show the vertical and horizontal displacement results for a model with a nonlinear halfspace and an elastic lithosphere. The magnitude of the vertical displacement diminishes and the magnitude of the horizontal displacement curves are predominantly positive. The horizontal displacement resembles the results of the channel model (Figure 5.1.3). The peripheral bulge is not evident in the vertical displacement, the minimum horizontal displacement is experienced at the edge of the load, and the maximum horizontal displacement is displaced away from the load.

Next, there are four figures which show the response to models with nonlinear zones beneath the elastic lithosphere (earth models given in Figures 5.4.1a and 5.4.1b), as shown in Figures 5.4.6, 5.4.7, 5.4.8, and 5.4.9. The results are very similar to the results of the lithosphere model. With an increase in the thickness of this nonlinear zone, the horizontal displacement experiences a slight increase in areas where there is positive displacement and the vertical displacement experiences a reduction in the magnitude of the peripheral bulge.

The next two figures show the results for a model with a nonlinear lower mantle below a linear upper mantle which extends from the base of the lithosphere to a depth of 670 km (see Figure 5.4.1c). Figure 5.4.10 shows that the horizontal displacement responds in a manner similar to that seen with a nonlinear halfspace. The magnitude of the displacement increases and though the shapes of the curves are consistent they are shifted in the positive direction similar to that seen in the results for the model with an entirely nonlinear halfspace. The vertical displacement, as shown in Figure 5.4.11, however, maintains the peripheral bulge which is not evident in the displacement curves of the model with a nonlinear halfspace. The addition of a low viscosity asthenosphere between the lithosphere and the nonlinear halfspace (see Figure 5.4.1d) increases the magnitude of both the horizontal and vertical displacements, as expected. This is demonstrated in Figures 5.4.12 and 5.4.13.

The study by Wu (1999) showed that a model with a nonlinear lower mantle had the best fit to the vertical displacement data. The horizontal displacement for this model is very distinct. The maximum displacement is predicted to occur on either side of the edge of the load and this displacement is predicted to be positive after the load has been emplaced. This implies that the displacement after the load is removed would be in a

negative direction, towards the center of the load. Since models with nonlinear lower mantles predict a different direction for the horizontal displacement, these types of earth models should be relatively easy to determine from data.

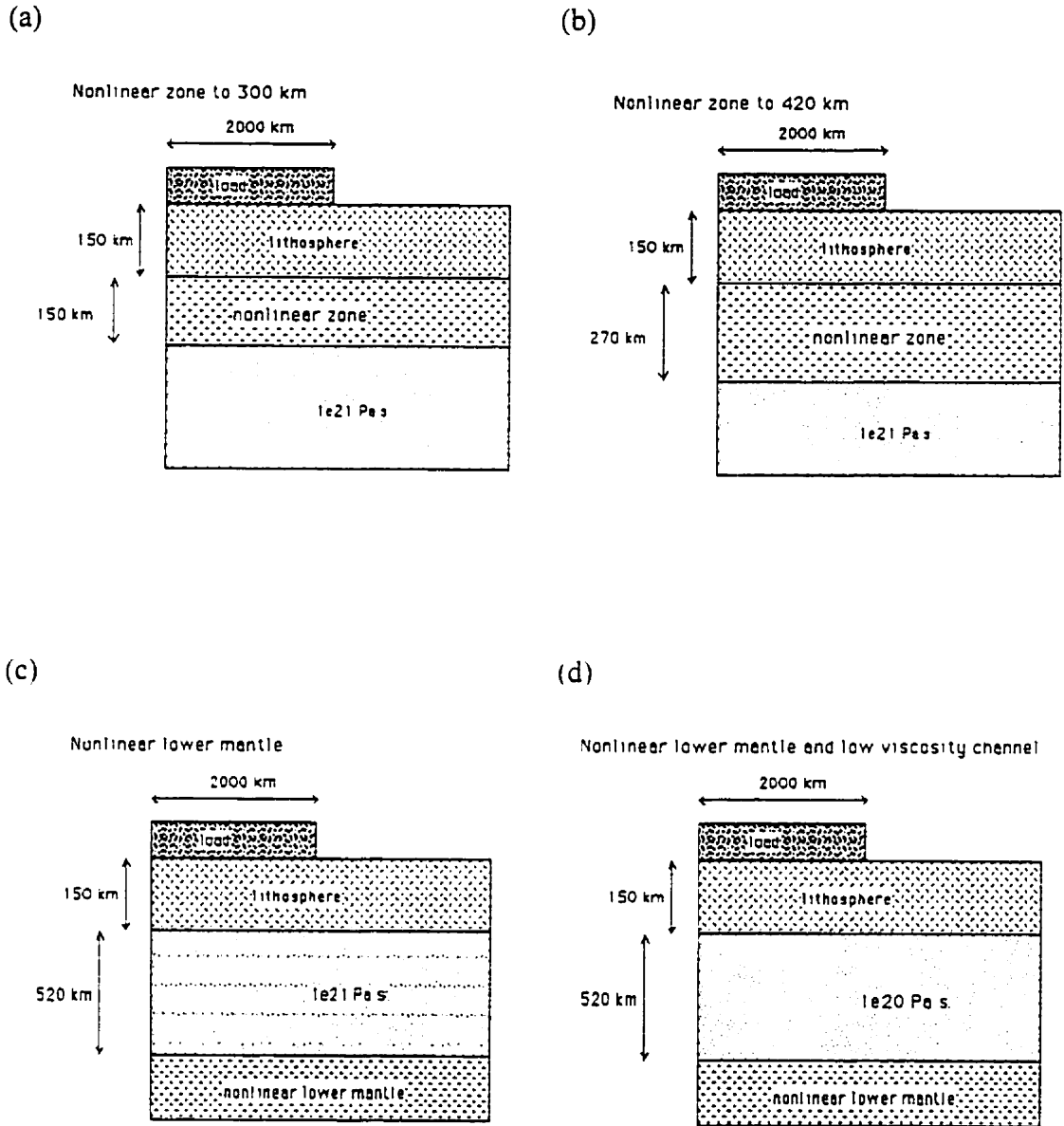


Figure 5.4.1: The earth models with nonlinear zones

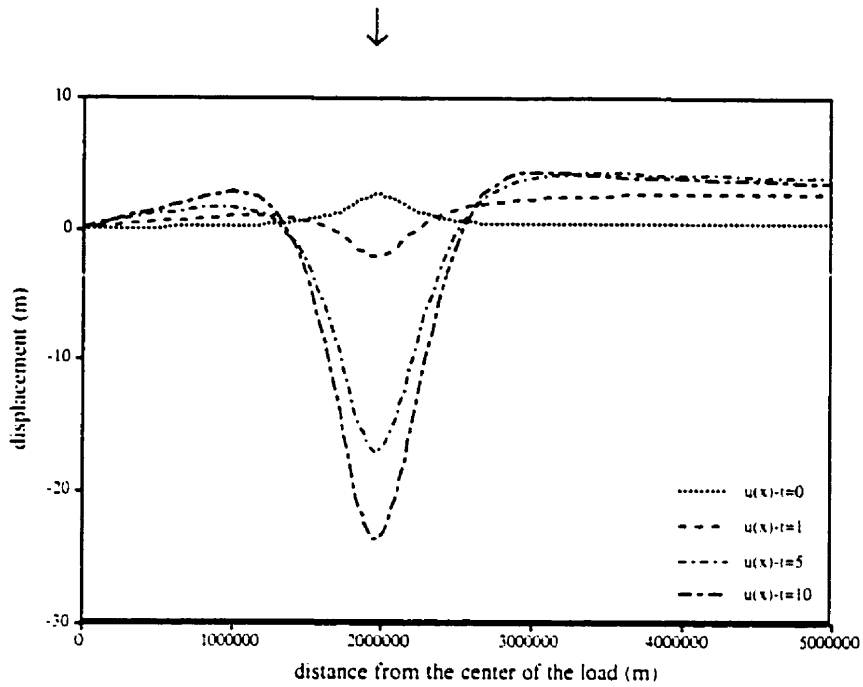


Figure 5.4.2: The horizontal displacement for the lithosphere model with linear rheology

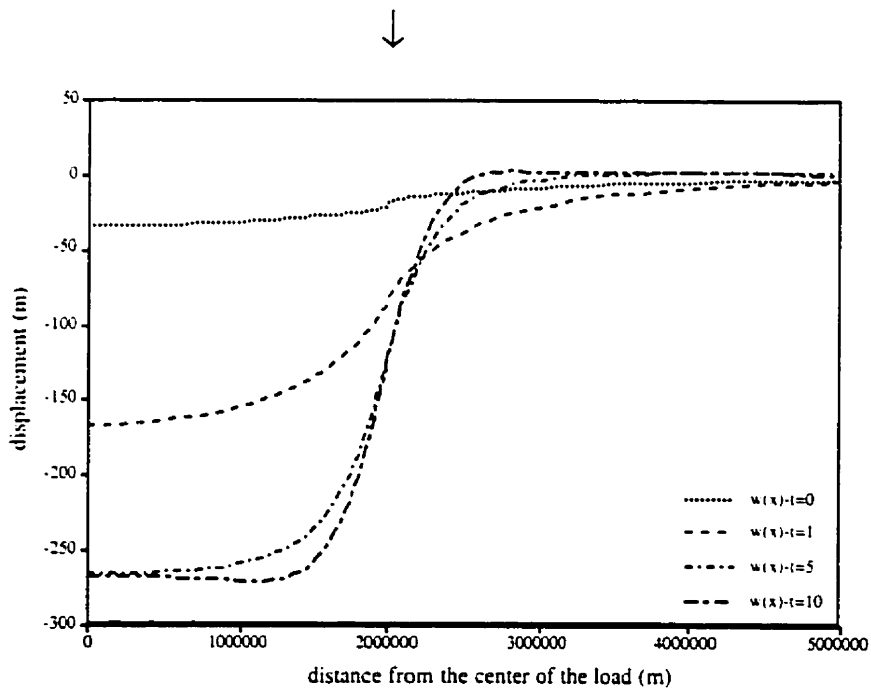


Figure 5.4.3: The vertical displacement for the lithosphere model with linear rheology

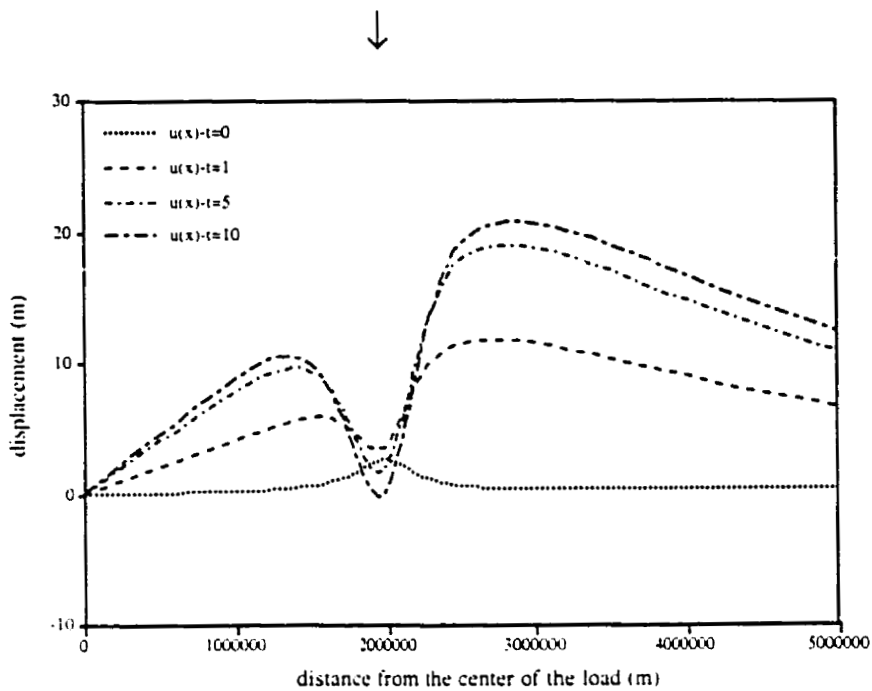


Figure 5.4.4: The horizontal displacement for the nonlinear halfspace model

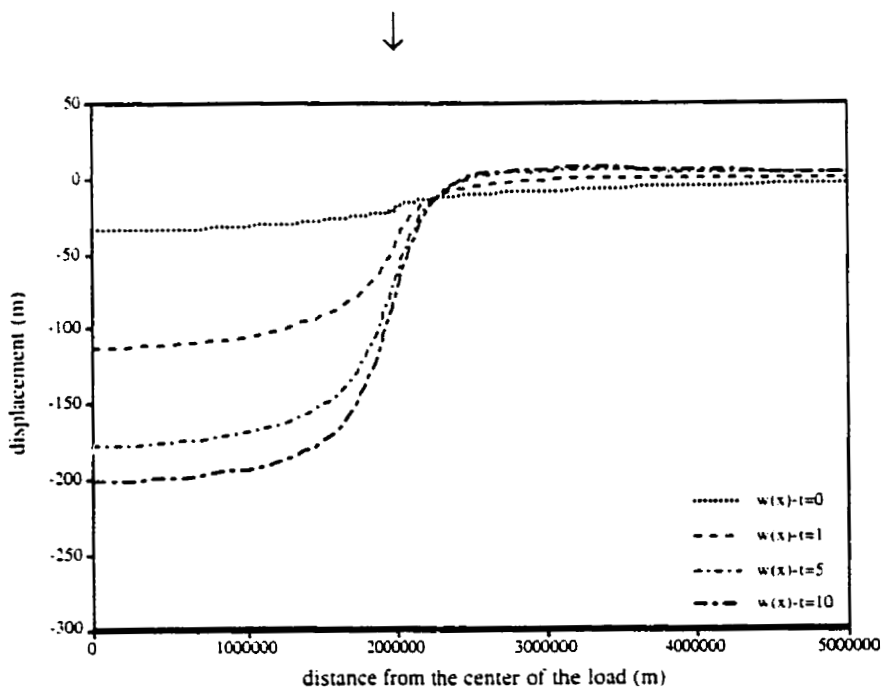


Figure 5.4.5: The vertical displacement for the nonlinear halfspace model

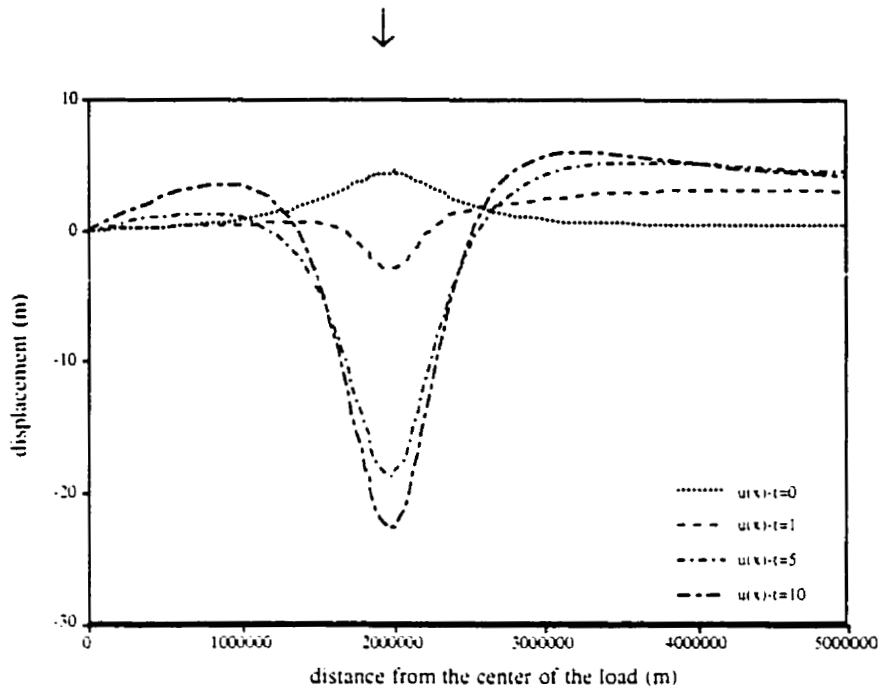


Figure 5.4.6: The horizontal displacement for the model in Figure 5.4.1a

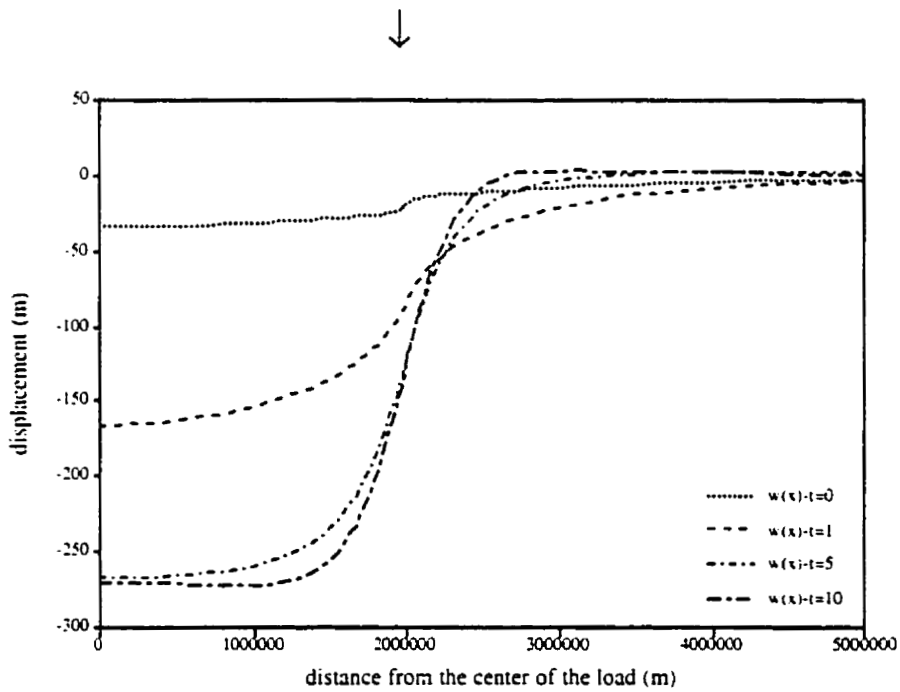


Figure 5.4.7: The vertical displacement for the model in Figure 5.4.1a

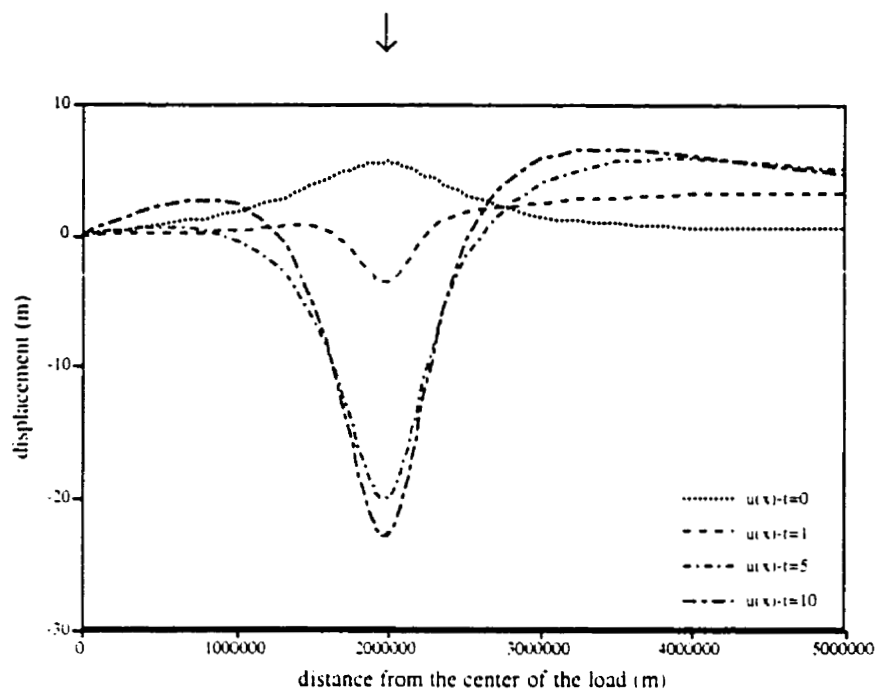


Figure 5.4.8: The horizontal displacement for the model in Figure 5.4.1b

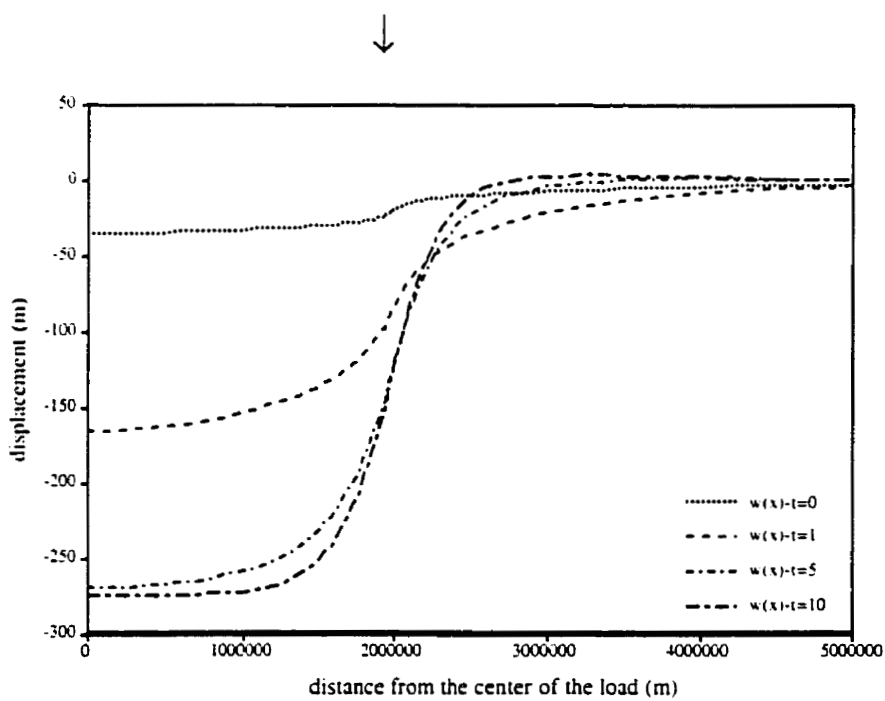


Figure 5.4.9: The vertical displacement for the model in Figure 5.4.1b

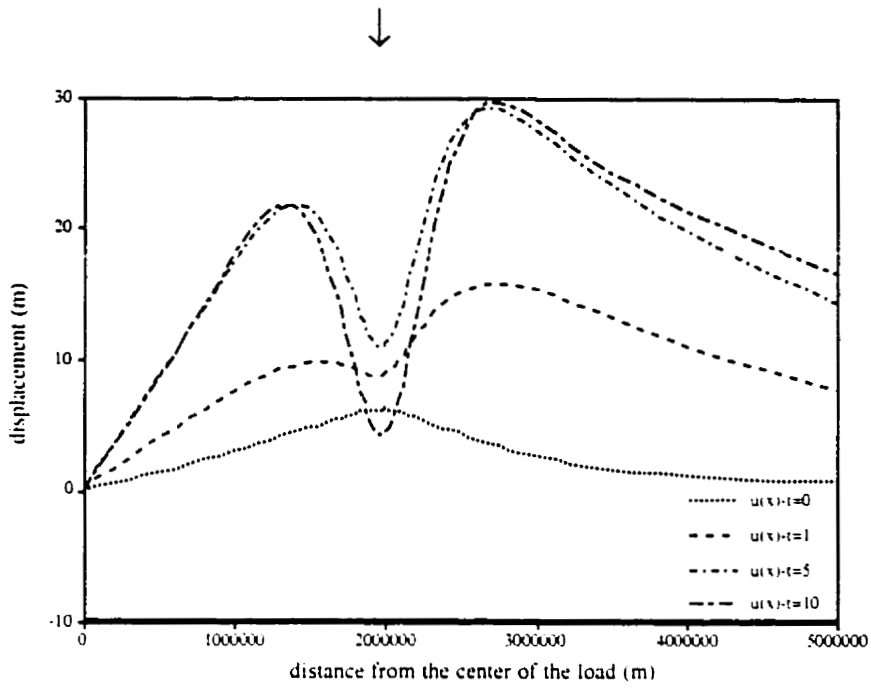


Figure 5.4.10: The horizontal displacement for the model in Figure 5.4.1c

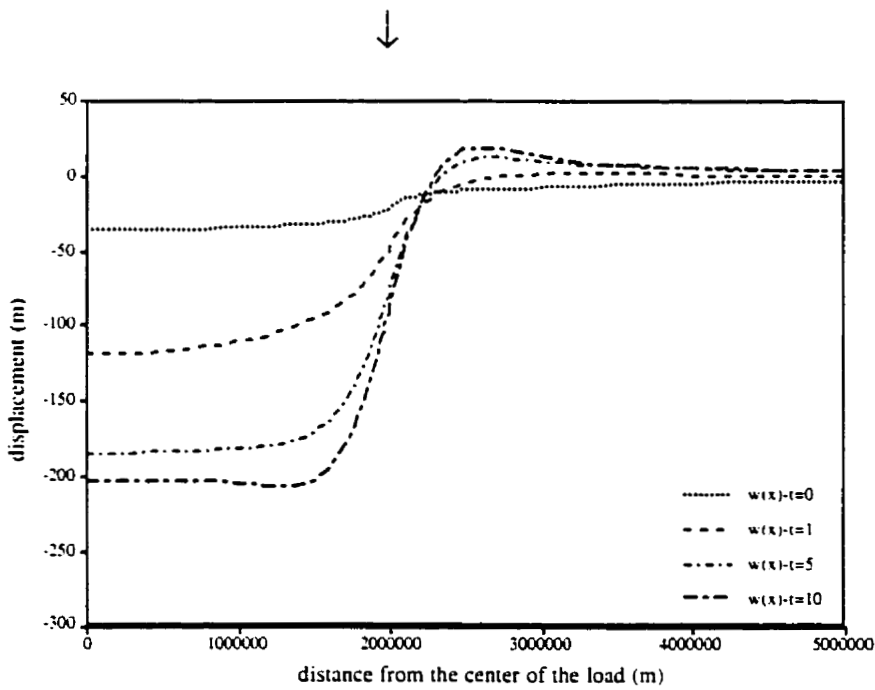


Figure 5.4.11: The vertical displacement for the model in Figure 5.4.1c

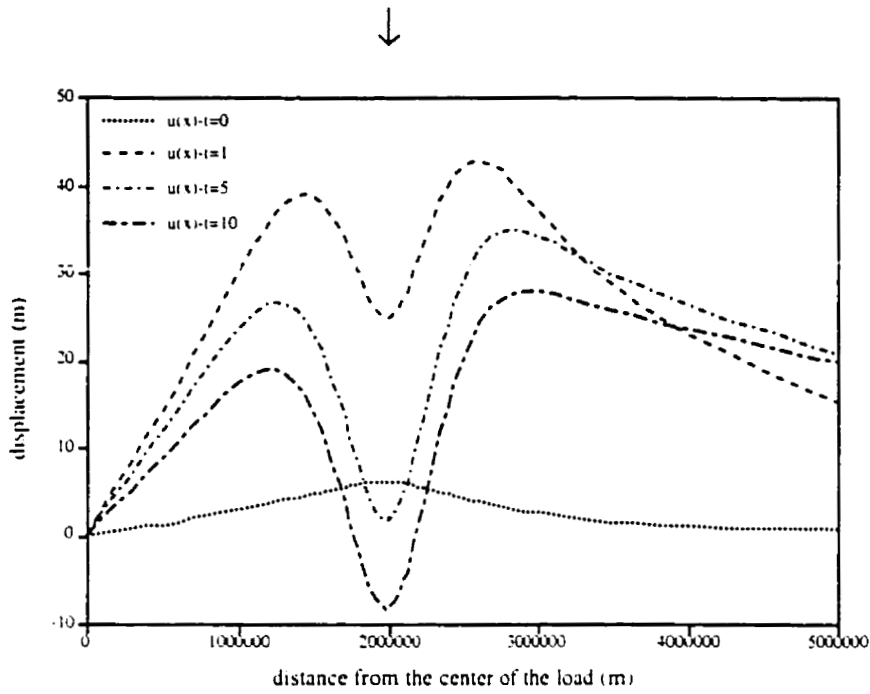


Figure 5.4.12: The horizontal displacement for the model in Figure 5.4.1d

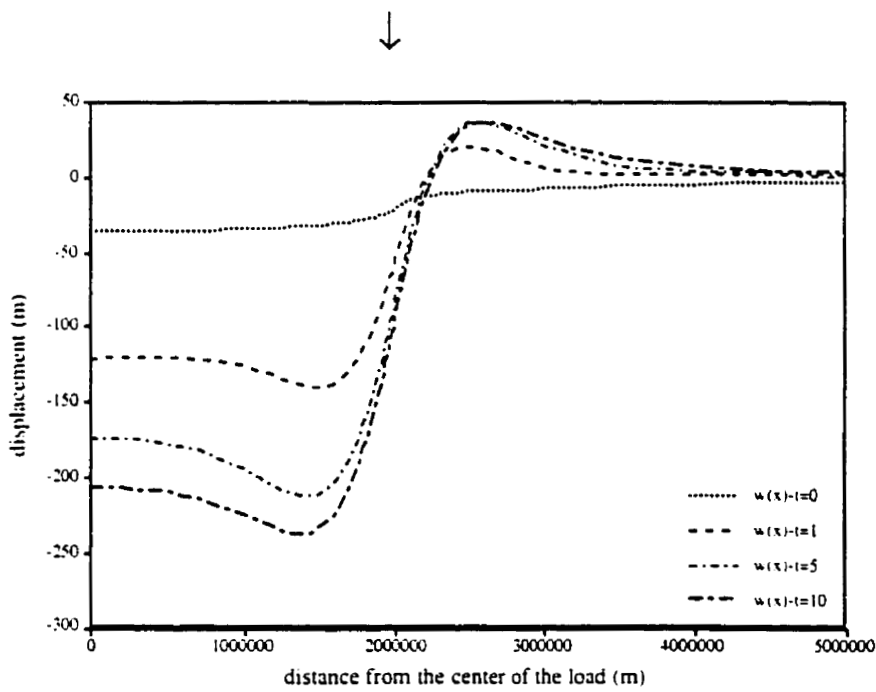


Figure 5.4.13: The vertical displacement for the model in Figure 5.4.1d

5.5: Time Dependent Creep

Another assumption in all of the models discussed so far is that there are no time dependent effects. It is assumed that the deformation is either an elastic deformation or viscous steady-state creep. However, there could be some sort of time dependent creep. The strain produced by these three components can be expressed as (Ranalli, 1987)

$$e(t) = e_e + e_i(t) + \dot{\epsilon}t$$

where e_e is the elastic strain,

e_i is the time dependent creep.

and $\dot{\epsilon}$ is the steady state strain rate.

A simple transient creep law is the Andrade-type time dependence, given by

$$e_i(t) = A\sigma^r t^{\frac{1}{r}}, \quad \text{where } r > 1.$$

In ABAQUS, this is expressed as

$$\frac{de}{dt} = A\sigma^m, \quad \text{where } m \leq 0.$$

Several values of m are tested to determine the effect of time dependent creep on the displacement that results from the loading of an elastic lithosphere overlying a viscoelastic halfspace. In all of these models the thickness of the lithosphere is 150 km and the

viscosity of the halfspace is 1×10^{21} Pa s. The material parameters are given in Table 9 in section 5.4. The halfspace is modeled with the time dependent creep.

Figures 5.5.1 and 5.5.2 show the horizontal and vertical displacements that result from a model with time dependent creep with $m = -0.05$. These results are similar to the results observed for a simple increase in the viscosity of the halfspace below the lithosphere (Figure 3.4.2). For very small values of m , the viscous displacement is reduced even further and only the initial elastic displacement is observed, as shown in Figures 5.5.3 and 5.5.4. Since even for very large values of m there is no peripheral bulge observed in the vertical displacement, this type of time dependent creep model does not seem appropriate.

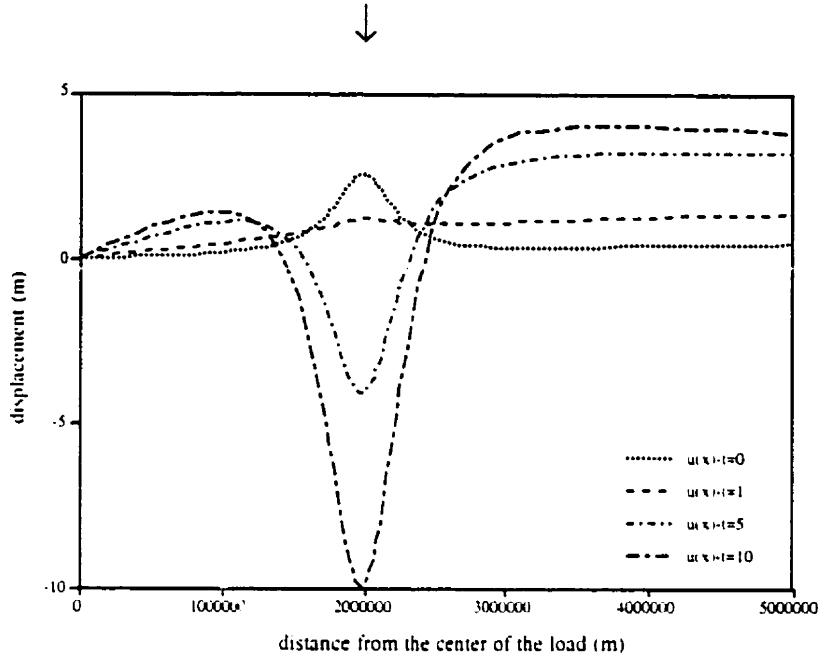


Figure 5.5.1: The horizontal displacement for a time dependent creep model with $m = -0.05$ in the mantle

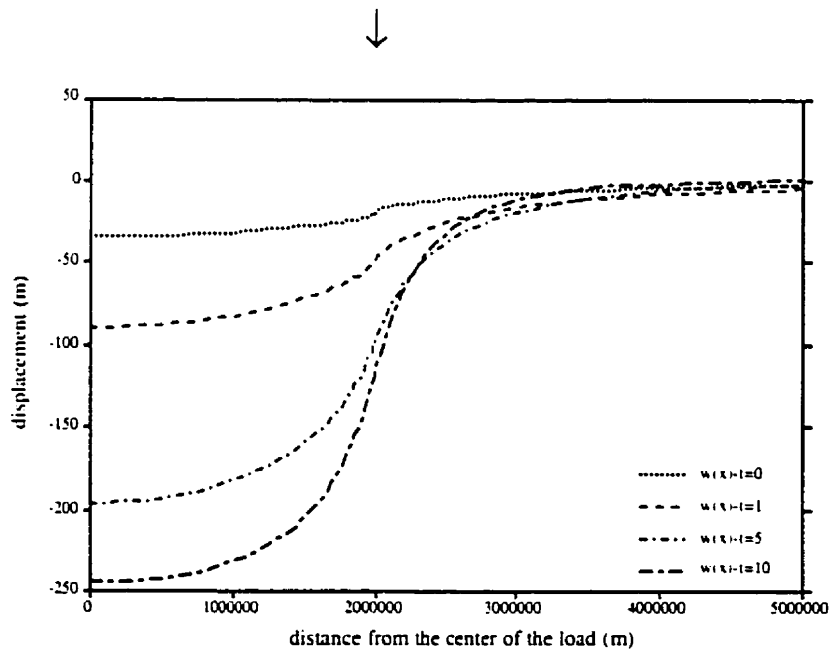


Figure 5.5.2: The vertical displacement for a time dependent creep model with $m = -0.05$ in the mantle

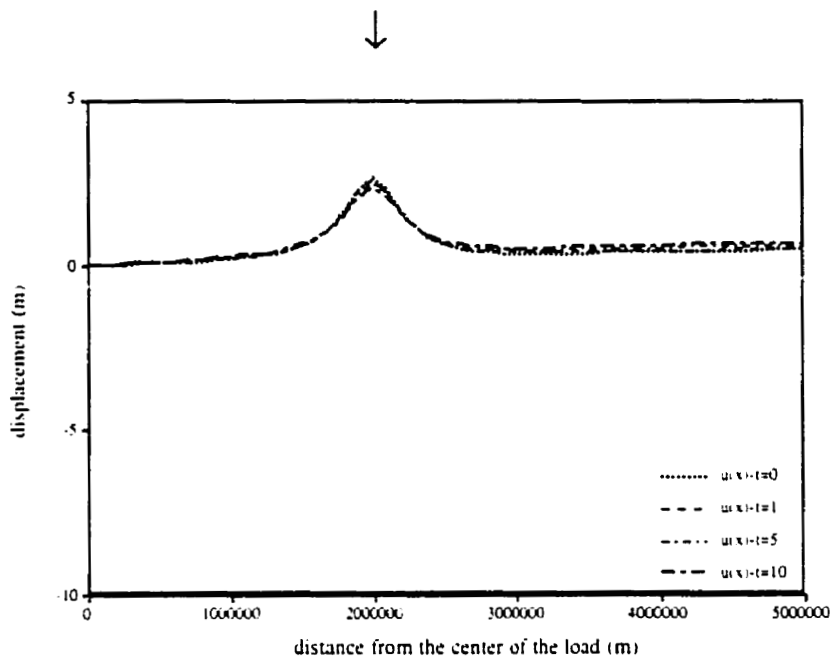


Figure 5.5.3: The horizontal displacement for a time dependent creep model with $m = -0.2$ in the mantle

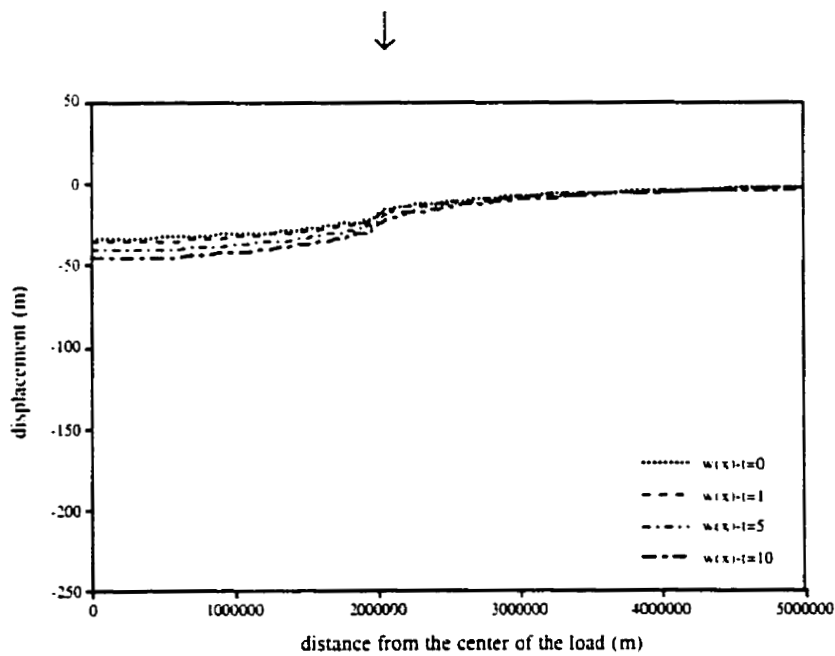


Figure 5.5.4: The vertical displacement for a time dependent creep model with $m = -0.2$ in the mantle

Chapter 6: Conclusions

In this thesis, the horizontal and vertical displacements that result from the loading of simple earth models were analyzed using three different techniques. The first method was to investigate the analytical solutions for the model of a halfspace, a channel and a lithosphere over a fluid. The second was to investigate the solution in the wavenumber domain through the use of relaxation and excitation strength diagrams so that the importance of various transitions could be determined. The final technique was to use ABAQUS, a finite element modeling package, to model the space and time domain displacements for more detailed models including models with nonlinear rheology, lateral variations and time dependent creep.

One of the most important elements of this thesis was the validation of the ABAQUS modeling program. The detailed analytical calculations of the solutions for three simple models were compared with the results from ABAQUS. The results compared favorably for all three models. The only case where ABAQUS failed to produce accurate displacements was in the horizontal displacement for the halfspace model.

In addition, the relaxation and excitation strength diagrams were determined for various models so that a systematic analysis of the horizontal displacement excitation strength could be undertaken. These diagrams demonstrate the impact on the relaxation times and viscous motions for models with different densities, shear moduli and layer thicknesses. The analysis of the model with an elastic lithosphere showed that the lithosphere is a very important component in a model, especially in terms of the horizontal displacement. In terms of the effect on the relaxation times and the excitation strengths the thickness of the lithosphere is the most important aspect. Simple two layer models with a density

variation show that density variations have a significant impact on the horizontal displacement. This is due to the fact that in these models the M0 mode of relaxation has a negative excitation strength for all wavenumbers. These models have a second mode of relaxation caused by the density discontinuity which resembles the relaxation curve of the channel model. Models with a discontinuity in the shear modulus have the same effect on the horizontal displacement excitation strength and there is the addition of a third mode of relaxation. For models with a discontinuity in either density or shear modulus the M0 mode of relaxation is virtually unchanged by the presence of the discontinuity in both the relaxation diagram and the vertical displacement excitation strengths. This is also seen in the results of the low viscosity channel model. The low viscosity channel model produces figures which are an amalgamation of the figures for the lithosphere model and the model with a shear modulus discontinuity.

The third objective of this thesis was to analyze the space domain solutions to determine the effect of lateral variations, nonlinear rheology and time dependent creep on the displacements that results from loading. It was found that the magnitude of the horizontal displacement is very sensitive to the thickness of the lithosphere and it decreases significantly with a decrease in lithospheric thickness. If the measured horizontal motion is quite large, a thicker lithosphere is favored. The horizontal displacement is also shown to be more sensitive to lateral variations than the vertical displacement. Also, radial variations in viscosity result in variations in the magnitude of the horizontal displacement, not just in the relative shape of the displacement curves as with the vertical displacement. Compared to precise displacement curves, magnitudes are more easily measured and less sensitive to the ice history. Therefore horizontal motions can be used as an important diagnostic tool to determine the lateral and radial characteristics of the subsurface. In general, most of the curves for the horizontal

displacement experience a displacement of approximately 30 meters over ten thousand years. This corresponds to an average speed of 3 mm per year.

The effect of the low viscosity channel is most readily apparent in the curves of the vertical displacement. The presence of the layer modifies the early viscous relaxation of the horizontal displacement and it magnifies the magnitude of the peripheral bulge of the vertical displacement and allows this peripheral bulge to persist over time.

The horizontal displacement that results from loading models with a nonlinear halfspace or nonlinear lower mantle is quite distinct, while a nonlinear zone seems to have little effect. Models with a nonlinear lower mantle give results similar to models with a nonlinear halfspace except that the peripheral bulge is preserved in the vertical displacement curves. The horizontal displacement is predominantly positive for both of these types of models. These are the only models for which a positive horizontal displacement is obtained except for the channel model.

When the effect of time dependent creep is incorporated into the system, the results for both the horizontal and vertical displacements are similar to those obtained from a simple increase in halfspace viscosity. The magnitudes of the displacements diminish and the peripheral bulge is suppressed. Since this does not agree with the measurements, this type of model does not seem to be a viable option for an accurate earth model.

Now that a detailed study of the horizontal displacement has been conducted and the results of the ABAQUS program have been shown to be consistent with the analytical solutions the next step is to obtain data for the region of Fennoscandia, which can be accurately modeled by a flat earth, and determine a possible earth model by combining

the data for the horizontal and vertical displacements. It would also be interesting to determine if and how the flat earth assumption affects the results. A further consideration when using a spherical earth model would be to include the effect of compressibility since this would more closely reflect the true characteristics of the earth.

Once more detailed data for the horizontal motions of the Earth's surface are obtained then the results from seismic tomography and the existing subsurface models determined from the vertical motions can be used to determine an even more detailed subsurface model. Not only will these detailed earth models be used to constrain tectonic and mantle convection models, but this will also allow for more accurate predictions of the motion of the crust. These predictions can be used to calibrate shifts in the locations of the stationary GPS base stations. Currently the positions of the base stations are recalibrated every few years however if a detailed glacial isostatic adjustment model is developed, then the base station positions could be accurately predicted without the need for recalibration.

References

- Anderson, Robert F. V., *Introduction to Linear Algebra*, Holt, Rinehart and Winston of Canada, Limited, New York, 1986.
- Boyce, William E. and Richard C. DiPrima, *Elementary Differential Equations and Boundary Value Problems*, John Wiley and Sons, Inc., New York, 1986.
- Cathles, Lawrence M., *The Viscosity of the Earth's Mantle*, Princeton University Press, Princeton, 1975.
- Chave, Alan D., Numerical Integration of related Hankel transforms by quadrature and continued fraction expansion. *Geophysics*, vol. 48, no. 12, pp. 1671-1686, 1983.
- D'Agostino, G., G. Spada and R. Sabadini, Postglacial rebound and lateral viscosity variations: a semi-analytical approach based on a spherical model with Maxwell rheology. *Geophysical Journal International*, vol. 129, pp. F9-F13, 1997.
- Farrell, W. E., Deformation of the Earth by Surface Loads. *Reviews of Geophysics and Space Physics*, vol. 10, no. 3, pp. 761-797, 1972.
- Giunchi, C., G. Spada and R. Sabadini, Lateral viscosity variations and post-glacial rebound: effects on present-day VLBI baseline deformations. *Geophysical Research Letters*, vol. 24, no. 1, pp. 13-19, 1997.
- Hibbitt, Karlsson and Sorensen, Inc., *ABAQUS*, Hibbitt, Karlsson and Sorensen, Inc., 1992.
- Hoffner, N. Scott, *Waterloo Maple Mathview™ User's Guide*, Waterloo Maple Inc., Waterloo, 1997.
- James, T. J. and A. Lambert, A comparison of VLBI data with the ICE-3G glacial rebound model, *Geophysical Research Letters*, vol. 20, no. 9, pp. 871-874, 1993.
- James, T. S. and W. J. Morgan, Horizontal motions due to post-glacial rebound. *Geophysical Research Letters*, vol. 17, no. 7, pp. 957-960, 1990.

- Kaufmann, G., P. Wu and D. Wolf, Some effects of lateral heterogeneities in the upper mantle on postglacial land uplift close to continental margins, *Geophysical Journal International*, vol. 128, pp. 175-187, 1997.
- Li, Xiang-Dong and Barbara Romanowicz. Global mantle shear velocity model developed using nonlinear asymptotic coupling theory, *Journal of Geophysical Research*, vol. 101, no. B10, pp. 22,245-22,272, 1996.
- Love, A. E. H., *Some Problems of Geodynamics*, Dover, New York, 1911.
- Malvern, L. E., *Introduction to the Mechanics of a Continuous Medium*, Prentice-Hall, Englewood Cliffs, 1969.
- Manga, M. and R. J. O'Connell. The tectonosphere and postglacial rebound, *Geophysical Research Letters*, vol. 22, no. 15, pp. 1949-1952, 1995.
- Marsden, Jerrold E., *Basic Complex Analysis*, W. H. Freeman and Company, San Francisco, 1973.
- Mase, George E., *Schaum's Outline of Theory and Problems of Continuum Mechanics*, McGraw Hill Inc., New York, 1970.
- Mitrovica, J. X., J. L. Davis and I. I. Shapiro. A spectral formalism for computing three-dimensional deformations due to surface loads 2. Present-day glacial isostatic adjustment, *Journal of Geophysical Research*, vol. 99, no. B4, pp. 7075-7101, 1994.
- Part-Enander, Eva, Anders Sjöberg, Bo Melin, and Pernilla Isaksson, *The MATLAB Handbook*, Addison-Wesley, New York, 1996.
- Peltier, W. R., The impulse response of a Maxwell earth, *Review of Geophysical and Space Physics*, vol. 12, pp. 649-669, 1974.
- Peltier, W. R., Glacial isostatic adjustment - II. The inverse problem, *Geophysical Journal of the Royal Astronomical Society*, vol. 46, pp. 669-705, 1976.

- Press, William H., Brian P. Flannery, Saul A. Teukolsky, and William T. Vetterling, *Numerical Recipes: The Art of Scientific Computing*, Cambridge University Press, Cambridge, 1986.
- Ranalli, Giorgio, *Rheology of the Earth: Deformation and flow processes in geophysics and geodynamics*, Allen and Unwin Incorporated, Boston, 1987.
- Stacey, Frank D., *Physics of the Earth*, Brookfield Press, Brisbane, 1992.
- Tranter, C. J., *Bessel Functions with Some Physical Applications*, Hart Publishing Company, Inc., New York, 1968.
- Turcotte, Donald L., and Gerald Schubert, *Geodynamics: Applications of Continuum Physics to Geological Problems*, John Wiley and Sons, New York, 1982.
- Tushingham, A. M. and W. R. Peltier, ICE-3G: A new global model of late Pleistocene deglaciation based upon geophysical predictions of postglacial relative sea level change, *Journal of Geophysical Research*, vol. 96, pp. 4497-4523, 1991.
- Wolf, Detlef, The normal modes of a layered, incompressible Maxwell halfspace, *Journal of Geophysics*, vol. 57, pp. 106-117, 1985.
- Wu, P., The response of a Maxwell earth to applied surface mass loads: glacial isostatic adjustment, *M.Sc. Thesis*, University of Toronto, Toronto, Ont., 1978.
- Wu, P., Deformation of internal boundaries in a viscoelastic earth and topographic coupling between the mantle and core, *Geophysical Journal International*, vol. 101, pp. 213-231, 1990.
- Wu, Patrick, editor, *Dynamics of the Ice Age Earth: A Modern Perspective*, Trans Tech Publications, Switzerland, 1998.
- Wu, Patrick, Modeling postglacial sea levels with power-law rheology and a realistic ice model in the absence of ambient tectonic stress, *Geophysical Journal International*, vol. 139, pp. 691-702, 1999.

- Wu, Patrick and Zhihong Ni, Some analytical solutions for the viscoelastic gravitational relaxation of a two-layer non-self-gravitating incompressible spherical earth, *Geophysical Journal International*, vol. 126, pp. 413-436, 1996.
- Wu, Patrick and W. R. Peltier, Viscous gravitational relaxation, *Geophysical Journal of the Royal Astronomical Society*, vol. 70, pp. 435-485, 1982.

Appendix A: The Equation of Motion

This appendix demonstrates how the equation of motion is derived from the basic principles of conservation of mass and linear momentum.

1. continuity equation (conservation of mass),

$$\partial_t \rho + \nabla \cdot (\rho \mathbf{v}) = 0 \quad (\text{A.1})$$

where ρ is the density,

and \mathbf{v} is the velocity vector.

2. conservation of linear momentum (body forces equal surface stresses):

$$\int_V \mathbf{F} dV + \int_S \mathbf{T} \cdot d\mathbf{a} = 0 \quad (\text{A.2})$$

where \mathbf{F} is the total body force vector,

and \mathbf{T} is the total surface stress vector.

Using the divergence theorem, we obtain:

$$\nabla \cdot \mathbf{T} + \mathbf{F} = 0 \quad (\text{A.3})$$

3. The total stress, \mathbf{T} , can be expressed as a combination of the perturbational stress, σ , and the hydrostatic (implies pressure, P) initial stress.

$$\mathbf{T} = \sigma - P_0 \mathbf{I} \quad (\text{A.4})$$

The hydrostatic initial stress is a result of the presence of a gravitational field, i.e. in this case self-gravitation. This prestress is carried along (advected) during any deformation.

This initial prestress is constant over time for any individual material element (particle).

$$d_t(P_0) = 0 \quad (\text{A.5})$$

However, there may be a variation in the prestress between different material elements.

From A.5 the prestress at a particular point in space may vary with time.

$$d_t(P_0) = 0 = \partial_t(P_0) + \mathbf{v} \cdot \nabla P_0 \quad (\text{A.6})$$

$$\therefore \partial_t(P_0) = -\mathbf{v} \cdot \nabla P_0 \quad (\text{A.7})$$

$$\text{Therefore } \partial_t(P_0) = P_0|_{t_0 - \delta t} - P_0|_{t_0} = -\int_{t_0}^{t_0 - \delta t} \mathbf{v} \cdot \nabla P_0 \quad (\text{A.8})$$

$$\therefore P_0|_{t_0 - \delta t} = P_0|_{t_0} - \int_{t_0}^{t_0 - \delta t} \mathbf{v} \cdot \nabla P_0 \quad (\text{A.9})$$

Assume that the motion that the material elements undergo is an instantaneous elastic displacement. The forces must balance to include this displacement.

$$\mathbf{v} = \mathbf{u} \delta(t - t_0) \quad (\text{A.10})$$

where \mathbf{v} is the velocity vector,

\mathbf{u} is the displacement vector,

and $\delta(t)$ is the Dirac delta function.

Therefore
$$P_0|_{t_0-\mathcal{G}} = P_0|_{t_0} - \mathbf{u} \cdot \nabla P_0 \quad (\text{A.11})$$

However, the viscous displacements are continuous functions of time so that

$$P_0|_{t_0-\mathcal{G}} = P_0|_{t_0} \quad (\text{A.12})$$

Therefore the equation of motion for an elastic body, so far, is:

$$\nabla \cdot \mathbf{T} + \mathbf{F} = 0 \quad (\text{A.13})$$

$$\nabla \cdot (\boldsymbol{\sigma} - P_0 \mathbf{I}) + \mathbf{F} = 0 \quad (\text{A.14})$$

$$\nabla \cdot \boldsymbol{\sigma} - \nabla P_0|_{t_0-\mathcal{G}} + \mathbf{F} = 0 \quad (\text{A.15})$$

$$\nabla \cdot \boldsymbol{\sigma} - \nabla P_0|_{t_0} + \nabla(\mathbf{u} \cdot \nabla P_0) + \mathbf{F} = 0 \quad (\text{A.16})$$

The equation of motion for a viscous body reduces to

$$\nabla \cdot \boldsymbol{\sigma} - \nabla P_0|_{t_0} + \mathbf{F} = 0 \quad (\text{A.17})$$

4. For a self-gravitating earth where the mass of the earth is large and isolated the gravitational attraction of other parts of the fluid provide the volume force on any individual element.

$$\mathbf{F} = \rho \mathbf{g} = -\rho \nabla \varphi \quad (\text{A.18})$$

$$\text{where } \nabla^2 \varphi = 4\pi G \rho$$

φ is the gravitational potential.

and G is the gravitational constant.

For a flat earth which is non-self-gravitating, the gravitational field is uniform. This is applicable when the mass of fluid concerned is much smaller than any neighbouring matter. In this case the body forces are defined as

$$\mathbf{F} = -\mathbf{g} = \text{constant.} \quad (\text{A.19})$$

5. Assume a zero order state of hydrostatic equilibrium (no motion).

$$\nabla P_0 - \mathbf{F}_0 = 0 \quad (\text{A.20})$$

$$\nabla P_0 + \rho_0 \nabla \varphi_0 = 0 \quad (\text{A.21})$$

6. Assume the perturbations have in the following form:

$$\rho(\mathbf{x}, t) = \rho_0(x_1) + \rho_1(\mathbf{x}, t) \quad (\text{A.22})$$

$$\varphi(\mathbf{x}, t) = \varphi_0(x_1) + \varphi_1(\mathbf{x}, t) \quad (\text{A.23})$$

$$\text{and } \nabla^2 \varphi_0 = 4\pi G \rho_0 \quad (\text{A.24})$$

$$7. \text{ Therefore } \partial_t(\rho_0 + \rho_1) = -\nabla \cdot ((\rho_0 + \rho_1)\mathbf{v}) \quad (\text{A.25})$$

$$\partial_t \rho_0 + \partial_t \rho_1 + \nabla \cdot (\rho_0 \mathbf{v} + \rho_1 \mathbf{v}) = 0 \quad (\text{A.26})$$

$$\text{Neglect second order terms: } \partial_t \rho_1 + \nabla \cdot (\rho_0 \mathbf{v}) = 0 \quad (\text{A.27})$$

$$\text{Integrate: } \rho_1 + \nabla \cdot (\rho_0 \mathbf{u}) = 0 \quad (\text{A.28})$$

Expand **F**. This equation is for elastic material only.

$$\nabla \cdot \boldsymbol{\sigma} - \nabla P_o \Big|_{10} + \nabla(\mathbf{u} \cdot \nabla P_o) + \mathbf{F} = 0 \quad (\text{A.29})$$

$$\nabla \cdot \boldsymbol{\sigma} - \nabla P_o \Big|_{10} + \nabla(\mathbf{u} \cdot \nabla P_o) - \rho_o \nabla \varphi_o - \rho_o \nabla \varphi_l - \rho_l \nabla \varphi_o - \rho_l \nabla \varphi_l = 0 \quad (\text{A.30})$$

Neglect second order terms and recall that $\nabla P_o = -\rho_o \nabla \varphi_o$

$$\nabla \cdot \boldsymbol{\sigma} + \nabla(\mathbf{u} \cdot \nabla P_o) - \rho_o \nabla \varphi_l - \rho_l \nabla \varphi_o = 0 \quad (\text{A.31})$$

But. $\nabla P_o = -\rho_o \nabla \varphi_o = \rho_o \mathbf{g} = -\rho_o g_o \mathbf{z}$. (A.32)

and $\rho_l = -\nabla \cdot (\rho_o \mathbf{u})$, and $\nabla \varphi_o = g_o \mathbf{z} = -\mathbf{g}$. (A.33)

Therefore $\nabla \cdot \boldsymbol{\sigma} - \nabla(\mathbf{u} \cdot (-\rho_o g_o \mathbf{z})) + (\nabla \cdot (\rho_o \mathbf{u})) \nabla \varphi_o - \rho_o \nabla \varphi_l = 0$ (A.34)

$$\nabla \cdot \boldsymbol{\sigma} - \nabla(-\mathbf{u} \cdot \rho_o g_o) + (\nabla \cdot (\rho_o \mathbf{u})) g_o \mathbf{z} - \rho_o \nabla \varphi_l = 0 \quad (\text{A.35})$$

Since ρ_o and g_o are functions of z only, we can reduce A.35 to the following.

$$\nabla \cdot \boldsymbol{\sigma} - \rho_o g_o \nabla u_z + [\rho_o (\nabla \cdot \mathbf{u}) + \mathbf{u} \cdot (\nabla \rho_o)] g_o \mathbf{z} - \rho_o \nabla \varphi_l = 0 \quad (\text{A.36})$$

8. Assume a flat elastic earth.

$$\partial_z \rho_o = 0 \quad (\text{A.37})$$

$$\nabla \varphi_l = 0 \quad (\text{A.38})$$

Therefore

$$\nabla \cdot \boldsymbol{\sigma} - \rho_o g_o \nabla u_z + \rho_o (\nabla \cdot \mathbf{u}) g_o \mathbf{z} = 0 \quad (\text{A.39})$$

This is the equation of motion for an elastic solid. Note that in all of the above equations a bold variable indicates that it is a vector. For a viscous fluid the equation of motion is

$$\nabla \cdot \boldsymbol{\sigma} + \rho_0 (\nabla \cdot \mathbf{u}) \mathbf{g} = 0 \quad (\text{A.40})$$

Appendix B: The Constitutive Relation

This appendix will discuss some of the assumptions associated with the constitutive relations. We assume that the displacements and displacement gradients are small enough that there is no difference between the material and space reference frames. We also assume that the deformation processes are isothermal (constant temperature).

The constitutive equations for a linear elastic solid relate the stress and strain tensors through the generalized Hooke's Law:

$$\sigma_{ij} = C_{ijkl} e_{kl} \quad (\text{B.1})$$

where σ_{ij} is the stress tensor.

e_{kl} is the strain tensor.

and C_{ijkl} is the tensor of elastic constants.

The tensor of elastic constants has 81 elements. 21 of which are distinct due to the symmetry of the stress and strain tensors. If the elastic properties are independent of the reference system, a material is said to be isotropic. For isotropy the number of independent elastic constant reduces to 2. Therefore we obtain Hooke's Law for an isotropic body:

$$\sigma_{kl} = \lambda e_{ii} \delta_{kl} + 2\mu e_{kl} \quad (\text{B.2})$$

where e_{kl} is the strain,

σ_{kl} is the stress,

λ and μ are the Lamé parameters,
and δ_{kl} is the Dirac delta function.

Define the bulk modulus: $\kappa = \lambda + 2/3\mu$. This relates pressure to cubical dilatation of the body.

For the incompressible case we impose the following restriction:

$$\lim_{\substack{\varepsilon \rightarrow 0 \\ \lambda \rightarrow \infty}} \varepsilon \lambda = \Pi \quad (\text{B.3})$$

where $\varepsilon = \Sigma e_{ii} = e_{rr} + e_{\theta\theta} + e_{zz}$

$\nabla \cdot \mathbf{u} = \varepsilon = 0$, ε is the dilatation

and \mathbf{u} is the displacement vector.

Therefore Hooke's Law for the incompressible case is:

$$\sigma_{kl} = -\Pi \delta_{kl} + 2\mu e_{kl} \quad (\text{B.4})$$

where e_{kl} is the strain,

σ_{kl} is the stress,

λ and μ are the Lamé parameters,

δ_{kl} is the Dirac delta function,

and Π is the pressure defined by $\lim_{\substack{\varepsilon \rightarrow 0 \\ \lambda \rightarrow \infty}} \varepsilon \lambda = \Pi$.

Appendix C: Derivation of the Correspondence Theorem

The following set of equations shows the derivation of the constitutive relation for a Maxwell body, where the stress and strain are expressed as tensors. Displacements (elastic and viscous) add tensorally and stresses are constant.

Therefore:

$$\partial_t \varepsilon_{kl} = \partial_t e^e_{kl} + \partial_t e^v_{kl} \quad (\text{C.1})$$

$$\tau_{kl} = \sigma^e_{kl} = \sigma^v_{kl} \quad (\text{C.2})$$

where e^e is the Hookean strain,

e^v is the Newtonian strain,

ε is the Maxwellian strain,

σ^e is the Hookean stress,

σ^v is the Newtonian stress, and

τ is the Maxwellian stress.

Following Cathles, 1975, p.23, the stress tensor is split into two component tensors. The first one is the hydrostatic stress tensor ($\sigma_{rr} = -3P$) and the second one is the deviatoric stress tensor.

The deviatoric stresses are defined as:

$$(\sigma^v_{kl})^D = \sigma^v_{kl} - \frac{1}{3} \sigma^v_{rr} \delta_{kl} \quad (\text{C.3})$$

$$(\sigma^e_{kl})^D = \sigma^e_{kl} - \frac{1}{3} \sigma^e_{rr} \delta_{kl} \quad (\text{C.4})$$

Using the definitions for the σ^e_{rr} and the σ^v_{rr} as given above for the Hookean and Newtonian bodies, we obtain the following form for the deviatoric stresses:

$$(\sigma^v_{kl})^D = 2\nu(\partial_t e^v_{kl} - \frac{1}{3}\partial_t e^v_{rr}\delta_{kl}) = 2\nu(\partial_t e^v_{kl})^D \quad (C.5)$$

$$(\sigma^e_{kl})^D = 2\mu(e^e_{kl} - \frac{1}{3}e^e_{rr}\delta_{kl}) = 2\mu(e^e_{kl})^D \quad (C.6)$$

Therefore for a Maxwell body:

$$(\partial_t \varepsilon_{kl})^D = (\partial_t e^e_{kl})^D + (\partial_t e^v_{kl})^D \quad (C.7)$$

$$(\partial_t \varepsilon_{ii})^D = \frac{(\sigma^v_{ii})^D}{2\nu} + \frac{\partial_t (\sigma^e_{ii})^D}{2\mu} \quad (C.8)$$

Since all stresses are equal

$$(\partial_t \varepsilon_{ii})^D = \frac{(\sigma_{ii})^D}{2\nu} + \frac{\partial_t (\sigma_{ii})^D}{2\mu} \quad (C.9)$$

Also

$$\partial_t \varepsilon_{rr} = \partial_t e^v_{rr} - \partial_t e^e_{rr} \quad (C.10)$$

$$\partial_t \varepsilon_{rr} = \frac{\sigma_{rr} + 3P}{3\eta + 2\nu} + \frac{\partial_t \sigma_{rr}}{3\lambda + 2\mu} \quad (C.11)$$

We can rewrite these last two equations as:

$$(a) \quad \partial_t \sigma^D_{kl} + \frac{\mu}{\nu} \sigma^D_{kl} = 2\mu \partial_t \varepsilon^D_{kl} \quad (C.12)$$

$$(b) \quad \partial_t \sigma_{kk} + \frac{3\lambda + 2\mu}{3\eta + 2\nu} (\sigma_{kk} + 3P) = (3\lambda + 2\mu) \partial_t \varepsilon_{kk} \quad (C.13)$$

If we take (B.12) + $\frac{1}{3}$ (B.13) δ_{kl} , where δ_{kl} is the Dirac delta function, then we get

$$\partial_t \sigma_{kl}^D + \frac{1}{3} \partial_t \sigma_{kk} \delta_{kl} + \frac{\mu}{\nu} \sigma_{kl}^D + \frac{1}{3} \frac{3\lambda + 2\mu}{3\eta + 2\nu} (\sigma_{kk} + 3P) \delta_{kl} = 2\mu \partial_t \epsilon_{kl}^D + \frac{1}{3} (3\lambda + 2\mu) \partial_t \epsilon_{kk} \delta_{kl} \quad (\text{C.14})$$

$$\partial_t \sigma_{kl} + \frac{\mu}{\nu} \sigma_{kl}^D + \frac{1}{3} \frac{3\lambda + 2\mu}{3\eta + 2\nu} (\sigma_{kk} + 3P) \delta_{kl} = 2\mu \partial_t \epsilon_{kl} + \lambda \partial_t \epsilon_{kk} \delta_{kl} \quad (\text{C.15})$$

Recall that $\sigma_{kl}^D = \sigma_{kl} - \frac{1}{3} \sigma_{kk} \delta_{kl}$ and $P = -\frac{1}{3} \sigma_{kk}$ if in a quasi-static state.

Therefore the stress-strain relation for a Maxwell Body is given by

$$\partial_t \sigma_{kl} - \frac{\mu}{\nu} (\sigma_{kl} - \frac{1}{3} \sigma_{kk} \delta_{kl}) = 2\mu \partial_t \epsilon_{kl} - \lambda \partial_t \epsilon_{kk} \delta_{kl} \quad (\text{C.16})$$

Now, if we perform the Laplace Transform on all of the elements of this equation, we obtain:

$$s \sigma_{kl} - \frac{\mu}{\nu} \sigma_{kl} - \frac{\mu}{\nu} \sigma_{rr} = 2\mu s \epsilon_{kl} + \lambda s \epsilon_{kk} \delta_{kl} \quad (\text{C.17})$$

Let the bold symbolize the variable transposed into the s domain.

Let $k = l = r$ to show that $\sigma_{rr} = (2\mu + 3\lambda) \epsilon_{rr}$. Substitute this into the previous equation.

Therefore we obtain:

$$\sigma_{kl} \left(s + \frac{\mu}{\nu} \right) = 2\mu s \epsilon_{kl} + \left[\lambda s + \left(\lambda + \frac{2}{3} \mu \right) \frac{\mu}{\nu} \right] \epsilon_{rr} \delta_{kl} \quad (\text{C.18})$$

or
$$\sigma_{kl} = 2\mu(s)\epsilon_{kl} + \lambda(s)\epsilon_{rr} \quad (\text{C.19})$$

where
$$\mu(s) = \frac{\mu s}{s + \frac{\mu}{\nu}} \quad (\text{C.20})$$

and
$$\lambda(s) = \frac{\left[\lambda s + \left(\lambda + \frac{2}{3} \mu \right) \frac{\mu}{\nu} \right]}{s + \frac{\mu}{\nu}} = \frac{\lambda s + \frac{\kappa \mu}{\nu}}{s + \frac{\mu}{\nu}} \quad (\text{C.21})$$

where κ is the bulk modulus.

μ is the shear modulus.

λ is a Lamé constant.

and ν is the Newtonian viscosity.

Appendix D: The Analytical Solution for the Halfspace Model

This is the case for an incompressible, flat earth in cylindrical coordinates. The matrix below satisfies equation (3.1.1).

$$A = \begin{pmatrix} 0 & -k & \frac{i}{\mu} & 0 \\ k & 0 & 0 & 0 \\ 4\mu k^2 \rho g k & 0 & -k & -k \\ \rho g k & 0 & k & 0 \end{pmatrix} \quad (D.1)$$

According to the Correspondence Theorem this is valid for the viscoelastic case if

$$\mu = \frac{\eta s \mu'}{\eta s + \mu'}$$

The eigenvalues are determined by solving equation (2.3.28):

$$\text{DET} = \begin{vmatrix} -\xi & -k & \frac{1}{\mu} & 0 \\ k & -\xi & 0 & 0 \\ 4\mu k^2 \rho g k & -\xi & -k & -k \\ \rho g k & 0 & k & -\xi \end{vmatrix} \quad (D.2)$$

$$\text{DET} = \xi^4 + k^4 - 2\xi^2 k^2 \quad (D.3)$$

$$\text{DET} = (k + \xi)^2 (-k + \xi)^2 \quad (D.4)$$

Therefore the eigenvalues are k and $-k$.

Now we need to calculate the eigenvectors by solving (2.3.31). This is done by row reduction.

$$\begin{pmatrix} -\xi & -k & \frac{1}{\mu} & 0 \\ k & -\xi & 0 & 0 \\ 4\mu k^2 & \rho \delta g k & -\xi & -k \\ \rho \delta g k & 0 & k & -\xi \end{pmatrix} \begin{pmatrix} U \\ W \\ T_{rz} \\ T_{zz} \end{pmatrix} = \begin{pmatrix} 0 \\ 0 \\ 0 \\ 0 \end{pmatrix} \quad (\text{D.5})$$

$$\begin{pmatrix} \frac{T_{rz}}{\mu} - \xi U - W k \\ -\xi W + U k \\ -\xi T_{rz} + 4\mu U k^2 - T_{zz} k + \rho \delta g W k \\ -\xi T_{zz} + T_{rz} k + \rho \delta g U k \end{pmatrix} = \begin{pmatrix} 0 \\ 0 \\ 0 \\ 0 \end{pmatrix} \quad (\text{D.6})$$

Therefore

$$-\xi W + U k = 0 \quad (\text{D.7})$$

$$W = \frac{U k}{\xi} \quad (\text{D.8})$$

$$\frac{T_{rz}}{\mu} - \xi U - W k = 0 \quad (\text{D.9})$$

$$T_{rz} = \mu \frac{(\xi^2 + k^2) U}{\xi} \quad (\text{D.10})$$

$$-\xi T_{rz} + 4\mu U k^2 - T_{zz} k + \rho \delta g W k = 0 \quad (\text{D.11})$$

$$T_{zz} = \frac{(\mu [-\xi^2 + 3k^2] \xi + \rho \delta g k^2) U}{\xi k} \quad (\text{D.12})$$

Now we will let $U = 1$, for simplicity:

$$U = 1 \quad (\text{D.13})$$

$$W = \frac{k}{\xi} \quad (\text{D.14})$$

$$T_{rz} = \frac{\mu (\xi^2 + k^2)}{\xi} \quad (\text{D.15})$$

$$T_{zz} = \frac{\mu(-\xi^2 + 3k^2)\xi + \rho\delta g k^2}{\xi k} \quad (D.16)$$

Therefore

$$\xi = k \quad \text{and} \quad \xi = -k$$

$$Y = A e^{kz} \begin{pmatrix} 1 \\ 1 \\ 2\mu k \\ 2\mu k + \rho\delta g \end{pmatrix} + B e^{-kz} \begin{pmatrix} 1 \\ -1 \\ -2\mu k \\ 2\mu k - \rho\delta g \end{pmatrix} + C e^{kz} \begin{pmatrix} 1 \\ 1 \\ 2\mu k \\ 2\mu k + \rho\delta g \end{pmatrix} + D e^{-kz} \begin{pmatrix} 1 \\ -1 \\ -2\mu k \\ 2\mu k - \rho\delta g \end{pmatrix} \quad (D.17)$$

To find another eigenvector for each of the eigenvalues, we will follow Boyce and DiPrima (1986, p. 366), and solve equation (2.3.32).

$$\begin{pmatrix} -\xi & -k & \frac{1}{\mu} & 0 \\ k & -\xi & 0 & 0 \\ 4\mu k^2 + \rho\delta g k & -\xi & -k & \\ \rho\delta g k & 0 & k & -\xi \end{pmatrix} \begin{pmatrix} u \\ v \\ \text{tr}z \\ \text{tzz} \end{pmatrix} = \begin{pmatrix} 1 \\ 1 \\ 2\mu k \\ 2\mu k + \rho\delta g \end{pmatrix} \quad (D.18)$$

$$\begin{pmatrix} \frac{\text{tr}z}{\mu} - \xi u - k v \\ k u - \xi v \\ -\xi \text{tr}z - k \text{tzz} + 4\mu k^2 u + \rho\delta g k v \\ k \text{tr}z - \xi \text{tzz} + \rho\delta g k u \end{pmatrix} = \begin{pmatrix} 1 \\ 1 \\ 2\mu k \\ 2\mu k + \rho\delta g \end{pmatrix} \quad (D.19)$$

$$\frac{\text{tr}z}{\mu} - \xi u - k v = 1 \quad (D.20)$$

$$\text{tr}z = \mu \frac{\xi - k + \xi^2 u + k^2 u}{\xi} \quad (D.21)$$

$$k u - \xi v = 1 \quad (D.22)$$

$$v = \frac{k u - 1}{\xi} \quad (D.23)$$

$$k \text{tr}z - \xi \text{tzz} + \rho \delta g k u = 2 \mu k + \rho \delta g \quad (\text{D.24})$$

$$\text{tzz} = \frac{(-\rho \delta g \xi - \mu k^2 - \mu \xi k) + (\mu \xi^2 + \rho \delta g \xi + \mu k^2) k u}{\xi^2} \quad (\text{D.25})$$

Now let $u = 1/k$:

$$u = \frac{1}{k} \quad (\text{D.26})$$

$$\xi = k$$

$$v = \frac{k u - 1}{\xi} \quad (\text{D.27})$$

$$v = 0 \quad (\text{D.28})$$

$$\text{tr}z = \mu \frac{\xi - k + \xi^2 u + k^2 u}{\xi} \quad (\text{D.29})$$

$$\text{tr}z = 2 \mu \quad (\text{D.30})$$

$$\text{tzz} = \frac{(-\rho \delta g \xi - \mu k^2 - \mu \xi k) + (\mu \xi^2 + \rho \delta g \xi + \mu k^2) k u}{\xi^2} \quad (\text{D.31})$$

$$\text{tzz} = 0 \quad (\text{D.32})$$

Now for the second eigenvalue / eigenvector:

$$\xi = -k$$

$$\begin{pmatrix} -\xi & -k & \frac{1}{\mu} & 0 \\ k & -\xi & 0 & 0 \\ +\mu k^2 & \rho \delta g k & -\xi & -k \\ \rho \delta g k & 0 & k & -\xi \end{pmatrix} \begin{pmatrix} u \\ v \\ \text{tr}z \\ \text{tzz} \end{pmatrix} = \begin{pmatrix} 1 \\ -1 \\ -2\mu k \\ 2\mu k - \rho \delta g \end{pmatrix} \quad (\text{D.33})$$

$$\begin{pmatrix} \frac{\tau z}{\mu} - \xi u - k v \\ k u - \xi v \\ -\xi \tau z - k t z z + 4 \mu k^2 u + \rho \delta g k v \\ k \tau z - \xi t z z + \rho \delta g k u \end{pmatrix} = \begin{pmatrix} 1 \\ -1 \\ -2 \mu k \\ 2 \mu k - \rho \delta g \end{pmatrix} \quad (\text{D.34})$$

$$\frac{\tau z}{\mu} - \xi u - k v = 1 \quad (\text{D.35})$$

$$\tau z = \mu \frac{\xi + (k u + 1) k + \xi^2 u}{\xi} \quad (\text{D.36})$$

$$k u - \xi v = -1 \quad (\text{D.37})$$

$$v = \frac{k u + 1}{\xi} \quad (\text{D.38})$$

$$k \tau z - \xi t z z + \rho \delta g k u = 2 \mu k - \rho \delta g \quad (\text{D.39})$$

$$t z z = \frac{\rho \delta g \xi + \mu k^2 - \mu \xi k + (\mu \xi^2 + \rho \delta g \xi + \mu k^2) k u}{\xi^2} \quad (\text{D.40})$$

Now let $u = -1/k$:

$$u = -\frac{1}{k} \quad (\text{D.41})$$

$$\xi = -k$$

$$v = \frac{k u + 1}{\xi} \quad (\text{D.42})$$

$$v = 0 \quad (\text{D.43})$$

$$\tau z = \mu \frac{\xi + (k u + 1) k + \xi^2 u}{\xi} \quad (\text{D.44})$$

$$\tau z = 2 \mu \quad (\text{D.45})$$

$$t z z = \frac{\rho \delta g \xi + \mu k^2 - \mu \xi k + (\mu \xi^2 + \rho \delta g \xi + \mu k^2) k u}{\xi^2} \quad (\text{D.46})$$

$$t z z = 0 \quad (\text{D.47})$$

Therefore the solution is (equation (3.1.2))

$$Y = C e^{kz} \begin{pmatrix} z + \frac{1}{k} \\ z \\ 2\mu k z + 2\mu \\ [\rho \delta g + 2\mu k] z \end{pmatrix} + D e^{-kz} \begin{pmatrix} z - \frac{1}{k} \\ -z \\ -2\mu k z + 2\mu \\ [-\rho \delta g + 2\mu k] z \end{pmatrix} + A e^{kz} \begin{pmatrix} 1 \\ 1 \\ 2\mu k \\ 2\mu k + \rho \delta g \end{pmatrix} + B e^{-kz} \begin{pmatrix} 1 \\ -1 \\ -2\mu k \\ 2\mu k - \rho \delta g \end{pmatrix} \quad (D.48)$$

Now, when we use the boundary conditions: as z goes to negative infinity, the solution must remain finite and at $z = 0$, we have $T_{rz} = 0$ and $T_{zz} = -\sigma$.

Therefore, from the first boundary condition, $B = 0$ and $D = 0$.

$$B = 0 \quad (D.49)$$

$$D = 0 \quad (D.50)$$

From the second boundary condition:

$$\begin{pmatrix} U \\ W \\ T_{rz} \\ T_{zz} \end{pmatrix} = A e^{kz} \begin{pmatrix} 1 \\ 1 \\ 2\mu k \\ 2\mu k + \rho \delta g \end{pmatrix} + C e^{kz} \begin{pmatrix} \frac{kz+1}{k} \\ z \\ 2\mu[kz+1] \\ [2\mu k + \rho \delta g] z \end{pmatrix} \quad (D.51)$$

at $z = 0$:

$$\begin{pmatrix} U \\ W \\ T_{rz} \\ T_{zz} \end{pmatrix} = \begin{pmatrix} \frac{C}{k} + A \\ A \\ 2\mu A k + 2\mu C \\ A[2\mu k + \rho \delta g] \end{pmatrix} \quad (D.52)$$

$T_{rz} = 0$

$$C = \frac{\sigma k}{2\mu k + \rho \delta g} \quad (D.53)$$

$$T_{zz} = -\sigma$$

$$A = -\frac{\sigma}{2\mu k + \rho \delta g} \quad (D.54)$$

These are given in equation (3.1.3).

Therefore the solution is (equation (3.1.4)):

$$\begin{pmatrix} U \\ W \\ Trz \\ Tzz \end{pmatrix} = \frac{\sigma e^{kz}}{2\mu k + \rho \delta g} \begin{pmatrix} kz \\ kz - 1 \\ 2\mu k^2 z \\ [-2\mu k - \rho \delta g][kz + 1] \end{pmatrix} \quad (D.55)$$

To determine the time dependent solution, we must first find M such that $M CN = BN$, where CN is a matrix of the constants, A, B, C, D and BN is the boundary condition matrix.

$$CN = \begin{pmatrix} A \\ C \end{pmatrix} \quad \text{and} \quad BN = \begin{pmatrix} 0 \\ -\sigma \end{pmatrix} \quad (D.56)$$

$$M = \begin{pmatrix} 2\mu k & 2\mu \\ 2\mu k + \rho \delta g & 0 \end{pmatrix} \quad (D.57)$$

We must first identify the poles:

$$|M| = 0$$

$$\left| \begin{pmatrix} 2\mu k & 2\mu \\ \rho \delta g + 2\mu k & 0 \end{pmatrix} \right| = 0 \quad (D.58)$$

$$\det M = -2 \frac{\mu' \eta (\rho \delta g [\eta s + \mu'] + 2\mu' \eta k s)}{(\eta s + \mu')^2} \quad (D.59)$$

$$s = -\frac{\rho \mu' \delta g}{(\rho \delta g + 2\mu' k) \eta} \quad (\text{equation (3.2.3)})$$

Now we need to determine the elastic asymptote (s goes to infinity), so that we can deduce the viscoelastic response.

$$Y_v = A Y_A + C Y_C - A_e Y_{Ae} - C_e Y_{Ce} \quad (D.60)$$

$$YA = e^{kz} \begin{pmatrix} 1 \\ 1 \\ 2 \frac{\mu' \eta s k}{\mu' + \eta s} \\ \frac{2 \mu' \eta s k + [\mu' + \eta s] \rho \delta g}{\mu' + \eta s} \end{pmatrix} \quad (D.61)$$

$$YC = e^{kz} \begin{pmatrix} z + \frac{1}{k} \\ z \\ 2 \frac{\mu' \eta [kz + 1] s}{\eta s + \mu'} \\ \frac{2 \mu' \eta k s + \rho \delta g [\eta s + \mu']}{\eta s + \mu'} z \end{pmatrix} \quad (D.62)$$

$$YAc = e^{kz} \begin{pmatrix} 1 \\ 1 \\ 2 \mu' k \\ 2 \mu' k + \rho \delta g \end{pmatrix} \quad (D.63)$$

$$YCc = e^{kz} \begin{pmatrix} z + \frac{1}{k} \\ z \\ 2 \mu' k z + 2 \mu' \\ [\rho \delta g + 2 \mu' k] z \end{pmatrix} \quad (D.64)$$

$$A = - \frac{(\mu' + \eta s) \sigma}{2 \mu' \eta s k + (\mu' + \eta s) \rho \delta g} \quad (D.65)$$

$$Ac = - \frac{\sigma}{2 \mu' k + \rho \delta g} \quad (D.66)$$

$$C = \frac{(\mu' + \eta s) \sigma k}{2 \mu' \eta s k + (\mu' + \eta s) \rho \delta g} \quad (\text{D.67})$$

$$C_e = \frac{\sigma k}{2 \mu' k + \rho \delta g} \quad (\text{D.68})$$

Therefore

$$Y_v = 2 \frac{(-\mu + \mu') \sigma k e^{kz}}{(\rho \delta g + 2 \mu k) (\rho \delta g + 2 \mu' k)} \begin{pmatrix} kz \\ kz - 1 \\ -\rho \delta g k z \\ 0 \end{pmatrix} \quad (\text{D.69})$$

$$Y_v = 2 \frac{\sigma \mu'^2 k e^{kz}}{(\rho \delta g + 2 \mu' k) (\rho \delta g [\eta s + \mu'] + 2 \mu' \eta k s)} \begin{pmatrix} kz \\ kz - 1 \\ -\rho \delta g k z \\ 0 \end{pmatrix} \quad (\text{D.70})$$

$$\text{where } \mu = \frac{\mu' \eta s}{\mu' + \eta s}$$

Therefore

$$Y_v = \frac{Q_v}{\det M} \quad (\text{D.71})$$

$$Q_v = -4 \frac{\sigma \mu'^3 \eta k e^{kz} s}{(\rho \delta g + 2 \mu' k) (\eta s + \mu')^2} \begin{pmatrix} kz \\ kz - 1 \\ -\rho \delta g k z \\ 0 \end{pmatrix} \quad (\text{D.72})$$

evaluated at $s = -\gamma$

$$Q_v = \frac{\sigma \rho \delta g e^{kz}}{k} \begin{pmatrix} kz \\ kz - 1 \\ -\rho \delta g k z \\ 0 \end{pmatrix} \quad (\text{equation (3.3.1)})$$

$$R = \frac{Q_v}{\frac{\partial}{\partial s} \det M} \quad \text{evaluated at } s = -\gamma$$

$$R = 2 \frac{\sigma \mu'^2 k e^{kz}}{(\rho \delta g + 2 \mu' k)^2 \eta} \begin{pmatrix} kz \\ kz - 1 \\ -\rho \delta g k z \\ 0 \end{pmatrix} \quad (\text{equation (3.3.3)})$$

$$Y_e = A e^{kz} + C e^{-kz} \quad (\text{D.73})$$

$$Y_e = \frac{\sigma e^{kz}}{\rho \delta g + 2 \mu' k} \begin{pmatrix} kz \\ kz - 1 \\ 2 \mu' k^2 z \\ [\rho \delta g + 2 \mu' k][kz - 1] \end{pmatrix} \quad (\text{D.74})$$

Therefore our solution is

$$Y_t = Y_e \delta + \frac{Q_v}{\frac{\partial}{\partial s} \det M \gamma} e^{-\gamma t} \quad (\text{D.75})$$

$$Y_t = 2 \frac{\sigma \mu'^2 k e^{kz}}{(\rho \delta g + 2 \mu' k)^2 \eta} \begin{pmatrix} kz \\ kz - 1 \\ -\rho \delta g k z \\ 0 \end{pmatrix} e^{-\gamma t} + \frac{\sigma \delta e^{kz}}{\rho \delta g + 2 \mu' k} \begin{pmatrix} kz \\ kz - 1 \\ 2 \mu' k^2 z \\ [\rho \delta g + 2 \mu' k][kz - 1] \end{pmatrix} \quad (\text{D.76})$$

$$e^{-\gamma t} = \frac{1 - e^{-\gamma t}}{\gamma}$$

For the Heaviside response, perform the following substitution $e^{-\gamma t} = \frac{1 - e^{-\gamma t}}{\gamma}$. Therefore the solution is

$$Y_t = 2 \frac{\sigma \mu' e^{kz} k}{\rho g (2 \mu' k + \rho \delta g)} \begin{pmatrix} kz \\ kz - 1 \\ -\rho \delta g k z \\ 0 \end{pmatrix} (-e^{-\gamma t} + 1) + \frac{\sigma e^{kz}}{2 \mu' k + \rho \delta g} \begin{pmatrix} kz \\ kz - 1 \\ 2 \mu' k^2 z \\ [\rho \delta g + 2 \mu' k][kz - 1] \end{pmatrix}$$

This is equivalent to equation (3.4.1).

Appendix E: The Analytical Solution for the Channel Model

This appendix will show the derivation of the time domain solution for the channel model. The results are summarized in section 4.1. The following derivation was accomplished using the mathematical manipulation program Mathview.

Love's Strain Function

$$\chi = A e^{kz} + B z e^{kz} + C e^{-kz} + D z e^{-kz} \quad (\text{E.1})$$

The displacement and stress are related to Love's Strain Function by the following formulas:

$$u = \frac{ik}{2\mu} \left(\frac{\partial}{\partial z} \chi \right) \quad (\text{E.2})$$

$$w = \frac{-k^2}{2\mu} \chi \quad (\text{E.3})$$

$$S_{xz} = \frac{ik}{2} \left(\frac{\partial}{\partial z} \left[\frac{\partial}{\partial z} \chi \right] + k^2 \chi \right) \quad (\text{E.4})$$

$$S_{zz} = \frac{1}{2} \left(\frac{\partial}{\partial z} \left[\frac{\partial}{\partial z} \left(\frac{\partial}{\partial z} \chi \right) \right] \right) - \frac{3}{2} k^2 \left(\frac{\partial}{\partial z} \chi \right) + \rho g w \quad (\text{E.5})$$

When the strain function is substituted into the previous equations, the following is obtained.

$$u = \frac{1}{2} \frac{A k^2 i e^{kz}}{\mu} + \frac{1}{2} \frac{B k i (kz + 1) e^{kz}}{\mu} - \frac{1}{2} \frac{C k^2 i e^{-kz}}{\mu} + \frac{1}{2} \frac{D k i (-kz + 1) e^{-kz}}{\mu} \quad (\text{E.6})$$

$$w = -\frac{1}{2} \frac{A k^2 e^{kz}}{\mu} - \frac{1}{2} \frac{B k^2 e^{kz} z}{\mu} - \frac{1}{2} \frac{C k^2 e^{-kz}}{\mu} - \frac{1}{2} \frac{D k^2 e^{-kz} z}{\mu} \quad (\text{E.7})$$

$$S_{xz} = A k^3 i e^{kz} + B k^2 i (kz + 1) e^{kz} + C k^3 i e^{-kz} + D k^2 i (kz - 1) e^{-kz} \quad (\text{E.8})$$

$$S_{zz} = -A k^3 (\beta + 1) e^{kz} - B k^3 (\beta + 1) e^{kz} z + C k^3 (-\beta + 1) e^{-kz} + D k^3 (-\beta + 1) e^{-kz} z \quad (\text{E.9})$$

$$\text{where } \beta = \frac{1}{2} \frac{\rho g}{k \mu} \quad (\text{E.10})$$

These equations satisfy the differential equations.

Therefore the displacements and stresses can be expressed as

$$\begin{pmatrix} u \\ w \\ S_{xz} \\ S_{zz} \end{pmatrix} = \begin{pmatrix} \frac{1}{2} \frac{k^2 i e^{kz}}{\mu} & \frac{1}{2} \frac{k i [kz + 1] e^{kz}}{\mu} & -\frac{1}{2} \frac{k^2 i e^{-kz}}{\mu} & \frac{1}{2} \frac{k i [-kz + 1] e^{-kz}}{\mu} \\ -\frac{1}{2} \frac{k^2 e^{kz}}{\mu} & -\frac{1}{2} \frac{k^2 e^{kz} z}{\mu} & -\frac{1}{2} \frac{k^2 e^{-kz}}{\mu} & -\frac{1}{2} \frac{k^2 e^{-kz} z}{\mu} \\ k^3 i e^{kz} & k^2 i [kz + 1] e^{kz} & k^3 i e^{-kz} & k^2 i [kz - 1] e^{-kz} \\ -k^3 [\beta + 1] e^{kz} & -k^3 [\beta + 1] e^{kz} z & k^3 [-\beta + 1] e^{-kz} & k^3 [-\beta + 1] e^{-kz} z \end{pmatrix} \begin{pmatrix} A \\ B \\ C \\ D \end{pmatrix} \quad (\text{E.11})$$

Express the boundary conditions in a matrix: 1. bottom of channel has zero displacement

2. surface boundary condition at $z = 0$.

$$\begin{pmatrix} k & -Hk + 1 & -e^{2Hk} k & [Hk + 1] e^{2Hk} \\ -1 & H & -e^{2Hk} & H e^{2Hk} \\ -k^3 [\beta + 1] & 0 & k^3 [-\beta + 1] & 0 \\ k & 1 & k & -1 \end{pmatrix} \begin{pmatrix} A \\ B \\ C \\ D \end{pmatrix} = \begin{pmatrix} 0 \\ 0 \\ -\sigma \\ 0 \end{pmatrix} \quad (\text{E.12})$$

$$\begin{pmatrix} A \\ B \\ C \\ D \end{pmatrix} = \begin{pmatrix} -\frac{[e^{4Hk} + e^{2Hk} + 2\{Hk - 1\} H e^{2Hk} k] \sigma}{\text{Det}} \\ -\frac{[2 H e^{2Hk} k^2 - e^{4Hk} k - e^{2Hk} k] \sigma}{\text{Det}} \\ -\frac{[-e^{2Hk} - 2\{Hk + 1\} H e^{2Hk} k - 1] \sigma}{\text{Det}} \\ -\frac{[-\{2 H k + 1\} e^{2Hk} k - k] \sigma}{\text{Det}} \end{pmatrix} \quad (\text{E.13})$$

$$\text{Det} = 2 \frac{[(-\cosh\{Hk\} \sinh\{Hk\} + Hk) \rho g - 2 \{(\cosh(Hk))^2 + H^2 k^2\} \mu k] e^{2Hk} k^2}{\mu} \quad (\text{E.14})$$

At $z = 0$ we obtain

$$\begin{pmatrix} u \\ w \\ S_{xz} \\ S_{zz} \end{pmatrix} = \begin{pmatrix} \frac{1}{2} \frac{k^2 i}{\mu} & \frac{1}{2} \frac{k i}{\mu} & -\frac{1}{2} \frac{k^2 i}{\mu} & \frac{1}{2} \frac{k i}{\mu} \\ -\frac{1}{2} \frac{k^2}{\mu} & 0 & -\frac{1}{2} \frac{k^2}{\mu} & 0 \\ k^3 i & k^2 i & k^3 i & -k^2 i \\ -k^3 [\beta + 1] & 0 & k^3 [-\beta + 1] & 0 \end{pmatrix} \begin{pmatrix} A \\ B \\ C \\ D \end{pmatrix} \quad (\text{E.15})$$

$$\begin{pmatrix} u \\ w \\ S_{xz} \\ S_{zz} \end{pmatrix} = \begin{pmatrix} -2 \frac{\sigma H^2 e^{2Hk} k^4 i}{\mu \text{Det}} \\ \frac{1}{2} \frac{[e^{4Hk} - 4H e^{2Hk} k - 1] \sigma k^2}{\mu \text{Det}} \\ 0 \\ \frac{\sigma k^3 [e^{4Hk} \{\beta + 1\} + 2 e^{2Hk} \{-2Hk\beta + 2H^2 k^2 + 1\} - \beta + 1]}{\text{Det}} \end{pmatrix} \quad (\text{E.16})$$

Therefore

$$u = - \frac{\sigma H^2 i k^2}{-2 \mu CB k + \rho CSA g} \quad (\text{E.17})$$

$$w = \frac{1}{4} \frac{\sigma (e^{4Hk} - 4H e^{2Hk} k - 1)}{(-2 \mu CB k + \rho CSA g) e^{2Hk}} \quad \text{or} \quad w = \frac{\sigma CSA}{2 k \mu CB - g \rho CSA} \quad (\text{E.18})$$

where $CSA = -\cosh(Hk) \sinh(Hk) + Hk$ and $CB = (\cosh[Hk])^2 + H^2 k^2$

$$\mu = \frac{\mu' s}{s + \frac{\mu'}{\eta}}$$

Transform into the time domain from the s - domain using

$$u = - \frac{\sigma H^2 i (\eta s + \mu') k^2}{\eta (-2 \mu' CB k + \rho CSA g) s + \rho \mu' CSA g} \quad (E.19)$$

$$w = \frac{\sigma (\eta s + \mu') CSA}{-g \rho \mu' CSA + \eta (2 k \mu' CB - g \rho CSA) s} \quad (E.20)$$

Define

$$\alpha = - \frac{g \rho \mu' CSA}{\eta (2 k \mu' CB - g \rho CSA)} \quad (E.21)$$

Therefore

$$u = - \frac{\sigma H^2 i (\eta s + \mu') k^2}{\eta (s + \alpha) (-2 \mu' CB k + \rho CSA g)} \quad (E.22)$$

$$w = \frac{\sigma (\eta s + \mu') CSA}{\eta (s + \alpha) (2 k \mu' CB - g \rho CSA)} \quad (E.23)$$

Separate into Elastic +Viscous parts:

$$\frac{\eta s + \mu'}{s + \alpha} = \eta + \frac{\mu' - \alpha \eta}{s + \alpha} \quad (E.24)$$

Therefore

$$u = - \frac{\sigma H^2 i k^2 \left(\frac{\mu' - \alpha \eta}{s + \alpha} + \eta \right)}{\eta (-2 \mu' CB k + \rho CSA g)} \quad (E.25)$$

$$w = \frac{\sigma \left(\frac{\mu' - \alpha \eta}{s + \alpha} + \eta \right) CSA}{\eta (2 k \mu' CB - g \rho CSA)} \quad (E.26)$$

For Heaviside Load:

$$U = \frac{\sigma i H^2 k^2}{\eta (2 k \mu' CB - \rho g CSA)} \left(\eta + \frac{\mu' - \alpha \eta}{\alpha} [1 - e^{-\alpha t}] \right) \quad (E.27)$$

$$W = \frac{\sigma CSA}{\eta (2 k \mu' CB - g \rho CSA)} \left(\eta + \frac{\mu' - \alpha \eta}{\alpha} [1 - e^{-\alpha t}] \right) \quad (E.28)$$

Defining

$$\gamma = -\frac{CB}{CSA} \quad (E.29)$$

$$U = -\frac{\sigma H^2 k^2 i}{(2\mu' k \gamma + \rho g) CSA} \left(1 + \frac{2\mu' k \gamma}{\rho g} [1 - e^{-\alpha i}] \right) \quad (E.30)$$

$$W = \frac{-\sigma}{2\mu' k \gamma + \rho g} \left(1 + \frac{2\mu' k \gamma}{\rho g} [1 - e^{-\alpha i}] \right) \quad (E.31)$$

These last two equations agree with equations (4.1.1) and (4.1.2).

Appendix F: The Analytical Solution for the Model of a Lithosphere Overlying a Fluid

In this appendix the derivation of the analytical solution in the k domain for the model of a lithosphere overlying a fluid is shown. This derivation was accomplished with Mathview. Note that there is no s dependence since the lithosphere is elastic and the halfspace is a fluid. The results are summarized in section 4.2a.

The displacements and stresses can be expressed as follows (as with the channel derivation):

$$\begin{pmatrix} u \\ w \\ S_{xz} \\ S_{zz} \end{pmatrix} = \begin{pmatrix} \frac{1}{2} \frac{k^2 i e^{kz}}{\mu} & \frac{1}{2} \frac{ki[kz+1]e^{kz}}{\mu} & -\frac{1}{2} \frac{k^2 i e^{-kz}}{\mu} & \frac{1}{2} \frac{ki[-kz+1]e^{-kz}}{\mu} \\ -\frac{1}{2} \frac{k^2 e^{kz}}{\mu} & -\frac{1}{2} \frac{k^2 e^{kz} z}{\mu} & -\frac{1}{2} \frac{k^2 e^{-kz}}{\mu} & -\frac{1}{2} \frac{k^2 e^{-kz} z}{\mu} \\ k^3 i e^{kz} & k^2 i [kz+1] e^{kz} & k^3 i e^{-kz} & k^2 i [kz-1] e^{-kz} \\ -k^3 [\beta+1] e^{kz} & -k^3 [\beta+1] e^{kz} z & k^3 [-\beta+1] e^{-kz} & k^3 [-\beta+1] e^{-kz} z \end{pmatrix} \begin{pmatrix} A \\ B \\ C \\ D \end{pmatrix} \quad (\text{F.1})$$

$$\text{where } \beta = \frac{1}{2} \frac{\rho g}{k \mu} \quad \text{and} \quad db = \frac{1}{2} \frac{d\rho g}{k \mu} \quad (\text{F.2})$$

The following boundary conditions are applied.

At $z = 0$, we have $S_{xz} = 0$ and $S_{zz} = -\sigma$

At $z = -H$, we have $S_{xz} = 0$ and $S_{zz} = (\rho + d\rho)\delta gw$

These boundary conditions can be written in matrix form.

$$\begin{pmatrix} ik^3 & ik^2 & ik^3 & -ik^2 \\ -[\beta+1]k^3 & 0 & [-\beta+1]k^3 & 0 \\ ie^{-Hk}k^3 & i[-Hk+1]e^{-Hk}k^2 & ie^{Hk}k^3 & i[-Hk-1]e^{Hk}k^2 \\ [db-1]e^{-Hk}k^3 & -[db-1]He^{-Hk}k^3 & [db+1]e^{Hk}k^3 & -[db+1]He^{Hk}k^3 \end{pmatrix} \begin{pmatrix} A \\ B \\ C \\ D \end{pmatrix} = \begin{pmatrix} 0 \\ -\sigma \\ 0 \\ 0 \end{pmatrix} \quad (\text{F.3})$$

$$\begin{pmatrix} A \\ B \\ C \\ D \end{pmatrix} = -\frac{\sigma k^7}{\text{DET}} \begin{pmatrix} [db+1][e^{2Hk}+2Hk-1]-2H^2k^2 \\ [\{db+1\}\{-e^{2Hk}+1\}-2Hk]k \\ [db-1][e^{-2Hk}-2Hk-1]+2H^2k^2 \\ [\{db-1\}\{e^{-2Hk}-1\}+2Hk]k \end{pmatrix} \quad (\text{F.4})$$

$$\text{DET} = ([\beta+db][e^{-2Hk}-e^{2Hk}-4Hk]+[\beta db+1][-e^{-2Hk}-e^{2Hk}+2]+4H^2k^2)k^{10} \quad (\text{F.5})$$

Therefore at $z=0$, we get:

$$\begin{pmatrix} u \\ w \\ S_{xz} \\ S_{zz} \end{pmatrix} = \begin{pmatrix} -4 \frac{\sigma H i [-2\mu H k^2 + d\rho g] k}{2[\rho+d\rho]\mu \text{CSAC} g k + 16\mu^2 H^2 k^4 + \text{CBC} [4\mu^2 k^2 + \rho d\rho g^2]} \\ - \frac{\sigma [2\mu \text{CSAC} k + \text{CBC} d\rho g]}{2[\rho+d\rho]\mu \text{CSAC} g k + 16\mu^2 H^2 k^4 + \text{CBC} [4\mu^2 k^2 + \rho d\rho g^2]} \\ 0 \\ -\sigma \end{pmatrix} \quad (\text{F.6})$$

where $\text{CSAC} = -4(\cosh[Hk]\sinh[Hk]+Hk)$ and $\text{CBC} = 4(-[\cosh\{Hk\}]^2+1)$